High Contrast Astronomy with Starshades

by

Anthony D. Harness

B.S., Astronomy/Astrophysics, Florida Institute of Technology, 2010

B.S., Mathematical Sciences, Florida Institute of Technology, 2010

B.S., Physics, Florida Institute of Technology, 2010

M.S., Astrophysics, University of Colorado, 2012

A thesis submitted to the

Faculty of the Graduate School of the

University of Colorado in partial fulfillment

of the requirements for the degree of

Doctor of Philosophy

Department of Astrophysical & Planetary Sciences

2016

This thesis entitled:
High Contrast Astronomy with Starshades
written by Anthony D. Harness
has been approved for the Department of Astrophysical & Planetary Sciences

Prof. Webster Cash

Prof. John Bally

Prof. Zachory Berta-Thompson

Prof. Jeremy Darling

Prof. Hanspeter Schaub

Date

The final copy of this thesis has been examined by the signatories, and we find that both the content and the form meet acceptable presentation standards of scholarly work in the above mentioned discipline.

Harness, Anthony D. (Ph.D., Astrophysics)

High Contrast Astronomy with Starshades

Thesis directed by Prof. Webster Cash

One of the most important scientific discoveries to be had this century is the spectroscopic characterization of Earth-like exoplanets to determine the occurrence rate of worlds capable of supporting life and to potentially answer: are we alone in the universe? To accomplish these lofty goals requires an advancement in the technology to separate the overwhelming starlight from that of the exoplanet. I believe starshades are the key technology that will enable these discoveries within our lifetime. This dissertation work is a contribution to the advancement of starshade technology to put us on the path towards discovery.

In this dissertation I present a number of suborbital methods developed for testing small-scale starshades, which include a Vertical Takeoff Vertical Landing rocket, the surface of a dry lake bed, and the heliostat of a solar telescope. The results from our high contrast observations are used to validate the optical model I developed to conduct tolerance analyses that will drive future starshade designs. The results from testing a formation flying sensor on the VTVL rocket demonstrate the rocket's potential for conducting starshade experiments in the stratosphere.

This dissertation (along with [58]) presents the first astronomical observations with a starshade that provide photometric measurements of stars, previously unobserved in the visible spectrum, in the proximity of Vega. These observations led to the development of a visual feedback system for the heliostat that allows us to push farther in separation and inner working angle. These high contrast observations were made using a starshade in the most flight-like configuration (in terms of Fresnel number, inner working angle, and resolution) to date.

The results of this dissertation have helped demonstrate the effectiveness and practicality of starshades for starlight suppression and have outlined a path forward to further advance starshade technology through optical testing and high contrast astronomy.

Dedication

To Brooklynn. I cannot wait to see all the amazing things you will accomplish.

Acknowledgements

I joined the starshade project because I was told there would be great adventures with Zeppelins, rockets, and climbing mountaintops, and it has most certainly lived up to its promise. I was given the opportunity to work in desolate, yet beautiful places, meet interesting people, and witness the amazing accomplishments of human knowledge. I owe this to my advisor, Web Cash, for taking me on and providing me these opportunities. It has been a privilege to work with Web over the years and his innovativeness, enthusiasm, and propensity to dream big is a model that I will strive to live up to throughout my career. Web has taught me the important lessons of how to succeed as a PI in the space sciences and to have the courage to stand up for what is right.

Every accomplishment in this work was made possible with the help of Ann Shipley who constantly provided me support and guidance and who taught me the skills needed to lead successful hardware projects in the future. She taught me how to fix things when they do not work as planned and, more importantly, to have the foresight to know that it will definitely not work as planned.

Through an unwavering partnership from which starshades originated, I have thoroughly enjoyed the continuous support and collaboration with a few great individuals at Northrop Grumman. It was a weekly pleasure to learn the ways of the (space science) world through the wise words of Ron Polidan. I would like to thank Tiffany Glassman and Steve Warwick for allowing me tag along on their research trips that were the highlight of my grad school work and which allowed me to get my foot in the door in the community, spin off my own projects, and are directly responsible for my future success in the field. These trips were great experiences and I enjoyed the time spent working with Megan Novicki, Danny Smith, and Michael Richards.

This work was made possible by 4 years of financial support from the NASA Space Technology Research Fellowship (grant # NNX13AM71H). Through this fellowship, I had the opportunity to work with a number of talented people at NASA institutions. My work on formation flying sensors and the suborbital rocket flight was done in collaboration with folks at NASA Ames Research Center, with Dayne Kemp sacrificing much of his time to develop the sensor electronics for the flight. I had a great experience at NASA Ames thanks in large part to Matt Sorgenfrei, Matt Nehrenz, and Elwood Agasid. Much of my modeling work was made possible through many productive conversations with Stuart Shaklan and Phil Dumont at the Jet Propulsion Laboratory.

I received support from many individuals on the different projects I worked on. To name a few that I would like to thank explicitly, Detrick Branston provided helpful support through all hours of the night while observing at McMath. Ben Zeiger helped on a number of McMath observations. Wayne Green and John Bally provided great advice on equipment and observing strategies at McMath. Travis O'Neal, Kyle Nyberg, and the rest of Masten Space Systems made for an enjoyable and successful flight campaign in Mojave.

The culmination of my life thus far is due to the collaborative effort of innumerable individuals whose love and support deserve the credit for my accomplishments. I would first like to thank all of my parents: Glenda, Mike, Sue, and Dennis for each playing a unique and important role in shaping who I am and providing me every opportunity to succeed. To my sister Angie, who not only taught me math and started me down this road, but who has been there everyday since, I owe everything. To my second family, the Whitlocks, thank you for always being there for me and making me a part of the family. And thanks for the socks. To round one of the Armer House: Devin, Jason, and Sam, thank you for taking me in and showing me that you can work hard, but still have fun. To round two of the Armer House: Grant, J'oj, Marek, Tristan, and Emily, I had an absolute blast living with you all and your support helped me through this more than you can imagine. To Ainsley, thank you for your support through the tough times. To the countless other individuals whom I have had the pleasure of meeting and experiencing life with, from childhood to college through grad school, thanks for the good times.

Every revolutionary idea – in science, politics, art or whatever – seems to evoke three stages of reaction. They may be summed up by the phrases:

(1) "It's completely impossible – don't waste my time"

(2) "It's possible, but it's not worth doing"

(3) "I said it was a good idea all along"

- Arthur C. Clarke, "The Promise of Space" (1968)

Contents

Chapter

Tables

Table

Figures

Figure

Chapter 1

INTRODUCTION

1.1 The Search for Life in the Universe

The scientific motivation for this dissertation work is to ultimately answer a question that has been asked for millennia[1], "Are we alone in the universe?". St. Albertus Magnus wrote, "Do there exist many worlds, or is there but a single world? This is one of the most noble and exalted questions in the study of Nature" [51]. I believe we are on the verge of possessing the technology to answer one of the most important questions of humankind. The work of this dissertation is a contribution to the path forward in discovering the prevalence of life in the universe.

1.1.1 Life as we know it

It seems an impossible task to find something when you do not know what you are looking for. As we only know of one instance of life, which we believe to have evolved from a common ancestor, we do not know if there are multiple paths for life to exist. There are basic chemistry arguments that suggest life will be similar to life on Earth, i.e., will be carbon-based and will require liquid water as a solvent for metabolic processes [18], but similar arguments can be made for life existing in vastly different forms. If there are a large number of configurations in which life can exist, but we do not know what those may be, the best methodology for leading a search that is not blindly

---

[1] In the 4th Century BC, Epicurus wrote to Herodotus, "Furthermore, we must believe that in all worlds there are living creatures and plants and other things we see in this world; for indeed no one could prove that in a world of one kind there might or might not have been included the kinds of seeds from which living things and plants and all the rest of the things we see are composed, and that in a world of another kind they could not have been" [24].

grasping for straws, and the method we have adopted thus far, is to search for life as we know it to be true.

1.1.2 Earth-like exoplanets

We apply our anthropological biases and narrow our search to look for what are called Earth-like exoplanets, or exo-Earths. Exo-Earths are planets around other stars that are deemed to be habitable and are capable of supporting life that is similar to life on Earth. Here, I list a number of criteria I believe are necessary for defining what a habitable planet is.

An exo-Earth must be a rocky planet or moon roughly the same size of the Earth, which is small enough to have a rocky or liquid surface that provides stability for organics to coalesce into larger proteins. The massive, gaseous envelopes of gas giants such as Jupiter and Saturn are chaotic and turbulent and the formation of life in these conditions would be difficult. The exoplanet must be massive enough to maintain a substantial atmosphere to provide radiation protection for surface life and must be massive enough to retain its internal heating to drive plate tectonic activity, which drives the carbonate cycle thought to maintain long term climate stability [38]. We set the range of planetary radii that satisfy these conditions as $\sim 0.5 - 2$ R$_\oplus$ [21, 1].

An exo-Earth must also be capable of persistently supporting liquid water (a necessary ingredient for all life on Earth) on its surface. To first order, a planet can have liquid water on its surface if it is at the orbital distance such that the equilibrium temperature from stellar heating is $\sim$300 K, a region commonly referred to as the “habitable zone”. Due to the 1/r-squared diminishing in flux, this distance scales as the square-root of the host star luminosity. We can simplify the criteria of supporting liquid water by saying a planet must orbit at the Earth equivalent insolation distance (EEID), which is the orbital distance of a planet from its host star such that it receives the same incident flux of starlight as the Earth receives from the Sun.

$$EEID = (1\text{AU})\sqrt{\frac{L_*}{L_\odot}} \tag{1.1}$$

The habitable zone is not a discrete point in space, but can extend radially inward or outward depending on the presence of a greenhouse atmosphere, rotation speed, etc. There has been extensive work to define the appropriate limits of the habitable zone and how to widen the limits for a more optimistic estimate of where life could persist. An optimistic definition of the habitable zone was given by [41] to be 0.75 - 1.75 AU EEID. For more details on the habitability of exoplanets, we point the reader to [38, 41].

The habitable planets I have described are picky Goldilocks planets, not too large and not too small, not too hot and not too cold. As we learn more about life on our own planet, we reveal the durability of life and are surprised in the conditions in which life can survive. Similar to how exoplanet discoveries radically changed our notion of where and how planets could exist, I believe discoveries of extraterrestrial life will surprise us in our ignorance.

1.1.3 Biological signatures of life

In the two decades since the first exoplanet was discovered, there has been a focus of study on what it takes to discover extraterrestrial life, how we will know when we have found it, and how we can be certain that it is not a false positive. To definitively say we have “found life” will take extraordinary evidence and the only evidence we will have is the globally averaged atmospheric composition of the planet. We must somehow be able to distinguish signals that could only be produced as a metabolic byproduct of life, which are referred to as biosignatures, from signals that could be produced abiotically.

There are many byproducts of life that are produced through other mechanisms and we cannot rely on one biosignature to be the smoking gun. A common suggestion for distinguishing the two is to search for an atmosphere that is chemically out of equilibrium in respect to certain gases and to claim that the only way this imbalance can exist over time is if it is continuously being replenished by biological processes [72]. In this case, it will require detections of a number of chemical species to determine the chemical equilibrium and verify it is of biological cause. Some of the commonly mentioned signatures that need characterization (all are not necessarily biosignatures, as the presence of some could help rule out an abiotic source) and the wavelength of their detections are listed in Table 1.1. Most importantly to note is that these gases spread over a large bandpass and many are in the visible band. This point will be important later as we argue the need for an instrument that can do spectroscopy over a large bandpass in the visible. For more details on biosignatures, we point the reader to [68, 21, 15, 71, 72, 70].

Species	**Wavelength [μm]**
O_3	<0.32, 0.584
O_2	0.689, 0.763, 1.27
CO_2	1.05
H_2O	0.724, 0.821, 0.941
CH_4	0.726,0.791, 0.892,0.997

Table 1.1: Biosignatures and the wavelengths of their important transitions in the visible band [21].

Note that I am not talking about searching for intelligent life as is done most famously by the Search for ExtraTerrestrial Intelligence (SETI) programs searching for radio signals. The existence of intelligent life requires an additional layer of constraint in allowing a species to evolve long enough to gain intelligence and begin broadcasting radio signals. We are simply searching for evidence of energy metabolization by the most basic lifeforms. Also note that I am focusing on the search for life outside of our solar system. There are promising aspects for life to exist within our solar system, such as in the liquid water ocean under the ice crust of the Jovian moon Europa, or in the methane lakes of the Saturnian moon Titan, which could possibly be detected in situ in future missions. However, we know that interplanetary contamination has occurred in the history of the solar system and life could have been transported between planets via panspermia. I think the philosophical implications of finding life outside of our solar system, life that could not have shared a common ancestor with us, are much more profound. It is often said that life in the universe is either singular or infinite, we are either completely alone or life is prevalent throughout. Just one detection of life with a non-common ancestor would imply the latter to be true.

1.2 The Path Towards Discovery

I have narrowed the search for life to rocky planets of radius 0.5 - 2 $R_\oplus$ and at a distance of 0.75 - 1.75 AU EEID around Sun-like (F,G,K) stars. This is a simplistic estimate of what type of planets could host life, but it is an informative place to start. Now the problem is not only to find, but to spectrally characterize this type of planet.

1.2.1 Exoplanet detection methods

The first exoplanet was discovered in 1995 with the radial velocity method [50]. Since that time, thousands more have been discovered, with the most proficient method of discovery being the transit method, thanks in large part to the Kepler mission [7]. A brief description of exoplanet detection methods are summarized below.

- Radial Velocity
    - High-resolution spectroscopy can reveal small shifts in the rest frame wavelengths of spectral lines from the host star, which are caused by the gravitational tug of the planet on the star.
    - Indirect detection.
    - Biased towards detecting massive, close-in, and edge-on planets.
    - Yields the mass (modulo an inclination factor) of the planet.
    - Exo-Earth is 10 cm/s signal and current state of the art is 80 cm/s [25].
- Transit Detection
    - As a planet passes in the line of sight towards a star, it blocks a fraction of the host star's light and can be seen as a dip in the time series lightcurve.
    - Indirect detection.
    - Biased towards detecting massive and close-in planets. Must be close to edge-on.

  - Yields the radius and orbital distance of the planet.
  - Planet masses can be determined through Transit Timing Variations if there are multiple planets in the system.
  - Characterization possible with transit spectroscopy (see below).
  - Exo-Earth is 10^{-4} signal (transit depth).
- Transit Spectroscopy
  - High signal-to-noise spectra can separate the absorption spectrum of the planet from that of the star with in- and out- of transit comparisons.
  - Direct characterization.
  - Only probes upper (optically thin) atmosphere of planet.
  - Exo-Earth is 10^{-4} signal (transit depth).
- Microlensing
  - Signal is caused by gravitational focusing of light as a star with a planet passes in front of a background star.
  - Indirect detection
  - Yields planet's mass.
  - Not available for follow up observations.
- Astrometry
  - Precise astrometry of a star can reveal the star's motion around the system's center of mass, which is offset from the star by the planet.
  - Indirect detection.
  - Yields planet's mass and orbit.
  - Exo-Earth is < 1 μ-arcsecond signal.

- Direct Imaging
  - Directly measure photons (reflected or thermal) from planet.
  - Direct detection and characterization.
  - Exo-Earth is 10^{10} times fainter than host star.

We have assumed an Earth-like exoplanet that could support life is of a certain size and at a certain orbital distance; this is a necessary, but not sufficient condition. A planet of the right size and distance could be habitable, but as [41] discusses, certain situations (e.g., runaway greenhouse effect) could cause a planet to be inhabitable. In order to truly determine a planet's habitability and search for biosignatures, we need spectroscopic characterization. The indirect methods mentioned above could possibly find an exo-Earth, but we would be limited in what we could say in terms of habitability and could not say anything about the presence of life. To do so requires spectra.

1.2.2 High contrast direct imaging

The future of exoplanet science is in direct imaging. Spectroscopic characterization opens the door to a new level of exoplanet science. We can study the composition, temperature, and structure of exoplanetary atmospheres in unprecedented detail, providing observational constraints to atmospheric models and helping to break current degeneracies. Compositions of a number of atmospheres will allow us to do comparative planetology to better understand the formation, evolution, and long term stability of atmospheres. This can help us better understand what the future of Earth's atmosphere is and how human-caused global warming can set that future on a different path. We can search for liquid water on the surface of planets, see if they have a benign atmosphere like the Earth's, and determine the true habitability of a planet. Finally, and most importantly, we can search for the biosignatures that are indicative of extraterrestrial life.

To do spectroscopy on exoplanets is no small technological feat. Using the numbers for an exo-Earth from above, it is 10^{10} times fainter than its host star in reflected light. At 10 pc, a search radius deemed necessary to have the chance of finding an exo-Earth, it orbits at a mere

100 milli-arcseconds away from its host star. Try to image this planet and you will be completely overwhelmed with starlight. Even if we neglect the contamination from the host star, we must do spectroscopy on a 30th magnitude object, a feat yet to be achieved by any observatory. To find an exo-Earth, we need a means to suppress the starlight by a factor of billions, while maintaining a high throughput that preserves the faint signal from the planet.

The technological challenge to direct imaging is controlling diffraction to separate the faint planetary light from that of the host star. The classic coronagraph works by placing an opaque circle at the image of the star to block the on-axis light, allowing the off-axis light of the planet to pass around the edge. The stellar light diffracted around the opaque circle is blocked with a field stop, or Lyot stop, named after the pioneer of this technique, Bernard Lyot, who used it to observe the solar corona [45]. Once the light enters the telescope, its energy cannot be removed and must be redirected to where it will cause the least trouble. The Lyot stop attempts this, but for the contrast levels needed for exoplanets, even the smallest percentage of stellar light that is scattered into the image will dominate the planet light. Advances in coronagraphy have led to a plethora of techniques aiming at redirecting the light diffracted by the coronagraph and are nicely summarized in [60].

The Achille's heel to internal coronagraphs is wavefront error. Using the classical coronagraph again as an example, in order to physically separate the on-axis and off-axis light when they differ by only 10s of milli-arcseconds, the coronagraphic mask must be perfectly sized and perfectly aligned to the PSF of the on-axis light. Any deviation from perfection, caused by wavefront errors introduced by imperfections in the optics, the atmosphere, thermal expansions, etc., will diffract light in an uncontrolled manner and that light will end up in the image. The solution to controlling wavefronts is to use deformable mirrors to reshape the errors out of the incoming wavefront, but the level of wavefront control that is needed is extremely difficult. Incident light of intensity I_0 that is not properly suppressed by the coronagraph due to a wavefront error of wavelength $\lambda = 2\pi/k$

and amplitude A will diffract with a diffraction efficiency of,

$$I = \left(\frac{1}{2}kA\right)^2 I_0 \tag{1.2}$$

If the incident intensity is the full strength of the host star, to suppress the light to 10^{-10}, wavefront errors need to be controlled to less than 2 picometers. This places an enormous constraint on the quality, thermal control, and stability of the entire optical system. In addition, trying to control diffracted light from within the telescope requires the light to be manipulated in such a way that it reduces the bandwidth and throughput of the coronagraph. One proposed solution to avoiding this problem is to block the starlight before it enters the telescope.

1.2.3 Starshades

The concept of a starshade is quite simple and one that people employ in their daily lives. Say you are on a stroll around the local pond on a sunny day and hear the majestic call of the red-winged blackbird flying overhead. You try to locate the bird, but are blinded by the Sun, so you outstretch your arm and use your hand to shield the sunlight from your eyes and are then able to see the blackbird against the blue sky. The starshade operates with the same concept, expect for your arm goes a third of the way to the moon and the blackbird you are searching for holds the most important discovery of modern times.

The idea of the starshade is as simple as that, but the diffractive nature of light causes problems when trying to see exoplanets. The main difficulty coronagraphs have in controlling diffraction is that the full strength signal enters the telescope and even small wavefront errors can contribute a large signal. An external occulter is a way to mitigate those problems by placing the light-suppressing optic at a large distance outside of the telescope. The large separation means wavefront errors on the diffracting element have a long path length to evolve and become in-phase. If the light suppression happens outside of the telescope, the I_0 entering the telescope is already small and wavefront errors in the telescope are negligible.

The starshade architecture is shown in Figure 1.1; the starshade flies in front of a space telescope and creates a long, deep shadow that suppresses on-axis starlight, but allows the off-axis light from the planet to enter unimpeded. A baseline architecture that has been studied in detail is the New Worlds Observer [12] that consists of a 60 m diameter starshade flying in formation with a 4 m telescope at a distance of 80,000 km. This mission has the potential to do the first spectroscopic characterization of an Earth-like exoplanet and begin the search for life in the universe.

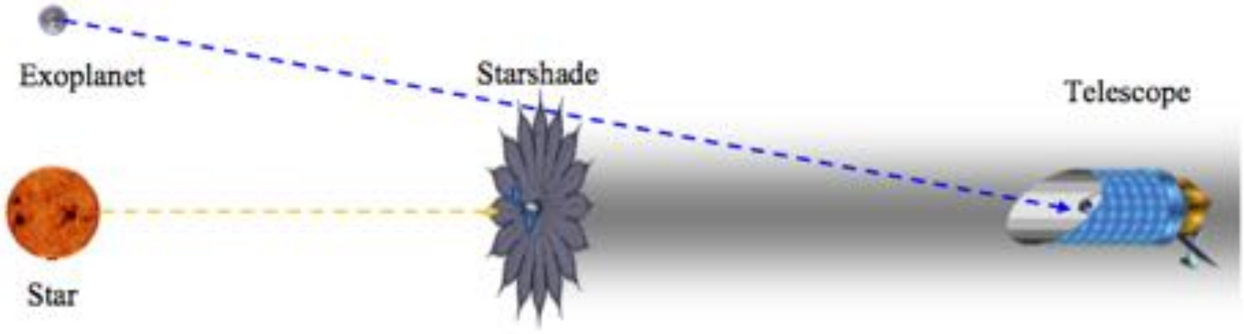

Figure 1.1: Schematic of the architecture of the New Worlds Observer mission [12], showing the basic operation of the starshade. A 60 m diameter starshade flies 80,000 km from a space telescope and creates a deep shadow that extinguishes the on-axis light from the host star while letting the off-axis planet light through.

The idea of using an external occulter to search for exoplanets was first presented by Lyman Spitzer in 1962 in a lecture on the early days of space astronomy [83]. Spitzer credits R. Danielson for suggesting the use of a large occulting disk outside of the telescope to detect planets around other stars. They knew that diffracted light would be the limiting factor to detecting faint and close-in planets, but suggested the diffraction could be reduced if the disk transparency was increased smoothly (or apodized) towards the edge of the disk. In 1985, Marchal [48] proposed a star-shaped external occulter to be flown with the upcoming “Space Telescope” (later to be named the Hubble Space Telescope) to search for planets around other stars. Marchal recognized that apodization could be achieved with a circularly symmetric binary occulter and that the width of the central shadow could be increased if the petals were “offset” and did not extend all the way to the center of the occulter. Both Spitzer and Marchal were unable to produce an apodization function that allowed for a practical occulter design and still needed occulters 100s of meters across at 100,000s kilometers separation.

The key breakthrough that brought the external occulter into realms of technical reality is the apodization function given in Equation 1.3 discovered by Webster Cash at the University of Colorado [10]. The apodization function, called an offset hypergaussian, is what gives the petals of the starshade their unique shape and was the first function of its kind to efficiently suppress diffraction by the 10 orders of magnitude needed to see an exo-Earth. In Equation 1.3, ρ is the radial coordinate of the starshade, a is the offset radius (within which the occulter is fully transparent), b is the radius from the offset radius to the $1/e$ inflection point, and n is the order of the hypergaussian, or how quickly the petals taper.

$$A\left(\rho\right)=\begin{cases}0 & \rho<a\\ 1-e^{-\left(\frac{\rho-a}{b}\right)^{n}} & \rho>a\end{cases} \tag{1.3}$$

The starshade has many advantages for starlight suppression over internal coronagraphs. The unwanted light is suppressed before it enters the telescope and the wavefront errors that challenge coronagraphs are dramatically reduced and wavefront control with deformable mirrors is no longer necessary. This means that there is significantly less stringent tolerances on the quality and stability of the optics and any standard telescope can be used. This reduces the cost and complexity of the mission (at least on the optics side) and provides the opportunity for telescopes with a primary mission other than direct imaging to be adapted to work with a starshade. Without the large number optics needed to manipulate the light to extract only the planetary light, the starshade has 100% throughput and is only limited by the normal throughput of the observatory. This is a major advantage over coronagraphs, which can have a throughput of only 1%, when trying to do spectroscopy on 30th magnitude objects. The starshade is also inherently broadband and standard spectroscopic instruments can be used.

There are disadvantages to the starshade, however; the most obvious being the size scale of the distributed architecture that requires launching and deploying a 60 m diameter screen in space. This large screen must then fly in formation to 1 m precision over 10s of megameters separation

(1 Mm = 10^6 m = 10^3 km). It is important to clarify that this is not an interferometer and the shape and positioning tolerances are not standard optical tolerances. The shape of the starshade needs to be built and held to millimeter - centimeter tolerances. The lateral position tolerance of the starshade is around 1 meter and we are insensitive along the line of sight to hundreds of meters. These are challenging specifications that need to be engineered properly, but there is no fundamental limitation that can be seen and the specifications can be achieved with today's technology.

To observe a new target, the starshade must slew across the celestial sphere at a radius of 10s of megameters, which takes time and fuel. Studies of the mission planning for starshades [88] find that the slew time and limited fuel supply are the main drivers for the number of targets the starshade can observe. For this reason, starshades are not meant to be a survey instrument, they are life-finding instruments that are best purposed to sit on a few dozen systems and characterize the atmospheres of their planets in detail and determine if they are habitable, or inhabited.

1.3 Motivation for this Dissertation Work

This dissertation is about the technical development and demonstration of starshades for high contrast astronomy. Throughout my research, my main theme has been to demonstrate the practicality of starshades and use them to do science at any level possible. To quote Professor Webster Cash, I want to "put starshades in the astronomer's toolbox"; that is, start doing astronomy with starshades and build the experience base using this new technology. I was also motivated to help develop the tools necessary to test and develop the technology at both a component and system level.

Today, starshades are mentioned in many of the conversations about the future of direct imaging and exoplanet science and there is even talk about a starshade to fly with the Wide Field InfraRed Survey Telescope (WFIRST) mission [73]. However, that was not always the case and there has been a long history of a stigma against and misconceptions about starshades and they were dismissed as not being practical, or even possible. A large motivation of the work done since the initial studies has been to demonstrate to the community that starshades indeed work in a practical manner and to dispel any misconceptions or disbeliefs in the technology. To convince people starshades work, we just had to go out and do it; use a starshade to achieve high contrast. However, with the large size scales and separations involved in the starshade architecture, testing them terrestrially (and cheaply) is difficult and requires us to get creative with our means of testing. This dissertation will outline a few methods that have enabled us to test and do astronomy with starshades.

1.4 Dissertation Organization

This dissertation is organized as follows. Chapter 2 introduces the theory of diffraction and how we are able to use starshades to manage it. Chapter 3 details my work in developing and testing formation flying sensors to aid in maintaining alignment with a distributed starshade-telescope system, both for use in space and in the stratosphere. Chapter 4 summarizes a flight campaign I led testing starshades on a suborbital rocket. Chapter 5 details my development of a optical diffraction model key for predicting the performance and tolerances of starshades for future missions. Chapter 6 has the validation of that model using data from tests in the field. Chapter 7 details the development and testing of a siderostat observatory to do high contrast astronomy with starshades, the results of which are presented in Chapter 8. Finally, I summarize, conclude, and outline future plans in Chapter 9.

Chapter 2

DIFFRACTION THEORY OF STARSHADES

2.1 Introduction to Diffraction

The theory of diffraction is personally one of the more interesting topics in the field of electromagnetism and optics that has been the focus of study many times over the past few centuries. The underlying physics to diffraction is contained in Maxwell's Equations, but generating an analytic solution to anything but the most simple situations is difficult. Much of the work in diffraction theory has been to search for assumptions that will allow for a closed form solution. In this chapter, we will outline the basics of diffraction, what elements of the theory are useful in describing the diffractive properties of starshades, and detail the assumptions made in our analyses. The main reference used for this introduction to diffraction is Born and Wolf's "Principles of Optics" [6].

2.1.1 The Huygens-Fresnel principle

A mathematical construction useful for envisioning the wave nature of light and its propagation was put forward by Christian Huygens [34, 6] and states that each point on a propagating wavefront can be considered the source of a secondary disturbance from which spherical wavelets emerge. The position of the wavefront at a later time is defined by the envelope of the secondary wavelets (Figure 2.1). As a wavefront is defined as a surface of equal phase, Huygens' theorem can easily be understood as the constructive interference of secondary waves defining the wavefront. Fresnel combined this construction with Young's Principle of Interference to describe diffraction phenomena [27, 6]. If a wavefront encounters an obstacle such as passing through an aperture, a new wavefront is generated from secondary wavelets sourced at the edge of the aperture and the resultant diffraction pattern can be thought of as a combination of the incident wavefront propagating through the aperture and a secondary *boundary diffraction wave* formed from the edge of the aperture [53, 54]. While the combination of the two wavefronts is not physically realistic, the boundary wave can be thought of intuitively as a passing EM wave exciting oscillations in the electrons on the surface of the obstacle, which absorb and then emit the light and serve as a new source of wavelets. The propagation of wavefronts by spherical wavelets is known as the Huygens-Fresnel principle and is an intuitive first place to start in understanding diffraction.

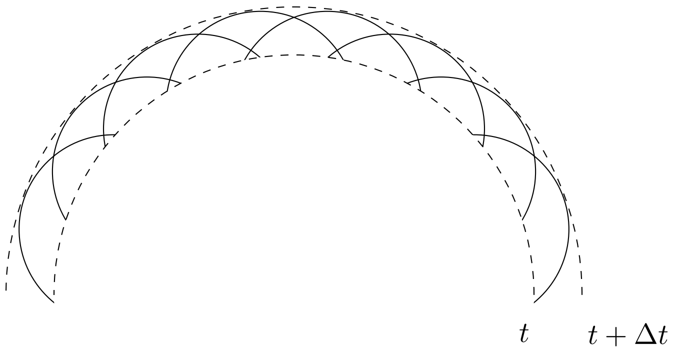

Figure 2.1: Schematic demonstrating Huygen's construction of wavefronts. Every point on a wavefront at time t can be thought of as the source for secondary spherical wavelets. The position of the wavefront at a later time $t + \Delta t$ is given by the envelope of the secondary wavelets.

The Huygens-Fresnel principle allows us to formulate the resultant diffraction pattern as a combination of wavefronts emanating from a diffracting screen and we can construct this formalism in terms of Fresnel half-zones (often referred to as just "Fresnel zones"). Fresnel zones are artificial constructions on a screen where wavefronts emanating from those points will reach an observation point in phase. Adjacent half-zones are π out of phase from each other and contribute destructively. Given the setup of Figure 2.2, the Fresnel half-zones at a given radius occur where the optical path difference between points is $\lambda/2$ (i.e., their phase differs by π).

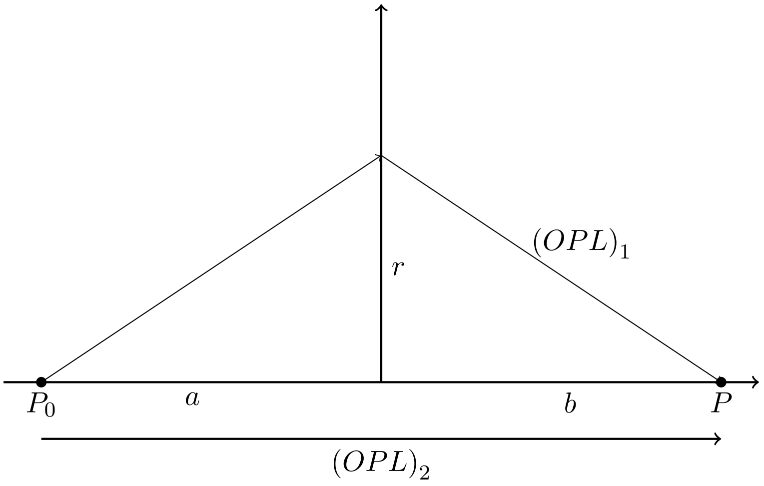

Figure 2.2: The radii of Fresnel half-zones are constructed for light propagating from P_0 to P by where the difference in the two optical path lengths is equal to one-half the wavelength. a and b are the distances from the diffracting screen to P_0 and P, respectively

$$\begin{aligned}\frac{n\lambda}{2} &= (OPL)_1 - (OPL)_2 \\ &= \left(\sqrt{a^2+r^2}+\sqrt{b^2+r^2}\right)-(a+b) \\ &\approx a\left(1+\frac{r^2}{2a^2}\right)+b\left(1+\frac{r^2}{2b^2}\right)-(a+b) \qquad (2.1)\end{aligned}$$

The radius of the n^{th} Fresnel half-zone is then given by,

$$\begin{aligned}r^2 &\approx n\lambda\frac{ab}{a+b} \\ &= n\lambda F_{eff} \qquad (2.2)\end{aligned}$$

where F_{eff} is the effective distance between the screen and observation plane.

The area of all half-zones are equal, so as the radius increases the separation between half-zones decrease and phase changes occur more rapidly. The total disturbance at P is given by the summed contribution of each half-zone,

$$\begin{aligned}U(P) &\approx \sum_{j=1}^{n}(-1)^{j+1}K_j \\ &= \frac{K_1}{2}\pm\left.\frac{K_n}{2}\right|_{-\ n\ even}^{+\ n\ odd} \qquad (2.3)\end{aligned}$$

with the first half-zone contributing half of the disturbance. If an opaque screen is placed in the path, the contribution comes from only unblocked half-zones. Summing over Fresnel zones is a useful way of thinking of diffraction when we begin to talk about external occulters. The basic description of how starshades work is that the petals cover a certain amount of each zone to balance the contribution of the zones so that the total disturbance tends to zero. We will see that areas in which a half-zone is left unbalanced by an adjacent half-zone will serve as a dominating source of light. From Equation 2.2 we can define a useful dimensionless parameter known as the *Fresnel Number*, which is the number of Fresnel half-zones across the radius of a diffracting screen.

$$N_F = \frac{r^2}{\lambda F_{eff}} \qquad (2.4)$$

As the Fresnel number increases, the Fresnel zones vary more rapidly and the contribution from any individual unbalanced half-zone has less of an impact. We will see this in Section 2.2.3

when we discuss how starshade performance scales with Fresnel number. The Fresnel number can serve as a similarity parameter in which the resultant diffraction is identical for a given Fresnel number. In order to demonstrate starshades at a smaller scale, we can scale the experiment to have the same Fresnel number and we will get the same diffraction performance.

2.1.2 Scalar diffraction theory

The full rigorous solution of diffraction requires solving Maxwell's Equations and keeping track of the vector properties of the light field everywhere. This is mathematically challenging and can only be solved in closed form for simple cases. We can greatly simplify the physics if we assume the EM field can be fully described by a complex scalar potential and neglect any vector propagation properties such as polarization. This approximation is generally valid when dealing with physical dimensions much greater than the wavelength, which is the case for most optics problems. We must also assume that the scalar potential can be described as a linear combination of monochromatic components and that there are no non-linear effects.

The theory of diffraction under this assumption is called *scalar diffraction theory* and is commonly invoked. We believe scalar diffraction theory is valid for the flight starshade architecture and we will continue to operate as such. However, a major motivation of this dissertation work is to validate that this assumption is correct. As we cannot optically test a full-sized starshade on the ground, it is critical we show this assumption is valid, otherwise we could miscalculate the in-flight performance. This assumption will be called into question in Section 6.6 when we discuss testing starshades with features that approach the size of the wavelength.

Assuming a scalar potential U, we can write the time-independent wave equation with wavenumber ($k = 2\pi/\lambda$) as the Helmholtz equation,

$$\left(\nabla^2 + k^2\right) U = 0 \tag{2.5}$$

We are trying to solve for the disturbance at a point P within a volume bounded by an arbitrary, closed surface S. If we assume the derivatives on the surface are continuous, we can

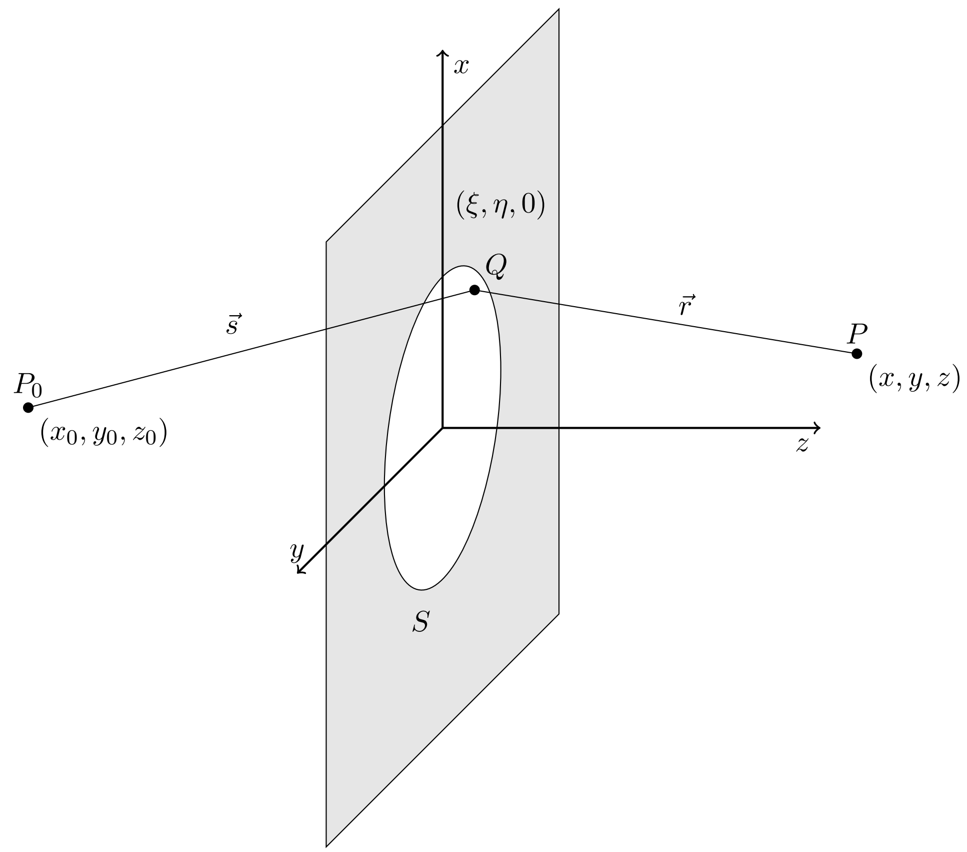

Figure 2.3: The coordinate system used to set up the derivation of diffraction problems. The source is located at P_0, the diffracting screen of surface S is located at the origin, and the observation point is at P.

use Green's theorem to express the volume integral over the bounded surface to reach the *integral theorem of Helmholtz and Kirchoff*,

$$U\left(P\right)=\frac{1}{4\pi}\iint_{S}\left(U\frac{\partial U'}{\partial n}-U'\frac{\partial U}{\partial n}\right)\,dS \tag{2.6}$$

where $\partial/\partial n$ is differentiation along the normal and both U and U' satisfy Equation 2.5. We examine an example diffraction problem of calculating the disturbance at a point P of a spherical wave originating from P_0 as it propagates through an aperture in an opaque screen (Figure 2.3).

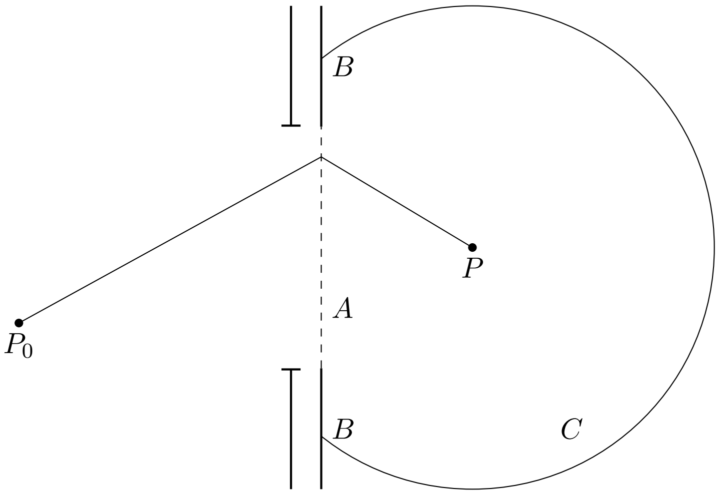

Figure 2.4: A spherical wave originating from P_0 passes through a transparent aperture in an opaque screen and is observed at P. The closed surface of integration can be broken into three components, the transparent opening A, the non-illuminated screen B, and a large circle C centered on P. As the radius of $C \to \infty$, causality states that the field on C is zero and there is no contribution to the integral from C.

In Figure 2.4, we break the closed surface S into three components, the opening A, the non-illuminated screen B, and a large circle C centered on P. We can make the radius of C large enough that if we assume the wave is generated at a finite time, causality states that there is no contribution to the integral from the surface C. We can then impose boundary conditions on the screen and aperture using Kirchoff's boundary conditions,

$$\begin{aligned} \text{on } A: &\quad U = U^{(i)}, \frac{\partial U}{\partial n} = \frac{\partial U^{(i)}}{\partial n}, \\ \text{on } B: &\quad U = 0, \frac{\partial U}{\partial n} = 0, \end{aligned} \tag{2.7}$$

where the incident field is a diverging spherical wave,

$$\begin{aligned} U^{(i)} &= \frac{Ae^{iks}}{s} \\ \frac{\partial U^{(i)}}{\partial n} &= \frac{Ae^{iks}}{s}\left(\frac{1}{s} - ik\right)\cos(n, s) \end{aligned} \tag{2.8}$$

The only contribution to the surface integral over S occurs on the surface A. The Kirchoff boundary conditions are known as Cauchy boundary conditions as they specify the function and its derivative on the surface. The Rayleigh-Sommerfeld diffraction equations of the first and second kind use Dirichlet and Neumann boundary conditions, respectively, to lessen the requirement of knowledge on the surface. It can be shown that the average of the RS equations of the first and second kind yield the results from the Fresnel-Kirchoff diffraction equation (Equation 2.10). We assume that the distance from the screen is much larger than the wavelength and invoke the paraxial assumption to assume

$$\begin{aligned} \cos(n, s) &\approx 1 \\ \left(\frac{1}{s} - ik\right) &\approx -ik \end{aligned} \tag{2.9}$$

We assume the same approximations hold for $\left(U' = e^{ikr}/r\right)$ and plug U, U' into Equation 2.6 to reach the *Fresnel-Kirchoff diffraction equation*,

$$U(P) = \frac{-ikA}{2\pi} \iint_S \frac{1}{rs} e^{ikr} e^{iks}\, dS \tag{2.10}$$

where the magnitudes of vectors r, s are given by,

$$\begin{aligned} s^2 &= (\xi - x_0)^2 + (\eta - y_0)^2 + z_0^2 \\ r^2 &= (\xi - x)^2 + (\eta - y)^2 + z^2 \end{aligned} \tag{2.11}$$

2.1.3 The Fresnel approximation

We assume the distance to the screen is much larger than any other physical dimension ($z >> x, y, \xi, \eta, \lambda$) to invoke the *Fresnel Approximation.* The approximation is made using the Taylor series expansion $(1+\epsilon)^{1/2} \approx 1 + \frac{1}{2}\epsilon - \frac{1}{8}\epsilon^2$ in Equation 2.11, where we keep the first order term in the amplitude and the second order term in the phase. This approximates the spherical Huygens wavelets from the diffracting screen as parabolic waves with a quadratic phase term,

$$\begin{aligned} s &\approx z_0 + \frac{(\xi - x_0)^2 + (\eta - y_0)^2}{2z_0} \\ r &\approx z + \frac{(\xi - x)^2 + (\eta - y)^2}{2z} \end{aligned} \tag{2.12}$$

The Fresnel approximation is valid if the third order term in the Taylor expansion does not contribute significantly to the phase, i.e., $\frac{kz}{8}\epsilon^2 << 1$ or,

$$\begin{aligned} z_0^3 &>> \frac{\pi}{4\lambda}\left[(\xi - x_0)^2 + (\eta - y_0)^2\right]^2 \\ z^3 &>> \frac{\pi}{4\lambda}\left[(\xi - x)^2 + (\eta - y)^2\right]^2 \end{aligned} \tag{2.13}$$

The diffracted field then becomes the familiar *Fresnel diffraction equation* with an incident spherical diverging wave,

$$U(x, y, z) = \frac{-ikA}{2\pi z z_0} e^{ik(z+z_0)} \iint e^{\frac{ik}{2z_0}\left[(\xi - x_0)^2 + (\eta - y_0)^2\right]} e^{\frac{ik}{2z}\left[(\xi - x)^2 + (\eta - y)^2\right]} \, d\xi \, d\eta \tag{2.14}$$

If we recombine the incident field into $U_0(\xi, \eta)$, the Fresnel diffraction equation becomes,

$$U(x, y, z) = \frac{e^{ikz}}{i\lambda z} e^{\frac{ik}{2z}\left(x^2 + y^2\right)} \iint U_0(\xi, \eta) \, e^{\frac{ik}{2z}\left(\xi^2 + \eta^2\right)} e^{-\frac{ik}{z}(x\xi + y\eta)} \, d\xi \, d\eta \tag{2.15}$$

The terms of Equation 2.15 can easily be understood physically. In front of the integral is a plane wave propagation and a quadratic phase factor propagating from the aperture to the observation point $\propto \left(x^2 + y^2\right)$. Inside the integral is a quadratic phase factor propagating from the source to the aperture $\propto \left(\xi^2 + \eta^2\right)$ along with a Fourier Transform to the observation plane $\propto (x\xi + y\eta)$. The Fresnel diffraction can then be thought of as a Fourier Transform ($\mathcal{F}[x]$) of the aperture distribution times a quadratic phase factor,

$$U(x, y, z) \propto \mathcal{F}\left[U_0(\xi, \eta) \, e^{\frac{ik}{2z}\left(\xi^2 + \eta^2\right)}\right] \tag{2.16}$$

2.1.4 The Fraunhofer approximation

If we further approximate Equation 2.12 to keep only the first order term in the phase (i.e., ignore the quadratic phase term), then we are in the far-field *Fraunhofer* regime and the diffraction pattern is simply the Fourier Transform of the incident field,

$$\begin{aligned} U\left(x,y,z\right) &\propto \frac{1}{\lambda z}\iint U_0\left(\xi,\eta\right)e^{-\frac{ik}{z}\left(x\xi+y\eta\right)}\,d\xi\,d\eta \\ &\propto \mathcal{F}\left[U_0\left(\xi,\eta\right)\right] \end{aligned} \tag{2.17}$$

The Fraunhofer approximation is valid for $z >> \frac{\pi\left(\xi^2+\eta^2\right)}{\lambda}$.

2.1.5 Babinet's principle

In building Equation 2.14, we were able to reduce the closed surface integral to only being calculated over the opening in the screen by extending the non-illuminated screen to infinite size. This is useful for apertures of finite extent, but for the case of an external occulter, our non-illuminated occulter is finite in size and the illuminated aperture is infinite. This poses a problem when trying to integrate the potential out to infinity (it is possible for simple cases, see Section 3.3.2). However, a mathematical construct known as *Babinet's principle* allows us to simplify the integral by integrating only over the finite size of the occulter.

The most simple form of Babinet's principle states that if we assume the disturbance due to a screen between a source and observation point to be U_1 and the disturbance due to a complementary screen (complementary means opaque where transmitting and vice-versa), then,

$$U_1 + U_2 = U_0 \tag{2.18}$$

where U_0 is the disturbance due to neither screen being present.

To apply Babinet's principle to the integration of an occulter, we assume screen 1, for which we are trying to calculate the diffraction, is show in Figure 2.5a. If we instead solve for the complementary screen 2 (Figure 2.5b) where we are able to use finite integration limits, then our solution for the occulter is simply $U_1 = U - U_2$. This is a powerful tool when calculating the diffraction for external occulters.

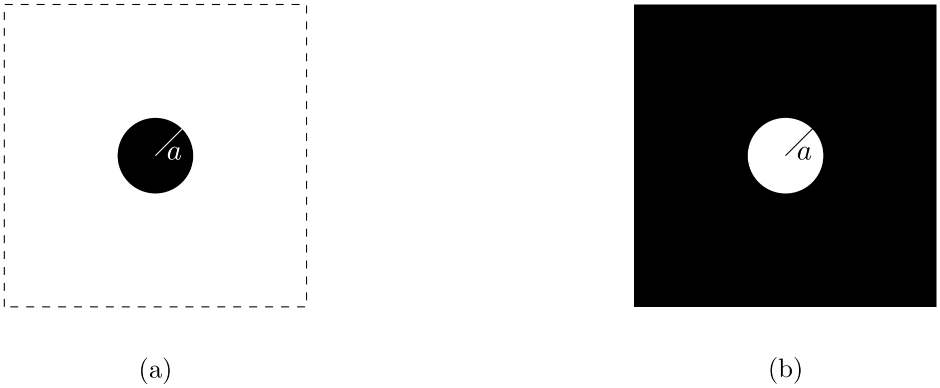

(a) (b)

Figure 2.5: (a) is the screen for which we are trying to calculate the diffraction pattern. (b) is the complementary screen that we use to solve the integral. Babinet's Principle states that the sum of the electric fields of the two screens are equal to the field that would exist if neither screen were present.

To show Babinet's principle in effect, we look to calculate the diffraction pattern of a circular opaque disk of radius a. We start with the on-axis calculation of the Fresnel diffraction equation for a circularly symmetric apodization function with uniform incident field U_0,

$$U = -\frac{ikU_0}{2\pi z} \iint A(\rho)\, e^{\frac{ik\rho^2}{2z}} \rho \, d\rho \, d\theta \tag{2.19}$$

where,

$$A(\rho) = \begin{cases} 0, & \rho <= a \\ 1 & \rho > a \end{cases} \tag{2.20}$$

Simplifying Equation 2.19 becomes,

$$U = -\frac{ikU_0}{z} \int_a^\infty e^{\frac{ik\rho^2}{2z}} \rho \, d\rho \tag{2.21}$$

Rather than try to evaluate this integral to infinity, we can invoke Babinet's principle and calculate the integral over the complementary screen $\rho \in [0, a]$, which has a simple closed form solution,

$$\begin{aligned} U_{\text{complementary}} &= -\frac{ikU_0}{z}\int_0^a e^{\frac{ik\rho^2}{2z}}\rho\, d\rho \\ &= U_0\left(1-e^{\frac{ika^2}{2z}}\right) \end{aligned} \tag{2.22}$$

If the incident field is U_0 then our answer is the well known solution,

$$\begin{aligned} U &= U_0 - U_{\text{complementary}} \\ &= U_0 - U_0\left(1-e^{\frac{ika^2}{2z}}\right) \\ &= U_0 e^{\frac{ika^2}{2z}} \end{aligned} \tag{2.23}$$

2.2 Diffraction by Starshades

2.2.1 Basic theory of starshades

We can use the basic concepts of diffraction learned in the previous section to understand how starshades are able to control diffraction to suppress on-axis light. The starshade operation can be envisioned by looking at Figure 2.6, which shows a starshade imposed on Fresnel half-zones of alternating phase. Only those regions which are not blocked by the starshade contribute to the total light intensity, with the odd and even Fresnel half-zones destructively interfering with each other. The shape of the petals are designed to contribute the right amount of light such that the total sum of the on-axis electric field goes to zero. The process of slowly reducing blockage (equivalently increasing transmission) of the occulter to stop the ringing caused by a truncation in spatial frequencies is called *apodization*. Rather than vary the transmission with a transparent screen, which has tight tolerances and suffers from chromatic effects, we can approximate a circularly symmetric apodization function by discretizing (adding petals to) a binary occulter, where binary means the screen is either fully transmissive or fully opaque. If the apodization function is a ratio of the blocked area by the total area, we can approximate the apodization function $A(\rho)$ with a binary shape $\theta\left(\rho\right)$ with N_p petals as,

$$\begin{aligned} A\left(\rho\right) &= \frac{\text{blocked area}}{\text{total area}} \\ &= \frac{N_p \rho^2 \theta\left(\rho\right)}{\pi \rho^2} \\ &= \frac{N_p}{\pi}\theta\left(\rho\right) \end{aligned} \tag{2.24}$$

The apodization function of the offset hypergaussian found in [10] is shown in Equation 1.3 and can be used to generate the petal shapes of a starshade that approximates that apodization function. Theoretically, the tips and valleys of the petals extend to infinity and beat against all Fresnel zones. In practice, the finite size of the petals means that at some point the petal must be truncated and a Fresnel zone is left uncovered. This leaves the field unbalanced and diffracted light will appear. At larger radii, the Fresnel zones alternate more rapidly as their widths shrink, so a defect at a large Fresnel number will have less significant error. Starshade designs (at least of the hypergaussian family) should try to extend tips as far as practical.

The contribution of the electric field from a starshade tip can easily be seen mathematically with the line integral version of the diffraction equation we will derive in Section 5.2. Equation 2.25 is the diffraction equation expressed as a one-dimensional line integral. Recalling Equation 2.4, we notice the argument in the exponential is π times the Fresnel number, or that the Fresnel number is just the number of wavelengths out of phase that the light from a given radius is.

$$U \propto \frac{1}{2\pi}\int_0^{2\pi} e^{\frac{ik}{2z}\rho(\theta)^2}\, d\theta \tag{2.25}$$

$$\propto \frac{1}{2\pi}\int_0^{2\pi} e^{i\pi N_F(\theta)}\, d\theta \tag{2.26}$$

$$\approx \frac{1}{2\pi}\sum_i \left(-1\right)^{N_{F\,i}} \Delta\theta_i \tag{2.27}$$

Equation 2.27 shows the simplistic calculation of the diffraction due to an occulter. As we follow the edge of the occulter around, we sum the angular contribution of the occulter alternating between positive and negative values, given the odd or even Fresnel zone we are in. If we take the simple case of a circular occulter, then $\rho\left(\theta\right) = \text{constant}$ and the intensity ($\left|U\right|^2$) of Equation 2.27 is exactly one, as is commonly known.

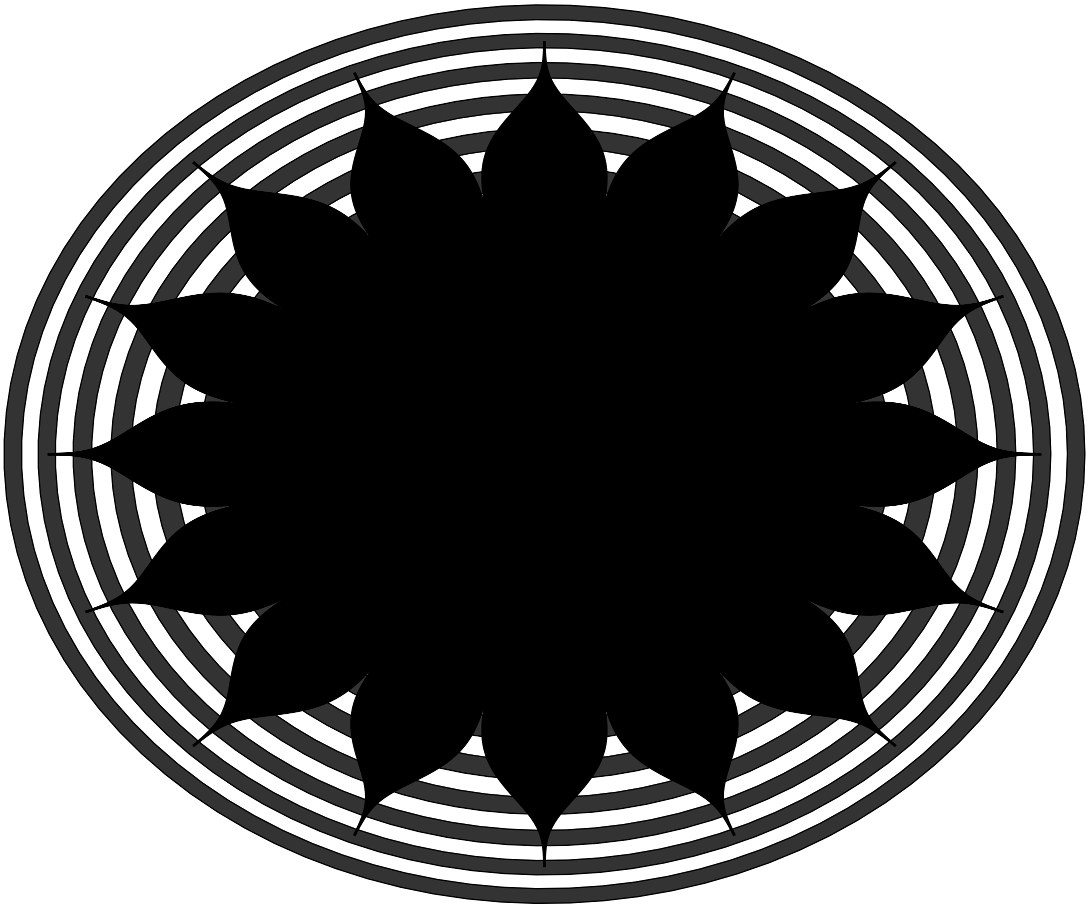

Figure 2.6: Hypergaussian starshade shape against a backdrop of Fresnel half-zones. The half-zones are regions of alternating phase where the phase difference between neighboring zones is exactly π. Each half-zone contributes positively or negatively to the total electric field. The apodization function of the starshade petals covers up the appropriate number of Fresnel half-zones to sum the on-axis electric field to zero.

For the more complex starshade shape, along the edges of the petal where the shape is nearly radial, there is little azimuthal contribution and as we quickly move across Fresnel zones, most of the contributions cancel each other out. However, at the tips and valleys where the petals truncate, there is an azimuthal edge that is contained within a single Fresnel zone and is not cancelled. The contribution to the field from this truncated tip can easily be estimated. We look at the simple case where a petal tip is truncated at a radius $r_t = 29$ cm, creating a blunt tip of width $x = 100$ μm. We can estimate the contrast from this error to be $C = \Delta E^2 \approx \left(\frac{1}{2\pi}\frac{x}{r_t}\right)^2 \sim 3 \times 10^{-9}$, which agrees to within 1% of the results from our optical model. To estimate the total performance of the starshade, we sum over all azimuthal errors. Equation 2.27 is a useful back of the envelope estimation of starshade performance for understanding the dominating error terms in the starshade design.

2.2.2 Definitions of contrast and suppression

There is a subtle, but important difference between the definitions of contrast and suppression that is important to know going forward, so here we give our interpretation of each definition.

Contrast is defined as the amount of light within a resolution element of a telescope (at the image plane), divided by the peak brightness of the main source as measured by that telescope when there is no starshade in place. This means that the contrast is a function of the telescope and the background light distribution. If you imagine the case where we have an infinitely large telescope with an infinitely small PSF, then we would have zero (perfect) contrast and no starshade is needed. Background light sources, such as dust (terrestrial or exozodiacal), can affect the contrast depending on its brightness and morphology. Contrast is a useful definition when talking about detectability of astronomical targets as it describes the noise contribution from residual starlight at the location of the object of interest. It is not always a useful definition when comparing starshade performance or the results of starshade tests as it is dependent on the telescope and the performance is not directly scalable to larger starshades. Contrast is beneficial when the starshade is spatially resolved as we can directly discriminate between light that is coming from the starshade and that which is a background source.

Suppression is defined as the total amount of light per area in space when the starshade is in place, divided by the total amount light per area in space when the starshade is not in place. It can be thought of as the ratio of the amount of light a lensless photometer receives when a starshade is in and out of place. Since the contributing light sources are not spatially resolved, background sources should be present in both and the distribution of that light is less important. Suppression is the best definition when talking about starshade performance as it is a direct measurement of that performance. When the starshade is put in place, any residual light is a measurement of the starshade performance (except for when there is diffracted light from supporting wires or stands). In recent tests, suppression has not been measured as the data from these tests are usually focal plane images, and there is not a straight forward way to convert between the two.

2.2.3 Starshade scaling relations

The performance of a starshade is mainly dictated by the Fresnel number and its three variables: starshade radius, wavelength, and separation (a, λ, F).

$$N_F = \frac{a^2}{\lambda F} \tag{2.28}$$

Under the assumption of scalar diffraction theory, the Fresnel number can be used as a similarity parameter for modeling and testing starshades of different scales and is directly related to the achievable suppression. The parameter that most strongly drives the achievable science is the inner working angle (IWA), or how close to the host star you can observe with sufficient contrast. Unlike a coronagraph, the IWA for a starshade is decoupled from the telescope and is simply the angular size of the starshade,

$$IWA = \frac{a}{F} \tag{2.29}$$

The decoupling of the IWA from the telescope size is a major advantage of the starshade over coronagraphs and allows smaller telescopes to be equally valuable in reaching smaller IWAs. The limiting factor in finding an exo-Earth is the number of habitable zones we can search. The smaller angle at which we can observe, the more distant stars we can observe into their habitable zones, and as the number of stars scales roughly as the distance cubed, a small difference in angle is a large increase in the number of accessible targets. Detailed design reference missions (DRM) [86, 87, 84] have demonstrated that the IWA is the driving design parameter, both for internal coronagraphs and starshades.

The next most important design parameter is the amount of starlight suppression the starshade provides. Focusing on the hypergaussian starshade, [11] came up with an analytic approximation for the suppression (modulo the $\sqrt{2/\pi}$ factor that we find yields a better agreement) as,

$$S = \left(\sqrt{\frac{2}{\pi}}n!\right)^2 \left(\frac{\lambda F}{2\pi ab}\right)^{2n} \tag{2.30}$$

where a, b, n are the hypergaussian parameters, with $n = 6$ commonly assumed. This can be expressed in terms of the Fresnel number as,

$$\begin{aligned} S &= (n!)^2 \left(\frac{2}{\pi}\right)^{2n+1} N_F^{-2n} \\ S &\propto N_F^{-2n} \end{aligned} \tag{2.31}$$

The comparison between the analytic expression of Equation 2.30 and results from the optical model are shown in Figure 2.7. This expression shows that the suppression gets better (smaller) at larger Fresnel number, which was mentioned in Section 2.2.1 as being due to the Fresnel zones alternating more quickly at larger Fresnel number. Using Equation 2.30, we can estimate that for 10^{-10} suppression we should not go below $N_F \sim 13$. The suppression also quickly degrades as λ^{2n} (the wavelength dependence of the on-axis suppression is shown in Figure 2.7), so the best performance is achieved at shorter wavelengths. One advantage of the hypergaussian over numerically-determined designs is that the hypergaussian is inherently broadband and only needs to be designed to meet spec at the longest wavelength of interest.

To estimate how quickly the suppression rises as you move off-axis, [11] came up with an analytic approximation. We modified this expression to include a J_0 Bessel Function term that comes from the diffraction of the inner opaque disk, which we feel better matches our model results.

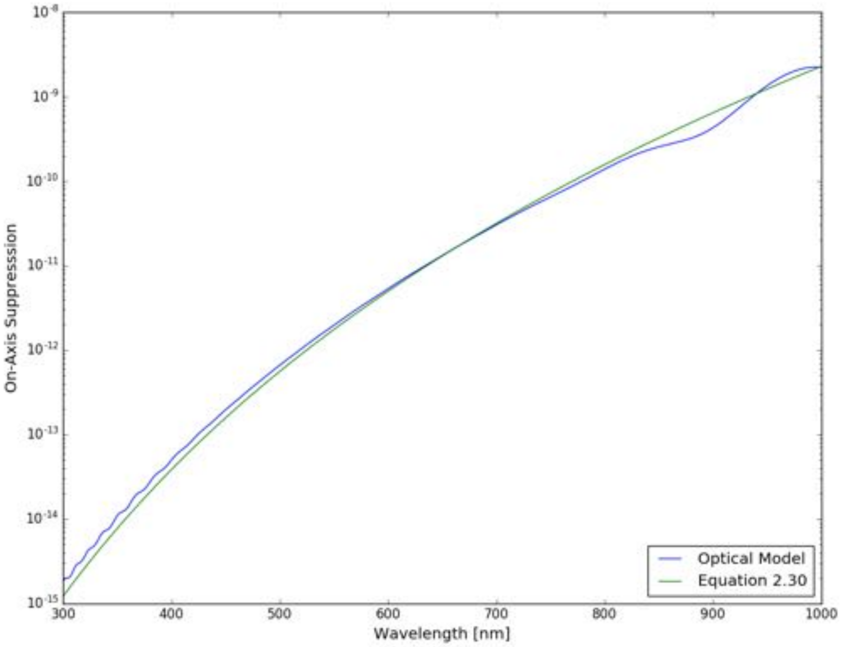

Figure 2.7: On-axis suppression as a function of wavelength for a hypergaussian starshade with $a = b = 8.5$ m, $n = 6$, and $F = 30,000$ km. The **blue** line was calculated by our optical model and the **green** line was calculated from Equation 2.30, which is similar to Equation 35 of [11].

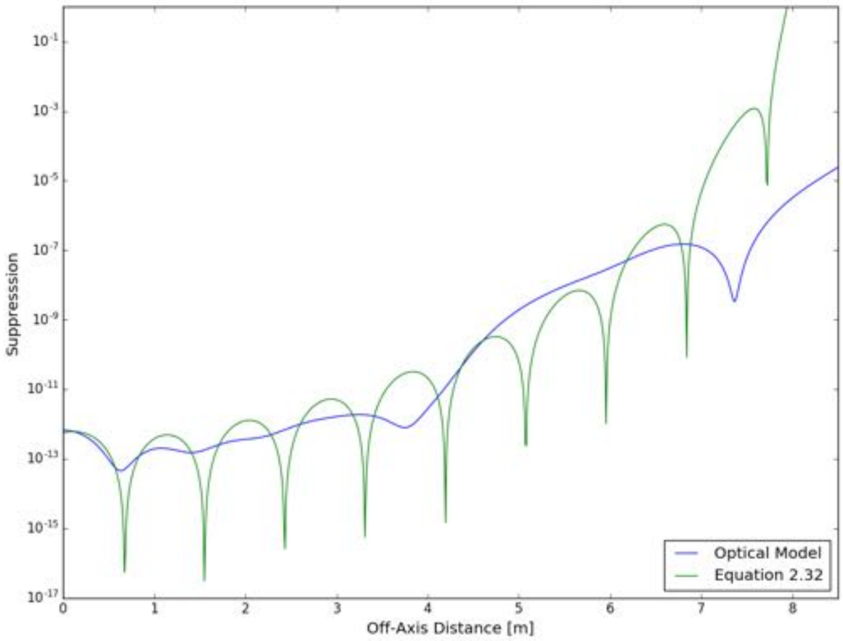

Figure 2.8: Suppression as a function of off-axis distance (σ) for the hypergaussian starshade in Figure 2.7 with $\lambda = 0.5$ μm. The **green** line was calculated from Equation 2.32, which is similar to Equation 38 of [11].

This expression, shown in comparison with the optical model in Figure 2.8, is given as a function of the off-axis distance σ as,

$$S = \left(\sqrt{\frac{2}{\pi}}n!\right)^2 \left(\frac{\lambda F}{2\pi\left(a-\sigma\right)b}\right)^{2n} J_0^2\left(\frac{2\pi a\sigma}{\lambda F}\right) \tag{2.32}$$

2.2.4 Example starshade design

The design of a starshade is wrapped up in a, λ, F. The main science driver is a smaller IWA to access the habitable zones of more targets. This can be accomplished with a smaller starshade or a larger separation. Smaller and closer is more practical, but in order to achieve the science goals, a modest telescope size is needed and that telescope must fit fully within the shadow. Increasing the starshade size, requires us to move farther away to keep the small IWA. As we move farther away, the Fresnel number decreases and we need to increase the size of the starshade to maintain suppression. So our need for a large telescope and small IWA is driving us towards larger starshades that are farther away. This presents obvious constraints as larger starshades are heavier and more difficult to launch, deploy, and maneuver, and the farther away it is, the longer it takes and more fuel is used to slew on the celestial sphere from target to target. DRM studies show that slew time and fuel are the limiting parameters of the number of habitable zones that are accessible [87].

The optimal design of a starshade requires a full DRM to explore the tradeoffs of fuel, mission lifetime, science goals, etc., but we can create a simple model to understand the basic trades. We start by defining the IWA to be 70 mas to reach the habitable zone (1 AU) out to 10 pc with a buffer of 30 mas to allow us to resolve the habitable zone from the IWA. We must also fit a 2.4 m diameter mirror in the shadow with ±1 m on each side to loosen the tolerance in formation flying. We can estimate the size of the deep shadow as 1/6 r_{ss}, which means we must have a minimum of a 12 m radius starshade. To reach 70 mas, we must be at least 35,000 km away, which gives us a Fresnel number of 6 (at our longest wavelength, 0.6 μm), which we know from Equation 2.31 will not provide the suppression we need. We can achieve 10^{-10} contrast on 10^{-9} suppression, which means we can go down to a Fresnel number of 10. We find a solution that gives us a 70 mas IWA and $N_F = 10$ with a starshade 36 m in diameter ($a = b = 9$ m) flying at 53,000 km separation.

Chapter 3

FORMATION FLYING SENSORS

3.1 Formation Sensing

Precision formation flying has been identified as a technology gap in need of development and demonstration for future starshade missions [43] and other distributed spacecraft architectures such as multi-spacecraft interferometers and long focal length x-ray observatories [77]. For a starshade mission, the rapid decline in contrast as you move radially from the center of the shadow places a tight constraint on the lateral position of the starshade relative to the telescope-star line of sight and maintaining alignment is imperative to achieving science goals. The baseline for an Earth-finding starshade mission requires maintaining line-of-sight alignment between starshade, telescope, and star to meter-level stability over 80,000 km of starshade-telescope separation [12], requiring position knowledge of 10 cm. This is a 250 μ-arcsecond parallactic measurement, a measurement which has only been achieved with dedicated astrometric missions. While the formation flying control in itself may not be too difficult, particularly if in a gravitationally benign orbit such as L2 or Earth-trailing, the accuracy of position sensing over the large separations required for starshades is unprecedented.

Previous studies have proposed *midpoint* sensors where the formation sensing is done at the starshade, where the position control occurs, allowing it to work with a passive telescope such as JWST [55]. Also proposed are *endpoint* sensors where the sensing is done at the telescope and position commands are relayed to the starshade. Alignment with a passive, distant celestial object naturally leads to enlisting a vision-based sensor to provide accurate position information, however, the disappearance of the stellar signal as it is occulted by the starshade adds a unique challenge to the precision alignment of starshades and drives the design of the sensor architecture.

This chapter details the development of two formation flying sensors, the **Offset Sensor** to be used in suborbital and ground-based starshade missions that value sensing speed over precision, and the **Arago Sensor** which utilizes diffracted light to provide high precision sensing to be used in the full-scale starshade mission. We are motivated to develop a positioning system that will address the issue of precision formation flying, prevent this technological gap from hindering the progress and scientific return of future missions, and open the door for new and innovative mission concepts.

3.2 The Offset Sensor

The Offset Sensor is advantageous for suborbital flights as it is an endpoint sensor that works with limited instrumentation at the starshade and takes advantage of real estate at the telescope end. This sensor architecture was chosen for the formation flying requirements of the Vertical Takeoff Vertical Landing (VTVL) rocket flights described in Chapter 4.

For a suborbital demonstration with a 0.5 m starshade and a few kilometers of separation, we need to keep the starshade in the LOS between a ground telescope and target star to within ± 3 cm and must track the star as it rotates across the sky throughout the night. This level of position sensing is a stretch for typical GPS systems and the LOS depends on the apparent position of the star in the sky, which can vary on minute timescales with changes in atmospheric temperature, making a visual sensor the most practical method. The strong vibrations from the VTVL during flight make a midpoint sensor difficult to build on a low budget, so we have decided to use an additional error telescope on the ground to serve as the endpoint sensor. A schematic of the operation of the sensor architecture can be seen in Figure 3.1. Using the error telescope to view beacons on the starshade relative to the target star (which remains unblocked to the error telescope), we can calculate the corrections needed to place the starshade into the line of sight relative to the science telescope and send these corrections to the VTVL's guidance system.

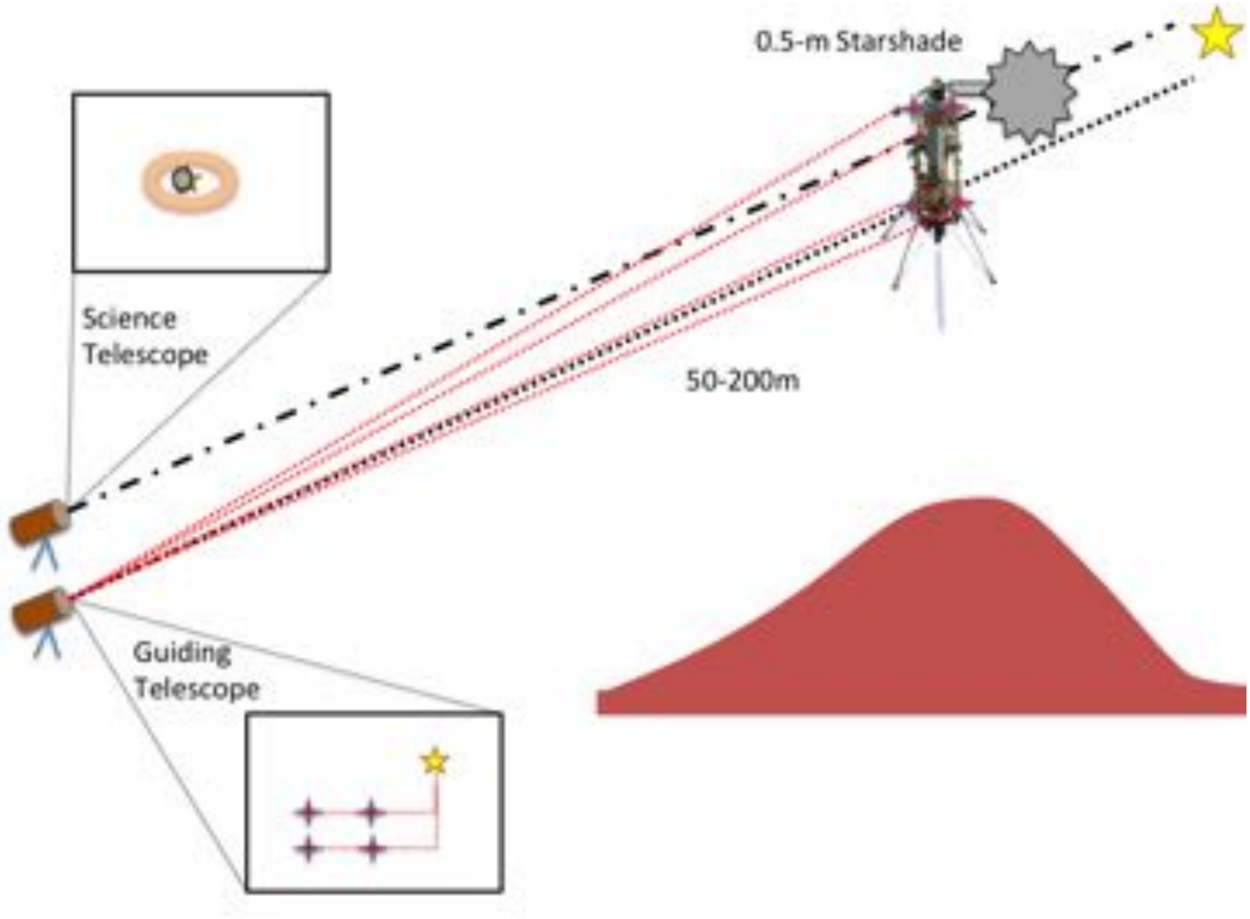

Figure 3.1: Cartoon diagram of the Offset Sensor architecture. A guiding telescope images LED beacons on a VTVL rocket to provide visual feedback to keep the starshade in the line of sight between a science telescope and background object.

3.2.1 6DOF pose estimation

With the quick timescales of disturbances and position changes in a suborbital flight, we require a fast and accurate control law to maintain alignment, which requires accurate knowledge of the full state of the vehicle, updated at a high rate. We also need relative information between the two bodies to account for the sensing being done separately from the control body. To achieve a full state 6 degrees of freedom (6DOF; 3 position, 3 attitude) relative solution of the control body using visual information, we use a pose estimation algorithm developed by [35] for their VisNav sensor. The VisNav sensor uses a Gaussian Least Squares Differential Correction (GLSDC) algorithm to compute a 6DOF solution from an array of fiducial markers with a known and fixed arrangement, allowing for pose estimation to be done from a single camera.

3.2.1.1 GLSDC algorithm

The use of the GLSDC algorithm for pose estimation with a single camera was detailed in [35] and our work drew additionally from [8] for reference material. The basic concept of this algorithm is to use Equation 3.1, iterated over i beacons, to solve for the relative position $\vec{t}$ and attitude $\vec{p}$ between the target and camera.

$$\vec{b}_i = C\left(\vec{p}\right)\left[\vec{B}_i - \vec{t}\right] \tag{3.1}$$

Shown in Figure 3.2, $\vec{b}_i$ is the position of the i^{th} beacon as seen in the camera; this value is measured with the camera. $\vec{B}_i$ is the position of the i^{th} beacon in the frame of the target; this value is known beforehand. $C\left(\vec{p}\right)$ is the cosine matrix of attitude $\vec{p}$. If we know $\vec{B}_i$ for four beacons and measure each $\vec{b}_i$, we have 8 equations (2 - (x, y) coordinates in the image - for each beacon) and 6 unknowns $(\vec{t}, \vec{p})$, and can solve the system via least squares. The GLSDC algorithm (an iterative variation of least squares) was proposed by [35] to robustly solve this problem; we point the reader to [35] for a more detailed description of the algorithm.

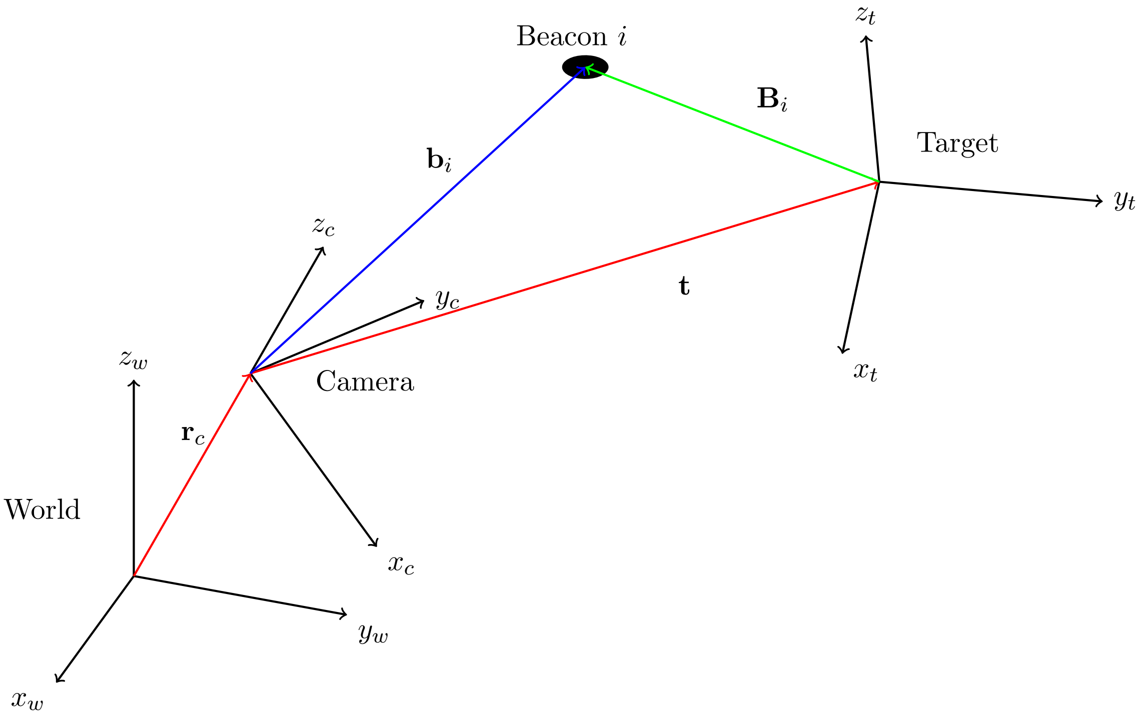

Figure 3.2: Coordinate system for the derivation of the GLSDC algorithm. The world frame is defined along the inertial Earth axes and is stationary. The position of the beacon in the target frame is fixed and known, the position of the beacon in the camera frame is measured, and the position of the target in the camera frame is what we are trying to solve for. To convert to an absolute position in the world frame requires knowledge of the position of the beacon or target in the world frame.

3.2.1.2 Transformation from relative to inertial reference frame

The GLSDC algorithm posed above allows us to solve for the relative position and attitude between camera and target. However, it is often useful to determine an absolute attitude relative to an inertial, global coordinate system, as is done in Section 3.2.2. To do so, we use the camera to measure 3 locations fixed in the inertial frame (e.g., the yellow markers in Figure 3.3). We only need to measure three since we are only solving for 3 unknowns (the attitude). Knowing the relative attitude of the camera in the inertial frame and the relative attitude of the target in the camera frame, a series of rotations allow us to calculate the ‘true’ attitude of the target in the inertial frame. This is useful in Section 3.2.2 as we are validating our algorithm by comparing our attitude solution of a target craft with the attitude calculated from an onboard Inertial Measurement Unit (IMU).

3.2.2 Lab demonstrations of pose estimation

To test our implementation of the pose estimation algorithms from Section 3.2.1 to be used in future rocket flights, we performed a series of lab demonstrations with an Offset Sensor (DSLR camera) and a simulated target spacecraft on an air bearing. Floating our target craft on a cushion of air on the air bearing allows for near frictionless motion of the craft in 3 degrees of rotation. Our lab configuration and a close up of the target craft can be seen in Figure 3.3 and Figure 3.4, respectively. Mounted to the target craft are four LEDs with a known separation and an IMU relaying angular rates to a laptop via an Arduino board with wireless communication. The singular blue LED is used as a reference to differentiate the LEDs in the image. Figure 3.4 was taken from a DSLR camera, serving as our camera craft, on a tripod 1 m above the air bearing. These tests were performed in the Generalized Nanosatellite Avionics Testbed (GNAT) Lab [81] at NASA Ames Research Center, which specializes in the design and testing of commercial components to be used on miniature satellites.

The truth attitude system that we have developed in the lab is not only useful as a formation

Figure 3.3: Image of the air bearing testbed in the GNAT Lab at NASA Ames Research Center. The test craft with IMU sensor spins on the air bearing while the visual attitude system images onboard LEDs and computes the attitude. Yellow markers on the air bearing allow us to transform to an inertial frame.

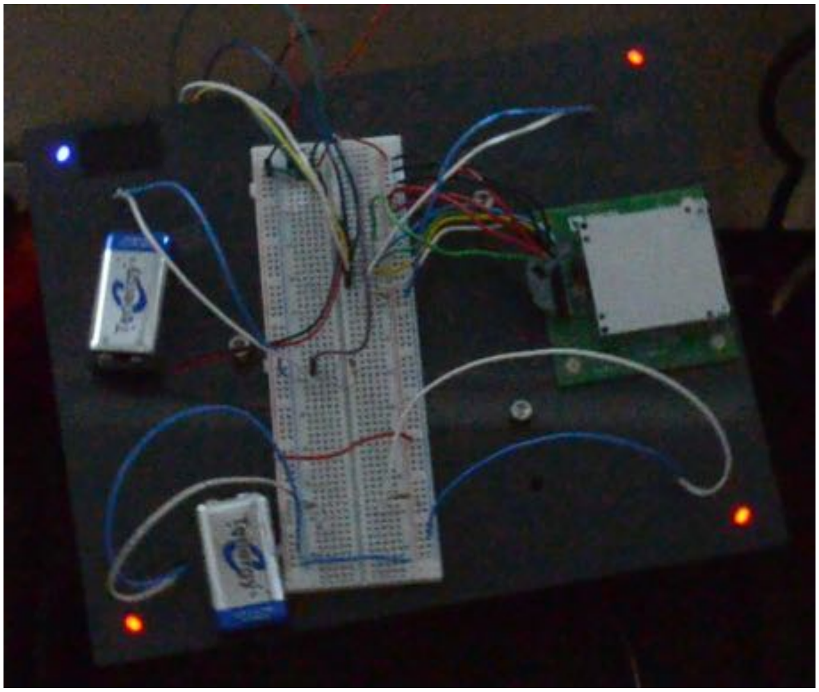

Figure 3.4: Image of the target craft on the air bearing testbed. Batteries power an onboard IMU collecting angular rate and acceleration data and four LEDs that are imaged by the visual attitude sensor. The blue LED in the top left corner allows us to differentiate LEDs.

flying instrument, but is useful for the development of cubesats and nanosats. In most testbeds, the craft's attitude is determined by integrating angular rates obtained from onboard IMUs. However, biases in the IMU's angular rates compound when integrated and can lead to a systematic error in the attitude determination. One utilization of this truth attitude system is to easily and accurately determine mass properties of a cubesat in the lab. With the cubesat rotating on an air bearing, the visual system can measure the true attitude of the system and thus accurately follow the dynamics of the cubesat. Fitting these data to a dynamical model will allow us to determine the moment of inertia tensor and center of gravity of the system, properties of the spacecraft that are important for on-orbit performance.

We performed a number of tests in the lab verifying the methodology of determining relative attitude and position between a target craft and camera. The first laboratory demonstration of this sensor was to detect small changes in position between the camera and target craft. The target craft was placed on an optical xyz-translation stage and mounted 1 m from the camera on an optical bench. The camera recorded images of the LEDs as the translation stage was moved in all three directions in increments of 25.4 microns. The centroids of the LEDs are found in each image and their locations are sent to the GLSDC algorithm, which solves for the position and attitude between camera and target craft. The results of this test can be seen in Figure 3.5. The red line shows the position of the camera in the target craft's frame as solved by the GLSDC solver, while the blue line is the expected movement. 'Y' is the horizontal axis, 'Z' is the vertical axis, and 'X' is along the optical axis. As can be seen in the plot, the target's relative movement matches well to the expected results, with a mean error between the observed and theoretical position of 8.8 μm (y-direction) and 29.7 μm (z-direction). The camera is able to detect small in-plane movements to high precision, but does not do well to detect axial movements as these can be masked by errors in the focal length of the camera.

The next laboratory demonstration of the sensor was to place the target craft on an air bearing to measure rotation in all three axes. With the configuration shown in Figure 3.3, we recorded images (at 25 fps) of the target craft suspended on a cushion of air above the air bearing

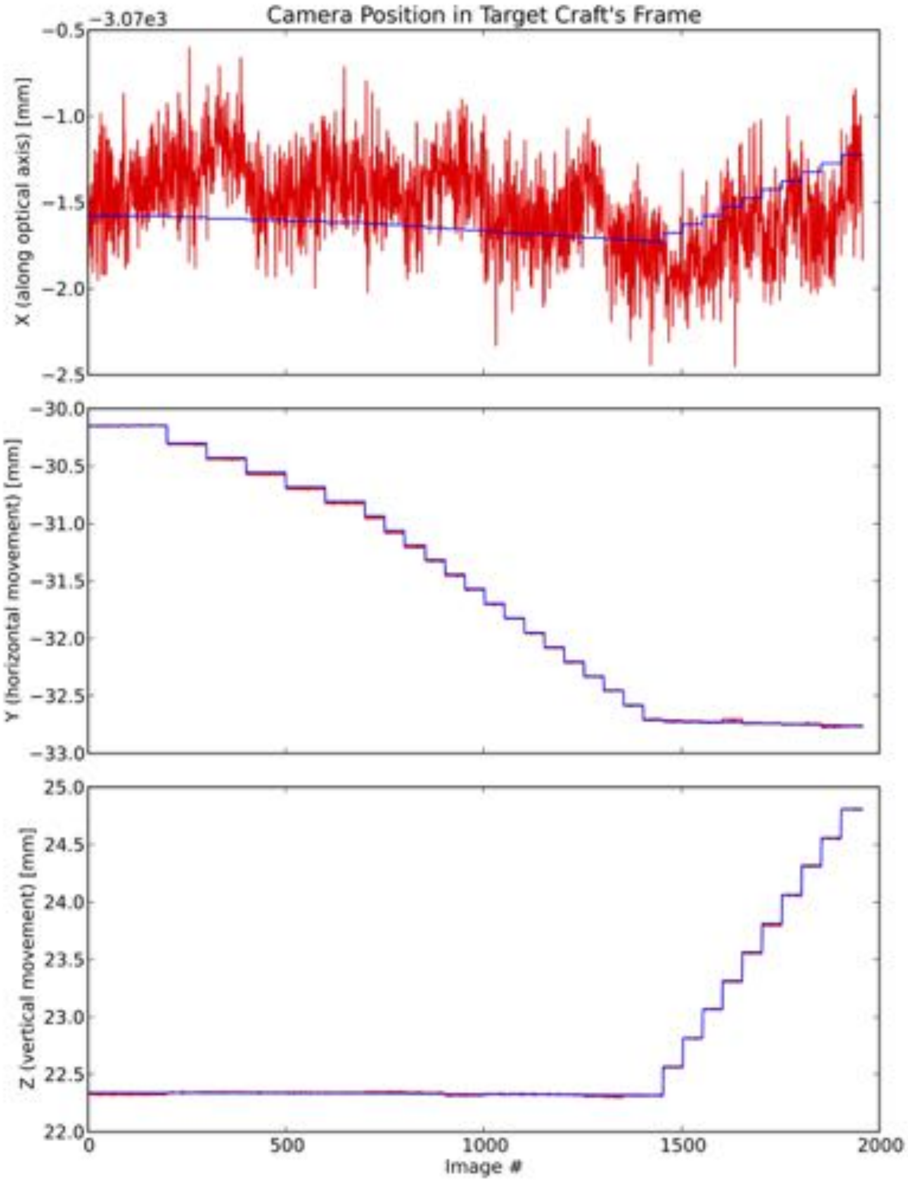

Figure 3.5: Results from the relative positioning test. The red line shows the unfiltered results from the GLSDC solver, while the blue line is the expected movement (in 25.4 μm increments). 'Y' is the horizontal axis, 'Z' is the vertical axis, and 'X' is along the optical axis.

as we gave it a perturbation about its rotation axis. The angular rates were recorded by an onboard IMU for comparison. The angular rates from the IMU are in the inertial frame, while the attitude solved for by our sensor is a relative attitude between the camera and target. To determine the true attitude of the target in the inertial frame, we must determine the attitude of the camera in the inertial frame and use the relative attitude to solve for the target's true attitude. Our inertial frame is set to be along the axes of the air bearing. Yellow markers on the air bearing (seen in Figure 3.3) allow us to solve for the attitude of the camera in the inertial frame, from which we can determine the true attitude.

The results from this test can be seen in Figure 3.6, which displays the 321 Euler angles (left panel) and angular rates (right panel) of the target craft as a function of time as it rotates about its 'yaw' axis on the air bearing. The red line shows the solution from the GLSDC solver, while the black line shows the data from the onboard IMU. The angular rates from the IMU have had their biases subtracted and are integrated forward in time to yield the 321 Euler angles and the 321 Euler angles from the camera are differentiated to yield the angular rates. The angle ψ corresponds to a rotation about the 'yaw' axis as the board is spun on the air bearing through four complete rotations. The angles θ and ϕ correspond to 'roll' and 'pitch' and are secondary perturbations. As can be seen from the figure, there is an excellent agreement between the IMU data and the visual data. After 10 seconds, the attitude solutions begin to slightly diverge, which is possibly a result of a misalignment between the IMU axes and our defined body axes. Any misalignment or bias in the IMU rates will cause the attitude solution to drift as the rates are integrated to obtain the Euler angles. We believe the camera, which does not suffer from such bias, yields a better solution for the true attitude than that from the IMU.

The largest sources of error in this lab demonstration are the physical size of the LEDs and the error in the measurement of the known position of the LEDs. The bulbs of the LEDs are extended objects (1 mm in diameter) whose flux diminishes off-axis, making it difficult to detect small changes in attitude, causing noise to be introduced into the solver. Noise is also introduced in the measurements of the true position of the LEDs on the target craft. For our proposed suborbital

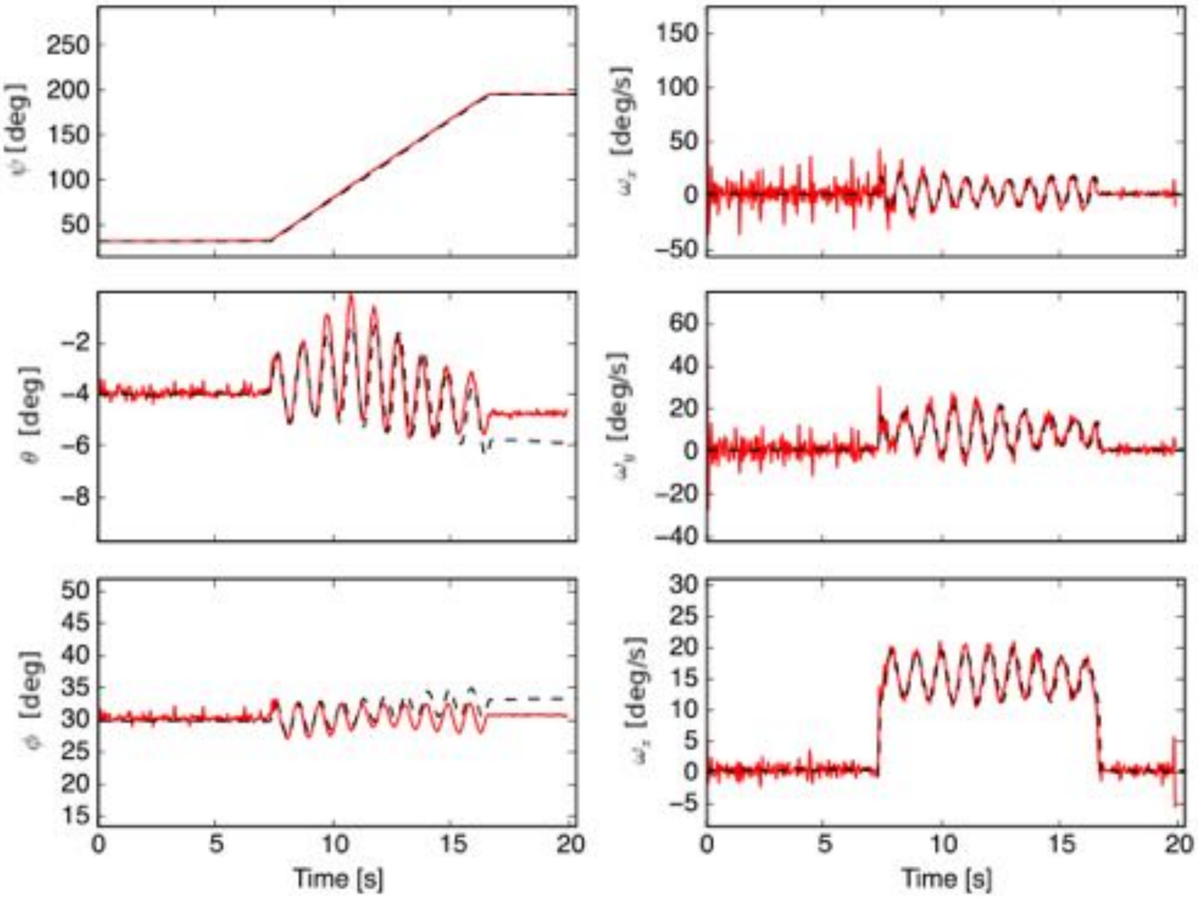

Figure 3.6: Results from the visual attitude determination test on the air bearing. The left panel shows the 321 Euler angles, the right panel shows the angular body rates. The **red** lines are the calculated solution from the camera data, the **black lines** are data from the onboard IMU.

missions, the LEDs will be point sources and the relative error in measuring the beacons' true position will be smaller as their separations are larger. Our lab demonstration shows that the attitude solution is stable to a few arcminutes and we expect an error in the attitude of less than a few degrees for our suborbital experiment.

3.2.3 Formation flying algorithms

The correction signal that will keep the starshade in the line of sight with the target is calculated by transforming the offset in the image between the starshade and target location from the camera's (sensor) frame to the platform's frame. The correction signals in the platform's frame $(\Delta x, \Delta y, \Delta z)$ can be calculated by minimizing,

$$\left\| R_{SS}^{CAM} \begin{pmatrix} \Delta x \\ \Delta y \\ \Delta z \end{pmatrix} - \left[\begin{pmatrix} x \\ y \\ f \end{pmatrix}_{SS}^{i,ST} - \begin{pmatrix} x \\ y \\ f \end{pmatrix}_{\star}^{i} \right] \times \frac{d}{f} \right\| = 0 \tag{3.2}$$

Here, $|| \; ||$ represents the vector norm. The physical coordinates of the starshade and target star on the sensor are $(x, y)_{SS}^{i,ST}$ and $(x, y)_{\star}^{i}$, respectively. The superscript ST in the starshade coordinates specify these are as seen by the science telescope. For an offset telescope these coordinates will differ from those seen in the guiding scope. R_{SS}^{CAM} is the rotation matrix given by the relative attitude between the starshade platform and camera, f is the focal length of the camera, and d is the distance between the camera and starshade. The distance, d, accounts for the 3D projection onto the image plane and can be determined using the same method as the attitude determination, or from GPS coordinates. Error in this value will serve to scale the magnitude of the correction signal and should be corrected for in the feedback loop.

One difficulty with an endpoint sensor in a starshade mission is that as the starshade occults the star, the signal from the star (the guiding reference point) is completely extinguished. Here, we propose two sensor architectures that utilize different methods to overcome the loss of the reference signal. The first architecture uses a single telescope for both science and guiding operations. Once the star's signal is lost, it uses background stars in the image to estimate the position of the target star. The second architecture uses a separate guiding telescope offset from the science telescope to perform the error sensing. This telescope is offset from the starshade's shadow and the target star remains visible.

3.2.3.1 Single telescope error sensing

A dichroic beamsplitter in the science telescope allows us to pick off longer wavelength light from the star and beacons on the starshade to use as a guiding signal. Once the starshade occults the target star and the signal is lost, we can use background stars in the image to estimate the position of the target star. During occultation, we use a pattern recognition algorithm (see Section 3.2.4.1) to match the stars in the field of view to a star catalog and use their positions to estimate the attitude of the sensor relative to the background star field. This 'celestial attitude', with rotation matrix R_{ECI}^{CAM}, can be used with the known fixed coordinates of the target star to estimate its position in the image. The position of the target star for which to guide the starshade to is given by,

$$\begin{pmatrix} x \\ y \\ f \end{pmatrix}_{\star}^{i} = \left| R_{ECI}^{CAM} \begin{pmatrix} x \\ y \\ z \end{pmatrix}_{\star}^{ECI} \right|_{z} \times f \tag{3.3}$$

where $| \ |_z$, represents normalizing the vector by the z component and $(x\ y\ z)_{\star}^{ECI}$ are the Earth-centered inertial coordinates of the target star.

Plugging Equation 3.3 into Equation 3.2 allows us to solve for the correction signal. The accuracy of the location of the target star depends strongly on the accuracy of the celestial attitude, which is a function of the number of stars in the field of view available (limiting magnitude) and the centroiding accuracy. If we shorten the focal length to increase the FOV and thus the number of stars available, we will be left with a larger centroiding error. However, if we assume we have a stable telescope mount for which its change in attitude is roughly constant, we can sample the celestial attitude at a lower rate and take deeper exposures, increasing the number of visible stars without having to reduce the focal length.

3.2.3.2 Offset telescope error sensing

To have the target star remain visible for the entire observation, an additional guiding telescope can be placed offset from the science telescope and out of the starshade's shadow. In this case, our correction signal is calculated by transforming coordinates from the science telescope to the offset guiding telescope. Calculating this new position requires rotating through an inertial frame in which the offset between the two telescopes is constant. The position of the starshade as seen by the science telescope is estimated by

$$\begin{pmatrix} x \\ y \\ f \end{pmatrix}_{SS}^{i,ST} = \left| \begin{pmatrix} x \\ y \\ f \end{pmatrix}_{SS}^{i,OT} \times \frac{d}{f} - R_{ECI}^{CAM} R_{NWU}^{ECI} \begin{pmatrix} x \\ y \\ z \end{pmatrix}_{offset}^{NWU} \right|_{z} \times f \tag{3.4}$$

where the observed position of the starshade as seen by the offset telescope is given by $(x, y, f)_{SS}^{i,OT}$.

The quantity $(x, y, z)_{offset}^{NWU}$ represents the difference in coordinates between the science and offset telescopes in the stationary horizon coordinate frame, NWU (right-handed, North-West-Up). The rotation matrix R_{NWU}^{ECI} represents the rotation from NWU coordinates to Earth-centered inertial (ECI) coordinates and serves as a middle step to rotate the constant offset between the telescopes into the current frame of the offset telescope. This rotation is known from propagating ephemeris data to the current local sidereal time. Plugging Equation 3.4 into Equation 3.2 allows us to solve for the correction signal needed to place the starshade into the line of sight of the science telescope. While this correction signal also depends on the accuracy of the celestial attitude, the more dominating source of error is the measured offset between the two telescopes, which must be measured in the NWU frame and can be measured via GPS or with surveyor tools (theodolites, etc.). The effect of this error is detailed in the next section.

3.2.3.3 Monte Carlo simulations

For a first order comparison between the two architectures (Single vs. Offset Scope), we performed a suite of Monte Carlo simulations to investigate how the calculated correction signal varies with parameter errors. The parameter values used in the simulations are those baselined to the suborbital mission and are shown in Table 3.1. The simulations reveal that the visual feedback loop makes our system quite forgiving to most errors, as long as we are able to sample at a sufficient rate. There are, however, errors that cannot be corrected for with visual feedback. For the Single Scope architecture, the main source of error, and one that cannot be corrected for, comes from using the celestial attitude (R_{ECI}^{CAM}) to estimate the position of the target star while it is obscured by the starshade. For the Offset Scope architecture, the main error source is in measuring the offset between the telescopes, $(x, y, z)_{offset}^{NWU}$.

Our simulations take a simulated image and use Equations 3.2 - 3.4 to determine the correction signal for the vehicle. This signal is passed through an MPC controller (see Section 3.2.4.2) to generate a velocity control signal to move the position of the starshade. We assume that there is no error in moving the starshade; a reasonable assumption for the mountaintop track, but not for the VTVLR in which flying to a few centimeters is the pushing the limit of its capabilities. For each timestep, we calculate the error as the lateral distance of the starshade from the apparent position of the star. This, along with the fraction of the time spent within the shadow, are our main metrics for comparing the two architectures. We baseline our errors to be 0.25 arcsecond for the celestial attitude determination ("Star Tracker") and 1 cm for the telescope offset measurement. Figure 3.7 shows the error as a function of time for one 60 second run. The top row is a run with the baseline error values (σ_{Offset}=1 cm, $\sigma_{StarTracker}$=0.25 arcsec) and the bottom row is a run with errors twice as large. For the baseline parameters, after the starshade enters the shadow, it remains in there for 80% of the time, with a mean lateral offset of 2 cm.

	Lab	Suborbital
f_{sensor}	50 mm	152 mm
D_{sensor}	110 mm	1500 mm
Separation	15 m	4000 m
$D_{occulter}$	3 cm	60 cm

Table 3.1: Scaling relations between demonstrations in the lab and the VTVL rocket suborbital mission detailed in Chapter 4.

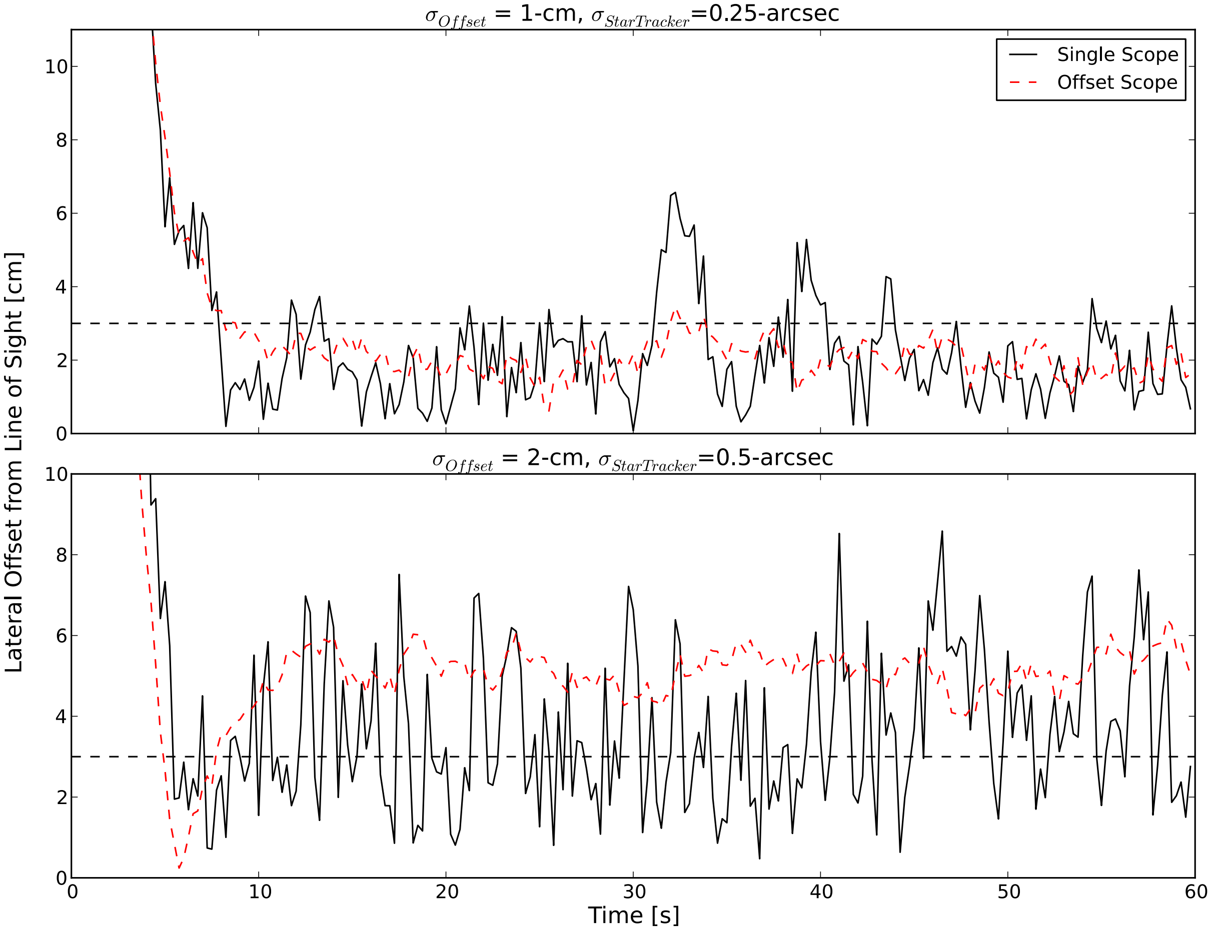

Figure 3.7: Simulation of a 60 second observing run showing the lateral offset from the line of sight as a function of time. Both the Single Scope (**black** solid line) and Offset Scope (**red** dashed line) architectures are shown with our baseline error values (**top** row) and twice those error values (**bottom** row). The horizontal line marks the 3 cm shadow.

Figure 3.8 shows the distributions of the two metrics computed from Monte Carlo simulations. The top row shows the results of the Single Scope architecture for various levels of error in the star tracker. The bottom row shows the results of the Offset Scope architecture for various levels of error in the telescope offset position. The left panel is the distribution in the lateral offset (once the starshade enters the shadow) and the right panel is the distribution in the fraction of time the starshade remains within the shadow (f_{time}).

As can be seen from Figure 3.8, the dominant error sources we have identified have a large effect on the performance on the formation flying and will set the requirements for the architecture. The main difference seen between the two architectures is in the distribution of f_{time}, with the Offset Scope having a more extended distribution. For the Offset Scope simulations with the larger error, runs in which we never enter the shadow (f_{time}=0) occur almost as frequently as runs in which we remain in the shadow the entire time (f_{time}=1). While for the Single Scope, a given error size often leads to a given level of performance. This behavior is contributed to how often the measurements are made. For the Offset Scope, the offset between the telescopes is measured once and is fixed for all subsequent observations. If this measurement is wrong, it will lead to a systematic offset in all determinations of the correction signal. For the Single Scope, the celestial attitude is measured at every time step, continuously introducing random error into the correction signal. This can easily be seen in Figure 3.7, in which doubling the errors causes a larger spread in the lateral offset of the Single Scope, while it leads to a systematic shift in the lateral offset for the Offset Scope. It is possible that the systematic error in the Offset Scope can be calibrated for with initial observations, however the random error in the Single Scope cannot. For this reason, and for the stringent requirements on the celestial attitude determination (0.25 arcseconds), we believe the Offset Scope architecture will offer the best results.

The contrast level that is achievable in an exposure is set by how often the starshade keeps the shadow over the telescope. If the telescope drifts too far from the shadow, that exposure is ruined by the overwhelming starlight. One option to alleviate the required tolerances on formation flying is to use an Electron Multiplying CCD (EMCCD) as our science detector. These detectors

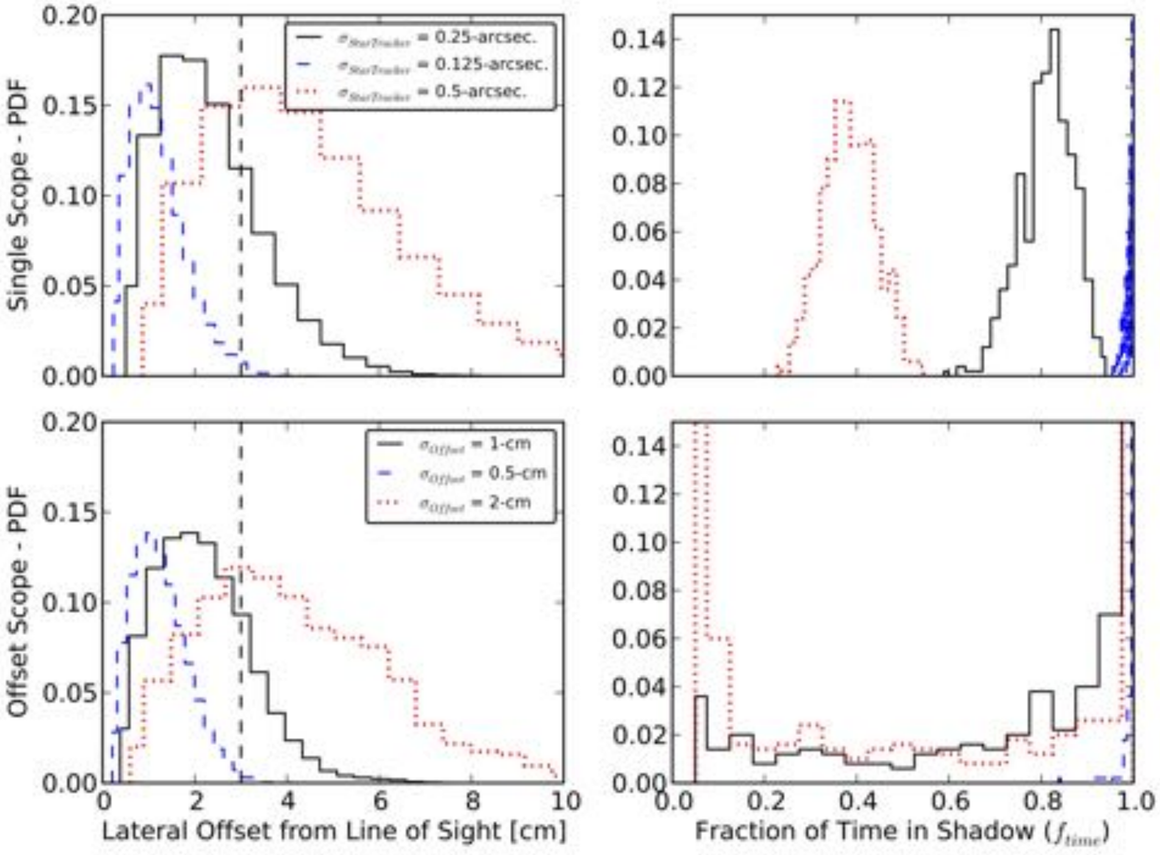

Figure 3.8: Monte Carlo simulations of lateral offset from the line of sight (**left** panel) and fraction of the time spent in the shadow (**right** panel) for the Single (**top** row) and Offset (**bottom** row) Scope architectures. The vertical line in the left panel marks the 3 cm shadow.

have close to zero readout noise, and therefore can make short exposures (at 30 fps), which can be combined together without a degradation in the signal-to-noise. This will allow us to discard any exposures for which the telescope left the shadow, loosening the requirements on the formation flying without sacrificing performance in the science.

3.2.4 Lab demonstrations of the Offset Sensor

We conducted a tabletop demonstration of the mountaintop mission in the lab to verify the derived formation flying equations and to serve as a system-level verification of the sensor. Shown in Figure 3.9, two linear actuators (each with a 12" stroke) and a ball-bearing track serve as a scaled model of the mountaintop track and provide vertical and horizontal positioning of a fake occulter. Four LEDs on the occulter allow for visual determination of the attitude of the track relative to the error telescope. Our error telescope is a 50 mm lens with 110 mm focal length mounted with a CMOS autoguiding sensor. An additional board with a configuration of LEDs serves as the target star with background star field. This board is mounted to a rotating arm to simulate rotation of the celestial sphere. The linear actuators and LEDs are controlled via an Arduino Uno board.

3.2.4.1 Star field pattern recognition

A key component to this architecture is attitude determination of the camera with respect to the background star field. This is important for estimating the position of the target star while it is occulted (in the Single Scope architecture) and for rotating into an inertial frame (for the Offset Scope architecture). The pattern recognition algorithm we use comes from [16] and uses planar triangles to match the observed star field to a star catalog. After finding the position vector of all stars in the image, planar triangles are formed between combinations of three stars. Two properties of the triangle, area (A) and polar moment (I), are computed along with their variances (σ_A, σ_I). Using the planar triangle with the largest area, we search the star catalog for triangles that have areas and polar moments between the range $A \pm \sigma_A$ and $I \pm \sigma_I$, respectively. If more than one solution exists, a second pivot triangle is formed using two of the stars in common with the first

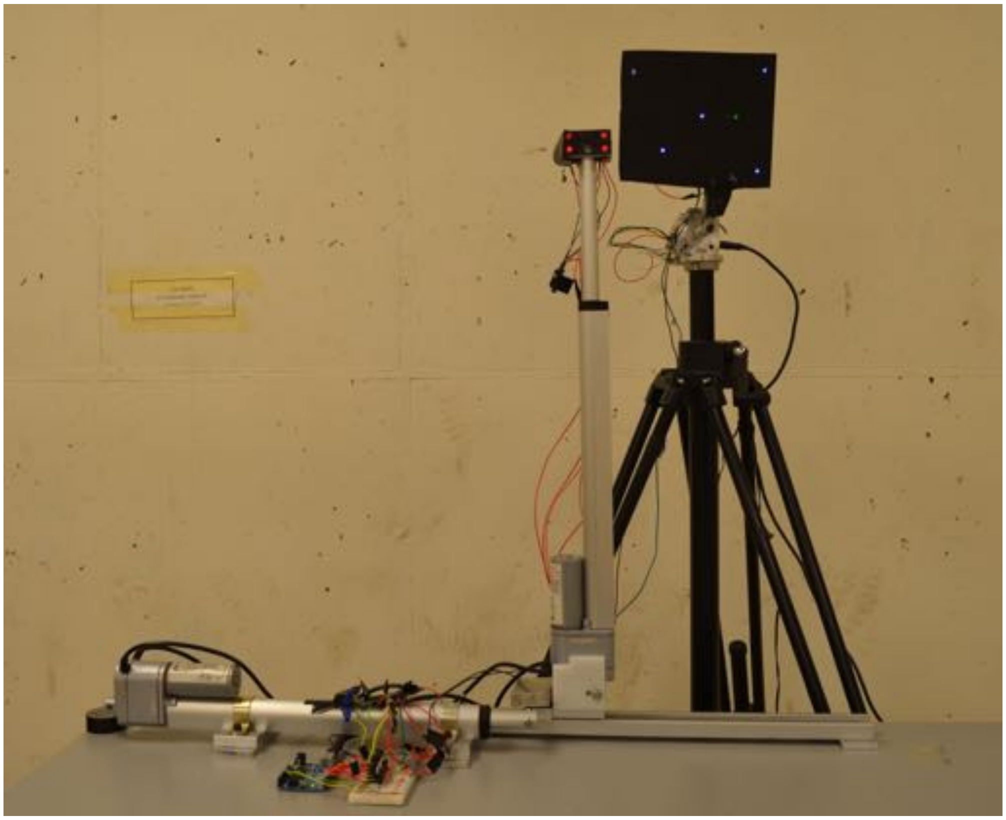

Figure 3.9: Lab setup of formation flying demo. In the foreground are two orthogonal linear actuators mounted to a ball bearing slide that serve as the two-dimensional track. On top of the vertical LA are four LEDs representing the fake occulter and allowing for visual attitude determination. In the background is a board mounted on a spinning motor with six LEDs that represent the background star field.

triangle and the catalog is searched for a match to that triangle. This is repeated until only one solution exists. Generally, a quadtree data structure is used for searching the large star catalogs. However, since we will never be in a "lost-in-space" configuration, we only need to search a small portion of the star catalog and do not require a tree data structure. Once all the stars in the field of view have been matched to the catalog and identified, we use the QUEST algorithm [74] to solve Wahba's problem for the celestial attitude. The accuracy of the attitude determination depends on how many stars are in the field of view and the centroiding accuracy. Monte Carlo simulations show that with a limiting magnitude of $m_V = 8$ and $f = 150$ mm, we are able to identify all stars in the field of view ∼98% of the time with an error in attitude of 3 arcseconds (in each Euler angle).

3.2.4.2 Model predictive control

Tracking a star across the sky with the starshade platform is a relatively simple trajectory tracking problem, as the motion of the star is constant and can be estimated with initial observations. The control law used for solving this trajectory tracking problem is a linear model-based predictive control (MPC) approach following that outlined by [42]. For the lab demos we adopt a simple, two-dimensional dynamical model of the starshade, but a more involved three-dimensional dynamical model will be necessary for the VTVLR flight. After initial observations of the star field is made, we account for atmospheric refraction and the orientation of the telescope and assume constant motion to model the star's trajectory. If the starshade's state is given by $\mathbf{x}$ and the reference trajectory state is $\mathbf{x}_r$, the control law works to find the optimal control input (the velocity of the linear actuators), which minimizes the error $\bar{\mathbf{x}} = \mathbf{x} - \mathbf{x}_r$ through a linearized cost function. At each measurement update, the model is used to predict the behavior of the system over a finite horizon and a trajectory is generated. The cost function is minimized with future values of the control input over the horizon. This yields a control signal, optimized using future values predicted by a dynamical model, to track the reference trajectory. This is repeated at the next sampling with updated measurements and a shifted horizon.

3.2.4.3 Test procedure

The procedure for the test is as follows:

(1) Take image of star field

(2) Match star pattern to catalog and calculate attitude of star field w.r.t. camera

(3) Choose target star from star field

(4) Cycle through LED beacons (turn on and take image)

(5) Use the beacons' positions to calculate attitude of the track w.r.t. camera

(6) Begin feedback loop

  (a) Take image

  (b) Find starshade in image (from beacons)

  (c) Determine target position in image

    - This depends on whether we are sensing from a Single or Offset telescope and whether or not the target star is occulted

  (d) Calculate correction signal (using Equations 3.2 - 3.4)

  (e) Pass correction signal through MPC controller and translate to a velocity signal

  (f) Move linear actuators

3.2.4.4 Results

The main results from our formation flying demos in the lab can be seen in Figure 3.10, where we plot the lateral offset of the occulter from the line of sight as a function of time. The different lines represent different test runs with either the Single or Offset scope architectures and whether the target star is moving or stationary. The purpose of these demonstrations is to verify the occulting equations derived, help develop the software, and to serve as a systems-level test of

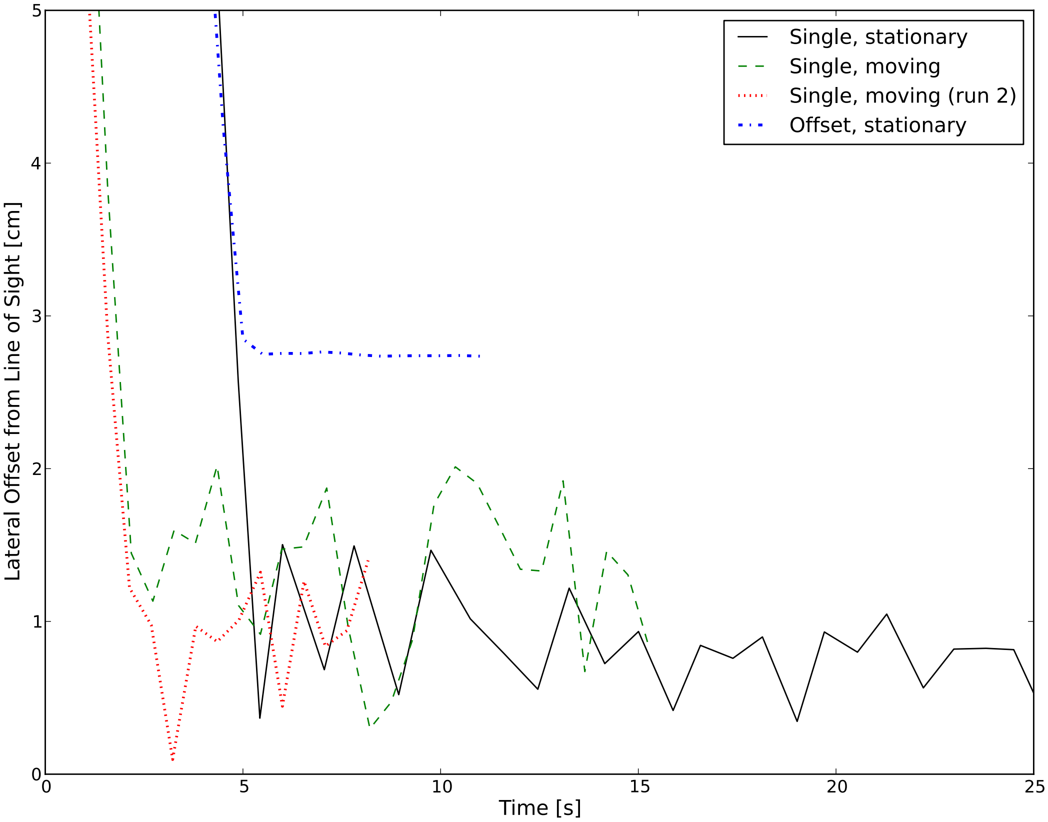

Figure 3.10: Main results from the formation flying demos in the lab as an occulter on a two-dimensional track 'flies' in formation with a background star. The lines show the lateral offset from the line of sight as a function of time. The different lines represent different test runs of either the Single or Offset Scope architectures and either a stationary or moving background star.

the formation flying sensor. The demos are not meant to directly scale to the expected performance of the suborbital mission. The main limitation of the lab demos is the precision with which the linear actuators can position the fake occulter. The actuators have a minimum speed at which they can move, which means we cannot fine tune the position and end up oscillating around the target position. We find that we are able to track both stationary and moving targets with both architectures.

The results in Figure 3.10 qualitatively match those seen in the Monte Carlo simulations, in which the Offset Scope architecture has a systematic offset that is not corrected for by the feedback loop. Additionally, the Offset Scope was less subject to random errors in determining the target star's position than with the Single Scope. Data from the Offset Scope tracking a moving target are not shown due to time constraints on analyzing the data. However, a by-eye analysis of the video shows we are successfully able to track the moving target. The length of the runs for the moving target is limited to how far the fake star board could rotate. While these demos are in their initial stages, they have been successful in developing the formation flying sensor as a system and have demonstrated that this methodology can be extended to further use in a suborbital starshade mission.

3.3 The Arago Sensor

This section details a proposed sensor, the **Arago Sensor**, that uses long wavelength light diffracted around the starshade (a phenomenon known as the Spot of Arago) to map the wavefront distribution of light at the aperture of the science telescope and guide to the center of the starshade's shadow [55]. We will detail scaling relations for the Arago Sensor and provide an efficient method to retrieve high precision starshade position information from the observed diffraction pattern. We will verify these arguments with our diffractive ray tracing code and outline future plans to validate with laboratory tests. This work is being done under a NASA Technology Development for Exoplanet Missions (TDEM) grant to advance the TRL of a starshade formation flying sensor.

3.3.1 Using the Spot of Arago for formation sensing

The starshade's performance degrades steeply with increasing wavelength (suppression $\propto \lambda^{12}$). For a given separation, as the wavelength increases ($\lambda >> 1\mu$m), the size of the Fresnel half-zones increase and become comparable to the change across the apodization function and the starshade appears to the light as a circular disk. Light diffracted around the edge of the starshade reaches the optical axis in phase and constructively interferes to recover to its unblocked intensity, producing a phenomenon known as the spot of Arago. Figure 3.11 shows the recovered intensity fraction as a function of wavelength for the WFIRST mission parameters (35 m starshade at 35,000 km separation from a 2.4 m telescope), demonstrating the steep increase with wavelength.

A unique property of the spot of Arago is that it is continuously formed along the optical axis, in other words, it has an infinite focal length. This means that as the starshade moves laterally, the spot is formed at the central axis of the starshade's new position and there is a one-to-one mapping in the lateral position of the spot and that of the starshade. This one-to-one mapping is what allows us to detect sub-meter movements over megameters of separation. Imaging the pupil of the science telescope provides a map of the incident intensity at the aperture and the center of the spot of Arago yields the position of the starshade. This unique diffraction property makes a pupil plane instrument advantageous over a focal plane instrument that would need to sense angular measurements of < 0.25 mas in order to detect positions accurate to the centimeter level.

3.3.2 Diffraction model of the Spot of Arago

At long wavelengths, the starshade can be approximated by a circular disk. The radius of this representative disk (R) can be approximated as the radius to the $1/e$ inflection point, $a + b$. The resultant diffraction pattern can be determined by solving Equation 3.5,

$$U\left(s,\phi,z\right) = \frac{e^{ikz}}{i\lambda z} e^{\frac{iks^2}{2z}} \iint U_0\left(\rho,\theta\right) e^{\frac{ik\rho^2}{2z}} e^{-\frac{ik\rho s}{z}\cos(\theta-\phi)} \rho \, d\rho \, d\theta \tag{3.5}$$

for a circular obstruction with circularly symmetric apodization function $A\left(\rho\right) = 1, \forall \rho > R$.

The simplicity of the apodization function allows us to solve Equation 3.5 without the need

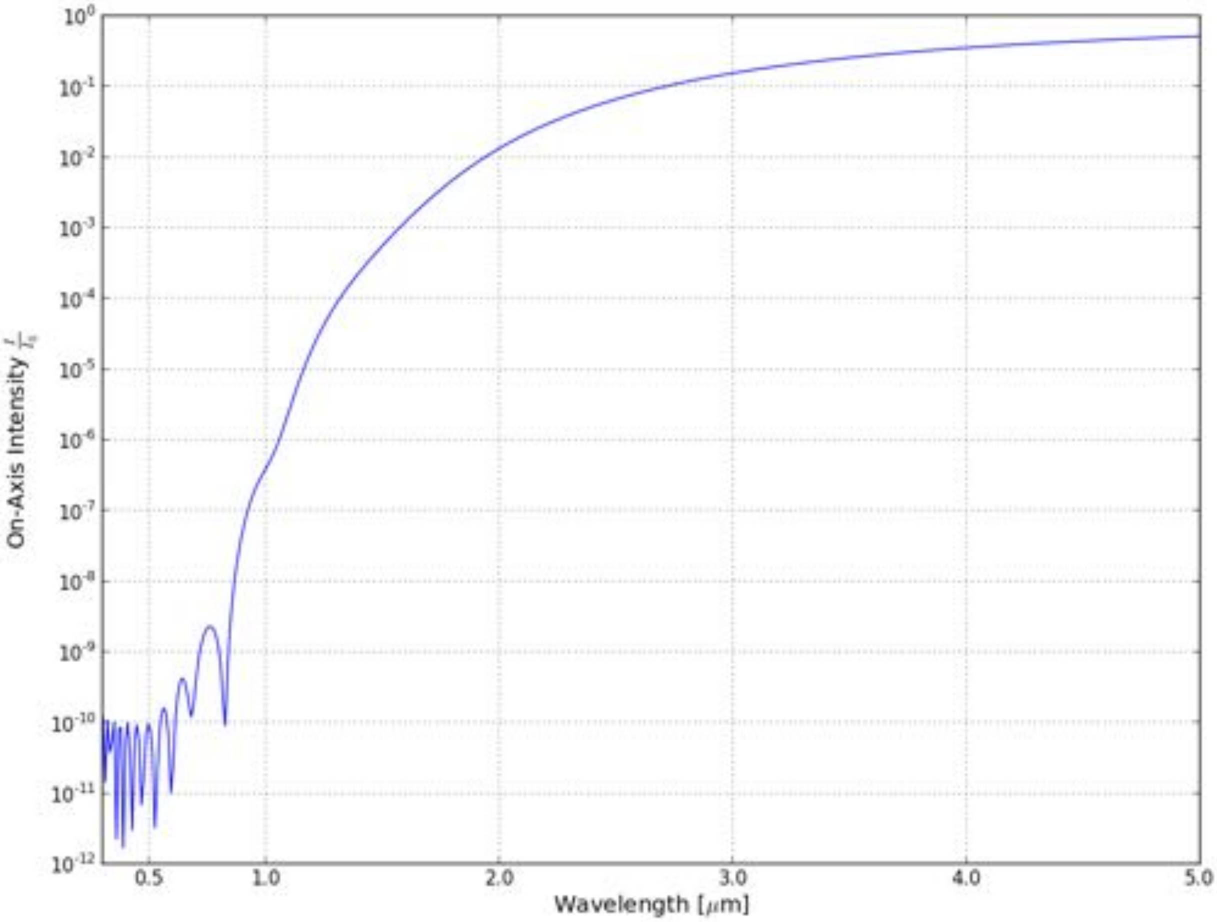

Figure 3.11: Simulated on-axis intensity fraction vs wavelength for WFIRST starshade.

of invoking Babinet's principle. We first assume a uniform incident field and integrate over θ using the relation,

$$\int_0^{2\pi} e^{ix\cos(\theta-\phi)}\,d\theta = 2\pi J_0\left(x\right) \tag{3.6}$$

where $x = \frac{k\rho s}{z}$. The remaining integral in ρ is then,

$$U\left(s,\phi,z\right) = \frac{ke^{ikz}}{iz} e^{\frac{iks^2}{2z}} U_0 \int_R^\infty e^{\frac{ik\rho^2}{2z}} J_0\left(\frac{k\rho s}{z}\right) \rho\, d\rho \tag{3.7}$$

changing the variable of integration to $t = \rho/R$ and defining,

$$\begin{aligned} u &= \frac{kR^2}{z} \\ v &= \frac{k\rho s}{z} \end{aligned} \tag{3.8}$$

yields,

$$U\left(s,z\right) = -iue^{ikz} e^{\frac{iks^2}{2z}} U_0 \int_1^\infty e^{\frac{i}{2}ut^2} J_0\left(vt\right) t\, dt \tag{3.9}$$

From [91], we can integrate the Bessel function in terms of n^{th} order Lommel functions of u, v given by Equation 3.11,

$$ue^{iu/2} \int_1^\infty e^{\frac{i}{2}ut^2} J_0\left(vt\right) t\, dt = V_1\left(u,v\right) + iV_0\left(u,v\right) \tag{3.10}$$

$$V_n\left(u,v\right) = \sum_{m=0}^{\infty} \left(-1\right)^m \left(\frac{v}{u}\right)^{n+2m} J_{n+2m}\left(v\right) \tag{3.11}$$

This leads to our solution for the field and intensity from a circular disk of radius R to be

$$U\left(s,z\right) = e^{ikz} e^{\frac{iks^2}{2z}} U_0 e^{iu/2} \left[V_0\left(u,v\right) - iV_1\left(u,v\right)\right] \tag{3.12}$$

$$I\left(s,z\right) = V_0^2\left(u,v\right) + V_1^2\left(u,v\right) \tag{3.13}$$

The intensity in the geometric shadow of the starshade $I(s)$, where s is the off-axis distance, can then be approximated by Equation 3.13 [79]. For $v << u$, we can ignore the higher-order terms in Equation 3.11 and approximate the intensity as

$$I(s) \approx J_0^2\left(v\right) \tag{3.14}$$

Figure 3.12 shows the radial intensity profiles of the resultant diffraction patterns of a starshade and a circular disk simulated by our diffractive ray tracing code (DRT; see Chapter 5). Also shown are the profiles from Equation 3.13 and Equation 3.14. This figure shows that the central region of the starshade's diffraction pattern at 2 μm can be approximated by a circular disk of radius $(a + b)$, using the approximation made in Equation 3.14. We see that only the central peak of the diffraction pattern agrees, as the wings of the diffraction pattern are receiving light diffracting in from the exponentially decaying apodization function past the offset radius (a) of the starshade. The width of the central peak of the spot of Arago can be approximated as the location of the first zero of J_0 and is approximated with Equation 3.15. If we choose our guiding bandpass appropriately, we will only receive appreciable intensity from the wings when the starshade is far off-center.

$$r_{SoA} \approx 0.38 \frac{\lambda F_{eff}}{R} \tag{3.15}$$

Note that in Equation 3.15 we use the effective separation (F_{eff}), which differs if using a diverging light source. If F_1 is the distance from the source to the starshade, and F_2 is the distance from the starshade to the telescope, then F_{eff} is given by Equation 3.16. If $F_1 = F_2$, $F_{eff} = \frac{1}{2}F_2$.

$$F_{eff} = \frac{F_1 F_2}{F_1 + F_2} \tag{3.16}$$

Figure 3.13 shows the wavelength dependence of the shape of the diffraction pattern, most importantly the width of the central spot.

Along with verifying the approximation of the diffraction pattern made in Equation 3.14, DRT is used to simulate images of a pupil imaging optic, which we can use to examine methods for determining the alignment of the starshade. The simulated images are created in the following manner. A wave of plane parallel, monochromatic light is diffracted around the starshade. The electric field at every point within the telescope aperture $E_0(x_0, y_0, 0)$ is calculated using the optical model presented in Chapter 5. This field is multiplied by the pupil function of the telescope $A(x_0, y_0)$ to account for obstructions caused by a secondary mirror and support structures (see Figure 3.14

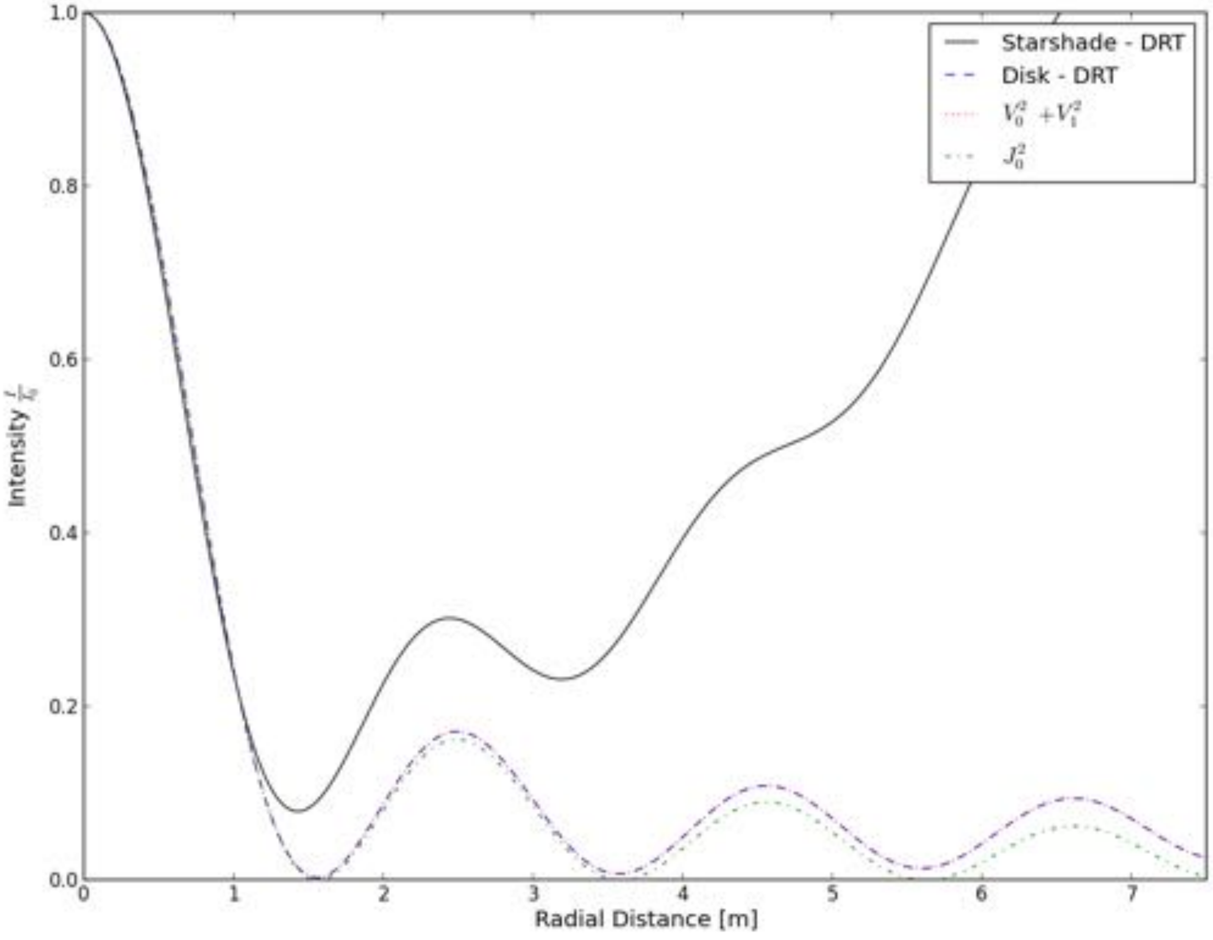

Figure 3.12: Radial profile of the simulated diffraction patterns of a WFIRST starshade (**black** solid line) and a circular disk (**blue** dashed line). The approximations of Equations 3.13 (**red** dotted line) and 3.14 (**green** dot-dash line) are also shown. ($\lambda = 2\ \mu$m)

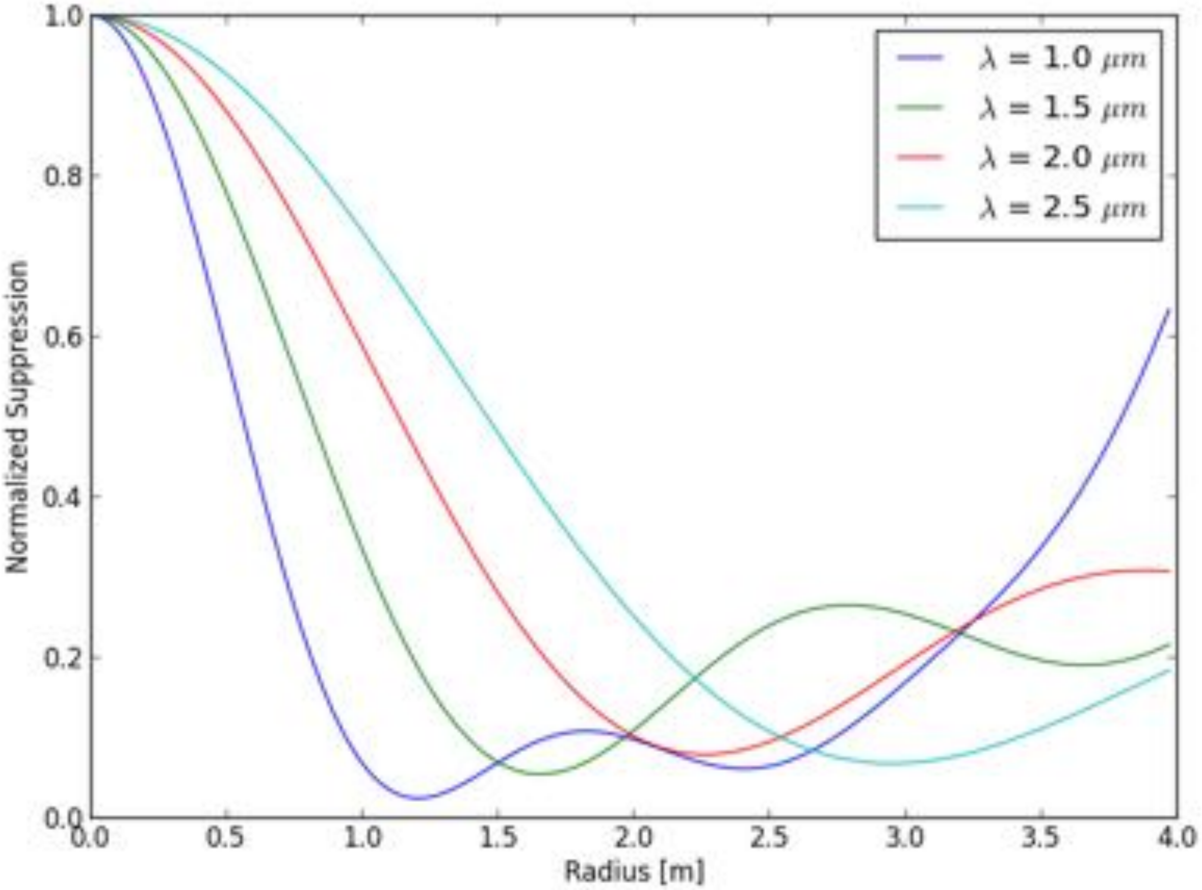

Figure 3.13: Simulation of the normalized suppression vs. radius and as a function of wavelength for a 35 m starshade at 35,000 km separation demonstrating the effect that wavelength has on the shape of the spot.

for the WFIRST pupil function). The resultant field at the focal plane of the pupil imaging optic is the Fresnel diffraction pattern after propagating through a primary optic and a pupil imaging optic. This is repeated for different wavelengths across a bandpass and the intensities are added incoherently. Example images of a starshade that is centered and one that is off-center by 0.5 m are shown in Figures 3.14a and 3.14b, respectively.

3.3.3 Position determination from the Spot of Arago

As the spot of Arago is continuously formed along the optical axis of the starshade, there is a one-to-one mapping of the center of the spot of Arago incident on the aperture and the center of the starshade relative to the line of sight between telescope and star. This means that finding the center of the spot of Arago within the aperture will directly yield the lateral offset of the starshade, so the accuracy in the position knowledge is limited to how well we can find the true center of the spot of Arago. There are a number of complications that prevent a simple centroiding algorithm from being the best option:

- As shown in Figure 3.14, WFIRST has a complex, non-symmetric pupil which can bias the centroiding algorithm.
- As the spot moves towards the edge of the aperture in one direction, the centroid becomes biased towards the opposite direction as there is no flux contribution from beyond the edge of the aperture.
- If the spot center has moved off the edge of the aperture, centroiding will not find the center.

To get a more accurate position of the spot center, we fit a model of the diffraction pattern to the image and solve for the center of the spot. Luckily, as we have shown earlier, the normally complex diffraction pattern from the starshade is simpler at longer wavelengths and can be approximated by Equation 3.14. This allows for an efficient method to accurately solve for the starshade's

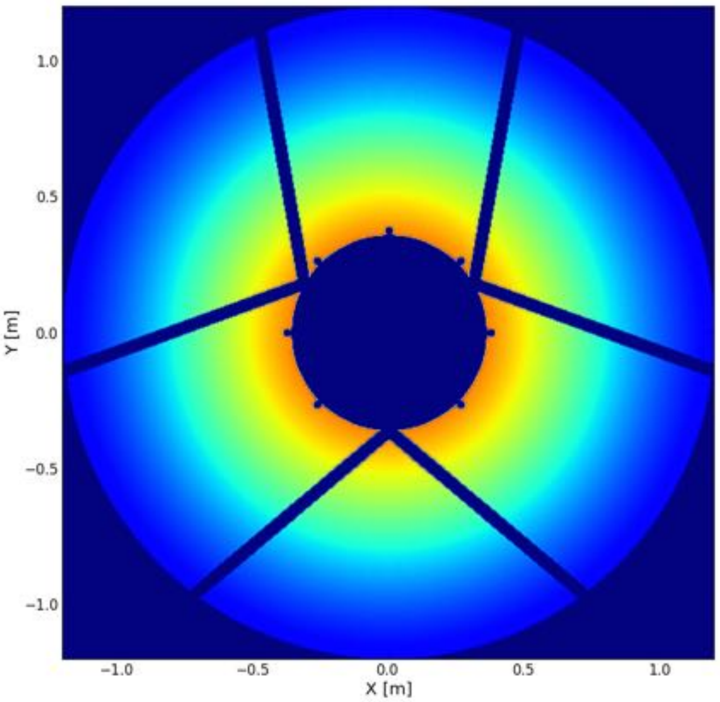

(a) Starshade centered on aperture

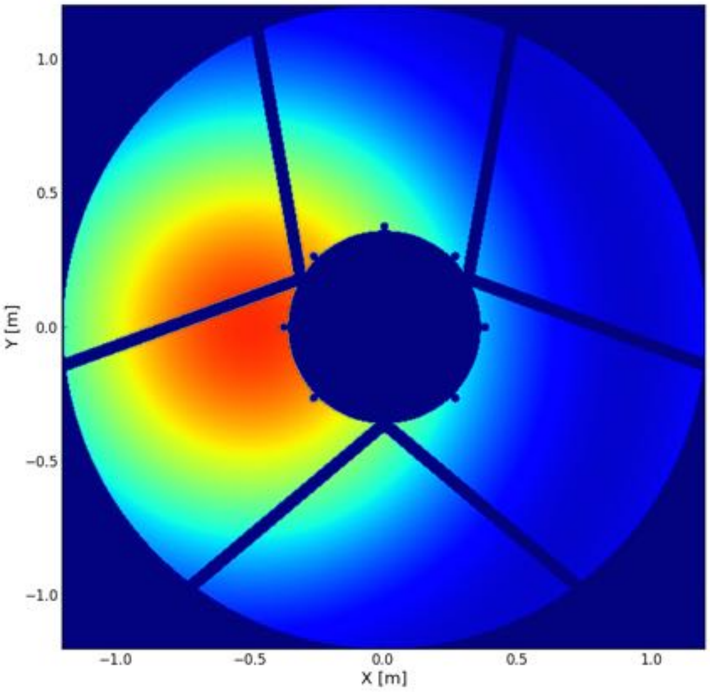

(b) Starshade off-center by 0.5 m

Figure 3.14: Simulated pupil images at $\lambda = 2$ μm with WFIRST pupil function

position, even when the spot is off the aperture. Figure 3.15 shows a simulation of the pupil image of an off-center starshade, along with the model used to fit for the center of the spot in the pupil.

3.3.3.1 Choice of guiding bandpass

The intensity and distribution of diffracted light incident on the telescope are a function of the starshade size, separation, and wavelength (Equations 3.13 and 3.15). The first two parameters are driven by science requirements, leaving a choice in only the position sensing wavelength. The factors motivating this decision are the intensity of the diffracted light, the size of the spot of Arago relative to the aperture size, and the availability of detectors in that bandpass.

The minimum wavelength is unimportant as the intensity at a given off-axis position is dominated by longer wavelengths (Figure 3.11). The lower bound for the maximum wavelength is set so that there is enough recovered signal to achieve a desirable signal-to-noise ratio. The upper bound for the maximum wavelength is set so the size of the spot is a certain fraction of the aperture size. If one imagines the extreme limit in which the spot size is larger than the aperture, then the aperture will be uniformly illuminated and it will not be possible to discern small movements of the starshade. We need the flux to drop off quickly enough within the aperture to determine a unique solution with our model fit, but not too quickly that there is too little signal or that the spot is completely hidden by the secondary mirror.

3.3.3.2 Centroiding simulations

We used the simulated images generated by DRT to investigate the ability to accurately determine the spot center within the aperture. We created a simulated image as we moved the starshade off-axis in 1 cm increments. The spot center was calculated with a standard centroiding algorithm and with a least squares fit to a model image approximated by Equation 3.14. Figure 3.16 shows the results from this simulation using a maximum wavelength of 2 μm. It shows the true position of the starshade for each position step and the positions calculated by the centroiding algorithm and by the model fit. Figure 3.17 plots the mean error in the starshade position, from

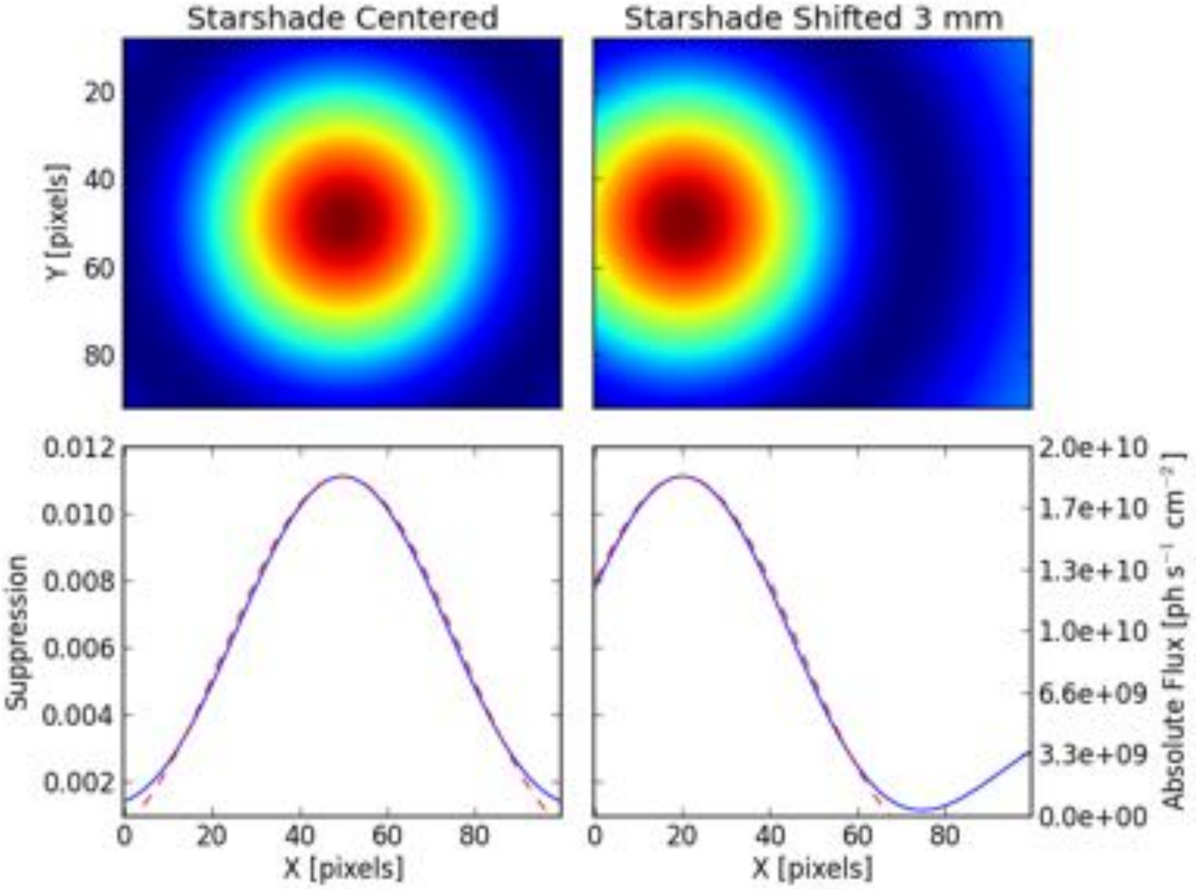

Figure 3.15: The **top** panel shows simulated pupil images using TDEM13 parameters of Table 3.2. In the **bottom** panel, the **blue** line is a cross-section of the image and the **red** dashed line is a model fit to the image using Equation 3.14. The **left** panel is when the starshade is centered on the aperture, the **right** panel is after the starshade has been shifted by 3 mm.

the theoretical position, as calculated by the centroiding algorithm and by the model fit. As can be seen in Figure 3.16, the model fit does an excellent job in getting around the central obscuration in the pupil to find the true center of the spot and is more robust than simple centroiding, especially at the edge of the aperture. Even without considerations of signal-to-noise (the intensity at 1 μm is 10^{-4} times that at 2 μm), we must extend our bandpass beyond 1 μm to get a spot size large enough to accurately fit our model to. While noise has not been included in these simulations, they are an instructive start to understanding the requirements that must go into designing an Arago Sensor.

3.4 Arago Sensor Field Tests

This section details the development plan for and purpose of the TDEM study to develop and demonstrate technologies critical to the formation flying of starshades. This study will investigate using long wavelength light diffracted around a starshade to provide accurate position information over large separations and advance the technology of a pupil imaging formation flying sensor. This will be the first investigation of starshades at wavelengths $\lambda > 1.5$ μm and will provide a critical datum for validation of optical models used to predict starshade performance.

The major milestones to be completed in this study will advance the technology of a pupil imaging formation flying sensor for starshades and provide insight into the future design of such an instrument. The milestones we have chosen will demonstrate the starshade's performance degrades at long wavelengths as predicted by theory and that this degradation provides a useful guiding signal at adequate signal-to-noise. They will also demonstrate that the spot of Arago provides a direct proxy of the starshade's position at large separations, can provide higher precision position information than obtainable with angular measurements in the focal plane, and that this signal can guide a telescope to the center of the shadow.

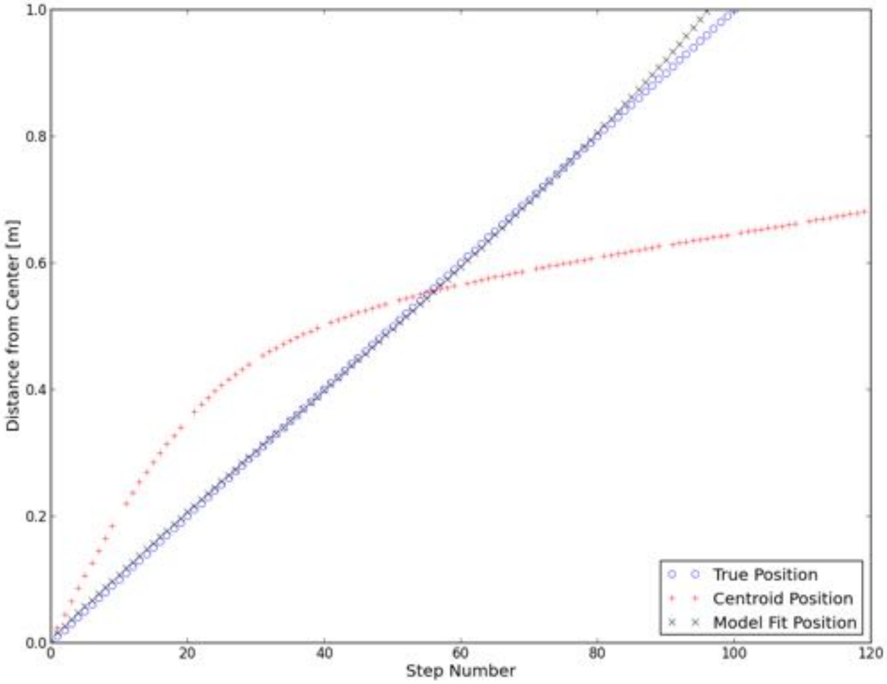

Figure 3.16: The true position of the starshade for each position step (**cyan** circles) with the position calculated by a centroiding algorithm (**red** plus) and by a model fit (**black** x).

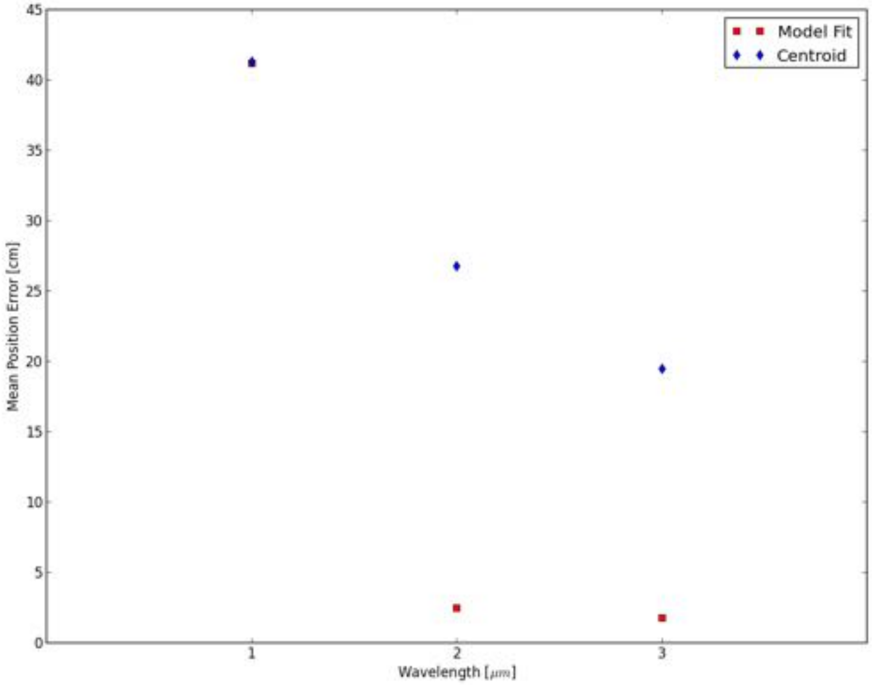

Figure 3.17: The mean error in starshade position, relative to the theoretical position, as calculated from the pupil image by a centroiding algorithm (**blue** diamonds) and by a model fit (**red** squares).

Two major milestones are defined as:

(1) Demonstrate recovery of long wavelength ($\lambda > 1.5$ μm) light diffracted around starshade. Demonstrate agreement between starshade performance at these wavelengths and model predictions.

(2) Demonstrate ability to use diffracted light to provide accurate measurements of the starshade's position while in its shadow.

3.4.1 Experiment description

For Milestone 1, the layout and test procedure of our experiment follow that of [29], except we will be observing at longer wavelengths and taking pupil plane, instead of focal plane, images. At one end of the setup will be a telescope with a NIR camera imaging the pupil plane (see Figure 3.18). We will use a commercial 6 inch telescope with various masks to stop down the size of our aperture. 2 kilometers away will be a bright artificial light source ($\lambda > 1$ μm). Halfway between will be a starshade on a translation stage. The prescription for the shape of the starshade is given by the hypergaussian analytical solution presented in [10] and uses the parameters, $a = b = 3$ cm, $n = 6$. In order to work with a starshade of a practical size, we will be using a 12 cm diameter (to the inflection point) starshade etched out of steel in a chemical bath. Starshades of this size have previously been demonstrated to provide sufficiently high-contrast [29, 58]. The physical parameters of the experiment are shown in Table 3.2 and compared to those of the proposed NWO mission [12] and the work of [29]. Note that our experiment is conducted at flight-like Fresnel numbers.

3.4.2 Optical system description + signal-to-noise calculations

The optical system is shown schematically in Figure 3.18, in which we use the secondary mirror of a 15 cm diameter Cassegrain telescope to reimage the defining pupil that is the aperture. A dichroic beamsplitter separates the light into infrared light reimaging the pupil plane and visible

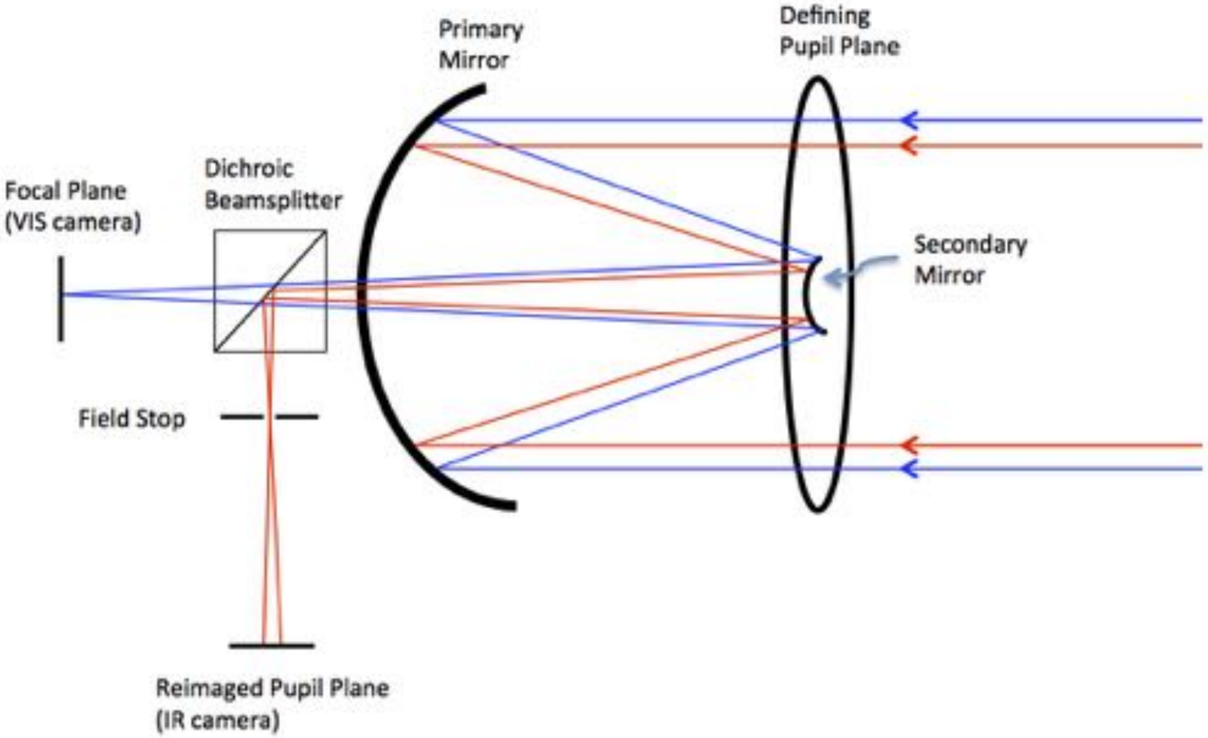

Figure 3.18: Schematic of optical layout with IR camera imaging the aperture (defining pupil) and visible light camera imaging the focal plane.

Mission/Mode	λ	$\mathbf{F}_{eff}$	$\mathbf{r}_{SS}$	**N**	$\mathbf{R}_{tel}$	$\mathbf{r}_{SoA}$
NWO Guiding	2 μm	80 Mm	25 m	3.9	2 m	2.5 m
TDEM13 Guiding	2 μm	500 m	6 cm	3.6	1 cm	6 mm
NWO Science	0.5 μm	80 Mm	25 m	15	2 m	-
TDEM13 Science	0.5 μm	500 m	6 cm	14	1 cm	-
NG TDEM Science	0.5 μm	500 m	24 cm	230	2 cm	-

Table 3.2: Physical parameters for a number of missions: full-scale NWO mission [12], CU's TDEM13 work, and NG's previous TDEM work [29], for different observing modes (guiding or science). λ is the wavelength of the observation, F_{eff} is the effective separation between starshade and telescope, $r = a + b$ is the radius of the starshade to its inflection point, N is the Fresnel number, R_{tel} is the aperture radius, and r_{SoA} is the radius of the spot of Arago at 2 μm. Note that this test is at a flight-like Fresnel number.

light imaging the focal plane. We will scale the pupil imaging camera so that 100 pixels cover a 2 cm diameter of the aperture [56]. We can alleviate the constraint on wandering of the spot due to the atmosphere, by allowing the field of view of the pupil imaging camera to extend the full aperture and creating 2 cm subapertures (spanned by 100 pixels) in software.

We baseline the artificial light source to output 1W optical power, which is focused to a 2.5° beam with a 85 mm camera lens, providing $\sim 10^{12}$ photons/s/cm^2 incident on our aperture. Assuming each pixel covers 200 μm of the aperture, a detector with 80% QE, and a recovered spot intensity of 1%, we expect $\sim 5 \times 10^6$ photons/s/pixel. We assume a detector readout noise of 60 e$^-$ and neglect any contribution from dust scattering to estimate a S/N of 100 with 2 ms integration (reading the camera at 300 fps). The brightness of the source and the level of recovered flux in the spot allow for short exposure times to help alleviate atmospheric effects. Figure 3.19 shows the estimated flux at the pupil as a function of wavelength. The flux (and S/N) drops dramatically with decreasing wavelength and the images will be dominated by longer wavelength light.

3.4.3 Dry lake bed test facility

We will complete our milestones performing all experiments on dry lake beds in open air. Dry lake beds are some of the flattest places on Earth and allow for the three-way alignment of a telescope, starshade, and artificial light source over kilometers of separation. We will utilize the dry lake bed test facility established with previous TDEM work led by the Northrop Grumman starshade team [29], which has been proven to be an efficient way to test 1/100$^{\text{th}}$-scale starshades (Chapter 6). The latest results from those tests [90, 30] show that the air beams are stable enough to perform high contrast imaging with starshades. In particular, it was shown that the fast twinkle of the atmosphere does not affect the light suppressing performance of the starshades. It was also shown there are longer timescale (i.e., minutes) drifts due to refraction in the atmosphere.

Extending to longer wavelengths will result in atmospheric effects that are less problematic than for [30]. The size of the atmospheric seeing disk, a characteristic length scale at which atmospheric turbulence starts to significantly affect propagating wavefronts, increases as $\lambda^{6/5}$ [28].

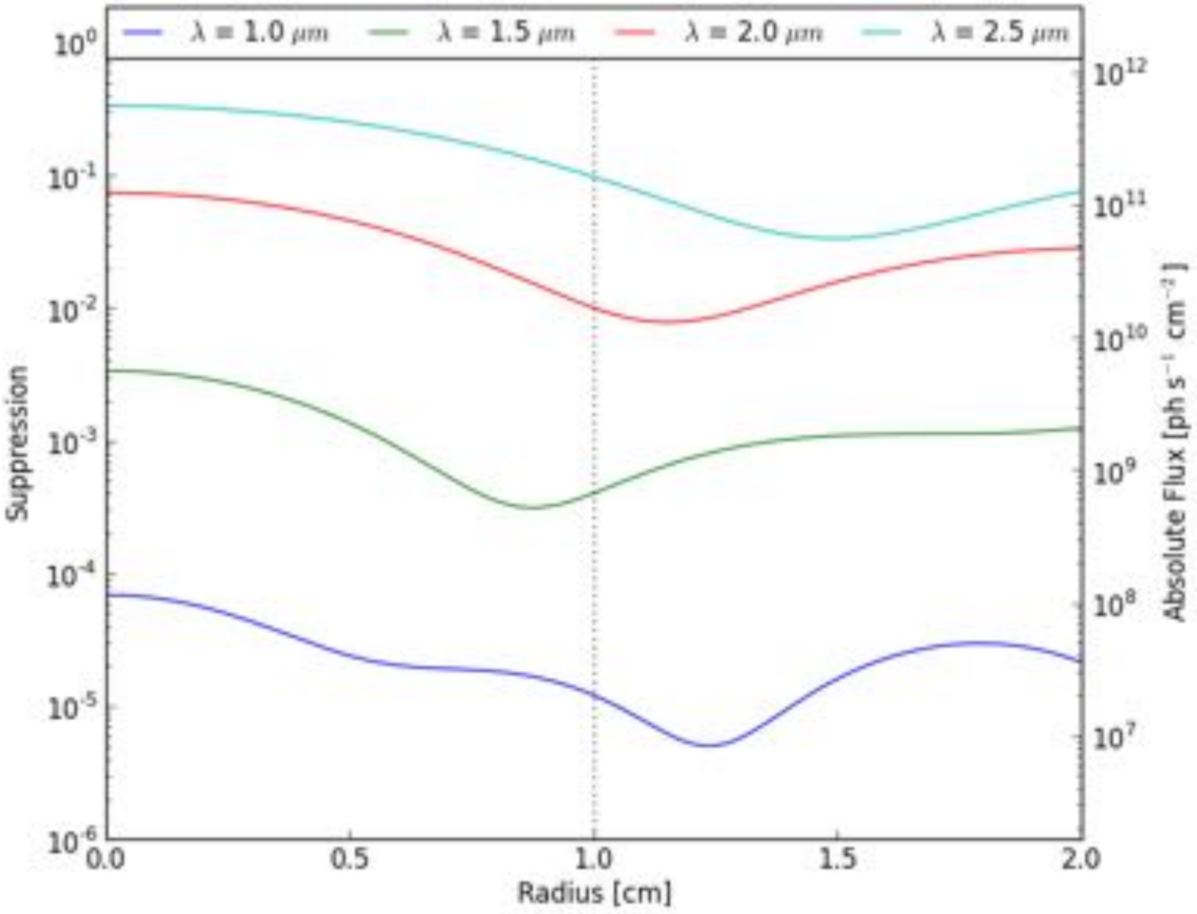

Figure 3.19: Simulated expected flux vs radius for different wavelengths using TDEM13 parameters in Table 3.2. The **left** axis is shown in units of suppression, the **right** axis is shown in absolute flux units [ph s^{-1} cm^{-2}]. The flux falls off dramatically at short wavelengths.

On a decently stable observing night, [30] saw an average of 8 arcseconds seeing, which gives a seeing disk size of $r_0 \sim 1.4$ cm at $\lambda = 0.55$ μm. At $\lambda = 2$ μm, this seeing disk size grows to $r_0 \sim 8$ cm and is larger than our aperture, meaning turbulence will not have a significant effect. [13] found that the average Strehl number of the spot of Arago propagating through a turbulent medium is less susceptible to turbulence strength than that of conventional imaging. Time variations in atmospheric properties will lead to changes in transmission, but if we take our unblocked calibration images close in time to the blocked images, we can sample the same atmosphere and these effects will be mitigated.

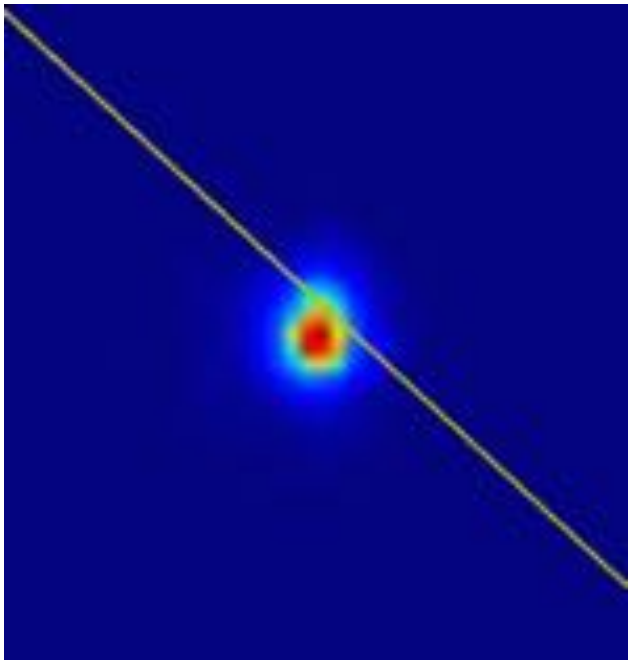

Figure 3.20: DSLR image of the spot of Arago produced by the star Vega, formed behind a 8 cm circular disk at a separation of 1 km.

The increase in seeing disk size at longer wavelengths and imaging the spot of Arago in the pupil instead of conventional imaging lead us to believe atmospheric effects will not limit the success of the experiment. Figure 3.20 shows an image of the spot of Arago formed by the star Vega and demonstrates the spot of Arago can be formed in the atmosphere over a large separation. This setup consisted of a camera positioned 1 km behind a 8 cm circular disk as the star disappeared behind the disk and reemerged as the spot of Arago. While we are relying on previous experience to estimate the atmosphere will not prevent the milestones from being reached, we will use off-axis lights to monitor the atmosphere during observations and use those data to include atmospheric effects in our models.

An additional atmospheric effect that needs to be considered is the slow image wander due to changes in atmospheric refraction. As the desert floor cools after the sun sets, the thermal structure of the air directly above the ground changes and results in a wandering image of the main source. [30] saw a maximum apparent movement of the light source at the starshade's distance of 2 cm/s. Experience in previous desert tests have taught us at which time of night this effect is worse and that we should not bother observing during the worst conditions. This will shorten the amount of observing time available during each trip, but there will be periods of stable air in which we can observe unhindered. Taking shorter exposures (a luxury we are allowed when not trying to reach 10^{-9} contrast) will allow us to throw out bad images and combine the good ones to increase signal-to-noise. Again, observing at longer wavelengths will lessen this effect [28].

A limiting factor to the achievable contrast of [29] was forward scattering of the main source off dust in the atmosphere. The forward scattering created a smooth background at the 10^{-8} contrast level, well below our expected noise floor and therefore will not be a contributing factor to our results.

3.4.4 Optical model validation

The size scales of the space-based starshade mission make it impossible to fully test the starshade as a system on the ground. This forces us to rely on optical models, invoking scalar diffraction theory, to predict performance. Scalar diffraction theory tells us that if we preserve the Fresnel number (Equation 3.17), we maintain similarity and probe the same physics. This allows us to validate our models with a smaller system and use those results to predict performance on the large scale. Optical model validation was a major milestone in [29] and this TDEM will extend that work to an unexplored wavelength regime. We will measure the intensity distribution across the aperture for wavelengths > 1.5 μm, with the starshade at different lateral displacements. The results of each configuration will be compared against state of the art diffraction codes (Chapter 5).

$$N = \frac{r^2}{\lambda F_{eff}} \tag{3.17}$$

An additional test that will be done if time allows, is to investigate the effect that tilting the starshade out of plane has on the formation of the spot of Arago. [29] has shown that tilting the starshade (up to 30°) has little effect on the light suppression performance of the starshade and we would like to verify that it will not have a strong effect on the guiding signal. Figure 3.21 shows a simulation of the pupil image for a starshade tilted by 20°. Tilting the starshade foreshortens one dimension of the starshade and as long as that smaller dimension does not enter an adjacent Fresnel half-zone (allowing 30° of tilt with our setup at $\lambda = 2$ μm), then the spot of Arago is still formed, but with a skewed PSF.

These tests, and the completion of Milestone 1, will help to validate these diffraction models in a parameter space not previously investigated and will help to define the robustness of the formation of the spot of Arago.

3.4.5 Starshade positioning tests

Milestone 2 will demonstrate the spot of Arago can be used to provide accurate position of the telescope in the starshade's shadow. This will be demonstrated through a number of positioning tests. The starshade will be mounted on a stage and stepped in precise movements across the field of view of the telescope, while images are taken at each step. The relative movement detected in the image will then be compared to the known movement of the starshade. In addition to the fast atmospheric twinkle ('seeing'), there will be a slow relative drift in the apparent position of the target source due to refraction in the atmosphere caused by temperature gradients above the desert floor. Experience in [29] has shown us that this effect is slow compared to our exposure time, and the effects can be mitigated by stacking multiple images. An off-axis light source set at the same height as the primary source will allow us to probe what the atmosphere is doing. In addition to detecting relative motion of the starshade, we would like to verify that we can use the spot of Arago to guide us to the center of the starshade. This will be done with human-in-the-loop visual feedback manually positioning the starshade to center over the telescope. We can verify we are in the center of the shadow by imaging a symmetric distribution of visible light diffracted at the base of the petals.

3.4.6 Additional tests

The following is a list of "nice to haves" i.e., tests that would be nice to complete should there be time in the schedule.

(1) Vary aperture size to investigate effect of resolution on guiding signal and match flight-like resolution.

(2) Obtain photometric measurements at narrow wavelength bands and compare the suppression's spectral response to that predicted by models.

(3) Investigate effect of tilting the starshade out of plane on the formation of the spot of Arago.

(4) Investigate the effect an obscuring secondary mirror has on determining the location of the spot in the aperture.

3.4.7 Differences between laboratory demonstrations and flight

The starshades used in this experiment are $\sim 1/420^{\text{th}}$ the size of that in the NWO mission and we use an artificial, diverging light source instead of collimated starlight. The diverging beam acts to decrease the effective separation between starshade and telescope by half. The diverging beam also changes the 1-1 relation between the movements of the starshade and spot of Arago to a 1-2 relation, respectively. Table 3.2 summarizes these parameters and shows that we have scaled the experiment to be at a flight-like Fresnel number. This means the same optical models used to

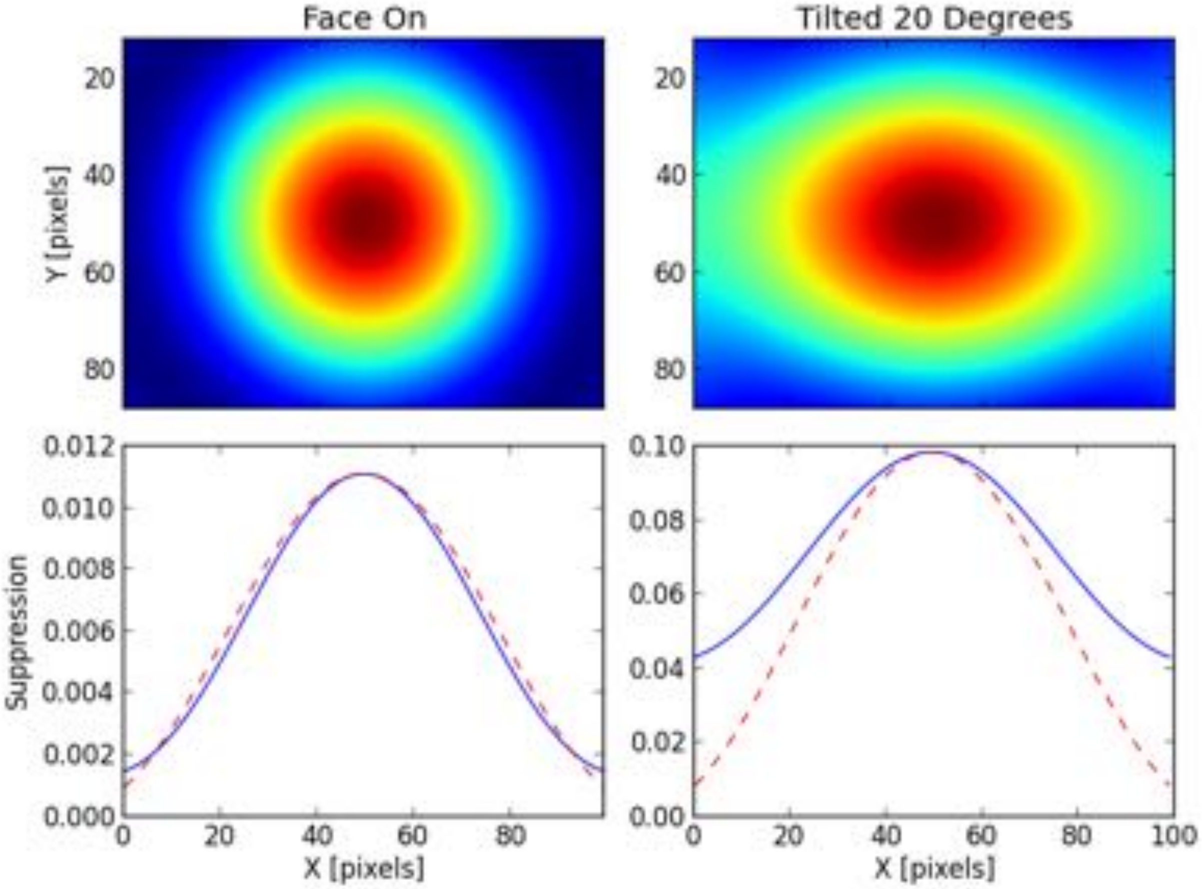

Figure 3.21: The **top** panel shows simulated pupil images using TDEM13 parameters of Table 3.2. In the **bottom** panel, the **blue** line is a cross-section of the image and the **red** dashed line is a model fit to the image using Equation 3.14. The **left** panel is when the starshade is face-on, the **right** panel is after the starshade has been tilted by 20°.

predict the performance of (and to be verified by) the small-scale tests can be used to predict the performance of the flight-like starshade.

The outdoor "laboratory" is a different environment than expected on orbit (in some senses less forgiving), but as demonstrated in [30], it should not affect the validity of our experiments. As mentioned in Section 3.4.3, the atmosphere will have a varying effect on light transmission, but will be accounted for with unblocked calibration images. The scattering of dust in the atmosphere should be a negligible background, and can easily be subtracted if present at higher levels than predicted.

3.4.8 Data measurement & analysis

The data product for each test will be pupil images recorded with a NIR detector, in the shadow of the starshade. The experimental methods for obtaining these data for the different milestones are explained in Section 3.4.1.

The analysis for Milestone 1 will be a comparison of the images to those generated by the numerical models. Comparison to the numerical models for will be done in units of **suppression**, in which the images are normalized by those of the unblocked source. The blocked and unblocked images will be taken in the shortest possible timeframe in order to sample the same atmospheric conditions. A number of filters from 1 μm - 2 μm will be used to assess the wavelength response of the starshade. Other standard image processing, such as dark subtractions, will also be done. Our main measurements to compare to the models will be the peak value and width of the central spot of the diffraction pattern.

The analysis for Milestone 2 will be to extract the relative position of the starshade from the images and compare against the known movement of the starshade. The relation between movement of the starshade and the position extracted from the images will be compared against theoretical predictions. We will investigate different methods of extracting the position from the images (centroiding, model fitting, etc.), which will be an additional informative product of this study. The Final Report to be submitted to the Exoplanet Exploration Program will contain the following data products:

(1) Model predictions of the resultant diffraction pattern incident on the pupil in units of suppression.

(2) Pupil plane images normalized by unblocked source.

(3) Agreement between measurements and predictions for the diffraction pattern at long wavelengths.

(4) Model predictions of relative position measurements of the starshade calculated from simulated images.

(5) Relative position measurements of the starshade calculated from pupil images.

(6) Agreement between measurements and predictions for relative position sensing.

(7) Quantification of atmospheric turbulence seen during testing.

3.4.9 Success criteria

For each milestone we list the criteria that serve as necessary requirements for the successful completion of that milestone along with the rationale for why the criteria demonstrate the intent of the milestone.

3.4.9.1 Milestone #1

With the starshade placed directly in the line of sight to a NIR source, measure the diffraction pattern in the starshade shadow and compare against numerical models to assess model validity.

The purpose for this first milestone is to demonstrate that at $\lambda > 1.5$ μm we can recover enough flux for a guiding signal at an adequate signal-to-noise. A perfectly circular disk should recover 100% of the intensity, however at these wavelengths, the apodization of the starshade's petals is still working to extinguish some of the light. Theory predicts the on-axis intensity in the shadow of a starshade at $\lambda = 2$ μm to be 1% of the unblocked source intensity, but as this is unexplored territory, we cannot say for certain what level of light will be recovered. Our success criteria is to measure the level of diffracted light at different wavelengths (1 μm - 2 μm) and demonstrate agreement with numerical models to 10%. These results will allow us to evaluate if the recovered flux is significantly bright and robust to be used as a guiding signal.

As mentioned in Section 3.4.4, we must rely on optical models to predict the flight performance of a starshade. Comparing images taken in the field with those predicted by our models will be an important anchor for model validation at long wavelengths. Additionally, working at a longer wavelength will allow us to work at a flight-like Fresnel number, an important consideration when validating the models. The measurement we are interested in for use as a formation flying signal, is the shape of the diffraction pattern in the shadow of the starshade. Comparison of the relative intensity and width of the central peak in the diffraction pattern will allow us to assess the validity of our models at these wavelengths. Our success criteria for this milestone is to obtain measurements at these wavelengths and document the agreement between experimental results and models. Our goal is for the agreement between results and models to be below 10%.

3.4.9.2 Milestone #2

Measure relative position of starshade and telescope and compare to known position to within error imposed by atmospheric seeing.

The purpose of Milestone 2 is to demonstrate we can use the light diffracted around the starshade to provide high-precision position measurements. The accuracy of these measurements depend on signal-to-noise, telescope resolution, and size of the central diffraction peak relative to the aperture size. Performing these tests in the atmosphere will also limit accuracy, but movements that are larger than the expected error due to seeing should provide a clear signal. Our success criteria are to define a relation between the movement of the starshade and the movement of the spot of Arago in the pupil plane and compare this relation to predictions. Our accuracy will be limited by the error introduced by atmospheric seeing. The accuracy of position sensing required by the NWO mission is 2% the width of the spot of Arago (±10 cm with a 5 m diameter spot). In order to reach that level with these tests, we need an accuracy of 240 μm, or ∼1 pixel. By monitoring off-axis lights at the distance of the starshade, we can estimate the contribution of image wander due to the atmosphere. Our goal for this milestone is for the RMS fluctuations detected in the position of the starshade as detected by the spot of Arago to agree with the RMS fluctuations seen in the positions of the off-axis lights by 10%. These data will allow us to assess the **Arago Sensor** as a means for accurate, long-range position sensing.

Chapter 4

SUBORBITAL FLIGHT DEMONSTRATION

4.1 Testing Starshades on Vertical Takeoff Vertical Landing Rockets

To help develop technology in preparation for a future starshade mission, we are attempting a number of suborbital demonstrations in which we can test starshades as a full system. While it is impossible to test a full-scale starshade system without going to space, we can scale down the architecture to a 0.5 m starshade at a few kilometers separation for tests in the troposphere. The difficulty then becomes finding a means to hold the starshade in the LOS to a background target. Atmospheric effects and the fast timescales of disturbances that occur when working in the troposphere make it difficult to maintain alignment between telescope, starshade, and star. We have investigated different platforms to provide this alignment such as Zeppelins [32], quadcopters, and stratospheric jets paired with high altitude balloons. Recently, we have identified vertical takeoff vertical landing (VTVL) rockets as a potential suborbital platform that will allow us to achieve high-precision line of sight (LOS) alignment between telescope, starshade, and astronomical target at kilometers of separation. The flight campaign of Technology #T0092, supported by the NASA Flight Opportunities Program, investigated VTVL rockets as a starshade platform and flight tested a vision-based formation flying sensor to enable high-precision alignment of the vehicle.

4.2 Flight Campaign Objectives

The main motivation of this flight campaign was to investigate VTVL rockets as a platform for testing starshades. Our primary objectives are summarized below.

(1) Investigate viability of VTVL rocket as stable platform for suborbital testing and demonstrations of starshades.

(2) Maintain stable hover of ±0.5 m in lateral axes and ±0.25 m in vertical axis with ±10° roll about vertical axis for 20 seconds with 60 cm starshade payload attached.

(3) Use near-infrared visual formation flying sensor for 6DOF determination.

(4) Investigate the effect the brightness of the rocket plume will have on astronomical observations.

(5) Flight test a number of COTS avionics sensors for use on future CubeSat spacecraft.

4.3 Experiment Setup

The policy of the flight provider, Masten Space Systems (MSS), is that all new payloads must be fully tested on the vehicle with a tethered flight campaign, before alllowing free-flight. For tethered flights, the vehicle is attached to a crane via a tether at all times during flight and takes off from 1 m high-stands (Figure 4.1) to a peak altitude of 2.8 m (1.8 m rise above 1 m stands). If anything off-nominal occurs with the vehicle during flight, the engines are immediately cut and the vehicle hangs safely under the support of the tether. All payloads must pass these validation tests in the same configuration planned for free-flight to verify there will be no interference from the payload that could cause damage to the vehicle.

The ground setup for this tethered flight campaign was meant to mimic the setup to be used in a free-flight science campaign, with the obvious difference being the rocket will not fly higher than a few meters off the ground. The separations between the rocket and telescope were also reduced to fit within the active flight area, but still maintain a direct line of sight to the rocket. A stable target behind the rocket was set up to serve as a reference point to which stability measurements could be made. Figure 4.2 shows a Google Earth view of the launchpad and the ground equipment. The background target is located 34 m behind the rocket on the launchpad.

Figure 4.1: Masten Space System's *Xaero-B* is seen tethered on the launchpad with our payload attached. The tall structure in the background are visual targets used as a reference when calculating the motion of the vehicle using camera data. Image credit: NASA.

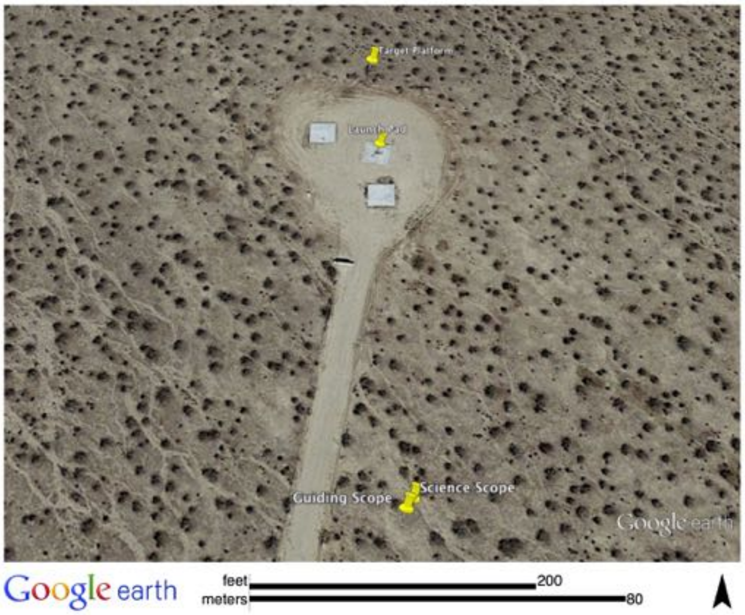

Figure 4.2: Google Earth screenshot of Masten Space Systems' launchpads and the location of the telescopes and background target during flight.

The FF sensor ("guiding telescope") and DSLR video camera ("science telescope") are separated by 1 m and located 103 m in front of the rocket. Achieving alignment between the telescope, rocket, and background target over those distances required both the telescope and target to be suspended high above the ground. Figure 4.3 shows all three components in alignment. Section 4.4 provides a more detailed description of each component of the ground equipment.

4.4 Payload Description

4.4.1 Formation flying sensor

To provide high-cadence, high-precision relative position information to maintain alignment, we developed a formation flying sensor that detects an arrangement of LED beacons on the rocket to solve for the relative 6DOF solution (position and attitude) of the rocket. Our detector is a near-infrared (NIR) position sensitive diode (PSD) with a fast ($\sim \mu$s) response time, allowing us to modulate the LED signal and filter out ambient light. The PSD directly measures the center of light incident on the focal plane, providing the location of the LED at a higher rate than would be possible if relying on image processing of a discrete sensor.

4.4.1.1 Position sensitive diode

A position sensitive diode is a high-resistivity semiconductor substrate covered by a resistive layer and a photoconductive layer. The resistive layers are connected to electrodes on opposing sides. An incoming spot of light strikes the conductive layer and generates an electric charge proportional to its intensity, which flows through the resistive layer to the pair of electrodes. The current generated at each electrode is inversely proportional to the distance traveled in the resistive layer and comparing the two currents provides the centroid position of the incident light in that direction. For two-dimensional PSDs, another pair of electrodes are orthogonal to the first to provide two dimensions of position sensing (Figure 4.4). Knowing the widths of the resistive layer (L_x, L_y) and measuring the voltages generated at each electrode (V_{x_1}, etc.), we can calculate the x, y

Figure 4.3: Image of the configuration during flight. In the foreground is the guiding telescope, in between is the rocket under tether, and in the background is the target platform. Image credit: NASA.

position of the incident light from Equation 4.1. Our formation flying sensor uses a two-dimensional duo-lateral type PSD from OSI Optoelectronics with a 10mm x 10mm sensing area.

$$
\begin{aligned}
x &= \left(\frac{L_x}{2}\right)\left(\frac{V_{x_2} - V_{x_1}}{V_{x_1} + V_{x_2}}\right) \\
y &= \left(\frac{L_y}{2}\right)\left(\frac{V_{y_2} - V_{y_1}}{V_{y_1} + V_{y_2}}\right)
\end{aligned} \tag{4.1}
$$

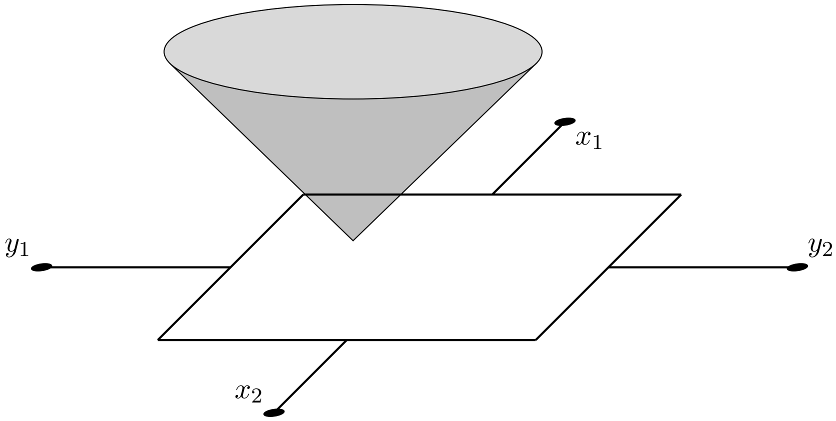

Figure 4.4: Schematic of light striking a Position Sensitive Diode. Comparing the voltages at electrodes x_1, x_2 yields the position of the light spot in the x-direction. The same holds for the orthogonal direction.

4.4.1.2 PSD readout electronics

The fast rise time of the PSD allows us to create an analog bandpass filter to filter out all ambient light except for the 10 kHz at which our LEDs are being modulated. The readout electronics for each of the four PSD channels are summarized in the following steps,

(1) Light strikes the PSD and generates a photocurrent that flows through the resistive layer to an electrode

(2) A transimpedance amplifier converts the current to a voltage and provides a gain

(3) A two stage - four pole bandpass filter destroys any signal outside of 10 kHz (with bandwidth = 2.5 kHz)

(4) A full wave rectifier turns the positive/negative analog signal centered around zero to only positive

(5) An envelope detector turns the 10 kHz signal to a constant signal of equal amplitude

(6) A low-pass filter filters out high frequency noise generated along the circuit path

(7) A 16-bit analog to digital converter (ADC) digitizes the analog signal

(8) An ATMEGA168 microcontroller reads the ADC via SPI protocol

(9) A UART to USB converter allows the microcontroller to communicate with the attached laptop

(10) A C script on the laptop records the DN ($\in [0, 65535]$) for each PSD channel which allows us to calculate the x, y position of the incident light from the LED.

The circuit and printed circuit board was designed and assembled by Dayne Kemp of NASA Ames Research Center (Figure 4.7). My role in the circuit design was to tune the circuits for our desired performance and write the embedded software to read the data from the sensor onto a laptop. The circuit diagram for filtering one channel of the PSD is shown in Figure 4.5. Most of the tuning was done on the BPF, which was a second-order active filter of the Voltage Controlled Voltage Source type. The basic operation of this filter is to high-pass filter, amplify with feedback (making it an active filter), and then low-pass filter. This process is done twice ("two-stage") with a total of four capacitors ("four pole") used.

Tuning was done using the circuit simulator, TINA, with breadboard verification, to choose the resistor and capacitor values such that we were able to achieve a narrow bandwidth, but with sufficient gain. We needed the BPF to have a high throughput of 10 kHz signal and sharp rejection of out of band signals.The rectifier needed to do a full swing to bring the negative values to match the positive values to not introduce a high frequency component into the signal. The envelope detector needed to have a quick rise and falloff time in order to capture the separation between beacons.

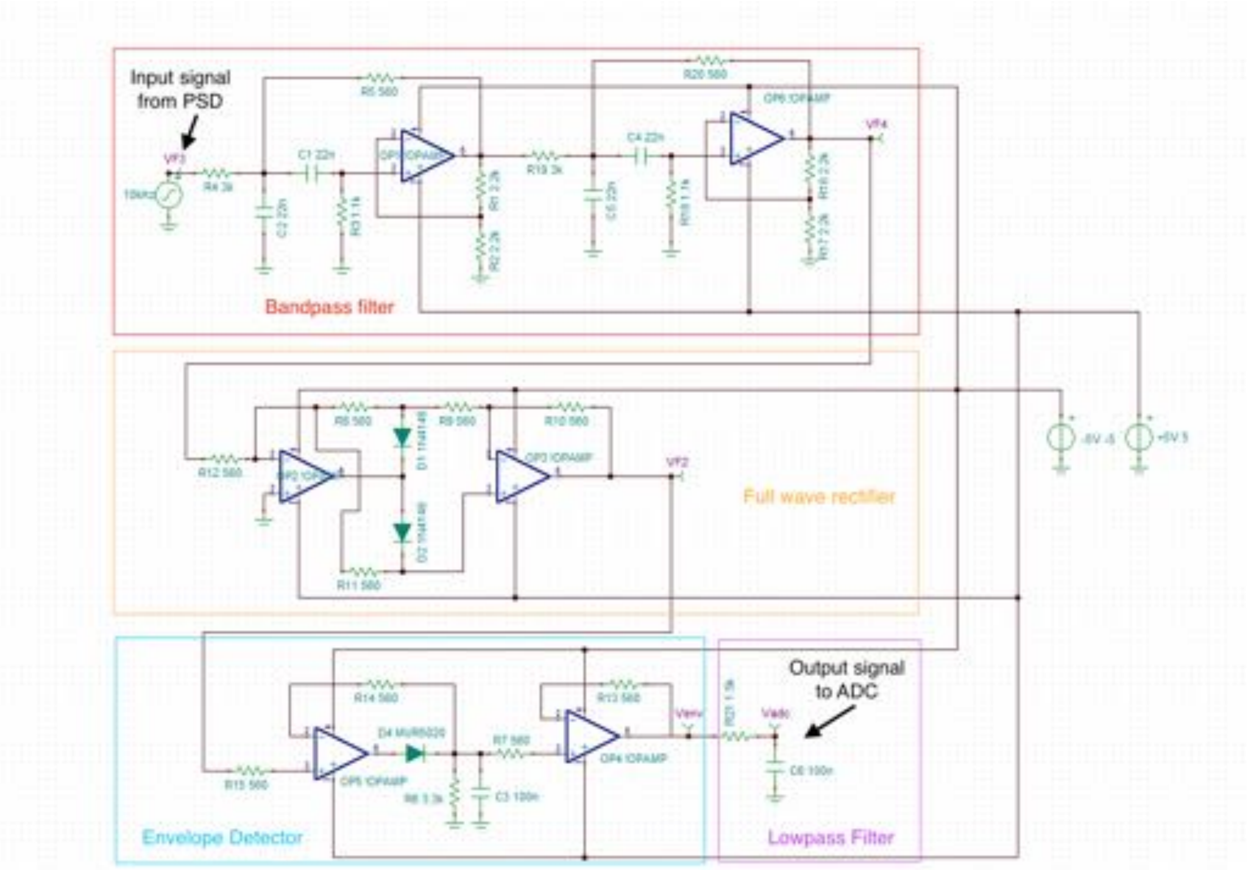

Figure 4.5: Circuit layout for the PSD electronics. The signal output from the PSD passes through a bandpass filter, full wave rectifier, envelope detector, and lowpass filter before being sent to the analog-digital converter.

A breakdown of the simulated signals is shown in Figure 4.6. Row 1 is the input signal of 10 cycles of 10 kHz square waves of amplitude 3 V, simulating the output signal expected from the PSD imaging a modulated LED. Row 2 is after the signal has passed through the bandpass filter and is centered around zero. You can see the quick rise and decay of the signal when the 10 kHz signal comes through. Row 3 is after the full wave rectifier has made the signal positive. Row 4 shows the envelope detector finding the following the shape of the FWR, which provides the stable value of the signal. The envelope detector does a good job of quickly falling to zero before the next wave train arrives. Row 5 is after a low-pass filter has filtered out any high frequency components and is the signal that is sent to the ADC. The signal does not have a perfect fall off, but most of the time is spent at the peak value (close to the input 3 V, so only a little signal is lost) and the sampling of the ADC should be able to distinguish when we are in the peak.

4.4.1.3 Readout software

The first digitization of the PSD signal comes when the 16-bit ADC converts the analog signal output from the low-pass filter into a digital number $\in [0, 65535]$. To extract that number from a computer for recording, we use an ATMEGA168 microcontroller to read the ADC via a Serial Peripheral Interface (SPI) bus. The microcontroller uses SPI to read the four channels of the ADC (one for each electrode of the PSD). The microcontroller then packages the data from the four channels and a timestamp into a string of bytes and writes out to the computer via a USB bus. The software embedded in the microcontroller was written in C, using the AVR chip libraries to access memory registers, and the software on the computer to read the incoming data over the USB bus was written in C.

4.4.1.4 Guiding telescope

The optics in front of our sensor is a single 80 mm convex lens with a focal length of 400 mm. A cold-mirror beam splitter in the optical train splits the incoming light at 0.7 μm into two beams. The transmitted NIR beam is sent to the PSD sensor and the reflected visible beam is sent to a

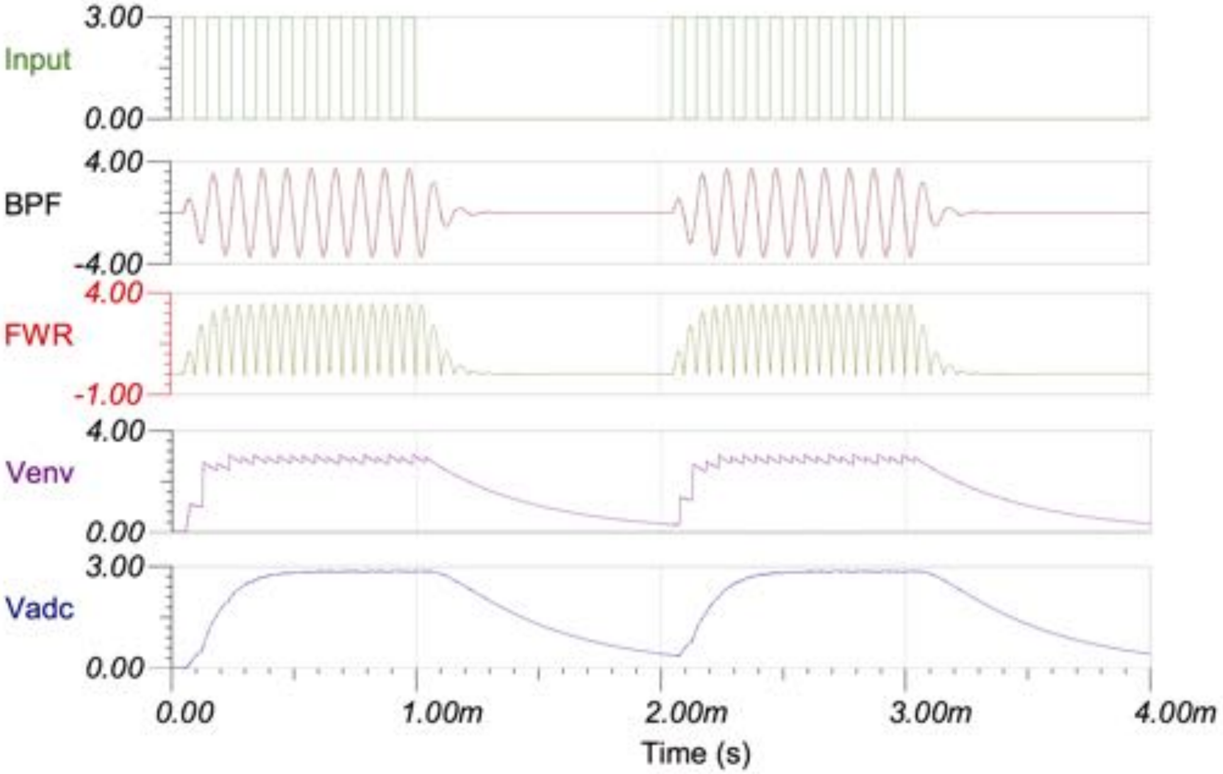

Figure 4.6: Simulation of PSD circuit run with the TINA software showing the response of the signal after each stage in the circuit shown in Figure 4.5. The plots are showing voltage [V] as a function of time as a square wave signal is input into the circuit. BPF is the bandpass filter, FWR is the full wave rectifier, Venv is the envelope detector, and Vadc is the signal sent to the ADC.

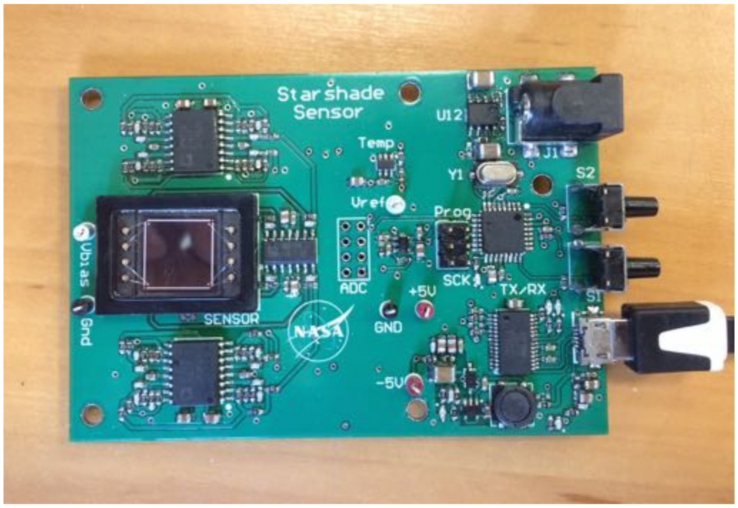

Figure 4.7: Image of the PSD sensor (black rectangle, top center) and its circuitry on printed circuit board. The circuit and PCB were designed by Dayne Kemp of NASA Ames.

visible light CMOS detector to allow for alignment of the scope and to filter unwanted visible light from the PSD. Prior to showing up at the launchpad, there was little information available about the terrain we would operate in and how high the telescopes and background target would need to be for a clear line of sight. This required us to adapt on-the-fly to get the three-way alignment between telescope, rocket, and target. Unfortunately, the only solution to alignment (given how high we could build a stable background target) required the telescope to be 3 meters off the ground and the only way we could achieve this was to place the telescope on top of a platform built onto the roof of our rental SUV (Figure 4.3). I know. While this isn't an ideal platform for a telescope, it was relatively stable and any motion in the camera was dominated by wind vibrating the tripod. This vibration is certainly a source of error in our position determination, but this is the sort of complications one must deal with when doing low-cost, rapid turnaround experiments in the field.

4.4.1.5 LED beacons

The four LED beacons on the vehicle were mounted at the corners of a rectangular aluminum frame that was attached to the payload module (Figure 4.11). Each beacon was comprised of 16 NIR LEDs in a 4x4 grid mounted to a PCB with circuitry to power the LEDs from the batteries in the avionics box. The LEDs have a peak wavelength of 0.95 μm, an opening angle of 20°, and a radiant intensity of 500 mW/sr. The modulation of the LEDs' amplitude at 10 kHz is driven by a BeagleBone Black single board computer flipping its general purpose input/output pins with a script written in Assembly. In order for the PSD sensor to distinguish between the beacons, we separate them temporally by cycling which beacon is on. The sequence of the LED cycling is shown in Figure 4.8. Running at 10 kHz, one beacon is on for 20 periods (running at a 50% duty cycle) and then turned off. All beacons are off for 20 periods and then the next beacon is turned on for 20 periods, and so forth. After the last beacon, all are off for 40 periods to mark the start of a new cycle. Each beacon is one for 2 ms and it takes 20 ms to complete one beacon cycle.

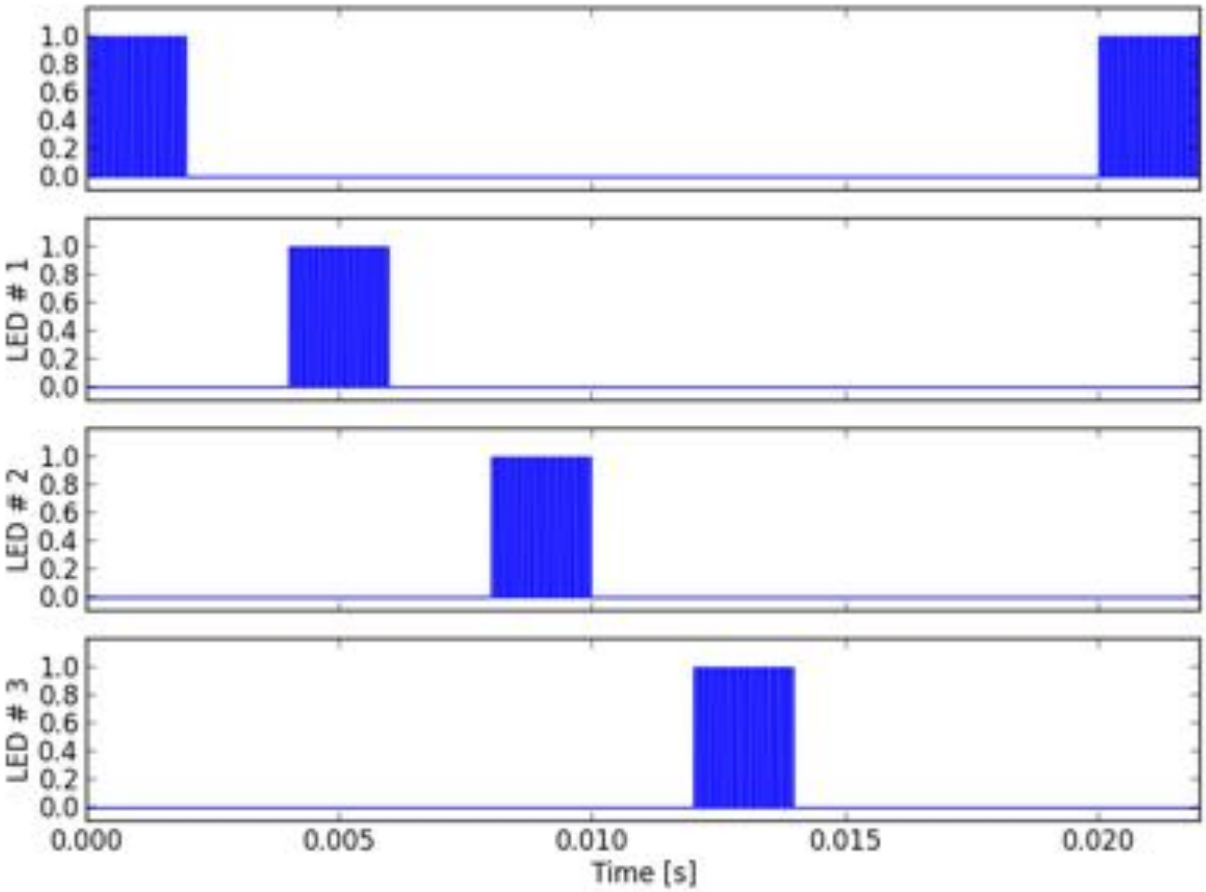

Figure 4.8: Diagram showing the sequence of cycling through the four LED beacons. The first beacon is on for 20 periods, then all are off for 20 periods, then the second beacon is on for 20 periods, and so forth. After the last beacon, all are off for 40 periods to mark the start of a new cycle.

4.4.2 Video recorder

To provide a visual confirmation of the stability of the rocket in flight and to provide videos for further analysis of the flight characteristics, a DSLR camera was placed next to the guiding telescope and recorded video of the flights at 25 fps. This camera also served as a placeholder for the science telescope, which is the telescope we are trying to place in alignment with the starshade and background target. Fiducial markers were centered over the beacons of the rocket and background target (black/white checkered boards in Figure 4.9 and Figure 4.11) and made so that an image processing algorithm could easily identify them and we could provide position information using still frames generated from the movies.

4.4.3 Background target

The background target (Figure 4.9) consisted of an arrangement of LED beacons and fiducial markers similar to those flown on the rocket. This pattern was suspended from a PVC pipe frame at a towering height of 20 ft. This height was necessary to be in the field of view of the guiding telescope at the same time as the rocket. The background target provided a reference point to measure the stability of the rocket in the images and also as a reference frame in which to transform the relative position of the rocket to an absolute position.

4.4.4 Avionics box

The avionics box was an aluminum shell mounted to the center of the payload module (Figure 4.11) and housed the batteries and computer to drive the LEDs and a suite of avionics sensors for flight testing. These COTS sensors were a secondary payload to obtain flight data from sensors that are not designed for use in spacecraft applications. Commercially available Inertial Measurement Units (IMUs) have size, mass, and power attributes that make them ideal for inclusion in nanosatellites, however little is known about their response to the space environment. These environmental factors can negatively impact their performance, which will significantly impact key subsystem technologies, such as attitude determination and control software. The purpose of this

Figure 4.9: Image of background target, with payload on rocket in the foreground. The checkered patterns are used for image recognition to track the position of the rocket relative to the background target during flight.

secondary payload was to study the possible negative impacts from operation in a flight-like environment [80]. The computer driving the LEDs was a BeagleBone Black single-board computer, an easy to program computer that can run a full Linux distribution and has potential to serve as the flight computer for CubeSat spacecraft. Also flown was a nine degree-of-freedom IMU made by SBG Systems, called the Ellipse (Figure 4.10).

4.4.5 Starshade

A 60 cm diameter starshade was mounted 60 cm off the side of the payload module (Figure 4.11). The starshade was chemically etched from 10 mil thick stainless steel and is identical to those used for field testing starshades on the dry lake beds (Chapter 6). These starshades have been shown to provide high-contrast at the separations we would use in observing campaign with the rocket. The starshade was mounted alee of the prevailing wind to minimize its disturbance on the flight stability of the rocket.

4.5 PSD Calibration

The PSD detector has some non-linearity in its response, especially when the PSF of the incident light falls partly off the edge of the detection area. There are also throughput differences in the readout circuitry for the four channels. Therefore we rely on a lens/sensor calibration to reliably convert the output voltage to an absolute position on the detector. The output signal from the sensor is four voltages passed through the readout circuits and read by the ADC, which is converted into an (x, y) position via Equation 4.1. We approximate the position as a n^{th}-order polynomial with the four voltages as,

$$\begin{aligned} x &= \sum_{i=0}^{n}\sum_{j=0}^{n}\sum_{k=0}^{n}\sum_{l=0}^{n} a_{ijkl} P_{ijkl}\left(V_{x_1}, V_{x_2}, V_{y_1}, V_{y_2}\right) \\ y &= \sum_{i=0}^{n}\sum_{j=0}^{n}\sum_{k=0}^{n}\sum_{l=0}^{n} b_{ijkl} P_{ijkl}\left(V_{x_1}, V_{x_2}, V_{y_1}, V_{y_2}\right) \end{aligned} \tag{4.2}$$

where the polynomial function is given by,

$$P_{ijkl}\left(V_{x_1}, V_{x_2}, V_{y_1}, V_{y_2}\right) = V_{x_1}^{i} V_{x_2}^{j} V_{y_1}^{k} V_{y_2}^{l} \tag{4.3}$$

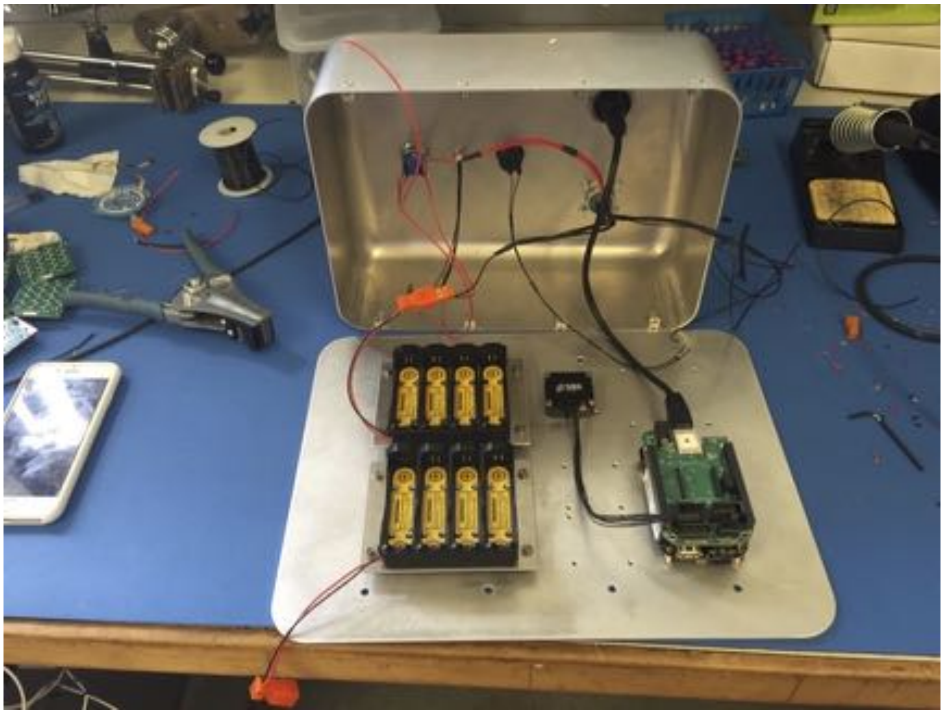

Figure 4.10: Image of avionics box payload that sat in the middle of the rocket's payload module during flight and housed an IMU and Beaglebone Black computer that recorded data during flight. The aluminum box was designed to access the computer while mounted on the rocket.

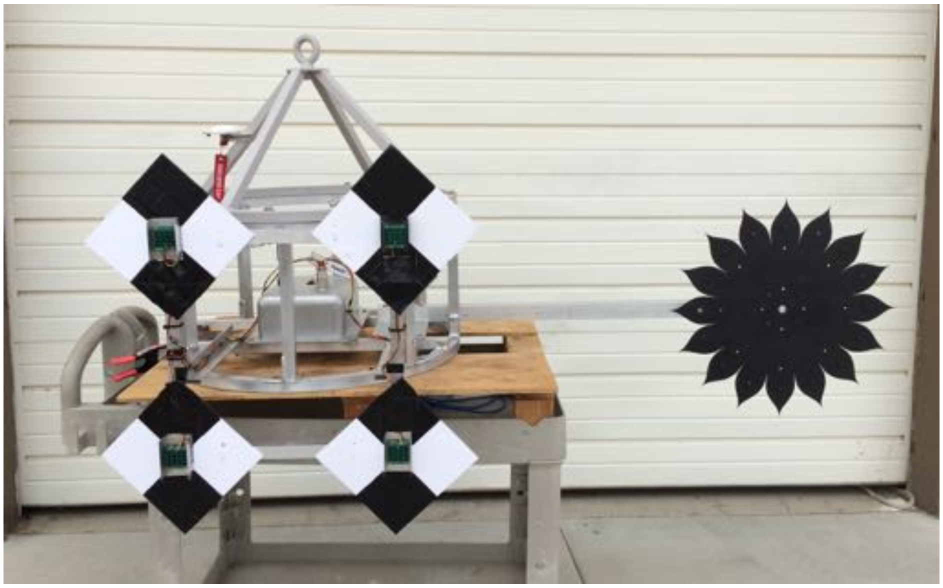

Figure 4.11: Image of the entire payload module separated from the rocket. In the center is the avionics box payload, the LED boards are mounted at the center of the checkered pattern fiducials, and the 60 cm diameter starshade is mounted to the right.

We perform a calibration in the lab by sampling the voltages over a large number of known positions of a light source. Doing so allows us to perform a least squares regression to solve for the coefficients of the polynomials in Equation 4.2, a_{ijkl}, b_{ijkl}. Equation 4.2 can be expressed in matrix form as,

$$\begin{aligned} X &= AP \\ Y &= BP \end{aligned} \tag{4.4}$$

If we record the voltages, build their polynomial matrix P, and build matrices for the expected x, y positions as g_x, g_y, we can solve for the coefficients via the least squares equation,

$$\begin{aligned} A &= \left(P^T W P\right)^{-1} P^T W g_x \\ B &= \left(P^T W P\right)^{-1} P^T W g_y \end{aligned} \tag{4.5}$$

where $W = cov\left(P_i, P_j, P_k, P_l\right)$ is the covariance matrix where the cross-terms are not necessarily zero (i.e., the voltages are not independent variables).

4.5.1 Calibration results

The sensor calibration was performed in the lab with a 10 kHz modulated NIR LED mounted to a translation stage 15 m from the detector. The stage was moved to cover the entire sensitive area of the detector in a grid pattern in 5 mm increments. The voltages at each LED position were recorded, along with the displacement of the LED. In order to correct for rotation of the translation stage axes relative to the telescope, a visible light CMOS recorded images of the LED and a rotation angle was fit to the translation stage and is corrected for in the expected positions (g_x, g_y).

The calibration results are shown in Figure 4.12. The best results are found with $n = 3$.The 'model' data are the theoretical x, y positions of the LED on the translation stage (g_x, g_y). The 'raw' data are the positions calculated directly from Equation 4.1; you can see at the edges of the sensor the positions get compressed together in a pin cushion-like distortion as the light spot falls off the edge of the sensor and the centroid is falsely stuck at the edge of the sensor. The 'corrected' data are the calibrated positions after we have applied the polynomial coefficients that were solved for using Equation 4.5. The corrected data fit well, with a reduced χ^2 of 2.18, and the distortion is removed.

4.5.2 Detector characterization

Along with calibrating the response of the detector in the lab, we were able to characterize the noise properties of the sensor. Figure 4.13 shows the voltage (saturation occurs at 2.5 V) vs time for the four channels during an observation of the LED in the lab. There is clearly structure to the Y_1 channel. This structure is also observed in other channels. A closer look at the structure in the signal reveals a 10 Hz envelope over a ∼150 Hz higher frequency component. This noise was not immediately noticed and the source of it is unclear.

Regardless of this structure, the other signals are quite noisy. For each of the grid points in the calibration, we took data for 1 second, sampling around 600 voltage readings. Figure 4.14 shows a histogram of the position difference from the mean for all data. There are large tails where every so often the position is far off, but if we exclude the errors beyond ±1 mm, the errors are gaussian distributed around zero and the 1σ random error bars on the position on the detector are: $\sigma_x = 0.25$ mm, $\sigma_y = 0.18$ mm. Assuming the errors are uncorrelated, $\sigma = 0.31$ mm. The voltage signal ranges from 5000 DN to 20000 DN (saturation occurs at 65535 DN), with no obvious trends of position error with signal strength, suggesting there was a dominating noise term not due to the photocurrent. With a focal length of 81 mm, this translates to an angular error of 13 arcminutes and a position error of 38 cm at 100 m distance. This large error, which we believe to be dominated by electronic noise, will limit the accuracy of a 6DOF solution during the rocket flights.

4.6 Summary of Flights

Our flight campaign occurred during the month of August 2015 at the Mojave Air and Space Port in Mojave, CA. Our flight provider was Masten Space Systems (MSS) and we flew on the

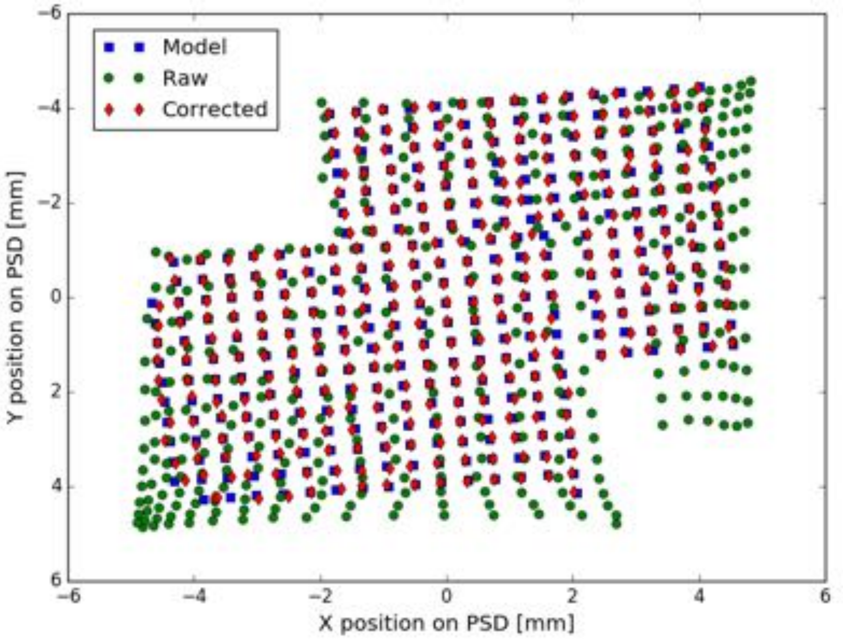

Figure 4.12: Plot of results from the calibration of the PSD by imaging an LED that is moved in a grid pattern on a stepper stage. The **blue** squares denote the model position of the light, the **green** circles are the positions of the light as calculated from the raw PSD data, and the **red** diamonds are the positions calculated after the calibration is applied.

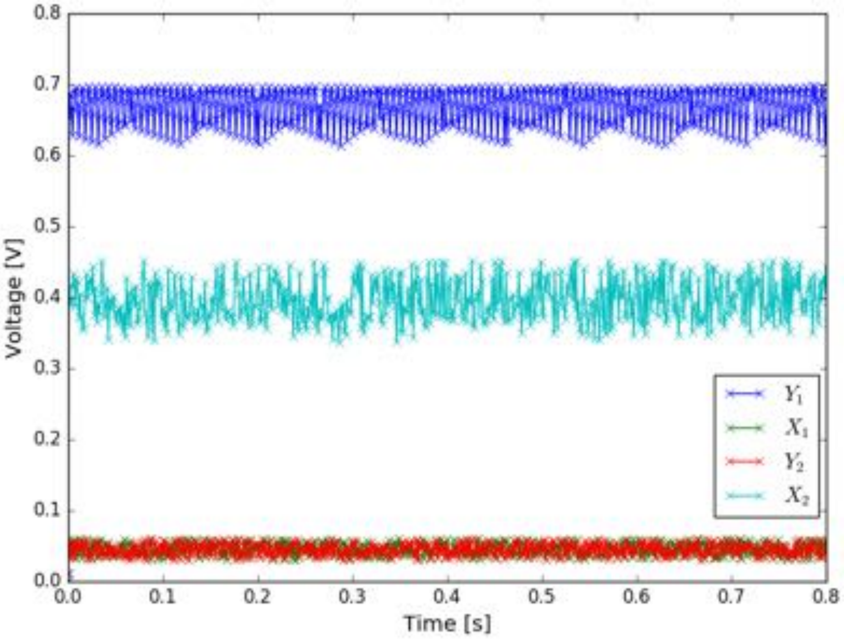

Figure 4.13: Stability of PSD sensor voltage over time when imaging a stationary LED. The four colors correspond to the four channels of the PSD. The voltages are noisy and there is an unknown fixed pattern of a 10 Hz envelope over a 150 Hz higher frequency component.

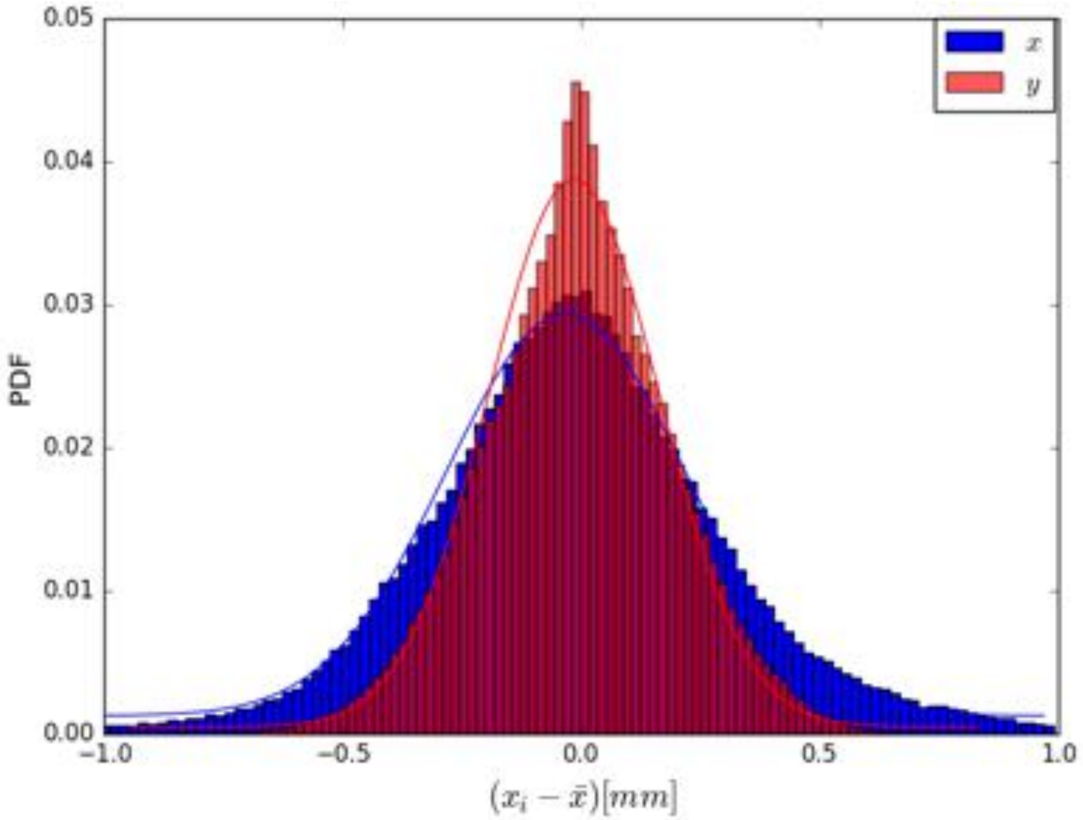

Figure 4.14: This plot shows the distribution of errors in the x (**blue**) and y (**red**) positions calculated by the PSD during the calibration. We have overplot a gaussian fit to the errors to show they are gaussian distributed.

VTVL rocket, **Xaero-B**. During this flight campaign we conducted 5 tethered flights on 4 separate days. The final milestone flight was flown at night. The flight profile was a stable hover 1.8 meters above the 1 meter highstands the vehicle takes off from. The flights are summarized in Table 4.1.

Flight #	**Date**	**Flight Duration [s]**
1	8/14/15	32
2a	8/18/15	32
2b	8/18/15	14
3	8/20/15	32
4	8/25/15	32

Table 4.1: Summary of VTVL rocket flights during the first flight campaign.

4.7 Flight Results

4.7.1 Formation flying sensor

The prime objective for testing the formation flying sensor was to detect the beacons on the rocket during flight and use their detected positions on the focal plane to solve for the position and attitude of the rocket relative to the telescope.

4.7.1.1 Data analysis

The data products from the FF sensor are voltages as a function of time for the four channels of the PSD sensor. Figure 4.15 shows a snapshot of the total voltage (the sum over the four channels) vs time. Summing the four channels increases the signal to noise and makes it easier to separate the peaks. There is a periodicity in these data showing four peaks in voltage, followed by a period of zero voltage. The four peaks correspond to the four beacons and the zero voltage period is the start of a new beacon cycle. A finely tuned peak finding algorithm was used to identify the peaks and their timestamps, and the beacon that each peak corresponded to was found from its position in the cycling sequence. For each cycle, the focal plane position of each beacon was calculated from plugging the voltages from the four PSD channels into Equation 4.1 and applying the calibration of Equation 4.2. Assuming the rocket does not move significantly over the course of one beacon cycle (20 ms), we can use the image positions of the four beacons in a given cycle to apply the GLSDC algorithm (Section 3.2.1.1) to solve for the position and attitude of the rocket at a given time.

4.7.1.2 Results

The top panel of Figure 4.16 shows the raw output from one channel of the PSD looking at one beacon during Flight #3. Similar to what we saw in the lab, the data are noisy with a strong 10 Hz component. Since these data were taken in the field and everything was powered off a battery, this noise is not due to the laptop's charger as originally suspected. The voltage from each channel is also lower than what we were working with in the lab, because of the larger distance. We apply a smoothing filter to the voltages to try and eliminate this noise. The bottom panel of Figure 4.16 shows the x position calculated from these voltages using Equation 4.1.

The focal plane positions for the four beacons during the flight can be seen in Figure 4.17. We find the 1σ stability of the positions calculated by the raw data to be $\sigma_x = 0.82$ mm, $\sigma_y = 0.55$ mm, or about 3 times larger seen in the lab, which could be attributed to the 10 times less flux. The stability of the positions from the smoothed voltages are $\sigma_x = 0.18$ mm, $\sigma_y = 0.09$ mm, which should make the position error at the distance of the rocket to be $\sim$5 cm. To simplify the propagation of the GLSDC algorithm, we focus on the portion of the flight where the rocket was stable at altitude (t =180 - 195 seconds). Using the beacon positions during this time, we can solve for the 6DOF solution of the rocket during stable flight; these are shown in Figure 4.18 and Figure 4.19. The 1σ error in the position of the rocket as calculated by the GLSDC algorithm is $\sigma_x \approx \sigma_y \approx 12$ m, $\sigma_z \approx 3$ m. These are larger than the we should expect from the position error on the detector. The 1σ error in the attitude of the rocket as calculated by the GLSDC algorithm is $\sigma_\phi \approx 0.2°$, $\sigma_\theta \approx \sigma_\psi \approx 0.7°$.

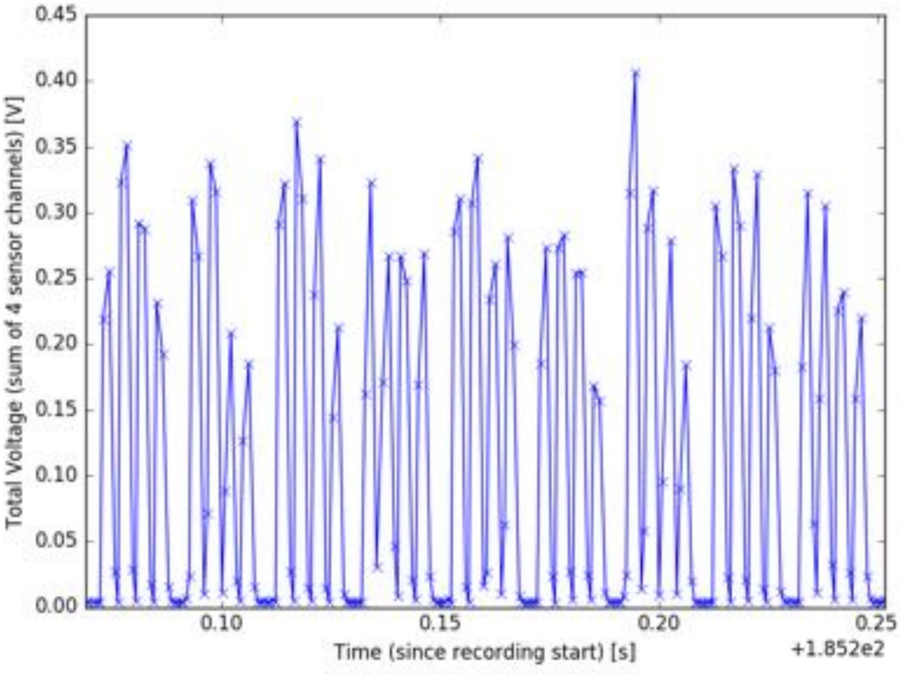

Figure 4.15: Snapshot of the total voltage from the PSD sensor vs time during steady flight. The four peaks in voltage correspond to the cycles of the four beacons. The 'dark' time after the beacon cycle marks the end of each beacon cycle and allows us to identify which peak corresponds to which beacon. These data are from Flight #3.

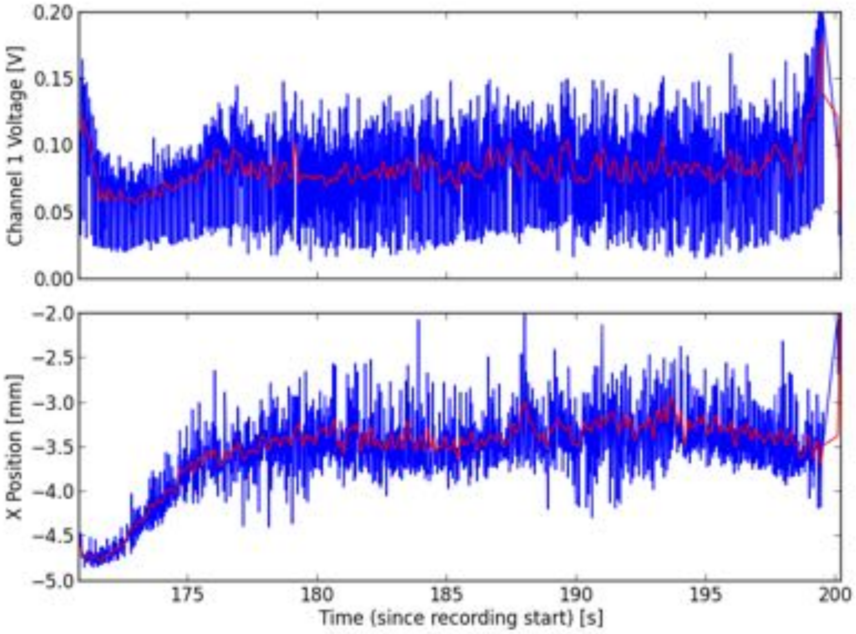

Figure 4.16: The **top** panel shows the raw (blue) and smoothed (red) voltage from one channel of the PSD sensor for Beacon # 1. The **bottom** panel shows the X position of Beacon #1 as calculated by the raw (blue) and smoothed (red) voltages. These data are from Flight #3.

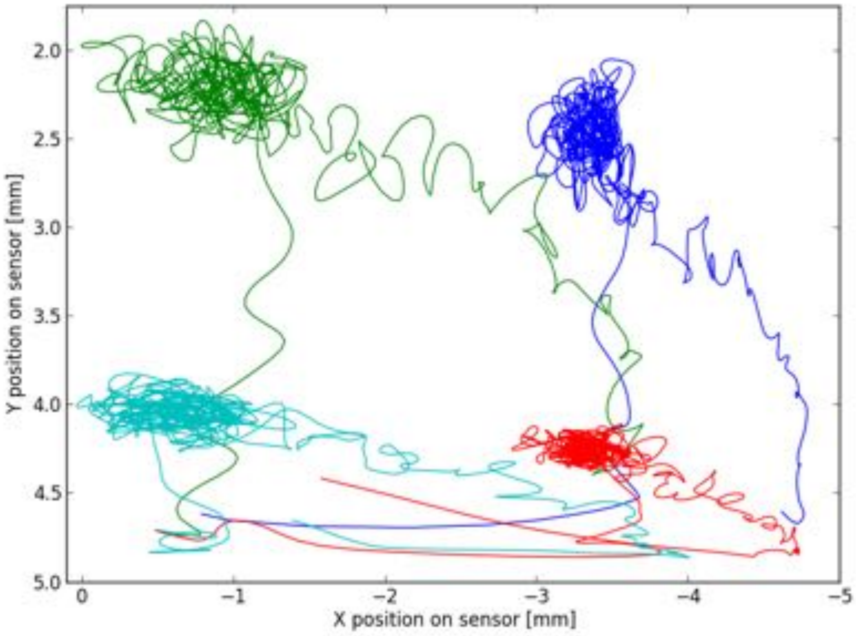

Figure 4.17: The X & Y positions of the four beacons (denoted with different colors) for the duration of the flight as calculated by the (smoothed) voltages measured by the PSD sensor. These data are from Flight #3.

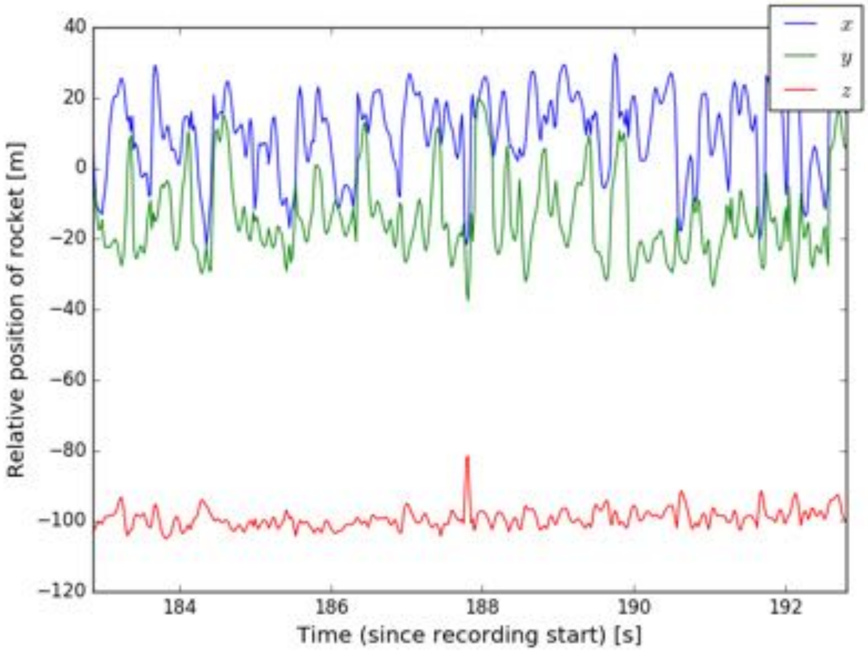

Figure 4.18: The position of the rocket relative to the formation flying sensor during stable flight. These positions were solved for with the GLSDC algorithm using the data from the PSD sensor. These data are from Flight #3.

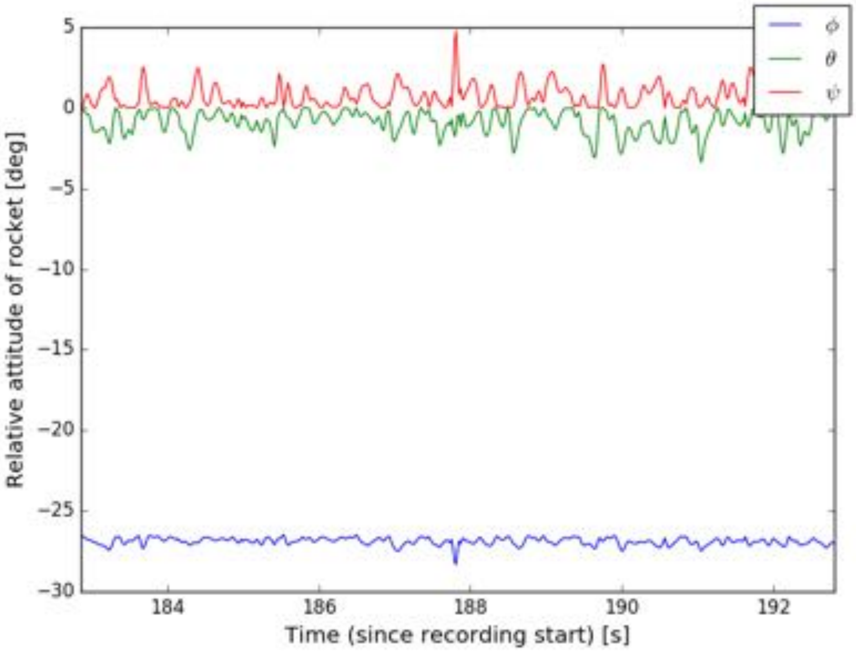

Figure 4.19: The 321 Euler angles attitude solution of the rocket relative to the formation flying sensor during stable flight. These attitude angles were solved for with the GLSDC algorithm using the data from the PSD sensor. These data are from Flight #3.

4.7.2 Video recorder

During each flight, we had a DSLR camera next to the FF sensor recording video and use visual fiducials on the rocket to verify the flight stability of the rocket and to serve as a reference for which we can compare to the FF sensor data. The visual fiducials used to track the rocket's position in the camera are black and white checkered cardboard located behind the LED beacons. Figure 4.20 is one frame from the video of Flight #3, in it you can see the fiducials on the rocket and the fiducials on the background target. The background target helps us keep a stable reference frame for which to measure the rocket's stability against, to correct for motion of the camera. A video from Flight #3 can be found at: `http://casa.colorado.edu/~harnessa/movies`.

For each frame of the video (running at 25 fps), the position of each fiducial is extracted by using the image processing library OpenCV. The algorithm for detecting the fiducials is summarized below.

(1) Create sub-image around best guess for beacon location

(2) Gaussian smooth the image

(3) Threshold the image to highlight only the darkest regions (the black squares)

(4) Contour the threshold to find the edges of the black square

(5) Use the area of the contour to eliminate false detections

(6) Use the four biggest lines of the contour to verify they intersect at four corners to make a square

(7) Use the orientation of the black squares to distinguish fiducials on the rocket from those on the background target

(8) Use the top and bottom square to find the center of the beacon

After the image location of all four beacons on the rocket and five beacons on the background target are found, we use the target as a stable reference to calculate the image motion of the rocket.

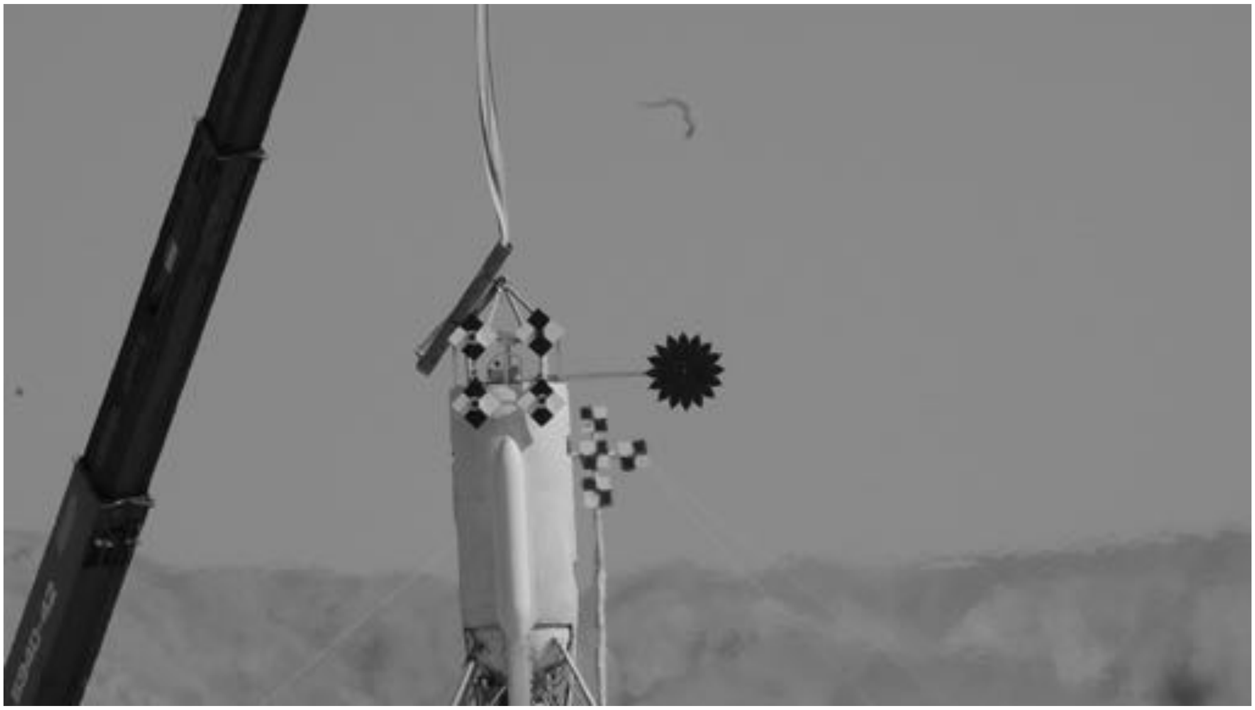

Figure 4.20: Image pulled from the video recorded by a DSLR near the guiding scope. This image is from Flight #3.

The x & y positions of the four beacons during flight are shown in Figure 4.21, and the in-plane motion of the rocket is shown in Table 4.2. These agree well with the results determined by the onboard NAV solution (Table 4.5).

σ_x [cm]	σ_y [cm]	Δ_x [cm]	Δ_y [cm]
2.27	0.90	5.47	2.41

Table 4.2: Vehicle position stability obtained from DSLR camera for Flight # 3. σ_i are the standard deviations of the positions and Δ_i are the maximum deviations from the median values during steady flight.

	x [m]	**y** [m]	**z** [m]	φ [°]	θ [°]	ψ [°]
$\bar{q}$	14.1	-11.3	-100.9	63.7	-0.58	0.49
σ_q	5.95	5.96	1.36	0.11	0.64	0.33

Table 4.3: 6DOF solution obtained from DSLR camera for Flight #3. $\bar{q}$ is the mean value and σ_q is the standard deviation for the relevant quantity. X & Y are in the plane of the camera detector and Z is in the LOS direction from the camera to the rocket.

We can also use the four beacons' positions to calculate a 6DOF solution like that done for the FF sensor. The position and attitude of the rocket relative to the DSLR camera, as calculated by the GLSDC algorithm are shown in Figures 4.22 & 4.23, respectively, and the results are summarized in Table 4.3. The errors in the 6DOF solution from this video camera are about twice as small as those from the FF Sensor, but still do not agree with the results from onboard sensors. The error in the image location from the DSLR should be lower than that of the PSD detector and we estimate we can detect motions of 5 mm at the rocket's distance, but the errors from the 6DOF solution are on the order of meters. This leads us to infer that the dominate error in the 6DOF solution is an algorithmic error, and not a sensing error, which could possibly be due to not having an accurate truth value of the beacons.

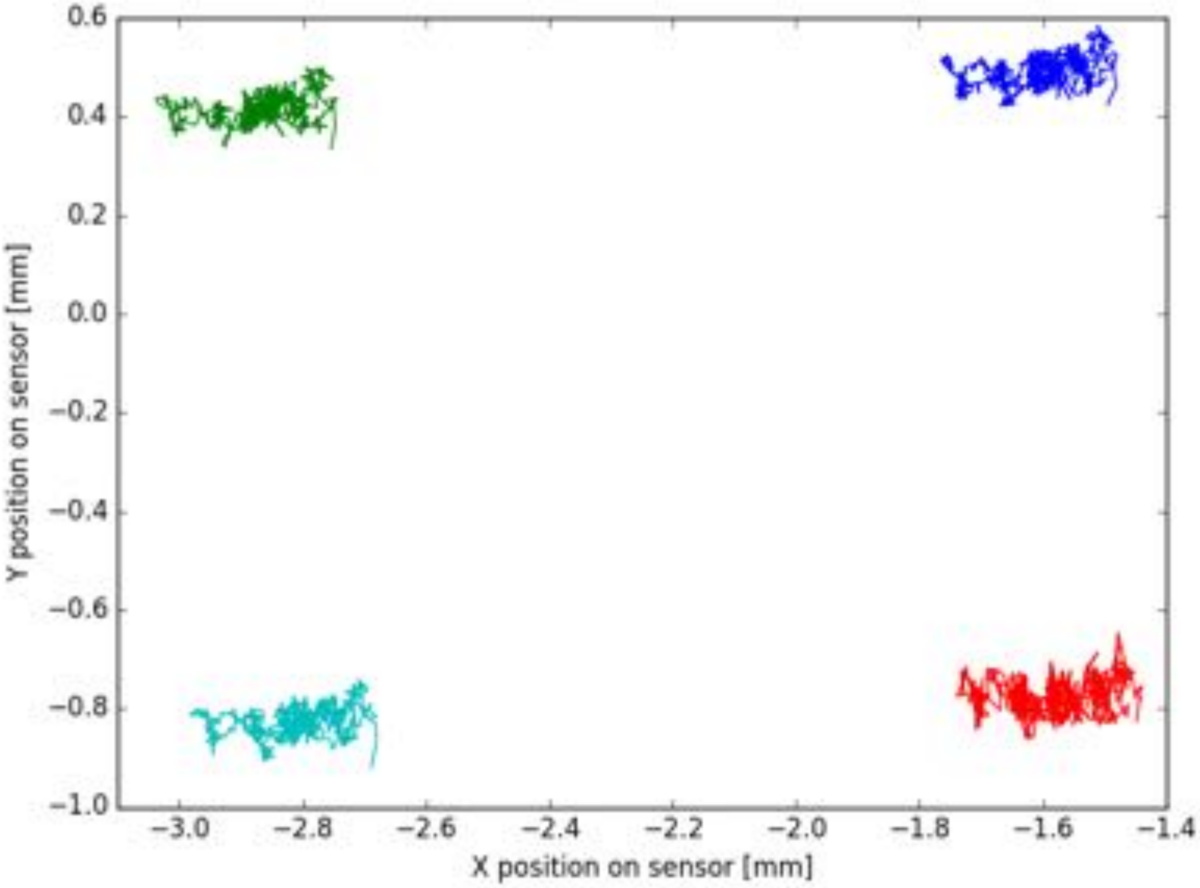

Figure 4.21: The X & Y positions of the four beacons (denoted with different colors) for the duration of the flight as calculated by pattern matching images from the DSLR video. These data are from Flight #3.

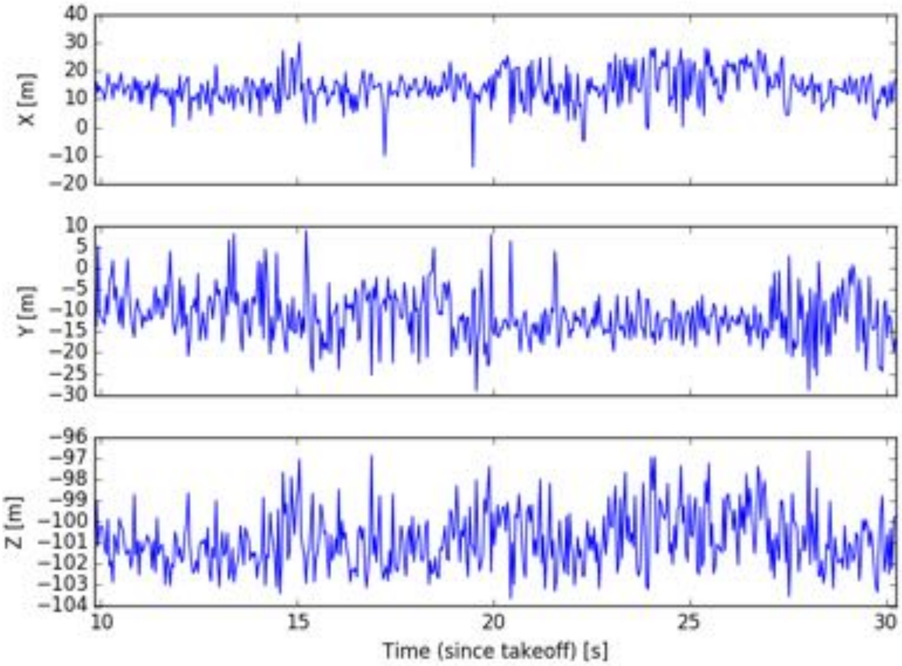

Figure 4.22: Relative position of the rocket as calculated by the 6DOF solution using beacon positions obtained from the DSLR images. These data are from Flight #3.

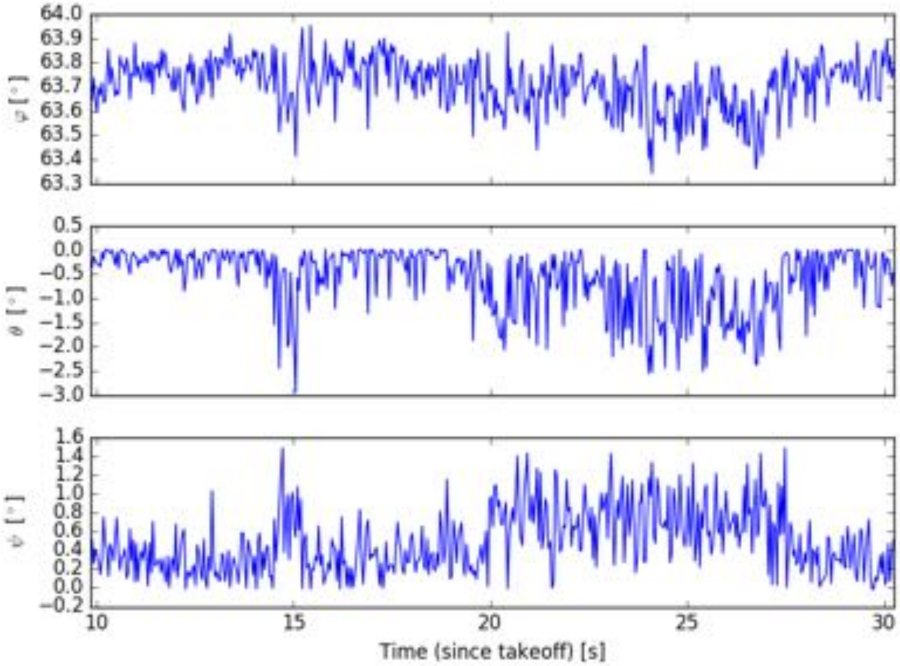

Figure 4.23: Relative attitude of the rocket as calculated by the 6DOF solution using beacon positions obtained from the DSLR images. These data are from Flight #3.

4.7.3 Inertial measurement unit

The data from the COTS ‘Ames’ IMU are body angular rates and accelerations vs time. We are interested in how the performance of the Ames IMU compares to that of the high-fidelity ‘Masten’ IMU in the rocket. A detailed analysis of the Ames IMU performance is beyond the scope of this work (see [80]), but we can do a rough qualitative comparison. The vehicle’s navigation (NAV) solution data provided by the flight provider gives the solution of the vehicle’s attitude as computed from a fusion of different sensors (IMU, accelerometer, GPS, etc.). We can differentiate the attitude solution to get the angular body rates for which we can compare directly to that from the Ames IMU, as shown with good agreement in Figure 4.24. If we integrate the angular body rates for the Ames IMU, we can calculate the attitude expressed as 3-2-1 ($\varphi - \theta - \psi$) Euler Angles. This comparison to the NAV solution is shown in Figure 4.25. The slight disagreement in attitude towards the end of the flight possibly comes from bias in the Ames IMU that is propagated forward in the integration. These data show that the rocket met the roll criteria established by the flight provider. A more detailed analysis of the flight performance of the COTS sensors will be detailed in [80].

4.8 Flight Accomplishments

In this campaign, we successfully completed 3/4 of our flight objectives. In the following sections, we will further describe each objective and the success criteria for determining if the objective was met.

4.8.1 Flight objective #1

This objective serves as a summary of the goals for the entire flight campaign and has qualitative, rather than quantitative, success criteria. This objective was satisfied in the sense that we started the investigation of using VTVL rockets as a starshade platform and learned about the realities of the performance and operation of the vehicle. We found that the flight of the rocket is

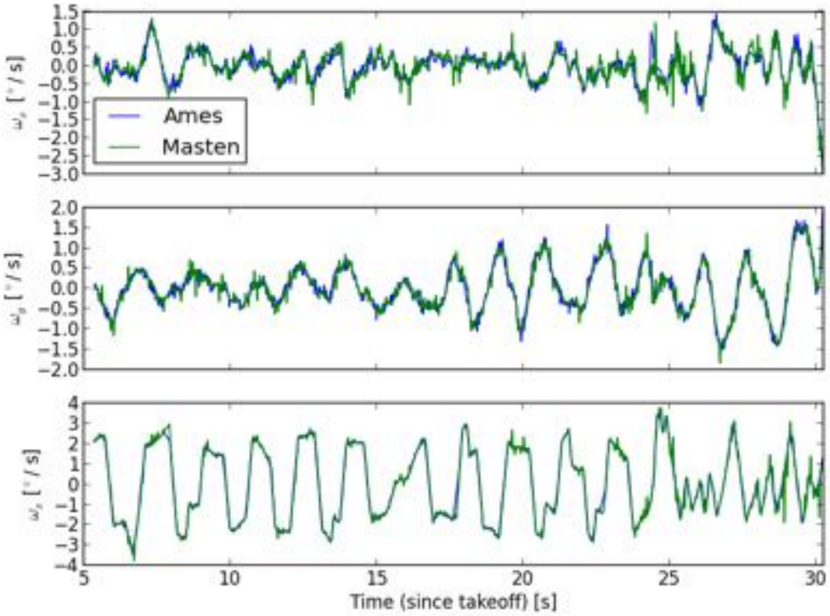

Figure 4.24: Angular body rates of the rocket during stable flight. The **green** 'Masten' line corresponds to the rates obtained by differentiating the NAV solution attitude. The **blue** 'Ames' line corresponds to the rates directly measured by the Ellipse IMU. These data are from Flight #4.

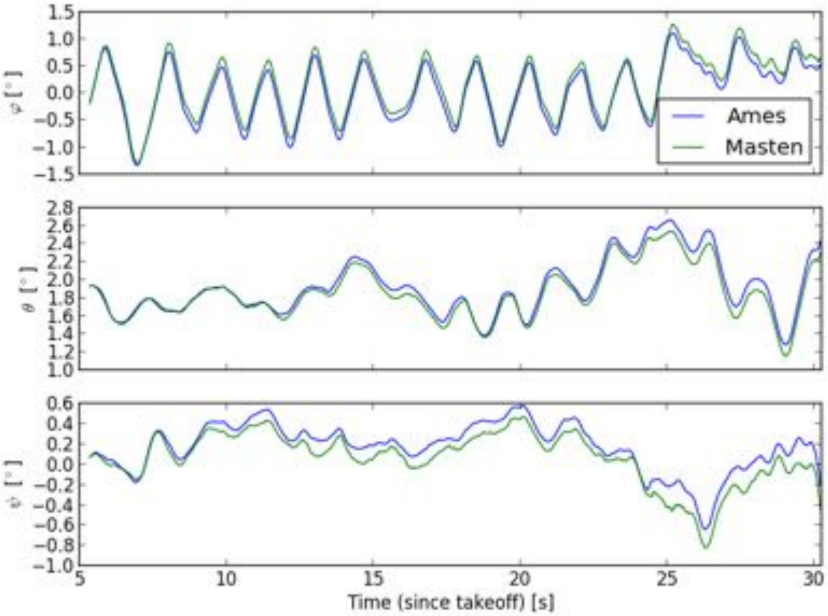

Figure 4.25: Attitude of the rocket during stable flight expressed as 3-2-1 Euler Angles. The **green** 'Masten' line corresponds to the attitude as given by the vehicle's NAV solution. The **blue** 'Ames' line corresponds to the attitude obtained by integrating the angular body rates recorded by the Ellipse IMU. These data are from Flight #4.

adequately stable for testing starshades and that the versatility of the vehicle makes it an appealing platform to work with. We think that with minimal additional visual information closing the loop, we could achieve the positioning requirements needed for a small scale starshade demonstration. We did find however, that in order to do astronomy, we need a way to shield the rocket plume from the view of the science telescope.

In this flight campaign, we found that an aspect of the vehicle's performance that may limit its efficiency as a starshade platform is its flight time and maximum achievable altitude. While these flights were only tethered flights, we got an understanding of the vehicle's fuel limitations and turnaround rate. As of now, a free flight in this vehicle can achieve about 80 seconds of flight time at an altitude of 500 meters. This is a good starting point, but for this to be a serious platform in which to do astronomy, we would need longer flight times at higher altitudes. We look forward to the continued progress of MSS and believe that their rockets will one day replace Black Brants as the standard for testing astrophysical instrumentation.

4.8.2 Flight objective #2

This objective has the quantitative success criteria of keeping the vehicle in a stable hover of ±0.5 m in lateral axes and ±0.25 m in the vertical axis with ±10° roll about the vertical axis for 20 seconds of flight time. This objective rests mainly on the performance of the vehicle as provided by the flight provider. To quote the vehicle's flight performance, we examine the flight time while the vehicle was in a steady state hover at 1.8 meters. This steady state lasted 24.9 seconds (greater than the required 20 seconds) and is marked by vertical lines in Figure 4.26. The vehicle met and surpassed these flight criteria.

We use the vehicle's navigation (NAV) solution data provided by the flight provider to calculate the stability in the vehicle's position. These data can be seen in Figure 4.26. The dotted horizontal lines represent the required bounds of the lateral and vertical axes relative to the median position. The vehicle stays within the bounds during the entire 25 seconds of steady flight. The $1-\sigma$ standard deviation and maximum deviation from the median value in the X, Y, and Z direc-

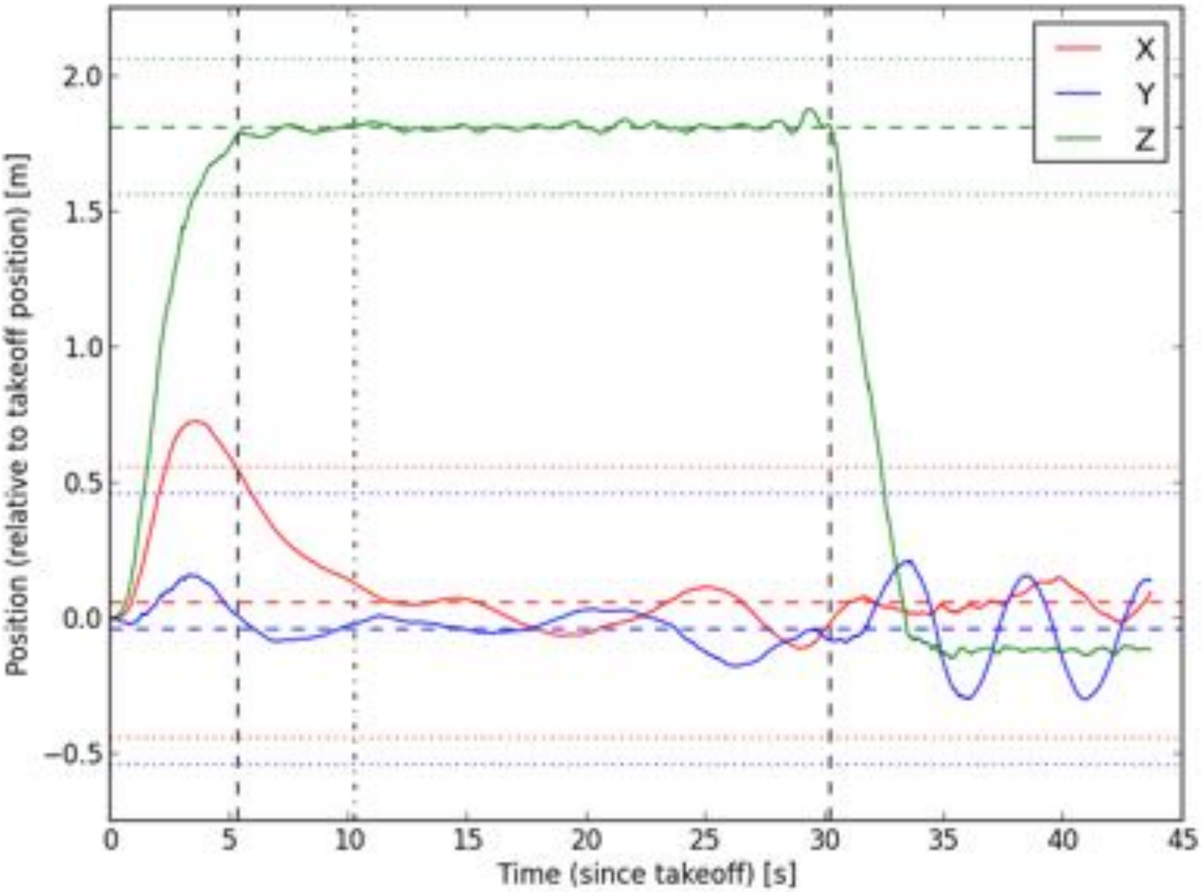

Figure 4.26: Position of vehicle relative to takeoff position as obtained from the vehicle's NAV solution. The vertical lines denote the start and end of the steady state hover time. The dotted horizontal lines represent the required bounds of the lateral and vertical axes relative to the median position. The vehicle stays within the bounds during the entire 25 seconds of steady flight. These data are from Flight #4.

tions during steady flight are given in the first row of Table 4.4. The large value in the X direction is dominated by the rocket settling into position after reaching altitude. If instead we look at the most stable 20 seconds of flight (starting at $t = 10.25s$), then the values are given in the second row of Table 4.4. In either case, the vehicle stayed well within its bounds for the duration of the flight.

t_{start}	σ_x [cm]	σ_y [cm]	σ_z [cm]	Δ_x [cm]	Δ_y [cm]	Δ_z [cm]
5.34 s	13.0	5.2	1.5	48.8	13.5	6.8
10.24 s	6.4	5.7	1.5	13.8	14.3	6.6

Table 4.4: Vehicle position stability results from Flight # 4. σ_i are the standard deviations of the position and Δ_i are the maximum deviations from the median value during steady flight. These data were obtained from the vehicle's NAV solution.

We use the NAV solution to calculate the vehicle's attitude stability. These data are also used to compare to the performance of the COTS IMU (Ellipse MEMS AHRS provided by NASA Ames) that we flew in the payload avionics box. Figure 4.25 shows the attitude of the rocket during stable flight expressed as 3-2-1 ($\varphi - \theta - \psi$) Euler Angles. The green line labeled 'Masten' corresponds to the attitude as given by the vehicle's NAV solution. The blue line labeled 'Ames' corresponds to the attitude obtained by integrating the angular body rates recorded by the Ellipse IMU. As can be seen in Figure 4.25, the roll about the vertical axis (given by φ) is well within the $\pm 10^\circ$ requirement. The $1-\sigma$ standard deviation and maximum deviation from the median value of the 3-2-1 Euler angles as calculated by the NAV solution are given by Table 4.5.

σ_φ [°]	σ_θ [°]	σ_ψ [°]	Δ_φ [°]	Δ_θ [°]	Δ_ψ [°]
0.54	0.28	0.26	1.52	0.73	0.92

Table 4.5: Vehicle attitude stability results from Flight # 4. σ_i are the standard deviations of the 3-2-1 Euler Angeles and Δ_i are the maximum deviations from the median value during steady flight. These data were obtained from the vehicle's NAV solution.

4.8.3 Flight objective #3

Our third flight objective was to demonstrate that the NIR formation flying sensor can provide high-precision position and attitude feedback to improve the flight stability of the vehicle and keep it in the line of sight to a ground telescope. We were able to use the sensor to detect the LEDs on the vehicle during flight and compute a 6DOF solution from the data, however, a combination of faint LEDs and a noisy sensor led to a noisy position solution. Even with the less noisy positions from the DSLR video, the 6DOF solution was worse than using a GPS solution. This technique holds promise, but requires further development of the sensor, a larger telescope, and brighter LEDs. A visual sensor will be needed regardless, as we need to account for atmospheric refraction to determine the apparent position of the star.

The rocket demonstrated stable flight and the requirements on the update rate of visual feedback provided by a formation flying sensor is less than anticipated. A possible closed loop solution could be to allow the rocket to rely on its own GPS and IMU instrumentation to maintain stability and provide updates on the apparent position of the star at a slower rate. If high speed is not required, we could use a simpler system using image processing of CCD images (similar to that done with the video recorder during these flights) to provide position information at higher precision.

4.8.4 Flight objective #4

Since the main reason we are using the VTVL rocket as a starshade platform is conduct high-contrast astronomy and search for faint astronomical targets, the brightness of the rocket plume is worrisome. Figure 4.27 is an image from our night flight (Masten Space System's first night flight with a customer) and shows the brightness of the plume. To test the effect the rocket plume has on an image of an astronomical target, we set an additional telescope 500 m from the launchpad and recorded the night flight with an electron multiplying CCD (EMCCD) detector. We had the sensor run at its fastest speed possible (50 fps) to minimize saturation of the image. Figure 4.28 shows the effect the heat from the rocket plume has on the image quality of a background source. The air turbulence caused by the heat increases the PSF of the background source by $> 5\times$ and significantly disturbs the image quality. Figure 4.29 shows an image of the rocket plume as seen by the EMCCD. As can easily be seen, the plume saturates the detector even at its shortest exposure time setting. The brightness of the plume and the image distortion it causes with atmospheric turbulence means that if we want to use this rocket to do astronomy, we need some way of shielding the plume from view of the science telescope.

4.8.5 Flight objective #5

We successfully recorded flight data from COTS sensors to evaluate their performance under strenuous flight conditions and evaluate their potential for use on future Cubesats. Figure 4.24 and Figure 4.25 show that the data from these sensors qualitatively agree with the high fidelity sensors on the rocket. Further analysis and interpretation of the data are being done by NASA Ames and will be presented in [80].

Figure 4.27: Image of **Xaero-B** and its impressively bright plume during the night flight.

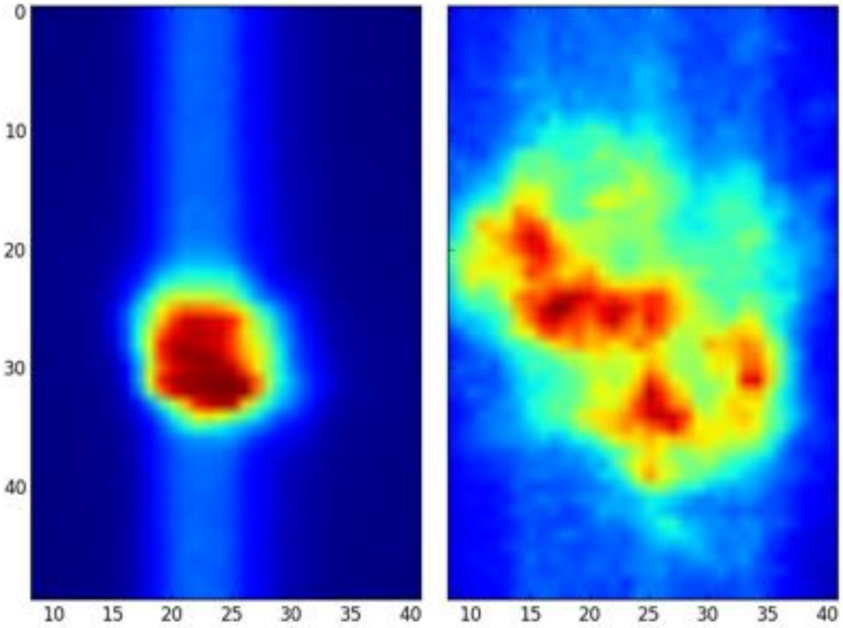

Figure 4.28: The **left** panel is an image of a background light source before takeoff. The **right** panel shows that same light source after the jetwash from the rocket plume as passed in front of the light. The heat of the plume could significantly affect astronomical images taken in its vicinity.

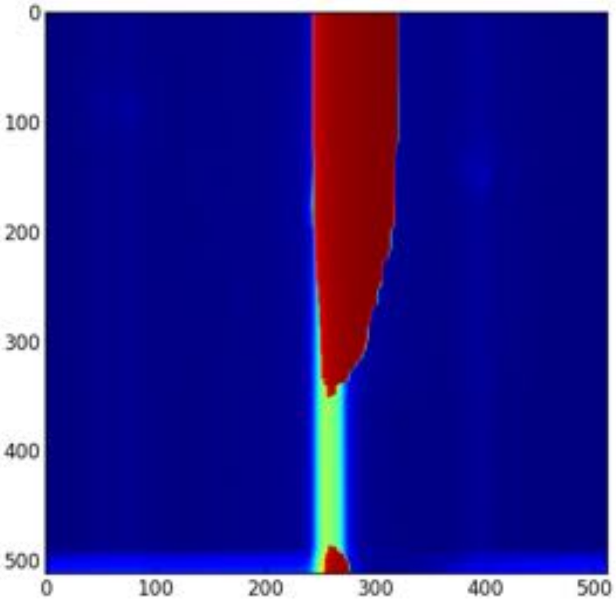

Figure 4.29: Image of the rocket plume as seen by the EMCCD detector. The rocket plume saturates the sensor even at its shortest exposure. This image is from the night flight.

Chapter 5

OPTICAL MODELING OF STARSHADES

5.1 High-Fidelity Optical Models

The large sizes and separations of the starshade architecture mean the optical performance of a full-scale system cannot be tested without going into space. When it comes time to build and launch a starshade, we will have to rely on optical models to demonstrate that it will perform as expected. The tolerances in the design and manufacturings will also be set by the optical models and once it is launched, there is no changing it. As such, the importance of these models being correct is paramount.

Other experiments have relied heavily on model predictions, but the starshade is a unique optical system, a diffractive optic in the Fresnel regime that requires suppression of one part in one billion. The level to which we are pushing the propagation of optical fields is unprecedented and a new set of tools needed to be developed. These models need to be able to accurately predict electric fields down to 10^{-6} of nominal. They must also be able to work on large dynamic ranges, model diffractive effects of millimeter-sized features on an object 10s of meters across over 10,000s kilometers separation. In this chapter I will outline the development of an optical model that is able to meet these requirements and whose versatility make it a useful tool for advancing starshade technology.

5.1.1 Development of a new optical model

I have developed a new optical model that is able to calculate and propagate diffraction from arbitrary shapes. The structure of the algorithms used to develop this model follow that by [11] and [22]. My model extends these by generalizing the diffraction equation to work with an incident spherical diverging wave (instead of parallel plane wave) and by allowing wavefront errors to be added to the incident wave. The model can simulate a transparent aperture, an opaque occulter, or a combination of both for any input shape, allows for defects to be built into that shape, and works for broadband light. This code is currently being used to predict performance of starshade tests and can be implemented to predict the performance of flight design starshades.

5.2 Derivation of 1D Diffraction Equation

We start with the Fresnel diffraction equation with a spherical diverging wave incident on a starshade (Equation 2.14),

$$U\left(x,y,z\right)=\frac{-ikA}{2\pi zz_0}e^{ik(z+z_0)}\iint e^{\frac{ik}{2z_0}\left[(\xi-x_0)^2+(\eta-y_0)^2\right]}e^{\frac{ik}{2z}\left[(\xi-x)^2+(\eta-y)^2\right]}\,d\xi\,d\eta \tag{5.1}$$

For easier reading, we will focus on the terms in the exponentials inside the integral, which we define as $f\left(\xi,\eta,x_0,y_0,z_0,x,y,z\right)=f\left(\phi\right)$ so Equation 5.1 has the form,

$$U\left(x,y,z\right)=C\iint e^{\frac{ik}{2}f(\phi)}\,d\xi\,d\eta \tag{5.2}$$

and the function in the exponential is,

$$f\left(\phi\right)=\frac{1}{z_0}\left[\left(\xi-x_0\right)^2+\left(\eta-y_0\right)^2\right]+\frac{1}{z}\left[\left(\xi-x\right)^2+\left(\eta-y\right)^2\right] \tag{5.3}$$

We scale the observation plane (x,y) and the source plane (x_0,y_0) by the factors a and b, respectively, where

$$\begin{aligned} a &\equiv \left(\frac{z_0}{z_0+z}\right) \\ b &\equiv \left(\frac{z}{z_0+z}\right) \end{aligned} \tag{5.4}$$

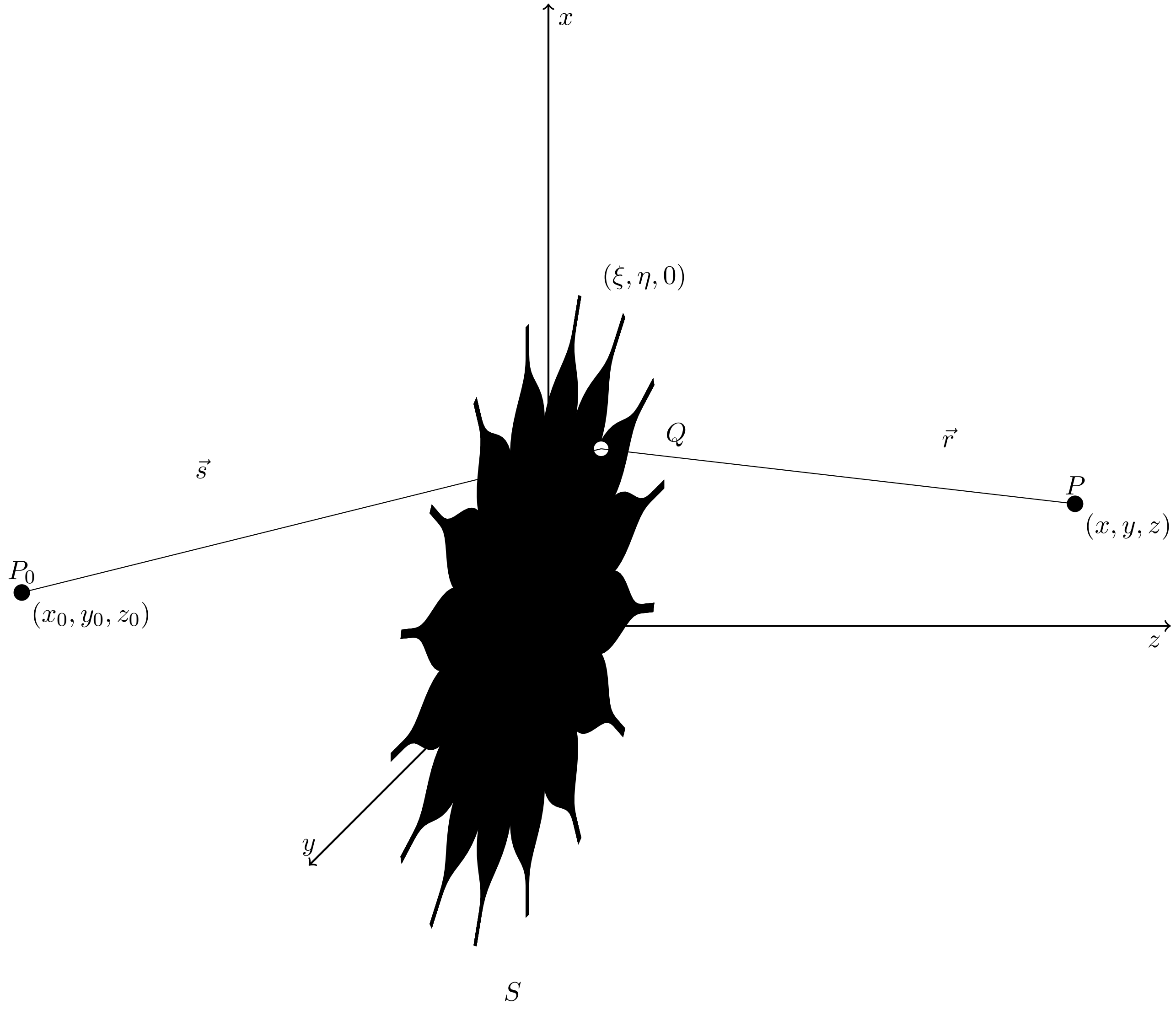

Figure 5.1: The coordinate system used to set up the derivation of diffraction problems. The source is located at P_0, the starshade is denoted as surface S and is located at the origin, and the observation point is at P.

With some educated forethought, we can make a substitution to center the coordinates of integration on the current point under consideration in the observation plane, which is also offset due to an off-axis point source. We define the new coordinates as,

$$\begin{aligned} x_c &= \xi - (ax + bx_0) \\ y_c &= \eta - (ay + by_0) \end{aligned} \tag{5.5}$$

Plugging the new coordinates into our exponential function and neglecting (for now) the η, y_0, y values gives,

$$\begin{aligned} f(\phi)_x &= \frac{1}{z_0}\left[x_c + x_0(b-1) + ax\right]^2 + \frac{1}{z}\left[x_c + bx_0 + x(a-1)\right]^2 \\ &= \frac{1}{z_0}\left[x_c - ax_0 + ax\right]^2 + \frac{1}{z}\left[x_c + bx_0 - bx\right]^2 \end{aligned} \tag{5.6}$$

Expanding the squares and collecting like terms we find,

$$\begin{aligned} f(\phi)_x &= x_c^2\left(\frac{1}{z_0} + \frac{1}{z}\right) + \frac{x_0^2}{z_0 + z} + \frac{x^2}{z_0 + z} - \frac{2xx_0}{z_0 + z} \\ &= x_c^2\left(\frac{z_0 + z}{zz_0}\right) + \frac{(x - x_0)^2}{z_0 + z} \end{aligned} \tag{5.7}$$

Bringing in a similar term for the orthogonal coordinates, our function in the exponential becomes,

$$f(\phi) = \left(x_c^2 + y_c^2\right)\left(\frac{z_0 + z}{zz_0}\right) + \frac{(x - x_0)^2 + (y - y_0)^2}{z_0 + z} \tag{5.8}$$

We take note that $d\xi d\eta = dx_c dy_c$ and plug our function $f(\phi)$ into Equation 5.1 to express the Fresnel diffraction equation in terms of our new coordinates,

$$U(x, y, z) = \frac{-ikA}{2\pi zz_0} e^{ik(z+z_0)} e^{\frac{ik\left[(x-x_0)^2 + (y-y_0)^2\right]}{2(z+z_0)}} \iint e^{\frac{ik}{2az}\left(x_c^2 + y_c^2\right)}\, dx_c\, dy_c \tag{5.9}$$

Inspection of Equation 5.9 will show that the integral is the same as the Fresnel diffraction integral for an on-axis observation point with an incident plane wave. This shows that the diffraction pattern for an incident diverging beam with coordinates scaled by $\left(\frac{z_0}{z_0+z}\right)$ is the same as that of an incident plane wave from a point source at infinity. This is known as *Isomorphic Diffraction.* This also means that we can center the limits of integration on each point in the observation plane and calculate the diffraction pattern as that coming from a plane wave. The phase terms in front of the integral account for the phase of the diverging beam propagating a total distance of $z + z_0$. Expressing Equation 5.9 as a combination of diffracting plane waves centered at each point of the observation plane allows us to integrate over the radius in closed form. Equation 5.9 can be expressed in polar coordinates as,

$$U\left(r, \phi, z\right) = \frac{-ikA}{2\pi z z_0} e^{ik(z+z_0)} e^{\frac{ikr^2}{2(z+z_0)}} \iint e^{\frac{ik\rho^2}{2az}} \rho \, d\rho \, d\theta \tag{5.10}$$

We set the intensity of the incident wave to be 1 at the screen to give $A = z_0$ and integrate over ρ to give,

$$U\left(r, \phi, z\right) = \frac{-1}{2\pi} \frac{z_0}{z_0 + z} e^{ik(z+z_0)} e^{\frac{ikr^2}{2(z+z_0)}} \int_0^{2\pi} e^{\frac{ik\rho(\theta)^2}{2az}} \, d\theta \Bigg|_{\rho_i}^{\rho_o} \tag{5.11}$$

where we invoke Babinet's principle to integrate only over the radius of the occulter such that ρ is evaluated from the inner radius (ρ_i) to the outer radius (ρ_o) for a given θ.

We have changed the two-dimensional diffraction integral into a line integral around the edge of the diffracting screen. To calculate this programmatically, for each point in the observation plane, we recenter the coordinates of the screen and calculate the line integral around the edge of the screen.

The inner and outer radii over which to integrate depends on if the observation point is inside or outside the aperture. Evaluating at the inner and outer radii, the integral in Equation 5.11 becomes,

$$U \propto \frac{1}{2\pi} \int_0^{2\pi} e^{\frac{ik}{2az}\rho_i^2} \, d\theta - \frac{1}{2\pi} \int_0^{2\pi} e^{\frac{ik}{2az}\rho_o^2} \, d\theta \tag{5.12}$$

If the observation point lies outside of the geometric aperture, as in Figure 5.2b, the radial integral crosses the aperture twice and must be evaluated at each radii, as in Equation 5.12. If, however, the observation point lies within the geometric aperture, as in Figure 5.2a, $\rho_i = 0$ and the integral becomes,

$$U \propto 1 - \frac{1}{2\pi} \int_0^{2\pi} e^{\frac{ik}{2az}\rho_o^2} \, d\theta \tag{5.13}$$

Keeping in mind that this calculation is for an open aperture, if we are integrating over an opaque occulter, then we must use Babinet's principle and subtract these integrals from 1. To determine if an observation point is within the aperture, we assume it is simply connected and use the *polywind* algorithm detailed in [62] to calculate the winding number. A winding number of 1 is inside the shape, a winding number of 0 is outside.

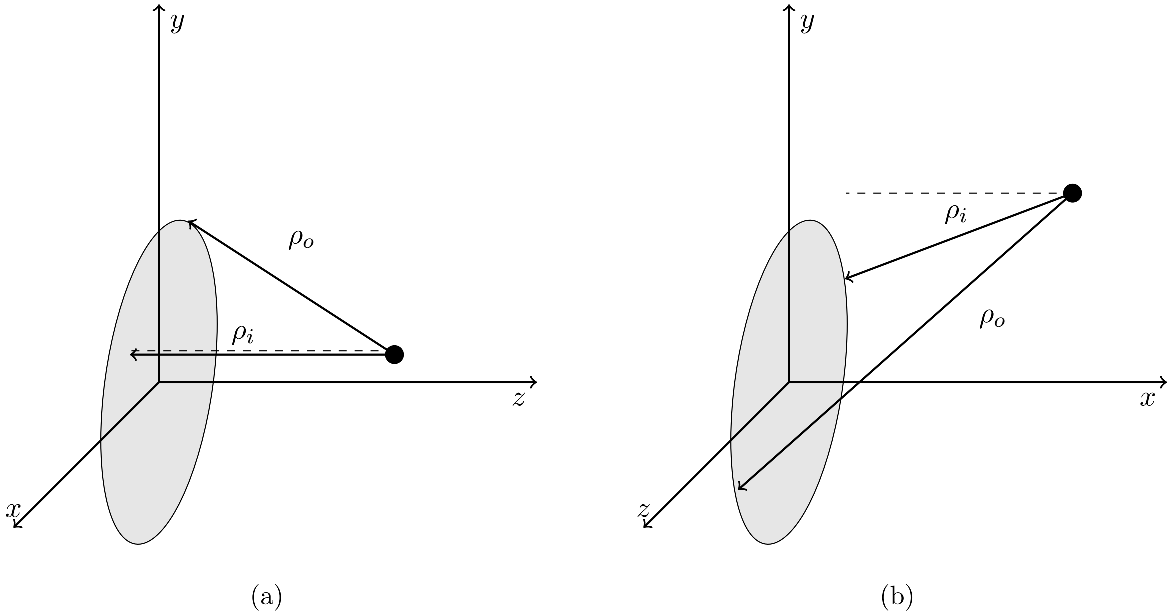

Figure 5.2: (a) shows when the observation point is inside the aperture and the winding number is 1. In this case, the inner radius is 0 and we can integrate using Equation 5.13. (b) shows when the observation point is outside the aperture and the winding number is 0. In this case, we must evaluate the integral at each crossing of the aperture using Equation 5.12

5.3 Software Description

Here we detail the development of an efficient and versatile software package created to implement Equation 5.11 to calculate the diffraction by an arbitrary occulter or aperture. This package was written in Python and has the working title "pyDRT" for Python Diffractive Ray Tracing. The main parameters input into the code are:

- Shape of diffraction screen
- Opaque occulter or transparent aperture?
- Radius of diffraction screen (a)

- Distance from light source to screen (z_0)
- Distance from screen to aperture (z)
- Diameter of aperture (D_{tel})
- Focal plane resolution (θ_{tel})
- Central wavelength (λ_0)
- Wavelength coverage ($\Delta\lambda$)
- Aperture sampling resolution (n_{pts})
- Edge sampling of diffraction screen (n_ρ)

5.3.1 Algorithm

The procedure for implementing the algorithm and calculating the image of a diffracting screen at the focal plane of a telescope is as follows.

(1) Generate loci of points defining the edge of the occulter

(2) Scale the aperture size and distance by $\frac{z_0}{z_0+z}$

(3) For each observation point in the (scaled) aperture:

  (a) Shift the coordinates of the occulter to the current observation point by Equation 5.5

  (b) Integrate the function in Equation 5.15 around the edge of the occulter

  (c) Calculate if the observation point is within the geometric shadow of the occulter using the *polywind* algorithm [62]

    - Apply the appropriate correction depending on if the point is inside or outside and if we are invoking Babinet's principle

  (d) Multiply by phase and scaling terms in front of the integral

    (e) Return the complex electric field due to the occulter at each point in the observation plane

(4) Repeat Step 3 for each wavelength

(5) Calculate the complex electric field at the aperture as if no occulter were present; this is the “unblocked source”

(6) Propagate complex electric field for each wavelength from the pupil plane to the image plane using Equation 5.16

(7) Calculate the broadband intensity in the image plane by incoherently adding the electric fields (Equation 5.20)

(8) Convert to a contrast value by dividing the broadband intensity by the unblocked source

5.3.2 Occulter shape creation

With the diffraction integral turned into a one-dimensional line integral, we can efficiently calculate the diffraction due to any shape; it need not be simply connected either. We define the diffracting screen by a series of (x, y) points describing the edge of the screen. The user can specify the shape of the screen as a simple geometric shape such as a circle or square, as a hypergaussian starshade of specified parameters, or by giving a pre-calculated series of edge points describing the occulter of their choice. The latter option is useful as manufacturing errors can easily be built into the shape to be modeled. The user can specify either an opaque occulter or a transparent aperture, which specifies whether or not to invoke Babinet’s principle.

The shape can be non-simply connected, as long as its able to be split into multiple simply connected shapes. An example of a non-simply connected occulter is the occulting mask for the Princeton test bed experiment (Section 6.6), shown in Figure 5.3. This occulter has an outer mask that it is connected to via radial struts. This outer mask allows for it to be physically mounted in the lab and also helps control diffraction from the tubes in the testbed. For this mask, rather than evaluate the integral over the occulter shape, we evaluate along the edges of the gaps between the struts and the inner and outer masks. Since we are evaluating in the transparent regions, which have a finite outer extent, we do not use Babinet's principle.

5.3.3 Diffraction by occulter

After we have defined our occulter shape, for each point in the observation plane we must calculate Equation 5.11. We use a midpoint integration scheme,

$$\int f(x)\,dx \approx \sum_i \frac{1}{2}\left[f(x_{i+1}) + f(x_i)\right](x_{i+1} - x_i) \tag{5.14}$$

where we are integrating the function,

$$f(\theta) = e^{\frac{ik}{2az}\left[x_c(\theta)^2 + y_c(\theta)^2\right]} \tag{5.15}$$

around the i^{th} occulter points. This provides the complex electric field at the entrance pupil of our aperture.

5.3.4 Fresnel propagation to the image plane

Once we have the complex electric field at the pupil plane of our aperture, we propagate to the focal plane using the Discrete Fourier Transform (DFT) algorithm. Recall from Equation 2.16 that the Fresnel integral can be expressed as the Fourier Transform of the incident field times a quadratic phase factor. The integral in Equation 2.16 is

$$\begin{aligned} U(x,y) &\propto \iint U_0(\xi,\eta)\exp\left\{-ik\frac{x\xi + y\eta}{z}\right\} d\xi\, d\eta \\ &\propto \iint U_0(\xi,\eta)\exp\left\{-2\pi i\frac{x\xi + y\eta}{\lambda z}\right\} d\xi\, d\eta \end{aligned} \tag{5.16}$$

where now (ξ, η) are the coordinates of the pupil plane and (x, y) are the coordinates of the focal plane. Assuming a square array, the DFT used in the Python package *numpy* is given by,

$$\mathcal{F}\{E\} = E_{jk} = \sum_{m=0}^{N-1}\sum_{n=0}^{N-1} e_{mn}\exp\left\{-2\pi i\frac{jm + kn}{N}\right\} \tag{5.17}$$

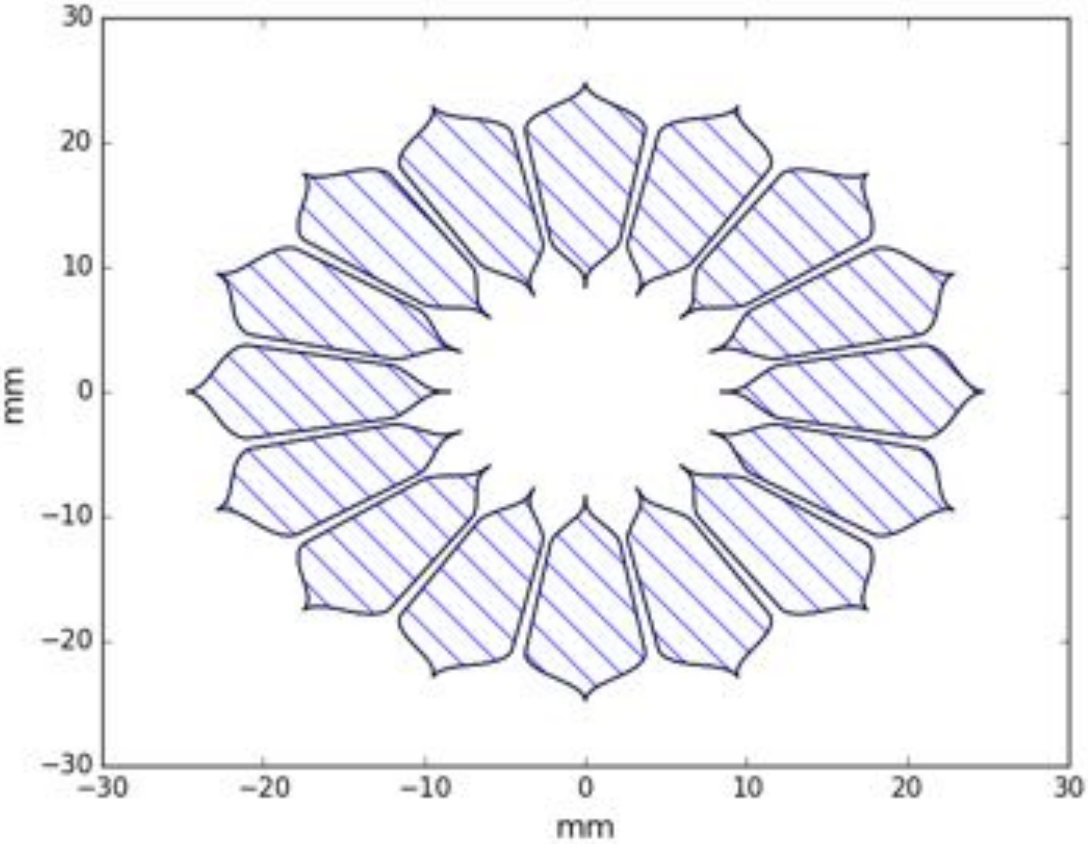

Figure 5.3: Design of 1 inch starshade mask to be used in the Princeton testbed. The blue hatched regions denote transparency. The starshade is supported by struts that extend radially from each petal tip and join an outer mask that is also apodized.

Therefore, to sample the proper spatial frequencies $(x, \xi)/\lambda z$ in the DFT, we set the size of our array as $N = \lambda z$. This size is accomplished by zero-padding the output array from our diffraction calculation such that $N = n_{\mathrm{pts}} n_{\mathrm{pad}}$. Inspection of Equation 5.16 and Equation 5.17, and defining $x = j\Delta x$, $\xi = m\Delta\xi$, will show that,

$$N \Delta x \Delta \xi = \lambda z \tag{5.18}$$

The input spatial sampling at the aperture is set by the sampling of the diffraction calculation, $\Delta\xi = D/n_{\mathrm{pts}}$, and the output spatial sampling at the focal plane is determined by Equation 5.18 and the total size of the array. In order to achieve a specified angular sampling in the focal plane, $\theta = \Delta x/f$, we must choose the padding size to be,

$$n_{\mathrm{pad}} = \frac{\lambda z}{D f \theta} \tag{5.19}$$

where D is the diameter of the aperture, f is the focal length, and z is the image distance given by the Thin Lens Equation. We include the Fresnel QPF in the kernel of the Fourier Transform in order to propagate to a distance different than the focal length of our telescope for when we are focusing on an object that is closer than infinity.

5.3.5 Contrast calculation

Once we have propagated the complex electric fields for each wavelength to the focal plane, we combine the different wavelengths incoherently to obtain a broadband image. For each wavelength, the intensity is calculated from the absolute square of the complex electric field and is weighted by a wavelength dependent weighting factor w_i. This weighting factor can encapsulate the measured spectral response of the detector, optics, and light source.

$$I = \frac{\sum_i |E_i|^2 w_i}{\sum_i w_i} \tag{5.20}$$

The final step is to convert the image into a contrast value, which is often used to measure the performance of an occulter. The contrast is given by Equation 5.21 and is the focal plane image divided by the peak brightness of an image of the unblocked source.

$$\text{Contrast} \equiv \frac{I_{\text{blocked}}}{max\left\{I_{\text{unblocked}}\right\}} \tag{5.21}$$

5.3.6 Numerical convergence

We ran a suite of tests to verify the code is numerically converged for the experiments under consideration. As mentioned previously, this model needs to be able to predict performance accurately to below 10^{-10} contrast value, meaning we need to accurately predict the electric field to one part in 100,000. The metric for evaluation of convergence is the peak contrast value in the focal plane image. We perform the convergence test using the HG Base starshade shape and the parameters for the dry lake bed tests (Section 6.5.2). The model parameters we seek convergence over are the number of points sampled in the pupil (n_{pts}) and the number of points sampled around the edge of the occulter (n_ρ). Figure 5.4 shows the change in peak contrast while varying n_{pts} and n_ρ. The base values are $n_{\text{pts}} = 512$, $n_\rho = 13{,}000$ and the difference in contrast is relative to the value at the farthest right on the plot. The nominal contrast for this case is $\sim 10^{-7}$ and we are converged well below 1% of that, which is also lower than the errors in the data for which we are validating against. Modeling the dry lake bed tests is more sensitive to sampling in the aperture because we are operating at a high Fresnel number in which our telescope is significantly over-resolving the starshade. In this case, small features on the starshade will have a separate contribution to the contrast of the focal plane, where sampling is important. The same feature at a lower Fresnel number will not be resolved and sampling plays less of a role. Modeling starshade designs that have a nominal contrast of 10^{-8} or lower, show that we still achieve <1% error, which brings us into agreement at the 10^{-10} level. We consider these results sufficiently converged.

5.3.7 Code performance

This code is written in Python (built and tested with Python 2.7) and can be ran in parallel using OpenMPI. We ran a series of performance tests on a local laptop. We used a 2013 Macbook Pro with a 2.7 GHz processor (Intel Core i7) and 16 GB of 1600 MHz DDR3 RAM running in

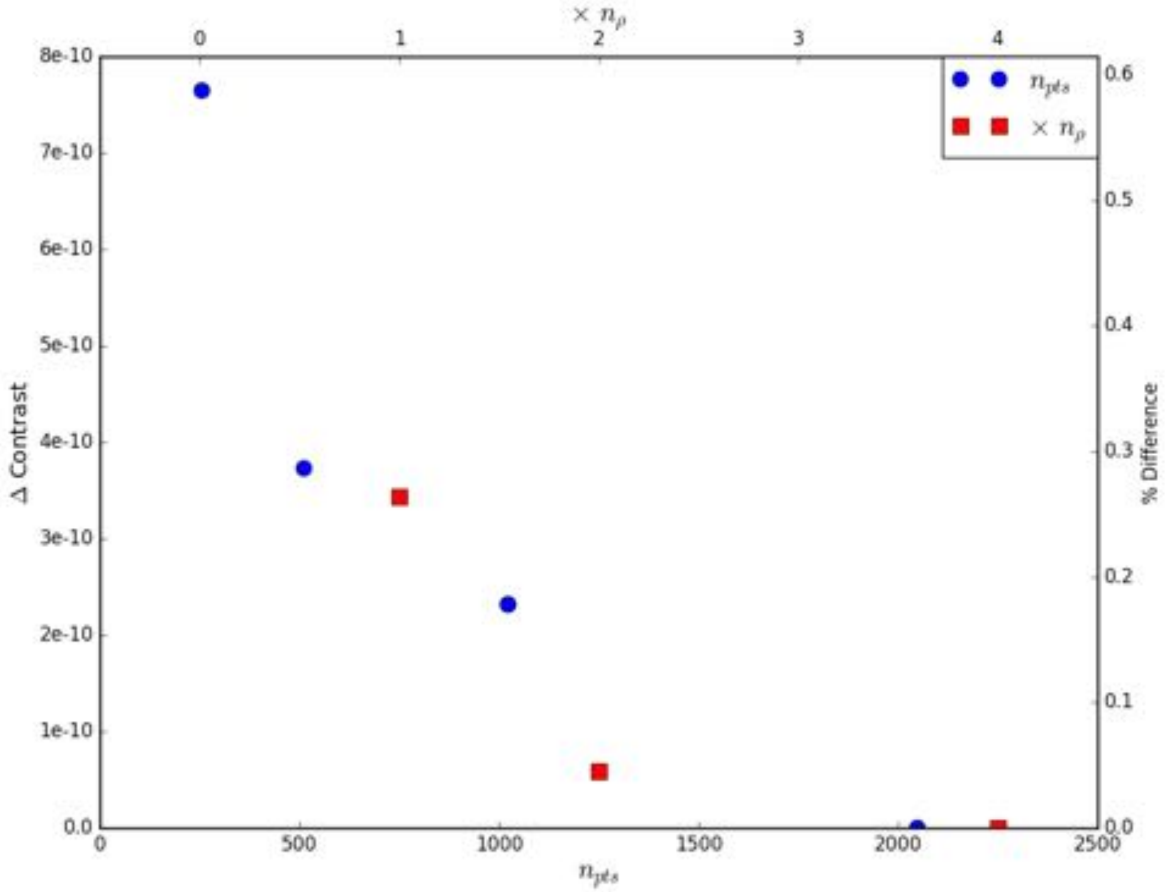

Figure 5.4: Convergence of code as a function of edge sampling (**top** x-axis, relative to 13,000 points) and length of sample grid in the pupil (**bottom** x-axis). The **left** y-axis is the change in contrast, the **right** y-axis is the percent difference.

parallel on 4 cores. We focus solely on the diffraction calculation in Section 5.2, as that is the novel piece of software. We can run a single wavelength (n_λ=1) on a 1024 x 1024 aperture grid (n_{pts}=1024) from an occulter with 13,000 edge points (n_ρ=13,000) in 120 seconds.

The run times scale as,

$$\begin{aligned} t_{\text{run}} &\propto n_{pts}^2 \\ &\propto n_\rho \log(n_\rho) \\ &\propto \sqrt{n_\lambda} \end{aligned} \tag{5.22}$$

5.4 Introducing Wavefront Errors

As we look at designing future starshade testbeds, we need a way to encapsulate in our optical models the possible limitations of the testbed environment that could prevent the experiment from reaching the necessary sensitivities. The main concern that frequently arises is the wavefront errors imposed by the atmosphere and whether or not testing in a vacuum line is necessary. The wavefront errors imposed by a siderostat mirror surface is another possible limitation of the siderostat facility to achieving the necessary contrast levels. We look at two classes of wavefront errors, periodic errors that can be used to approximate figure error on a mirrored surface and random errors due to the turbulent atmosphere. We first detail how these errors are implemented into our optical model and then give results from the two classes.

5.4.1 Implementation in the optical model

The optical model we developed solves the diffraction equation with a one-dimensional line integral around the edge of the diffracting shape. We are able to make this simplification because we assume the occulter has a binary apodization profile and therefore the electric field interior to the edge satisfies the Helmholtz Equation. If we want to include a phase perturbation across the region of integration, we must be able to describe the field interior to the edge. If you imagine a gaussian phase perturbation across a circular aperture such that the peak is in the center of the aperture and the field approaches zero at the boundary, then Dirichlet boundary conditions would not be sufficient as they would assume the field is zero across the aperture. However, if we assume the phase perturbation is due to the superposition of plane waves infinite in extent, each of which is a solution to the Helmholtz equation, then knowledge of the plane waves at the edge means we can reconstruct the field at any point interior. Representing the field as such is called the angular spectrum of plane waves and can be thought of as a Fourier decomposition of the complex field into plane waves. For a function $f(x)$, we relate the angular spectrum, $A(\alpha)$, of plane waves at angle α as,

$$f(x) = \int A(\alpha)\, e^{i2\pi\alpha x}\, d\alpha \tag{5.23}$$

The diffraction equation we are trying to solve is Equation 5.10 modified by a phase perturbation, $\phi(\rho, \theta)$, which we simplify to one dimension as,

$$U(p) \propto \int e^{\frac{ik}{2z}(x-p)^2} e^{i\phi(x)}\, dx \tag{5.24}$$

We express the phase perturbation as its angular spectrum to get,

$$\begin{aligned} U(p) &\propto \int e^{\frac{ik}{2z}(x-p)^2} \int A(\alpha)\, e^{i2\pi\alpha x}\, d\alpha\, dx \\ &\propto e^{\frac{ik}{2z}p^2} \int A(\alpha) \int e^{\frac{ik}{2z}x^2} e^{-i2\pi x\left(\frac{p}{\lambda z}-\alpha\right)}\, dx\, d\alpha \\ &\propto e^{\frac{ik}{2z}p^2} \int A(\alpha)\, \mathcal{F}\left[e^{\frac{ik}{2z}x^2}\right]_{\left(\frac{p}{\lambda z}-\alpha\right)} d\alpha \end{aligned} \tag{5.25}$$

where $\mathcal{F}[f(x)]_{(\alpha)}$ is the Fourier transform of $f(x)$ evaluated at α.

The Fourier transform is just the solution to Equation 5.10, for which our optical model solves, evaluated at each plane wave angle shifted by the angle to the observation point $(p/\lambda z)$. Additionally, the angular spectrum $A(\alpha)$ is just the Fourier transform of our phase perturbation. We can use the convolution theorem to express the diffracted field of our occulter with an incident phase perturbation as,

$$U(p) \propto e^{\frac{ik}{2z}p^2} \left[A * \mathcal{F}\right]_{\left(\frac{p}{\lambda z}\right)} \tag{5.26}$$

To implement this into our model, we calculate the diffracted field at our telescope aperture as normal and convolve the end result with Fourier transform of our incident phase map. To approximate the time averaged intensity that is seen by the detector, we generate a sample of random phase perturbations and incoherently add them in the image plane.

5.4.2 Periodic wavefront errors

Periodic errors have the largest effect on starshade performance as they can beat against the periodic behavior of the Fresnel zones to negate the apodization. These errors can come from figure errors on a siderostat mirror where the characteristic spatial frequency of error can be approximately periodic, or from standing waves in the atmosphere of a tube. Features of size D will scatter light at the diffraction angle, $\theta = \lambda/D$. If there is a characteristic size scale diffracting at the same angle (as in periodic errors), then they will add constructively at that angle. The efficiency at which they coherently add (the *diffraction efficiency*) for a sine wave can be approximated as $\left(\frac{1}{2}kA\right)^2$, where k is the wavenumber of light and A is the amplitude of the error. If we express the amplitude in terms of mirror surface quality $A = \lambda/\sigma$, the diffraction efficiency is independent of wavelength and simply becomes π^2/σ^2.

Figure 5.5 diagrams the effect a periodic error will have on the starshade to shift the shadow at the angle θ. Error spatial frequencies that we are susceptible to are frequencies at which the angle diffracts light into our aperture. Low spatial frequencies (blue curve in Figure 5.5), such as figure across an entire mirror or large seeing cells, will diffract at small enough angles that it will not be able to shift the shadow far enough to make a difference. Higher spatial frequencies will diffract at a larger angle and will move the shadow entirely off the aperture (red curve in Figure 5.5). In the case where we have a finite mirror with an outer shadow, high spatial frequencies, like the surface roughness of a mirror, will diffract at angles large enough to miss the aperture entirely. This means we are only susceptible to a range of spatial frequencies.

We will now derive relations for the wavefront error modes we are most susceptible to. The problem is set up in Figure 5.6 with a starshade of radius r_s in front of a mirror of radius r_m at a distance z from a telescope of radius r_t. Incident on the starshade is a sinusoidal wavefront error of amplitude A and spatial frequency $1/D$. The radius of the “sweet spot” of the shadow for which

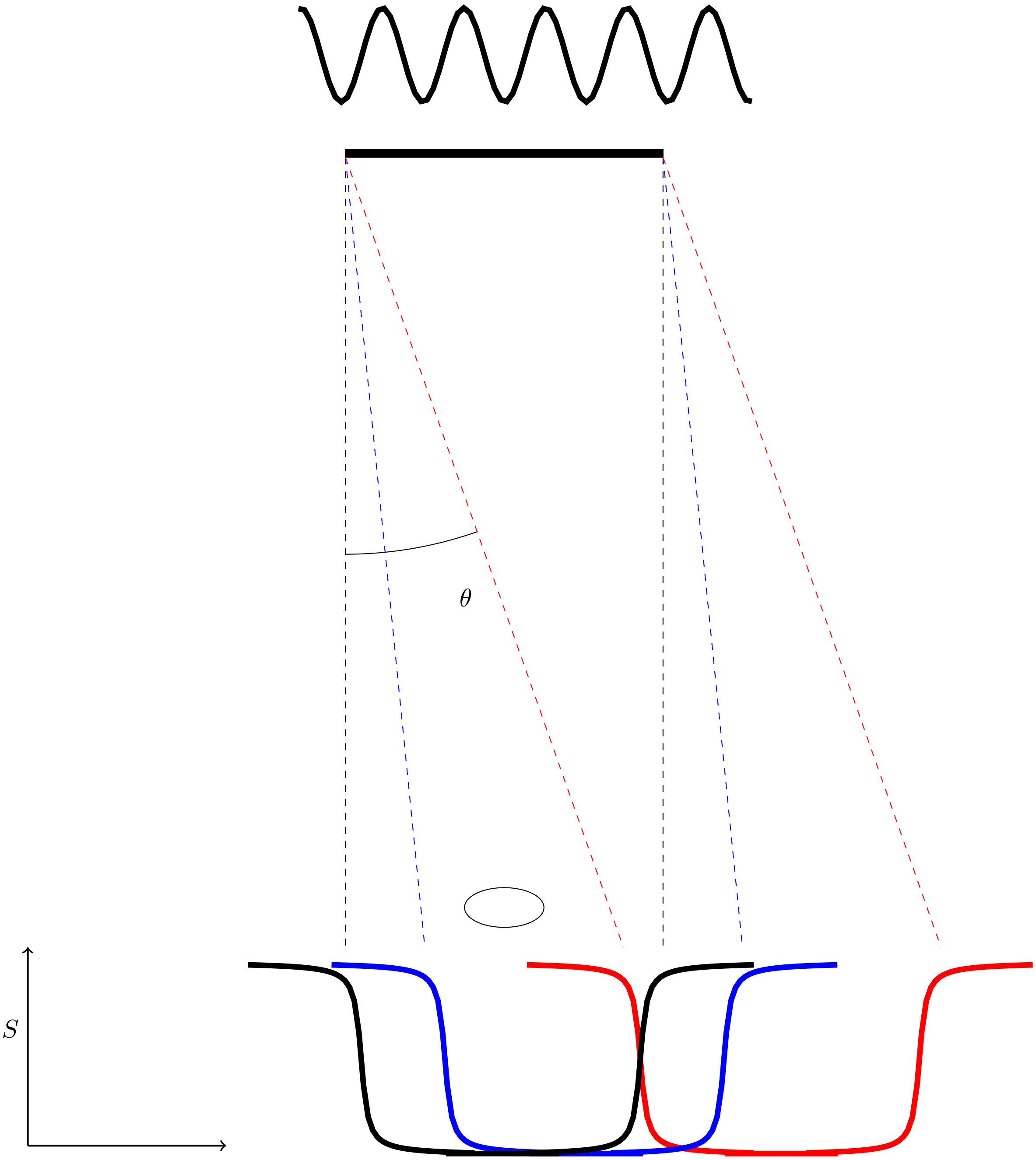

Figure 5.5: The solid 'U' shaped lines show the intensity as a function of position and represent the width and position of the shadow cast by the starshade (black horizontal bar on top). The oval in the center represents the telescope pupil. As a periodic wavefront error hits the starshade, depending on the diffraction angle (denoted by different colors, **black** is nominal), the shadow may shift a little and cause a small increase in suppression (**blue**), or the shadow may move completely off the aperture (**red**).

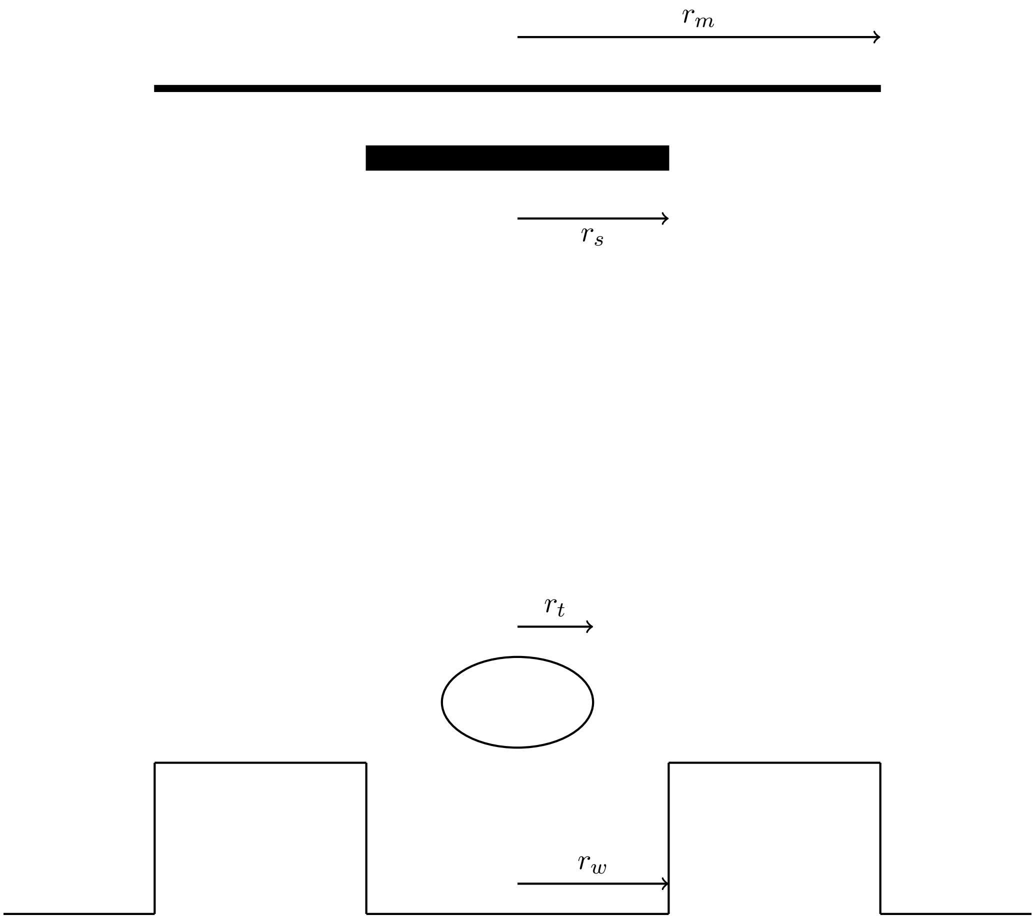

Figure 5.6: The top horizontal bar represents the siderostat mirror of radius r_m, the thick horizontal bar below represents the starshade of radius r_s. The oval is the telescope of radius r_t and the square wave is high in regions of illumination and low in regions of shadow. The width of the starshade's shadow is of radius r_w.

we achieve our required suppression is given by r_w. The range of spatial frequencies that move the shadow off the aperture, but do not bring the outer shadow onto the aperture, i.e., the *bad* frequencies are given by,

$$\frac{r_w - r_t}{z} < \frac{\lambda}{D} < \frac{r_m + r_t}{z} \tag{5.27}$$

Rather than speak in absolute terms, we examine errors in terms of the number of modes across the starshade (n_s), related to the spatial frequency by $A\sin\left(2\pi x/D\right) = A\sin\left(n_s \pi x/r_s\right)$. Plugging D into Equation 5.27 and recognizing the Fresnel number N_F, we find that we are affected by modes above,

$$n_s > 2\left(\frac{r_w - r_t}{r_s}\right) N_F \tag{5.28}$$

If the shadow is shifted by an angle θ, the suppression incident on the aperture will be $\pi^2/\sigma^2 S\left(\theta z\right)$, which we require to be less than the minimum suppression S_{min} driven by science requirements. If we have an estimate or expression of the suppression in terms of the starshade radius, then the shadow width can be written as $r_w = \alpha\left(S_{\text{min}}, \sigma\right) r_s$ and occurs where $\pi^2/\sigma^2 S\left(\alpha r_s\right) = S_{\text{min}}$.

A common way to express the telescope size relative to the starshade is in terms of the number of resolution elements that sample across the diameter of the starshade, allowing us to write r_t as,

$$\begin{aligned} \frac{n_{\text{res}}\lambda}{2r_t} &= \frac{2r_s}{z} \\ \frac{r_t}{r_s} &= \frac{n_{\text{res}}}{4N_F} \end{aligned} \tag{5.29}$$

Finally, we can express the *bad* modes that contribute to our suppression in terms of the Fresnel number, minimum suppression, telescope resolution, and mirror quality σ.

$$n_s > 2N_F \alpha\left(S_{\text{min}}, \sigma\right) - \frac{1}{2} n_{\text{res}} \tag{5.30}$$

Similarly, we can find an upper bound in the number of modes we are sensitive to, which depends on the size of the mirror relative to the starshade. We can *neglect* modes larger than,

$$n_s > 2N_F \left(\frac{r_m}{r_s}\right) + \frac{1}{2} n_{\text{res}} \tag{5.31}$$

Figure 5.7 and Figure 5.8 show Equation 5.30 in action. The plots show the maximum suppression in the aperture as a function of the number of periodic phase modes across the starshade with a wavefront error amplitude of 50 nm (black circles) and 100 nm (red diamonds). The horizontal line specifies the minimum suppression (S_{min}) we are trying to obtain. The vertical lines mark the number of modes, as calculated by Equation 5.30, where we should cross over S_{min}. α was calculated from a functional fit to the maximum suppression as a function of off-axis distance. These plots demonstrate that Equation 5.30 can be used to predict the sensitivity to periodic errors.

As a further example of Equation 5.30 in use, we plug in values for a flight-like configuration $N_F = 14$, $n_{\mathrm{res}} = 4$, where we require $S_{\mathrm{min}} = 10^{-9}$ from a $\lambda/20$ siderostat mirror that is 3× the diameter of the starshade. We find $\alpha = 0.14$ and we must work to minimize errors of the order $2 < n_s < 86$. For our McMath tests using a 30 cm starshade, we need to maintain $\lambda/20$ figure for all scales over 0.35 cm $<$ D $<$ 10 cm. As the starshade radius increases with increasing baseline, the physical size scale of the modes also increase and smaller errors can be neglected.

Note that these expressions assume there is only one mode contributing to the total suppression. In reality, there will be a number of modes with different strengths. This can be expressed as a power spectrum of the mirror's figure. The convolution of the PSD with the expected suppression will determine α and set the minimum suppression constraints.

5.4.3 Modeling turbulence in the atmosphere

A wavefront propagating through a turbulent medium accumulates phase errors as it passes through varying indices of refraction caused by temperature (and thus density) fluctuations. The effect these phase errors have on the light field depends on the characteristic size scales of coherent structures in the turbulence. Large turbulent eddies are generated by solar heating and wind shear, which proceed to break into smaller scales in a turbulent cascade [40]. [40] proposed that energy exists on spatial scales that follow a power law $\propto \kappa^{-11/3}$. It can be shown that the power spectrum of the phase fluctuations is given by [28],

$$\Phi\left(\kappa\right) = 0.023 r_0^{-5/3} \kappa^{-11/3} \tag{5.32}$$

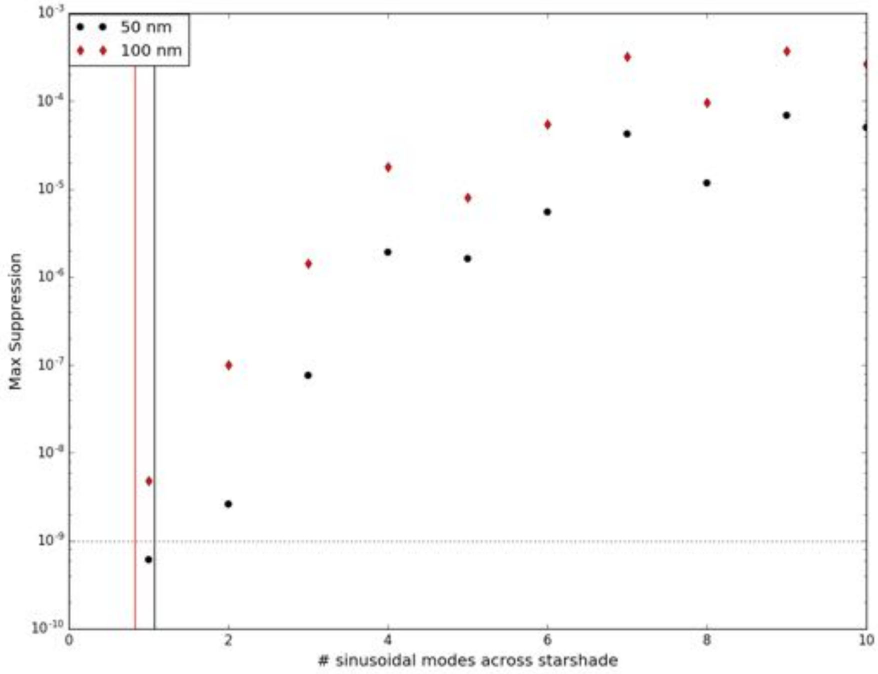

Figure 5.7: Results from our optical model of the **Princeton** testbed. The suppression is charted as a function of the number of sinusoidal modes of wavefront error that are across the starshade. **Black** is for a wavefront error of amplitude 50 nm, **red** is for a wavefront error of 100 nm. The horizontal lines indicate where Equation 5.30 predicts we will rise above our suppression threshold.

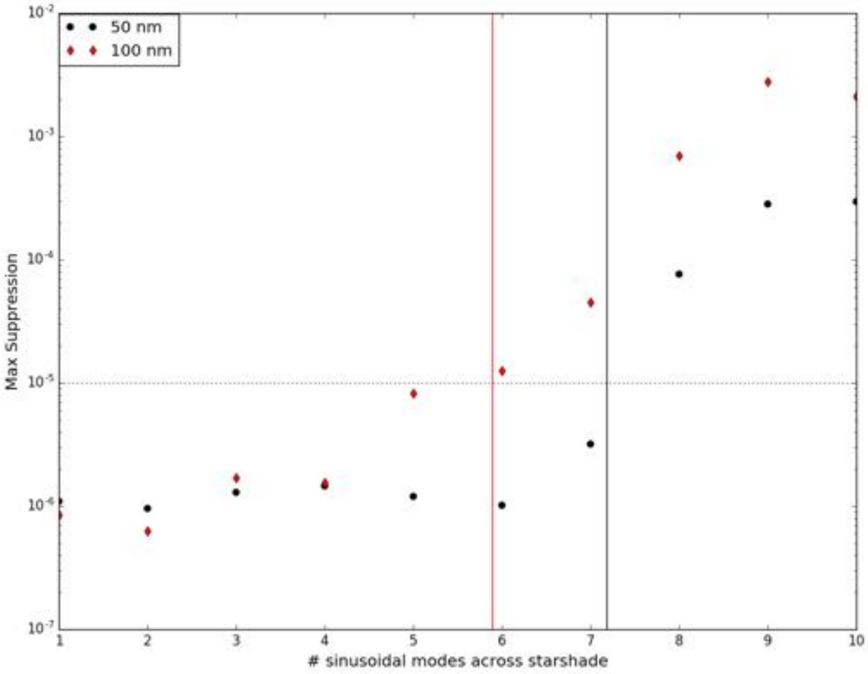

Figure 5.8: The same as Figure 5.7, except for modeling the **McMath** tests.

where r_0 is the Fried parameter.

The Fried parameter is a characteristic size scale over which there is long term coherence; an imaging system whose resolution is limited by the atmosphere will have a resolution equivalent to that of an aperture the size of the Fried parameter. The Fried parameter can be calculated as,

$$r_0 = \left[0.423k^2 \int C_n^2 \left(z'\right) \, dz'\right]^{-3/5} \tag{5.33}$$

where $C_n^2 \left(z\right)$ is the refractive index structure constant, which is proportional to the strength of the turbulence [28].

To simulate a phase screen that follows a Kolmogorov power spectrum, we assume the turbulence is a gaussian white noise process and use with Wiener-Khinchin Theorem to describe the autocorrelation of the phase as a Fourier transform of the power spectrum [14]. A random phase map is generated by seeding the autocorrelation with random phases pulled from a Normal distribution with $\mu = 0, \sigma = 1$ $\left(N\left(0,1\right)\right)$.

$$\phi\left(x,y\right) = \mathcal{R}\left\{\mathcal{F}^{-1}\left[\sqrt{\Phi\left(\kappa_{u,v}\right)}\left\{N_{u,v}\left(0,1\right) + iN_{u,v}\left(0,1\right)\right\}\right]\right\} \tag{5.34}$$

A random phase map generated with $r_0 = 3$ cm is shown in Figure 5.9. We verified proper sampling of the power spectrum by matching the variance of the phase as to that expected from theory [66],

$$\sigma^2 = 1.02\left(D/r_0\right)^{5/3} \tag{5.35}$$

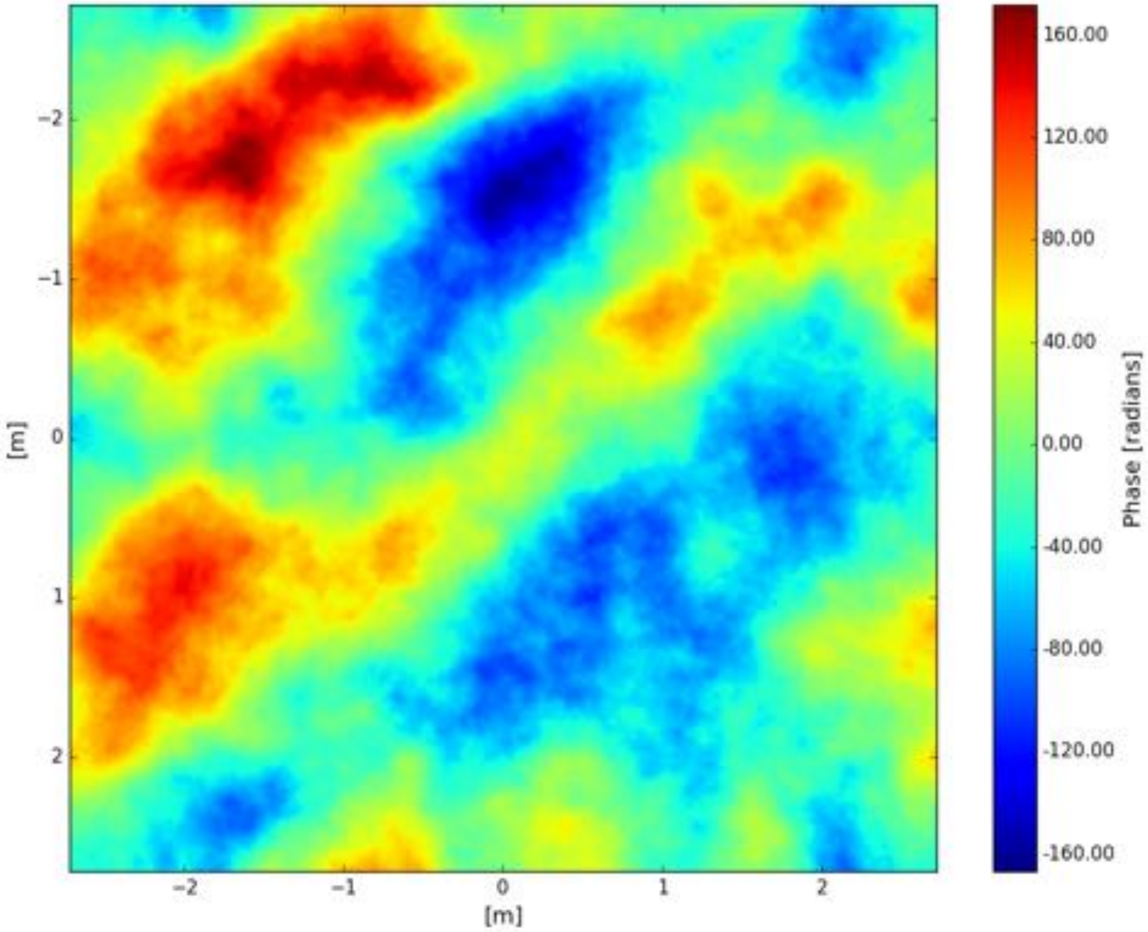

Figure 5.9: Random phase map generated assuming a Kolmogorov power spectrum with Fried parameter $r_0 = 3$ cm.

Chapter 6

OPTICAL MODEL VALIDATION WITH FIELD DATA

6.1 Validation of Optical Models

There are three key technology areas for starshades that the NASA Exoplanet Exploration Program has determined in need of development [75]:

(1) Diffraction and scattered light control for starlight suppression

(2) Lateral formation flying sensing

(3) Precision deployable structures

The work of this dissertation advances areas TA1 (this chapter) and TA2 (see Chapter 3). The highest priority need for TA1 is optical demonstration and optical model validation. In Chapter 2 we described how our understanding of starshade diffraction and the tolerances on the shape are based on the assumption that scalar diffraction theory is sufficient to model the underlying physics of diffraction. This is appropriate for most optical experiments, but the large dynamic range (both in size scales and electric field strengths) of the starshade system is unprecedented and this assumption needs to be thoroughly examined. This is the main motivation for validation of our optical models with field testing of starshades. **We need to verify that our optical models working under the assumption of scalar diffraction theory can accurately predict starshade performance down to contrast levels of 10^{-10}.**

6.2 Validation Tests

Optical tests of a full-scale starshade architecture is impossible without going to space, so we must rely on validation through sub-scale tests on the ground. Scalar diffraction theory states that if we preserve the similarity parameter of Fresnel number, $N_F = a^2/(\lambda F)$, then the physics is the same, so our validation tests need to work towards achieving a flight-like Fresnel number of ~ 14. Reaching this Fresnel number is still not trivial, as it scales with the square root of the separation and as we must keep the starshade to macroscopic sizes to avoid non-scalar effects of wavelength-sized features, the separation becomes large and is difficult to achieve on the ground.

Ideas on how to test starshades suborbitally and on the ground are detailed throughout this dissertation; in this chapter we will focus on three ground tests: NCAR, Dry Lake Bed, and Princeton, which are summarized in Table 6.1 (see Chapters 7 & 8 for results from the McMath tests). For each of these tests, the goal is to measure contrast (or suppression) from a starshade of a specified shape and reproduce those results with our optical models.

The NCAR tests were the first ever tests that demonstrated starshades can achieve high levels of starlight suppression. The Dry Lake Bed tested large ($1/100^{\text{th}}$-scale) starshades that had errors built into the shape to test tolerance sensitivities. The Princeton tests are upcoming lab tests with the goal of achieving high suppression (10^{-9}) at the correct Fresnel number. I argue in Section 7.4 and Section 6.6.6 that an additional testbed that is larger than the Princeton testbed is needed to support experiments that fully explore the critical scaling issues of starlight suppression.

6.3 Comparison with Other Models

Before we can compare our model predictions to the experiments, we must verify that our models agree with each other and that we are confident we are capturing the relevant physics. The model described in Chapter 5 is an expansion of the model presented in [11] that has been used for tolerance analysis of flight-like starshades. This model had been cross-checked with other models [2, 89], but as we moved to simulating starshade experiments in the laboratory and field, i.e., moved

Parameter	**NCAR**	**Dry Lake Bed**	**Princeton**	**McMath**	**Flight**
D_{SS}	32 mm	48 cm	26 mm	24 cm	40 m
F_1	19 m	1 km	50 m	2.4 km	55,000 km
F_2	23 m	1 [2] km	27 m	∞	∞
IWA	175”	50”	55”	10”	75 mas
N_F	49	230 [173]	15	12	15
D_{tel}	2 mm	4 cm	3.85 mm	2 cm	2.4 m
$\Delta\lambda$ [nm]	390 - 550	425 - 775	633.0	400 - 750	400 - 750

Table 6.1: Parameters for various optical model validation experiments. F_1 is the starshade-telescope separation, F_2 is the source-starshade separation, N_F is the Fresnel number calculated at 500 nm (except for the Princeton testbed).

the input light source from infinity and made into a diverging spherical wave, the models diverged from each other and were no longer in agreement with each other or with experimental data. In some cases they differed by a few orders of magnitude (Figure 6.1) [30, 57]. Thus the new model was developed to be compatible with parameters of the ground-based experiments, in terms of the input light source and the size scales of the starshade. We have shown that the new model is in agreement with that of [11] in the limit of an infinite plane wave.

We have been working towards agreement with two independent models, both of which turn the 2D diffraction integral into a 1D line integral around the occulter shape and all are based on scalar diffraction theory. One is developed at NASA JPL and is based on boundary diffraction integrals [9] and one is developed at Northrop Grumman and includes an extra order of terms than is included in the standard Fresnel approximation. Since the development of our new model, we have shown that it is in good agreement with the JPL model, but the Northrop model agrees for some cases, but not all (Figure 6.2) [57]. The JPL model is more similar to our own than that of Northrop and it is important to have agreement between models that are distinct from each other. We are working hard to bring the Northrop model into agreement with ours and JPL’s and to confirm that the latter models are not missing important physics by not including higher order terms.

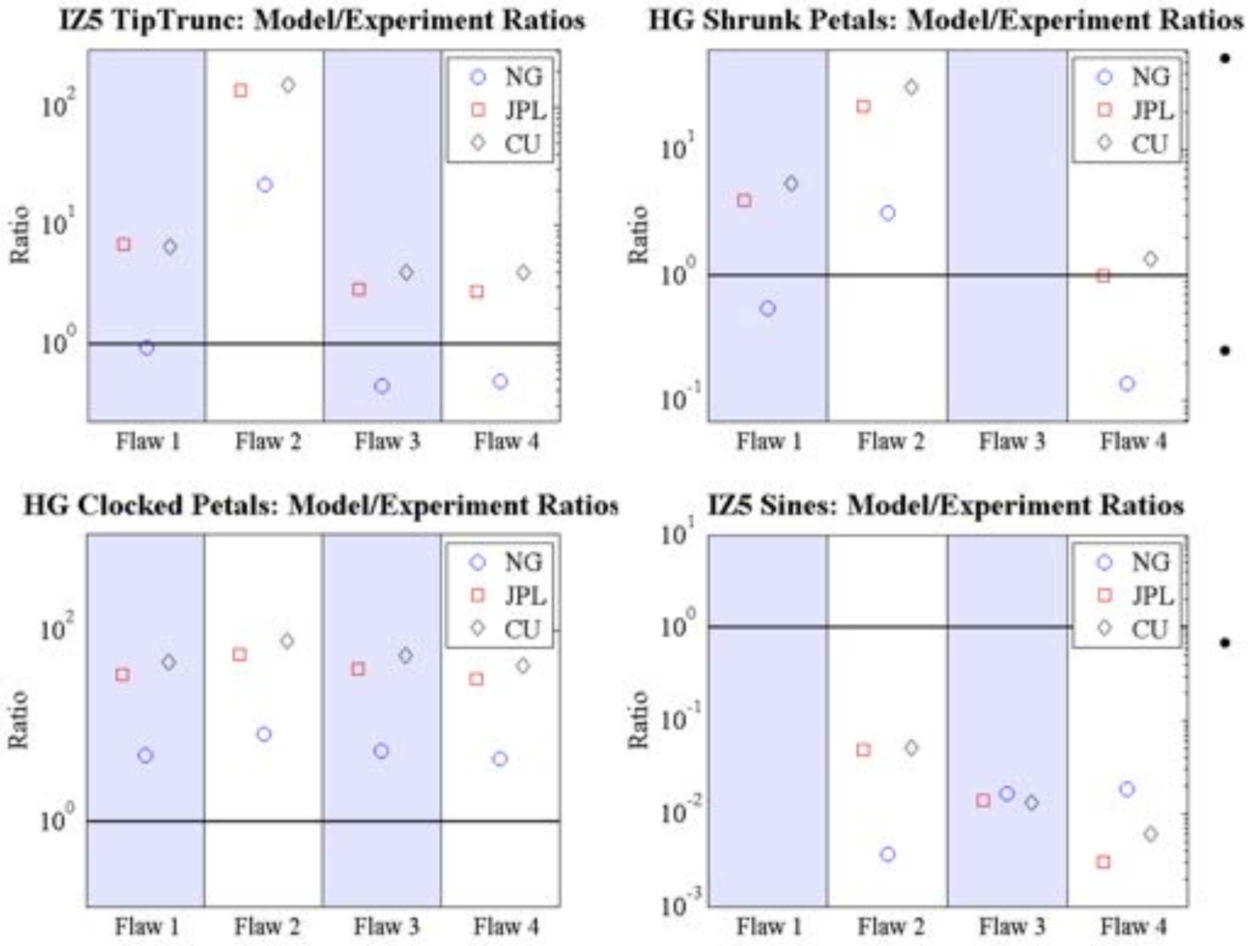

Figure 6.1: This figure (taken from [57]) shows the comparison of the three models to the dry lake bed experimental data as the models stood in January 2016. The data are the ratios of the peak contrast measurements of the flaws. At that time, there was not good agreement between models nor with the data.

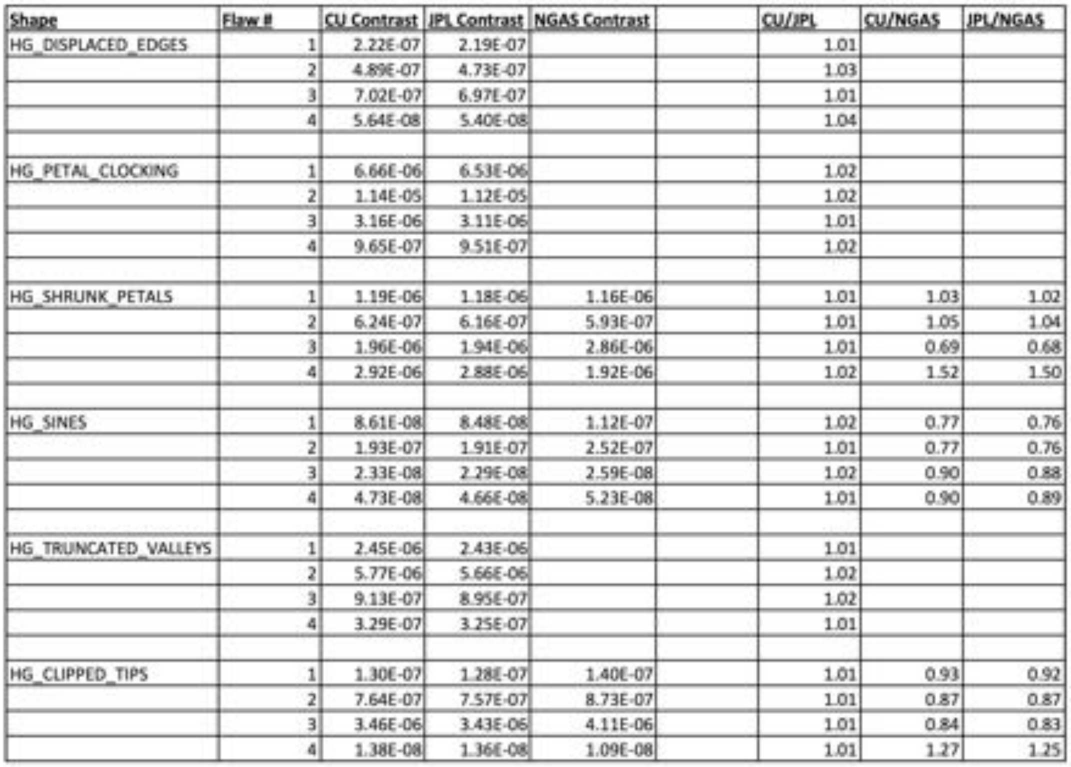

Shape	Flaw #	CU Contrast	JPL Contrast	NGAS Contrast		CU/JPL	CU/NGAS	JPL/NGAS
HG_DISPLACED_EDGES	1	2.22E-07	2.19E-07			1.01		
	2	4.89E-07	4.73E-07			1.03		
	3	7.02E-07	6.97E-07			1.01		
	4	5.64E-08	5.40E-08			1.04		
HG_PETAL_CLOCKING	1	6.66E-06	6.53E-06			1.02		
	2	1.14E-05	1.12E-05			1.02		
	3	3.16E-06	3.11E-06			1.01		
	4	9.65E-07	9.51E-07			1.02		
HG_SHRUNK_PETALS	1	1.19E-06	1.18E-06	1.16E-06		1.01	1.03	1.02
	2	6.24E-07	6.16E-07	5.93E-07		1.01	1.05	1.04
	3	1.96E-06	1.94E-06	2.86E-06		1.01	0.69	0.68
	4	2.92E-06	2.88E-06	1.92E-06		1.02	1.52	1.50
HG_SINES	1	8.61E-08	8.48E-08	1.12E-07		1.02	0.77	0.76
	2	1.93E-07	1.91E-07	2.52E-07		1.01	0.77	0.76
	3	2.33E-08	2.29E-08	2.59E-08		1.02	0.90	0.88
	4	4.73E-08	4.66E-08	5.23E-08		1.01	0.90	0.89
HG_TRUNCATED_VALLEYS	1	2.45E-06	2.43E-06			1.01		
	2	5.77E-06	5.66E-06			1.02		
	3	9.13E-07	8.95E-07			1.02		
	4	3.29E-07	3.25E-07			1.01		
HG_CLIPPED_TIPS	1	1.30E-07	1.28E-07	1.40E-07		1.01	0.93	0.92
	2	7.64E-07	7.57E-07	8.73E-07		1.01	0.87	0.87
	3	3.46E-06	3.43E-06	4.11E-06		1.01	0.84	0.83
	4	1.38E-08	1.36E-08	1.09E-08		1.01	1.27	1.25

Figure 6.2: This chart shows the comparison of the three optical models as of July 2016. All the CU and JPL models agree to better than 5% and the NGAS models agree that well on some. This is a significant improvement over the results of Figure 6.1 .(NGAS data taken from [57])

6.4 Earliest Starshade Tests at NCAR

The first ever starshade tests were conducted in the High Altitude Observatory vacuum facility at the National Center for Atmospheric Research (NCAR) in Boulder, CO [44, 69]. These were the first demonstrations of starshades, showing that they were not just an analytic solution and that they could achieve unprecedented levels of suppression, and set them on the path they are on today. These tests showed that starshades work without vacuum and developed the tools and procedures for testing starshades that are still in use today. The results presented in [44] still holds the record for the highest suppression demonstrated with a starshade.

Details of the experiment setup can be found in [44], but the basic setup is shown schematically in Figure 6.3. A heliostat feeds light from the Sun through a pinhole on one end of a 50 m long dark tunnel and a photomultiplier tube on the other end maps the irradiance in the dark shadow of a 35 mm diameter starshade. The optical parameters are shown in Table 6.1.

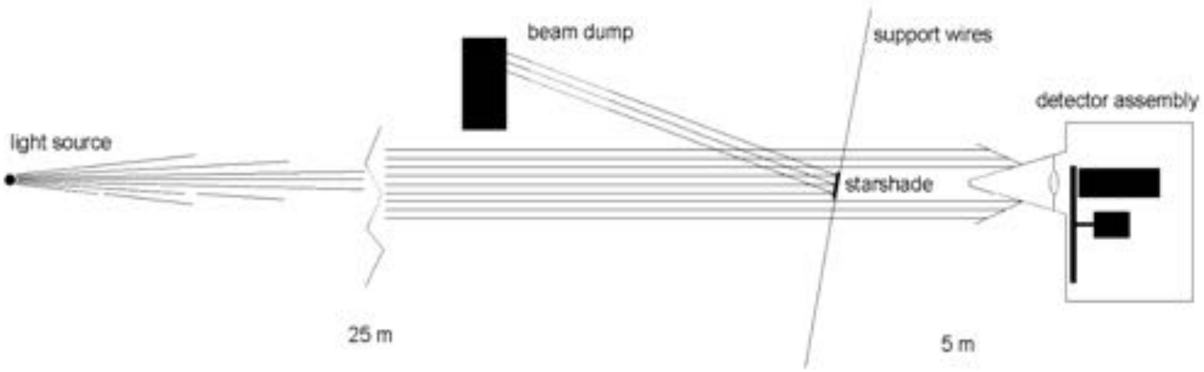

Figure 6.3: Experimental setup of the starshade testbed at NCAR (Figure 1 in [44])

6.4.1 Comparison to model predictions

We modeled this experiment (assuming 5 μm gaps at the starshade tips and valleys) with our optical model to see if we were able to agree with the experimental results. The predicted suppression across the aperture is shown in Figure 6.4 where we predict an integrated suppression with a 2 mm square aperture of 1.33×10^{-7} (we use an integrated suppression because the detector in the original experiment was a lensless photomultiplier tube "light bucket" over a 2 mm aperture). [44] reported a raw suppression of 8.4×10^{-7}. They also reported a modified suppression, where they subtracted light diffracted off the wires suspending the starshade and replaced light from the worst defects (broken tips, etc.) with an average defect value. This modified suppression was 3.3×10^{-7}. They were able to correct for the flaws not attributable to starshade performance by taking a focal plane image of the starshade and locating on the image the major sources of light. These images were compared to the actual test article to verify there were defects at the same location.

A comparison of the modeled and experimental focal plane images and irradiance in the shadow are shown in Figure 6.6 and Figure 6.5, respectively. A reanalysis of the data (independent in the sense that the analysis was done before this model was run) puts the experimental modified contrast at $1.3 \times 10^{-7} \pm 0.09 \times 10^{-7}$ (Doug Leviton, private communication, August 2016). This result is in excellent agreement with that predicted by our model. This result is by no means a complete validation of our optical model, but it is promising that our model is able to accurately reproduce the results of the deepest suppression achieved to date (a level of suppression that is nearly sufficient for the flight mission).

6.5 Testing on Dry Lake Beds

This effort was led by our collaborators at Northrop Grumman, Tiffany Glassman and Steve Warwick, and was supported through a NASA TDEM. The motivation for testing on dry lake beds is that they are some of the flattest places on Earth and allow us to align three objects (light source, starshade, and telescope) over large separations. In April 2012, I did the first proof of concept on the dry lake bed El Mirage Lake in CA aligning a flashlight, starshade, and telescope with a mere 200 m separation between each. The starshade was 60 cm in diameter and laser-cut from ABS plastic, so there was significant edge scattering, but the test was just a proof of concept showing we could achieve alignment (Figure 6.7).

In the following years, the Northrop team expanded this concept and did a number of ex-

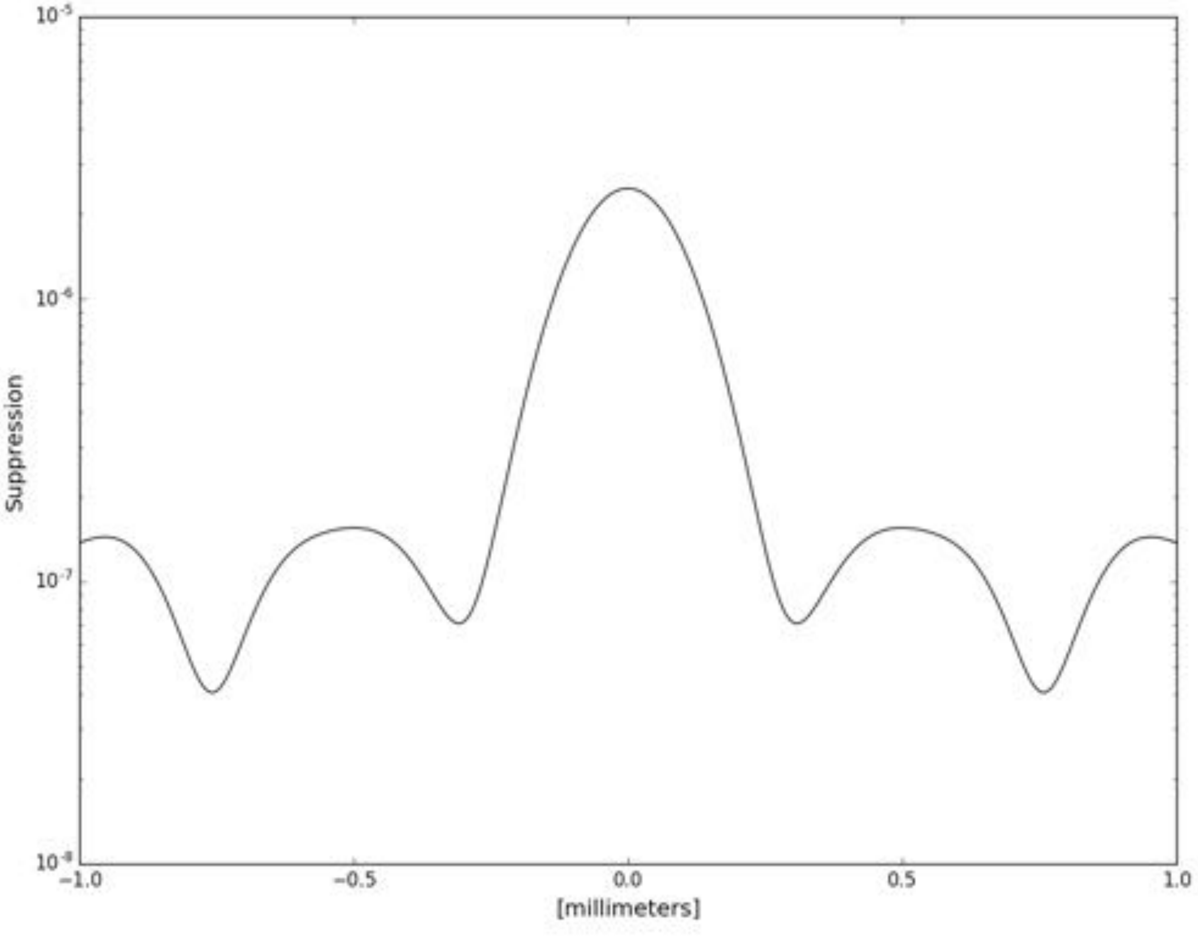

Figure 6.4: Simulation prediction of broadband suppression at the pupil of the NCAR tests. The plot is a cut across the 2 mm square aperture.

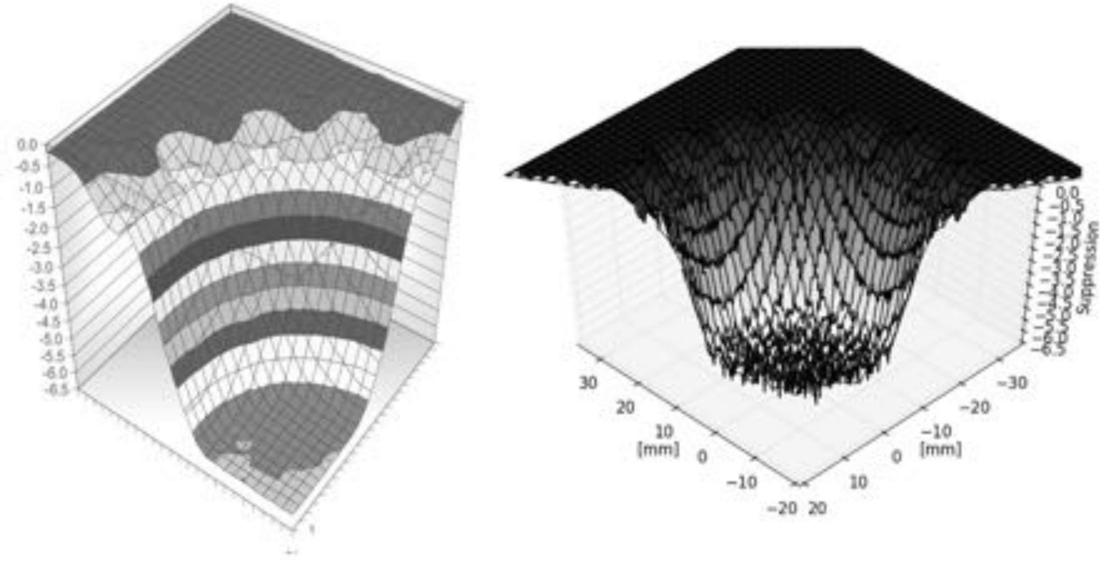

Figure 6.5: The **left** image is Figure 8 from [44] showing the measured suppression in the shadow of the starshade at the NCAR tests. The **right** image is the model prediction of the shadow.

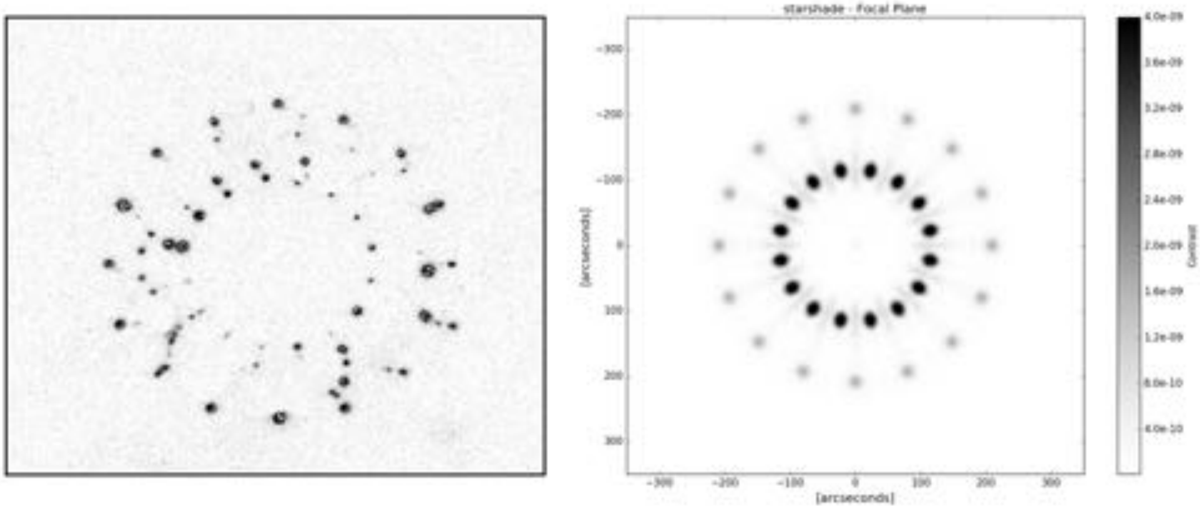

Figure 6.6: The **left** image is Figure 11 from [44] showing the focal plane image of the starshade at the NCAR tests. The **right** image is the model prediction.

periments achieving high contrast with 1/100$^{\text{th}}$-scale starshades. I assisted Northrop on most of these tests, but merely as a pair of hands to help run the different stations. For a more thorough description of the experiment and a presentation of the main results, see [29, 30, 78]. There were two milestones for this TDEM: 1) achieve 10^{-9} contrast on 60 cm starshades and 2) demonstrate agreement between optical models and experimental results. They were able to complete milestone #1 and are still in the process of satisfying milestone # 2, which I will describe below.

6.5.1 Achieving high contrast with 60 cm starshades

The following section will summarize Northrop Grumman's work to achieve high contrast at the dry lake bed. The experiment setup on the dry lake bed can be seen in Figure 6.8, with the optical parameters summarized in Table 6.1. Utilizing the vast expanse and flatness of the Smith Creek dry lake bed in central Nevada (at 6000 ft elevation), a telescope, 60 cm starshade, and extremely bright light source (1 W LED behind a lens) are placed in alignment. The starshade is 1 km from the telescope and the light source is an additional 1 km (2 km in some cases) behind the starshade. Along with the main light source that simulates a star, there are a number of fainter offset light sources to simulate planets. These "planets" vary in brightness from 10^{-5} to 10^{-9} times as bright as the main source. Even with 1 km separation, the Fresnel number is large (∼200) and the contrast is being significantly helped by such.

The same data collection procedures used in the McMath observations (Chapter 8) are used, where long exposures (10 s) are taken of the light source while it is blocked by the starshade and periodic observations of the unblocked source are taken to get a reference brightness. A neutral density filter is needed for the unblocked images as the light source is extremely bright. Similar to our experience at McMath, observations are complicated by atmospheric disturbances. The starshade, telescope, and light source are at most 2 meters above the ground and the light path is subject to an atmospheric ground layer that is strongly varying in temperature.

Unlike McMath, the dominant effect is not turbulent "seeing", rather it is image wander due to atmospheric refraction. The dry lake bed is baked by the sun throughout the day and when the

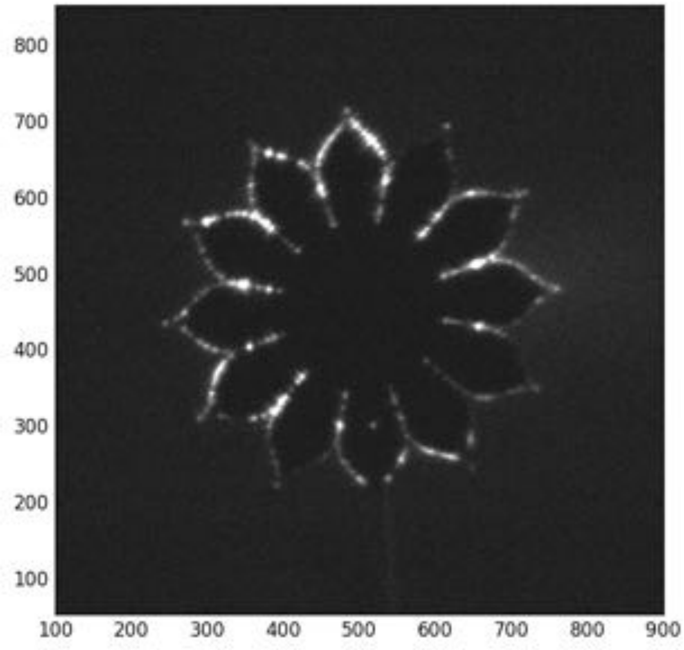

Figure 6.7: Image of a 60 cm diameter starshade at 200 m separation taken during the first dry lake bed test in April 2012. The starshade was laser-cut from plastic and has significant scattering off the edge. This test demonstrated the concept of testing starshades on dry lake beds.


Field Testing 2014/15

THE VALUE OF PERFORMANCE.
NORTHROP GRUMMAN

NASA JPL /
Northrop Grumman
100th Scale
Starshade

Light Sources

7

Approved for public release: NGAS Case 15-1679 dated 8/26/15.

Figure 6.8: Images from the Northrop Grumman-led project field testing starshades on dry lake beds. The telescope is circled in **yellow**, the 60 cm starshade, located 1 km away is circled in **blue**, and the light source, located an additional 1 km away is circled in **green**. (Taken from [90])

sun goes down, the dry desert air quickly cools, creating a strong temperature gradient between the desert floor and the air in the first few meters above. This gradient causes the apparent position of the light source to wander over long distances throughout the night. At some points, we have to raise the starshade an additional 2 meters from its nominal position to correct for that motion. Over the course of a 10 s exposure (needed to overcome the readout noise of the detector), the light can move from behind the starshade and ruin the image. This effect will also be important when doing model comparison as the contrast is steeply dependent on the alignment.

The other main limitation to this experiment is forward scattering off dust in the atmosphere. This dust generates a uniform background around the starshade that contributes photon noise and sets the noise floor for the best contrast we can achieve. They attempt to model and subtract the dust, but this becomes difficult to disentangle at the edge of the starshade. The best contrast achieved in these tests was obtained with a combination of 285 10 second dust subtracted images. The contrast was measured by calculating the 3σ errors in 20 arcsecond boxes at different radii outside the starshade. The best contrast achieved at the edge of the starshade is $7.31 \times 10^{-10} \pm 2.40 \times 10^{-10}$ and is shown in Figure 6.9 [30]. The dominant source of error in the contrast calculation is due to scintillation of the unblocked source.

6.5.2 Testing flawed starshade shapes

To explore the sensitivities of different manufacturing flaws to the starshade performance and how our models are able to predict them, we tested a number of starshades with intentional flaws built into the shape. These flaws are of the classes similar to what we might expect from a deployable starshade in flight. The flaws also provide a strong signal above the dust background to provide a highly significant reference point to compare our model predictions to. The base starshade shape is a hypergaussian design ($a = b = 12$ cm, $n = 6$, $r_{max} = 0.29$ cm) and the different flaws we tested are:

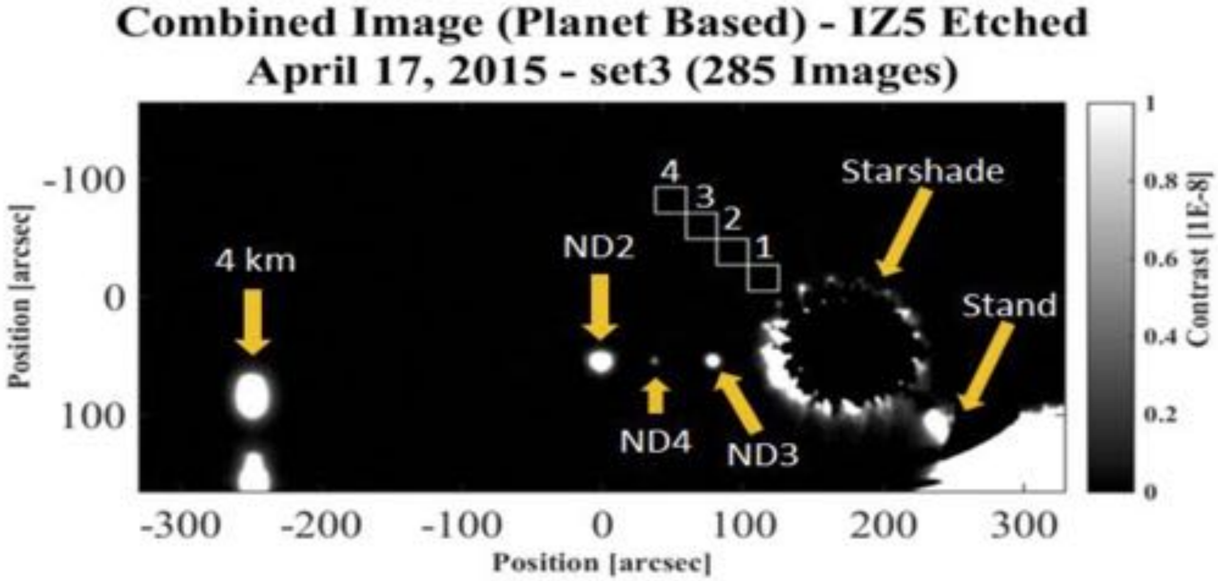

Figure 6.9: Image of the best contrast achieved, 7×10^{-10} at 60″ IWA (box 1), during Northrop Grumman's dry lake bed tests. The far left light is 4 km away and is for monitoring the atmosphere, the ND2, ND3, ND4 lights are dim light sources near the main source to simulate planets. Their relative brightnesses to the main source are: 8.65×10^{-7}, 9.74×10^{-8}, 6.09×10^{-9}, respectively. (Taken from Figure 4-3 of [30])

- Displaced Edges
  - Figure 6.10
  - A 14 mm long section of the petal is displaced normally from the petal edge.
- Petal Clocking
  - Figure 6.11
  - A petal is shifted in plane linearly with radius. The clocking angle is measured at the tip of the petal.
- Shrunk Petals
  - Figure 6.12
  - The size of the entire petal is shrunk by a given percentage.
- Sines
  - Figure 6.13
  - Sine waves of a given amplitude and frequency are built into the edge of the petal.
- Truncated Valleys
  - Figure 6.14
  - Rather than extend to the radius of the inner disk, the valleys at which the petals join are truncated at a larger radius.
- Clipped Tips
  - Figure 6.15
  - The tips of the petals are prematurely truncated at a smaller radius.

For each starshade, four flaws with increasing amplitude are built into the petals evenly clocked around the starshade. The amplitude of the flaws are presented in Table 6.2.

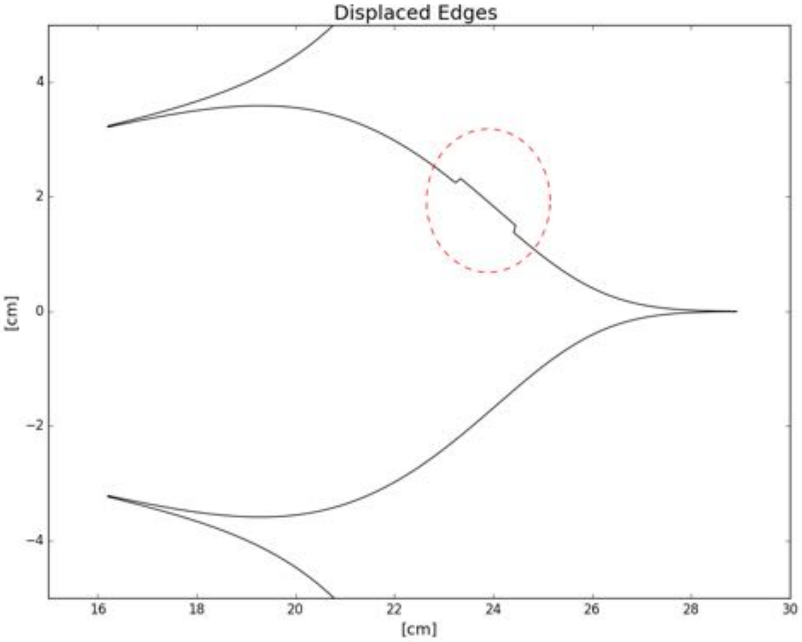

Figure 6.10: “Displaced Edges”. A section of the petal edge is jutted out normally to the petal. The quoted error amplitude is how far out it juts.

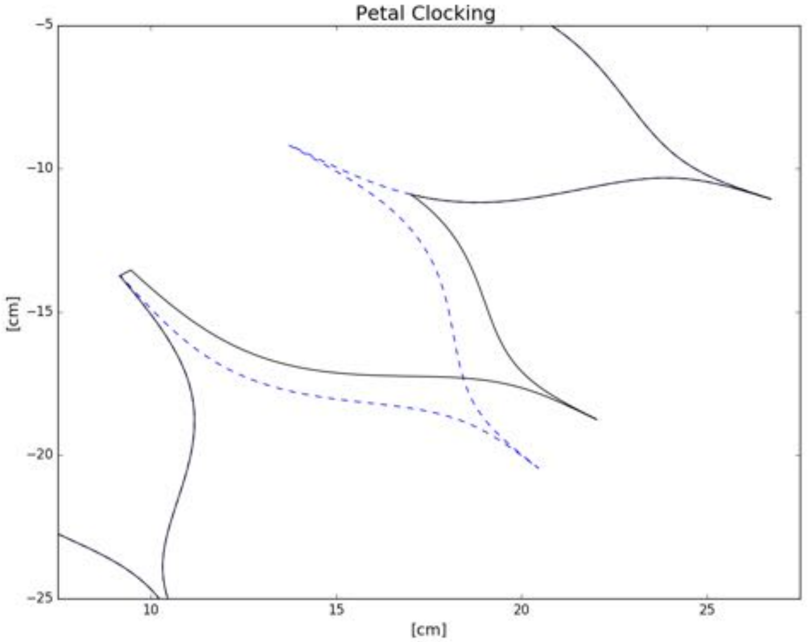

Figure 6.11: “Petal Clocking”. The valleys are fixed and the petal is clocked at angle that increases linearly with radius. The quoted error amplitude is the offset angle at the petal tip.

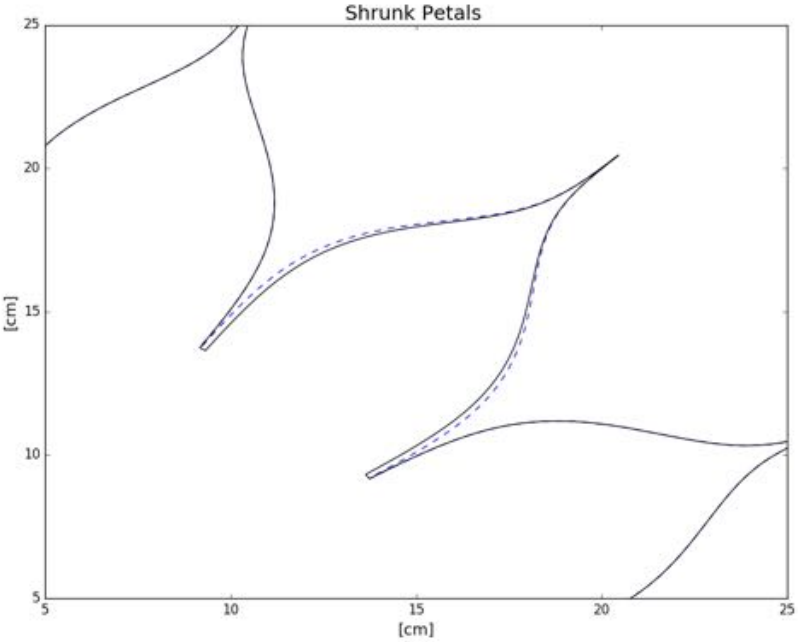

Figure 6.12: “Shrunk Petals”. The entire petal is shrunk by a certain percentage (the quoted amplitude).

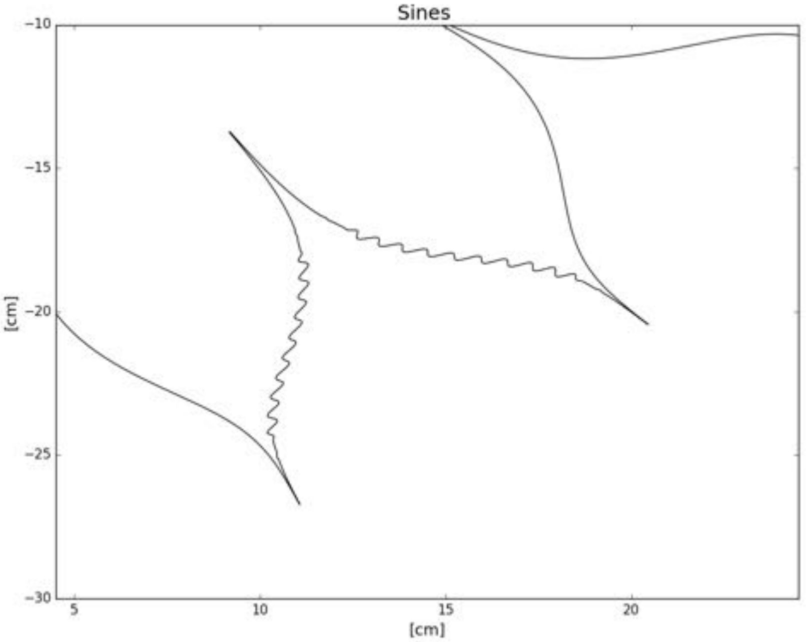

Figure 6.13: “Sines”. Sine waves are built into the petal edge. The quoted error is the spatial frequency across the petal edge (N) and the amplitude of the sine wave.

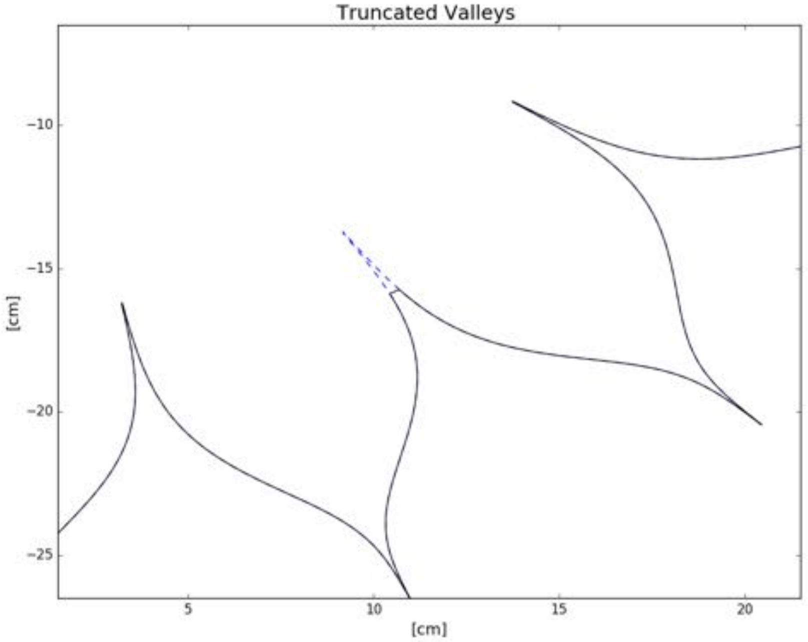

Figure 6.14: “Truncated Valleys”. Rather than extend to the radius of the inner disk, the valleys at which the petals join are truncated at a larger radius (the quoted amplitude).

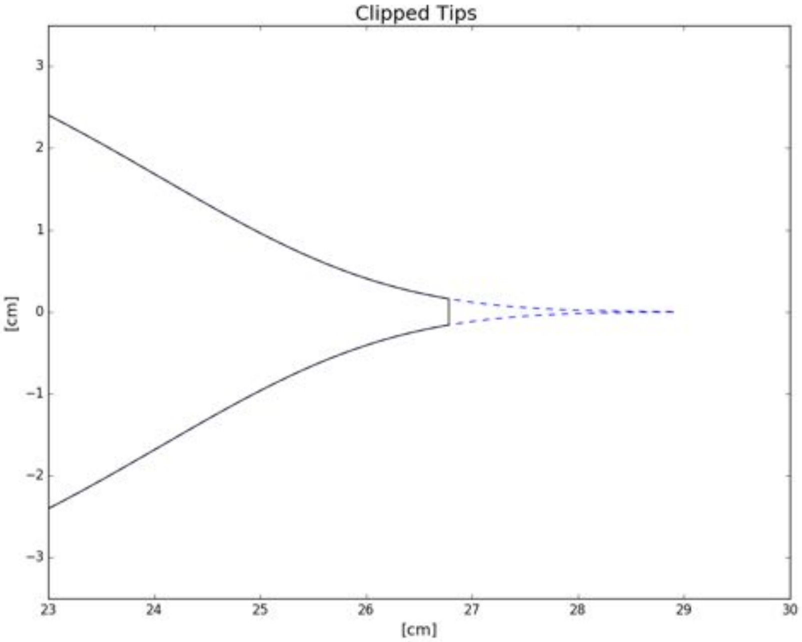

Figure 6.15: “Clipped Tips”. The tips of the petals are prematurely truncated at a smaller radius (the quoted amplitude).

Error Type	**Error # 1 Amp**	**Error # 2 Amp**	**Error # 3 Amp**	**Error # 4 Amp**
Displaced Edges	1.2 mm	0.9 mm	0.6 mm	0.3 mm
Petal Clocking	0.08 radians	0.06 radians	0.04 radians	0.02 radians
Shrunk Petal	-5%	-4%	-3%	-2%
Sines (freq,amp)	N=25, 0.15 cm	N=60, 0.1 cm	N=60, 0.15 cm	N=25, 0.1 cm
Truncated Valleys	0.175 m	0.180 m	0.185 m	0.190 m
Clipped Tips	0.2831 m	0.2781 m	0.2731 m	0.2681 m

Table 6.2: This table shows the amplitudes of the flaws that were intentionally manufactured into each starshade shape. The amplitude of the flaw is generally decreasing with Error #. Images showing these flaws built into the shape are shown in Figures 6.10 - 6.15. (Replicated from Table 5-2 of [30]).

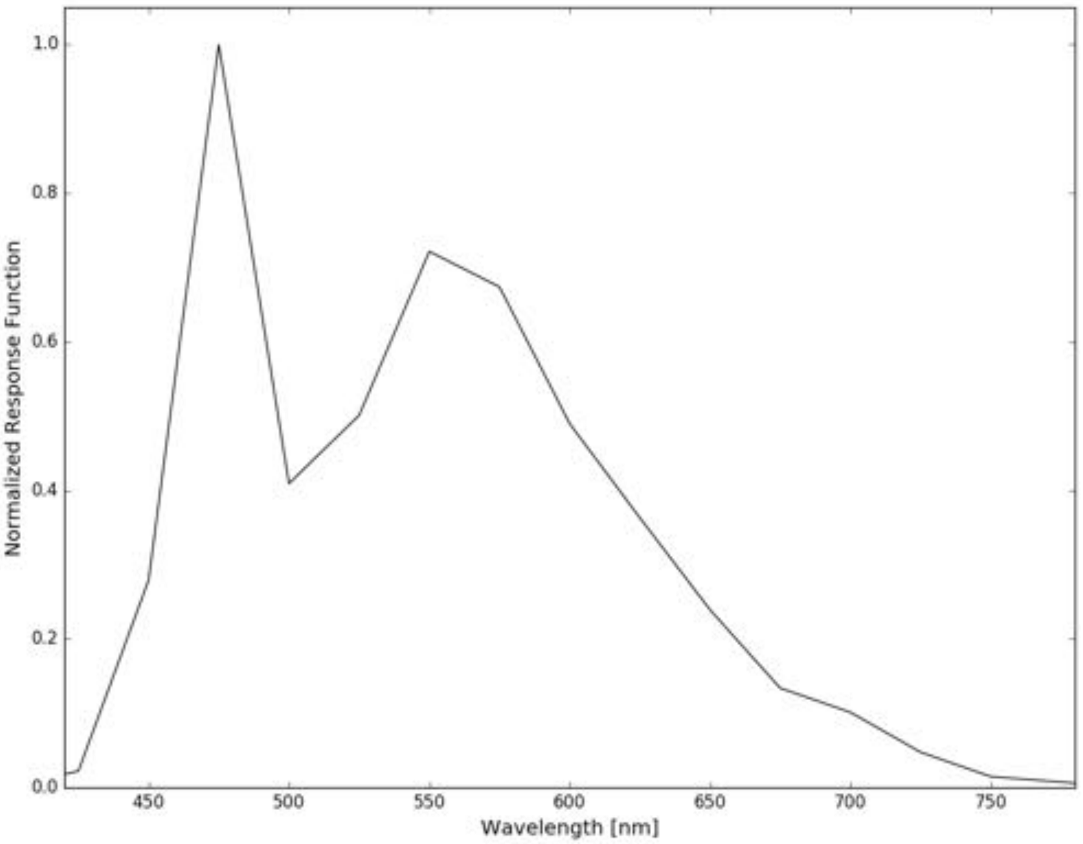

Figure 6.16: The normalized wavelength response function for the telescope and LED that simulated the bright star in the dry lake bed tests.

6.5.3 Comparison of model predictions to field data

The following results contain data taken in the field by the Northrop Grumman team in October 2015 at the Smith Creek lake bed in Nevada and were obtained with the parameters of Table 6.1 in the configuration with $F_2 = 2$ km. These data were produced by Northrop Grumman[1].

The model predictions I calculated were on a 512 x 512 grid sampling the telescope's aperture with 90,000 points sampled around the shape of the occulters. The occulter shapes were generated using measurements of the as-built starshades. Focal plane images were generated with a pixel size of 0.55 arcseconds for 20 wavelengths evenly spaced between 425 nm - 775 nm and were incoherently combined with the intensities at different wavelengths weighted by the measured spectral response of the LED-telescope-detector shown in Figure 6.16.

The expected contrast of the nominal hypergaussian shape measured at the petal valleys and petal tips is 1.3×10^{-7} and 2.1×10^{-9}, respectively. The comparisons between the model predictions and measured results are shown in Figure 6.17 and are expressed as ratios in Figure 6.18. The contrast values were calculated by integrating over each flaw with a photometric aperture of $5''$ - $10''$ across and dividing by the total brightness of the unblocked source integrated over the same sized aperture.

Side by side comparison of the modeled images and the images from the field are shown in Figures 6.19-6.24; the comparisons are meant to be of qualitative nature only. The images are oriented such that the brightest flaw is located in the upper left quadrant of the image, and flaws decrease in brightness as they go clockwise around the starshade. Log-scaled model images are provided in Figure 6.25.

This comparison of the models to the data is a first round attempt and there is still work to be done to bring the two into agreement. However, comparing to the status this was in previously, we are making large strides to reach agreement. We have the right slope in relative brightness between flaws for most of the shapes and we are within an order of magnitude for most. I believe the main difficulties in reaching agreement between the two are modeling the exact shape that was

---

[1] Approved for public release; NGAS Case 16-2294 dated 22 November 2016.

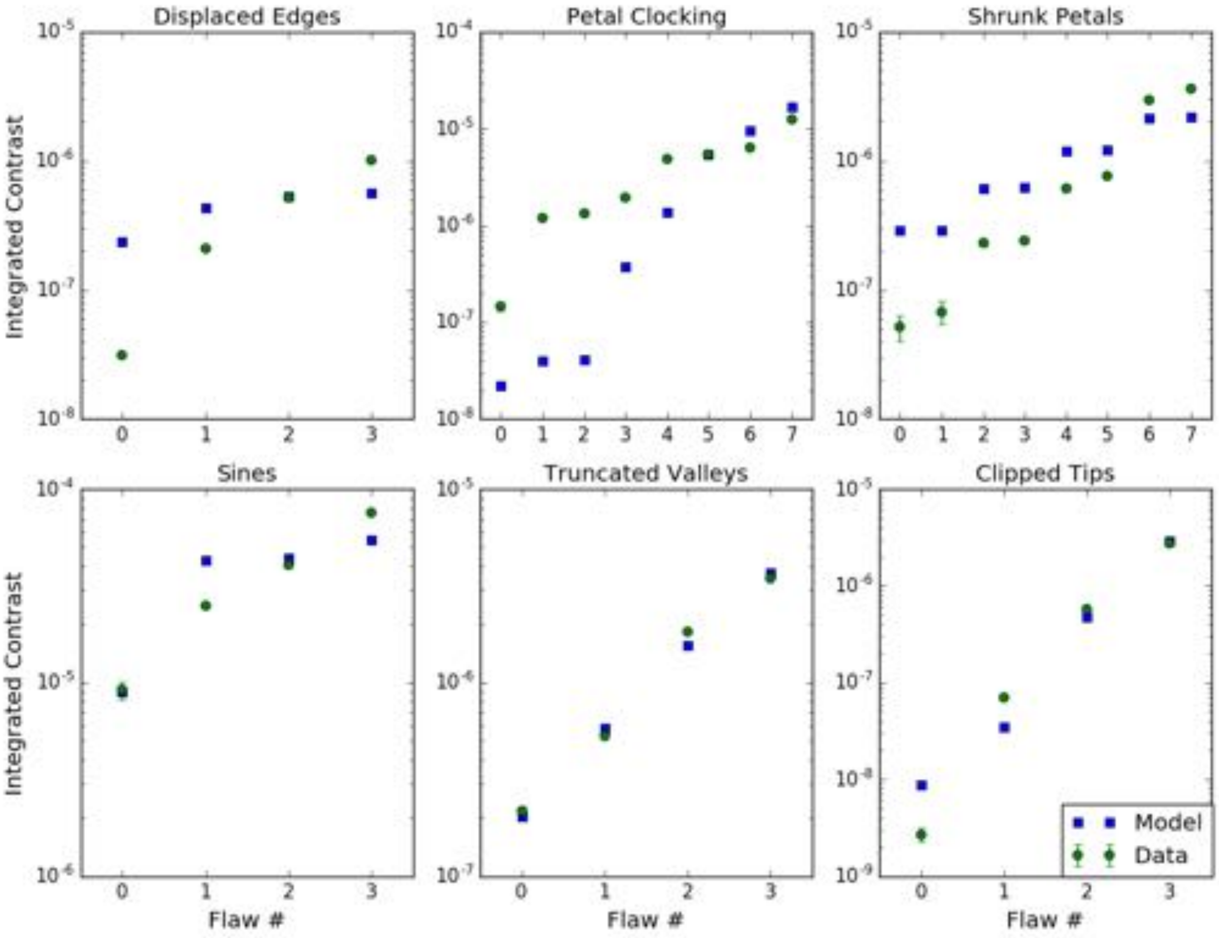

Figure 6.17: Comparison of the latest dry lake bed results (obtained by NG) and models (calculated by the author). The contrast was calculated by summing over each flaw with a photometric aperture of 5″ - 10″ across and dividing by the total brightness of the unblocked source integrated over the same sized aperture. In this test, the flight source was 2 km from the starshade. The field data were produced by Northrop Grumman[1].

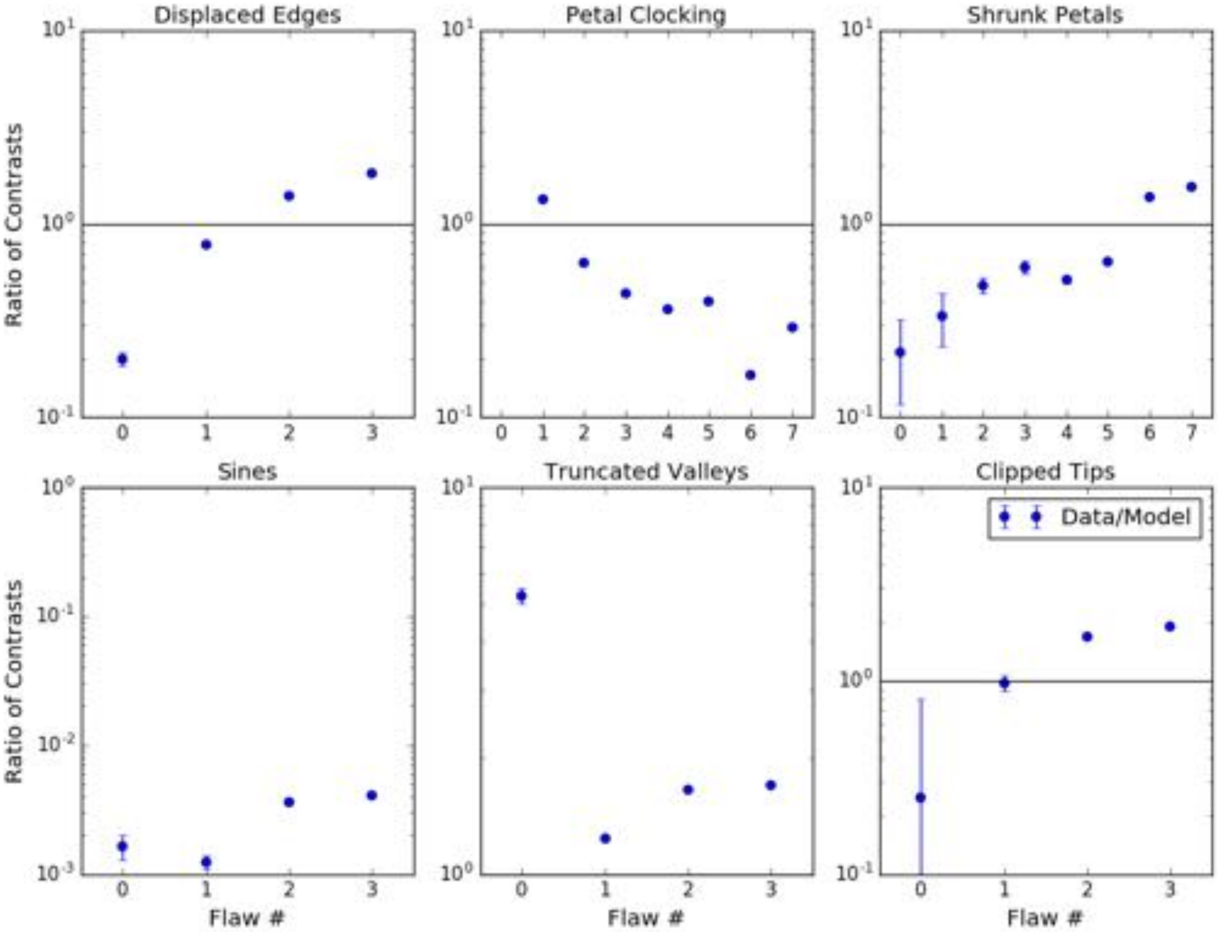

Figure 6.18: Same results as Figure 6.17, but expressed as a ratio of the data over the model. The field data data were produced by Northrop Grumman[1].

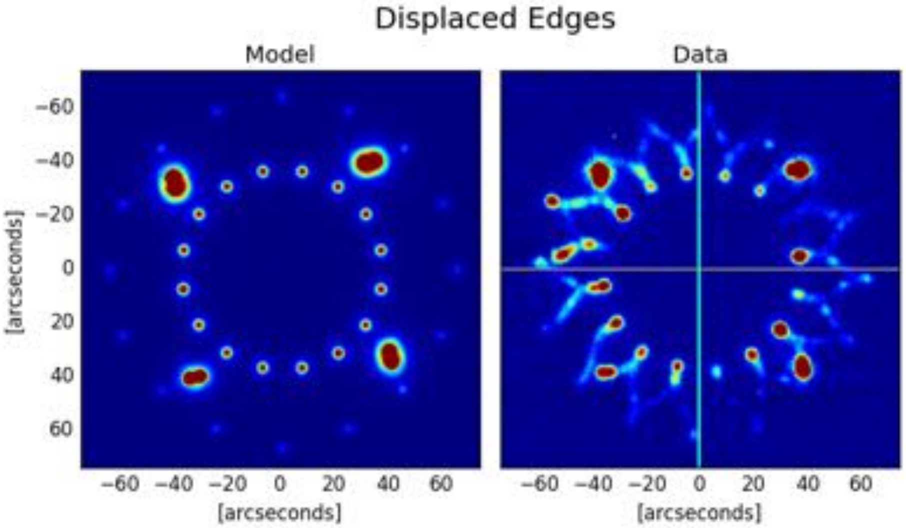

Figure 6.19: “Displaced Edges”. The model on the **left**, the field data (produced by Northrop Grumman[1]) on the **right**

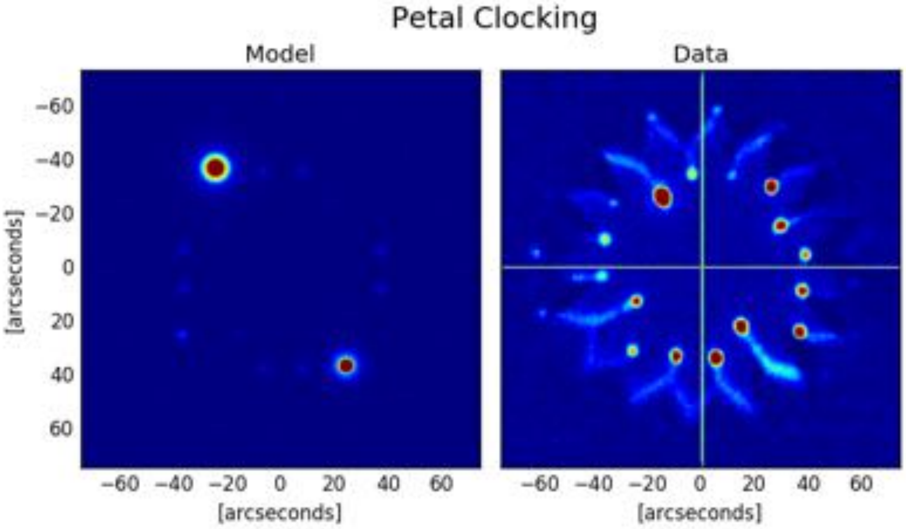

Figure 6.20: “Petal Clocking”. The model on the **left**, the field data (produced by Northrop Grumman[1]) on the **right**

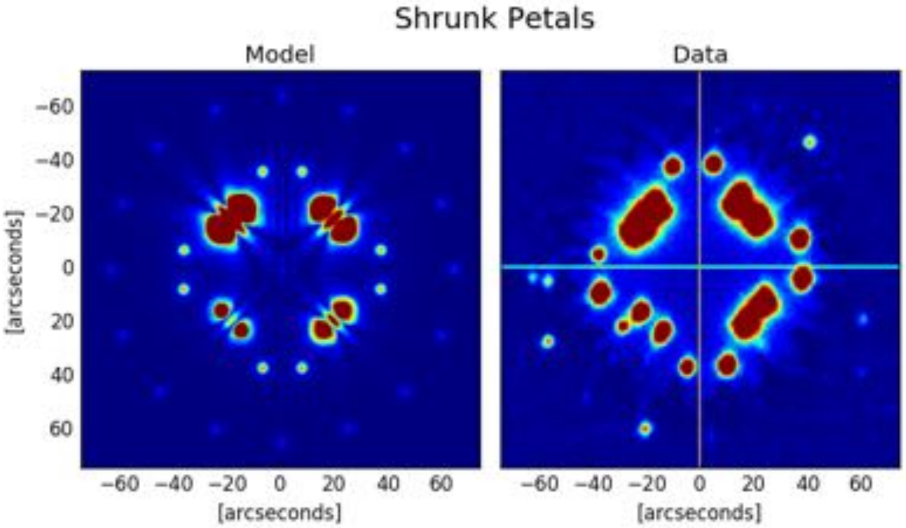

Figure 6.21: “Shrunk Petals”. The model on the **left**, the field data (produced by Northrop Grumman[1]) on the **right**

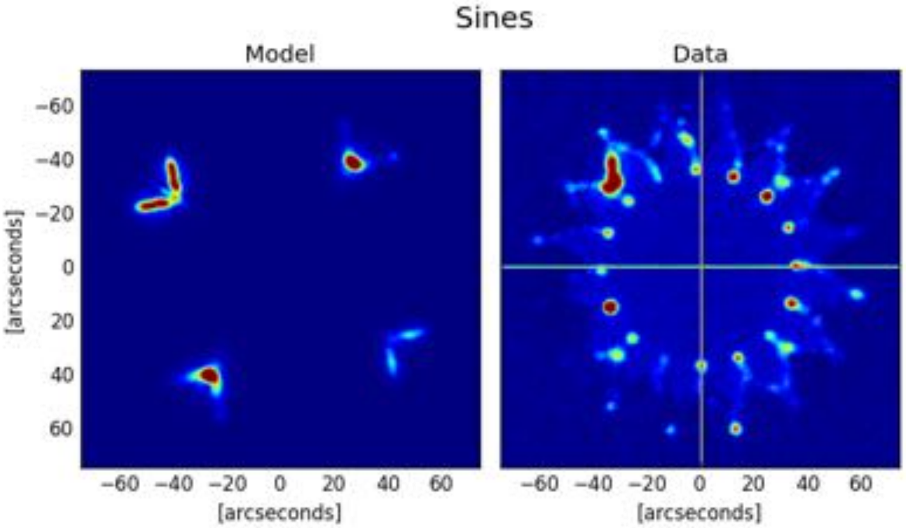

Figure 6.22: “Sines”. The model on the **left**, the field data (produced by Northrop Grumman[1]) on the **right**

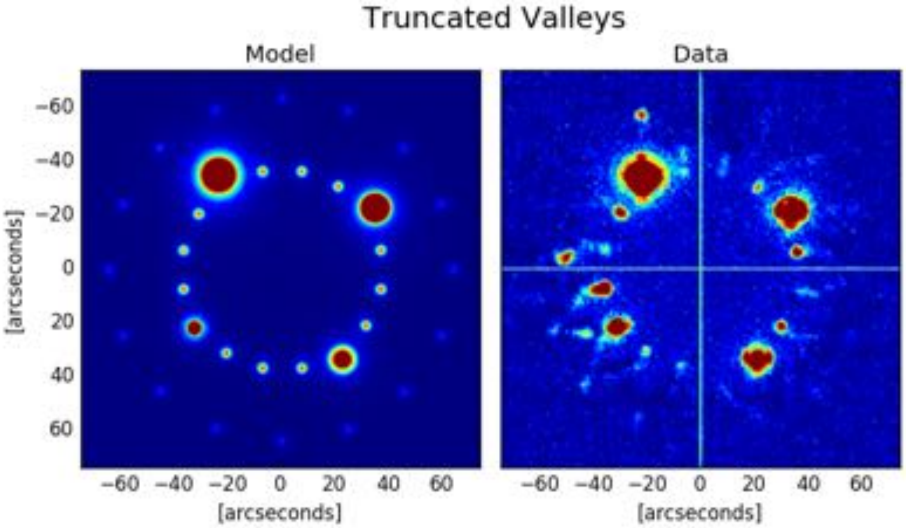

Figure 6.23: “Truncated Valleys”. The model on the **left**, the field data (produced by Northrop Grumman[1]) on the **right**

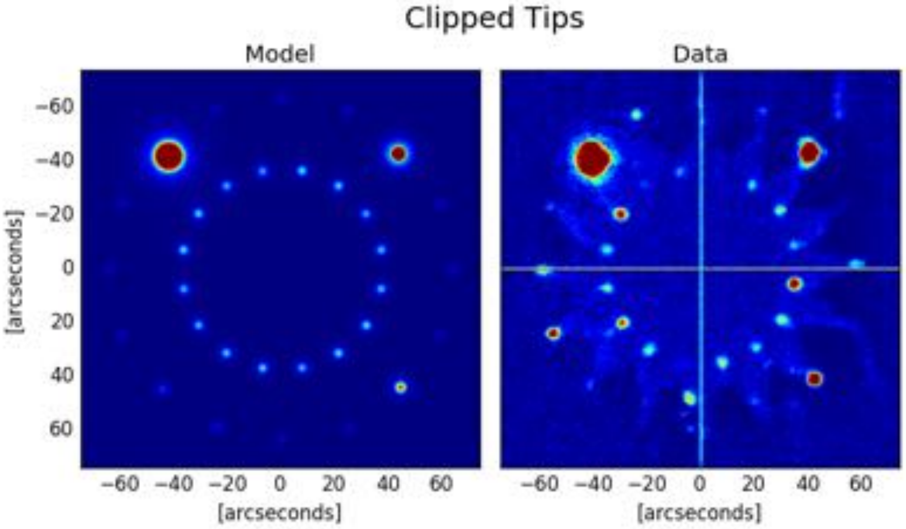

Figure 6.24: “Clipped Tips”. The model on the **left**, the field data (produced by Northrop Grumman[1]) on the **right**

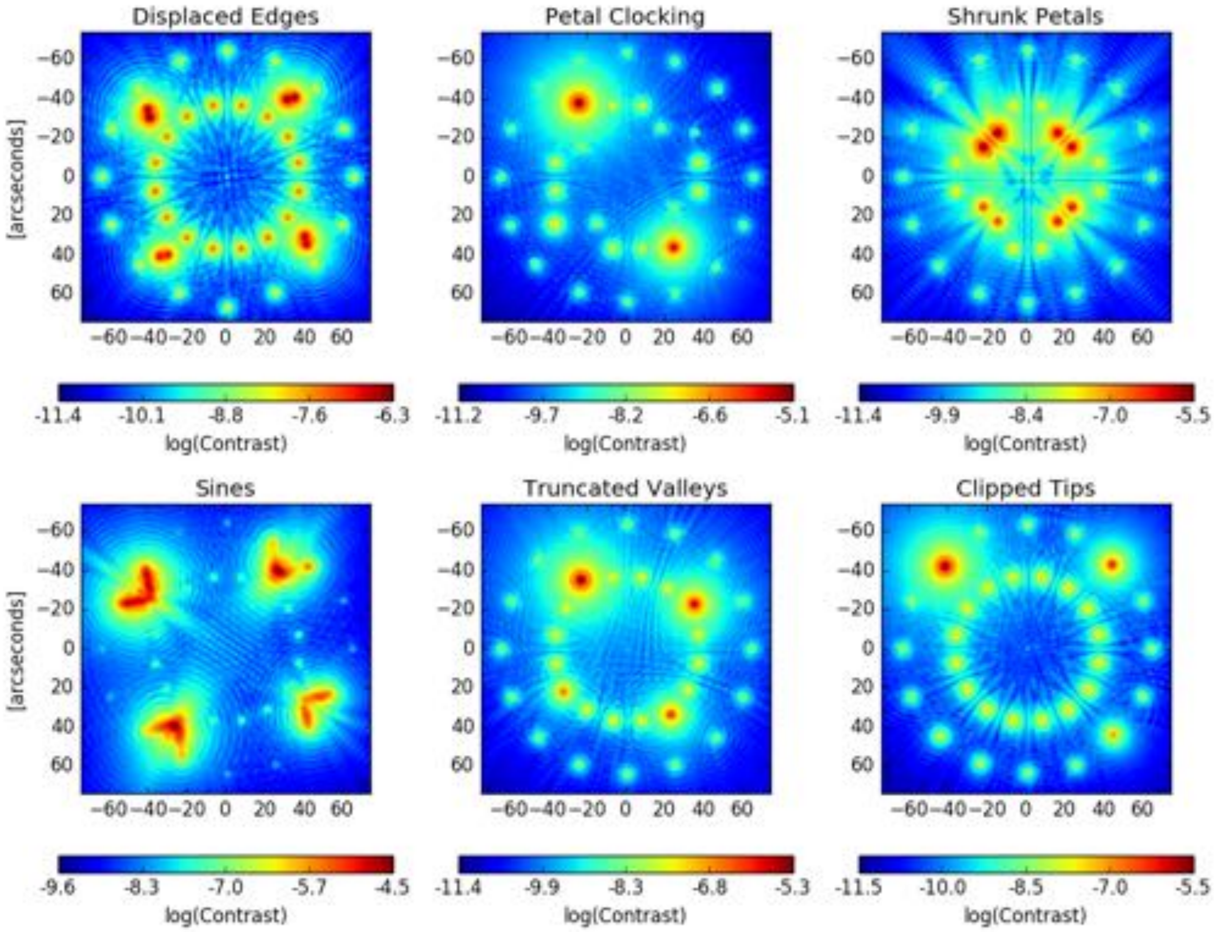

Figure 6.25: Log-scaled model images of all flawed shapes

manufactured, subtracting the background dust, and measuring an accurate value of the unblocked source to convert to a contrast measurement.

6.6 Upcoming Princeton Tests

In the plan to advance the optical modeling of starshades to TRL 5, there is a current TDEM study led by Jeremy Kasdin at Princeton University to achieve 10^{-9} suppression in the lab. This experiment uses a 1 inch starshade (Figure 5.3) at 50 m separation and with 633 nm laser light to reach a flight-like Fresnel number. The beam line is contained in 1 m diameter plastic tubing (not evacuated) to seal the testbed from stray light and dust and to help stabilize the atmosphere. Diffraction from the finite extent of the tube is suppressed by an apodization around the outer edge of the mask (essentially an inverse starshade). This outer mask also allows the fragile silicon mask to be supported by struts. More details on the experiment can be found in [39] and [76].

As this experiment is in the process of being constructed, we can use the power of our optical models to predict the performance of the experiment, identify potential risks, set tolerance limits, and ultimately help drive the design of the experiment. The contrast and suppression predicted for an ideal mask is shown in Figure 6.26, with the peaks of both at $\sim 10^{-10}$.

The starshade mask to be used is designed specifically for this experiment. A linear model of the apodization function, subject to various size and performance constraints, is used to minimize suppression over a specified aperture [76]. This optimization scheme can generate a mask that achieves high suppression, but is sensitive to perturbations in the experiment. The following sections describe the results of modeling the testbed and potential risks we have identified that could prevent the experiment from reaching its milestone of 10^{-9} suppression.

6.6.1 Avoiding wavelength-sized features

As mentioned in this chapter and in Chapter 2, all modeling and studies of starshade performance uses the assumption that scalar diffraction theory is sufficient to explain the optical physics of the starshade. A major motivation for doing optical demonstrations of starshades and model

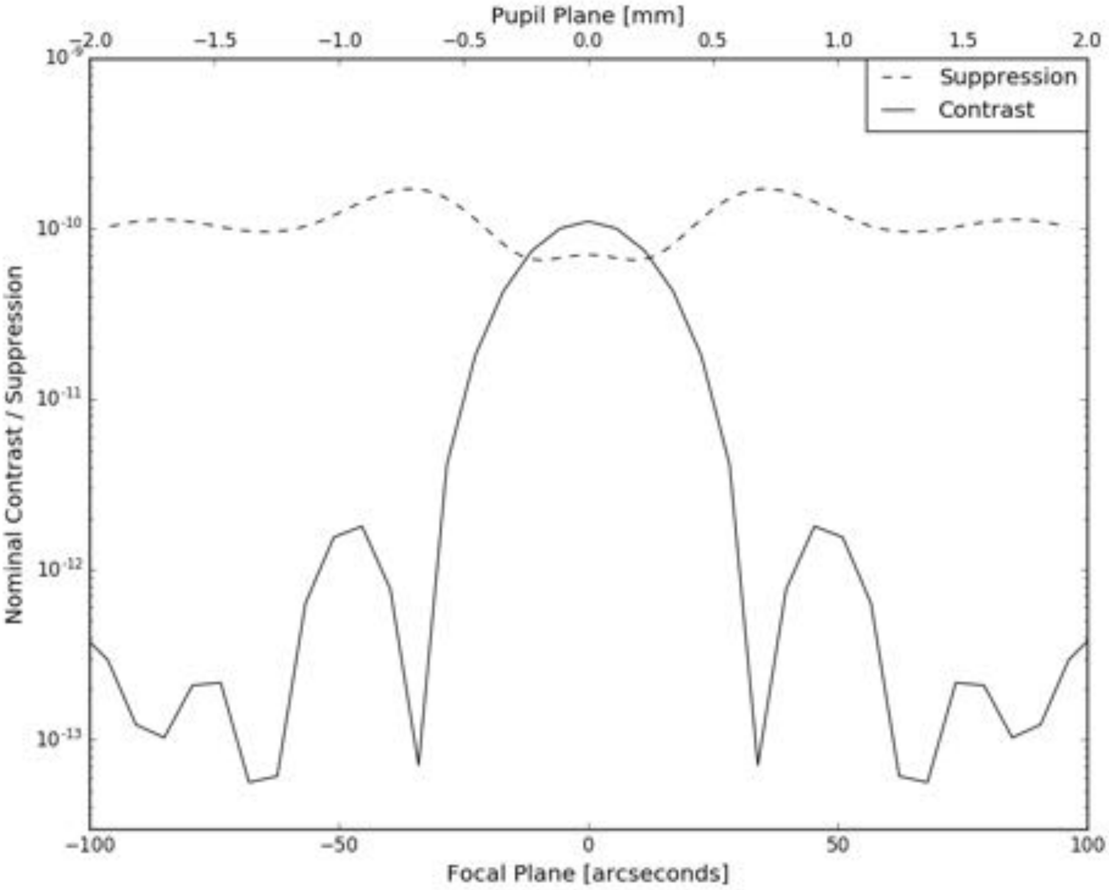

Figure 6.26: Model predictions for the suppression and contrast to be achieved in the Princeton tests, assuming a perfectly built starshade. The suppression and contrast are both at 10^{-10}.

validation experiments is to verify this assumption is true. This means we must avoid building features into the starshade that are sizes on the order of the wavelength, where scalar diffraction is known to break down. A valley between the petals that is less than a few microns could act as a waveguide to propagate photons through more efficiently. Or polarization of the light can couple with the surface charge density on the mask to remove energy from the beam, in which case vector diffraction is needed to explain the physics. Even if our model agrees with the experiment, if we are not testing the appropriate physics, our model validation is irrelevant. The current design of the mask has valleys that go down to 0.25 μm widths, which makes it difficult to squeeze a 0.633 μm photon through. We have voiced a concern over this and the mask is being redesigned to limit the minimum feature size to 7.5 μm.

6.6.2 Starshade manufacturing

The starshade mask is etched out of 25 μm thick silicon wafer by a direct write process at JPL's Micro Devices Laboratory. This process can etch the silicon wafer to a claimed 0.25 μm precision, but the manufacturing is a delicate process and there are occasional errors that get built into the shape. The mask for the latest design was examined under a microscope and all defects (either an excess or deficit in material) down to 4 μm were recorded. We added these defects to the nominal occulter design and modeled the performance. The resultant suppression compared to the nominal design is shown in Figure 6.28, where we find that the peak suppression rises slightly above 10^{-9}. If a few of these defects are mitigated in the next manufacturing process and no new defects arise, the suppression should be sufficient.

While the etching process has a precision of 0.25 μm, its overall accuracy is not as good and there is a possibility that a mask is over- or under-etched so that the mask has the correct shape, but with a multiplicative size difference. We modeled values of over- and under-etch of ± 0.1 μm, ± 0.5 μm, and ± 1 μm and found that this has by far the largest effect on the suppression. Figure 6.27 shows that with even 0.1 μm of etching error leads to an order of magnitude degradation in the suppression. A constant size difference on the mask is the same as moving the starshade relative to the telescope, or changing the wavelength; we are operating at a different Fresnel number. So just as the suppression is sensitive to changes in the wavelength (Figure 6.31), any deviation from the nominal Fresnel number changes the size of the apodization features on the mask relative to the Fresnel zone widths and they are no longer able to properly suppress the light.

Finally, we modeled a random error in the etching process by giving a random over- or under-etch of ± 0.1 μm, ± 0.5 μm, and ± 1 μm to each point on the mask, with the error being constant over either a 4 μm or 20 μm distance. Larger coherence scales of the errors are more detrimental as this approaches the case where there is a constant multiplicative size difference. These results are shown in Figure 6.27 and all results from manufacturing errors are summarized in Figure 6.28.

6.6.3 Atmosphere induced wavefront errors

The entire experiment is in a light-tight 1 m diameter tube, but is still at nominal atmospheric pressure. We investigate what the atmospheric conditions could be inside the tube and if they will cause significant wavefront errors, addressing the concern that these experiments need to be done in vacuum. With the dimensions of the experiment, using Equation 5.28, we find that a WFE of 10 nm with $n_s > 7$ modes or a WFE of 100 nm with $n_s > 2$ modes will cause outside light to be scattered into our aperture. Simulated results of this are shown in Figure 6.29. Vibrations in the tube can induce standing waves across the tube. If the tube is vibrating at a harmonic (N) of its natural frequency, we expect to excite modes in the air as,

$$n_s = \frac{N}{\pi} \frac{c_{s,\mathrm{tube}}}{c_{s,\mathrm{air}}} \tag{6.1}$$

where c_s are the corresponding sound speeds. For the properties of the tube, this corresponds to $n_s \sim 6N$, meaning oscillations at the natural frequency of the tube can induce modes in the air to scatter light into our aperture and ruin the required 10^{-9} suppression.

If there is sufficient air circulation in the tube, the damaging wavefront errors can come from a turbulent atmosphere. For a 1 m diameter tube, the air flow becomes turbulent (the Reynolds number, Re, > 2000) for an air velocity of only 3 cm/s. This air flow can be generated by a

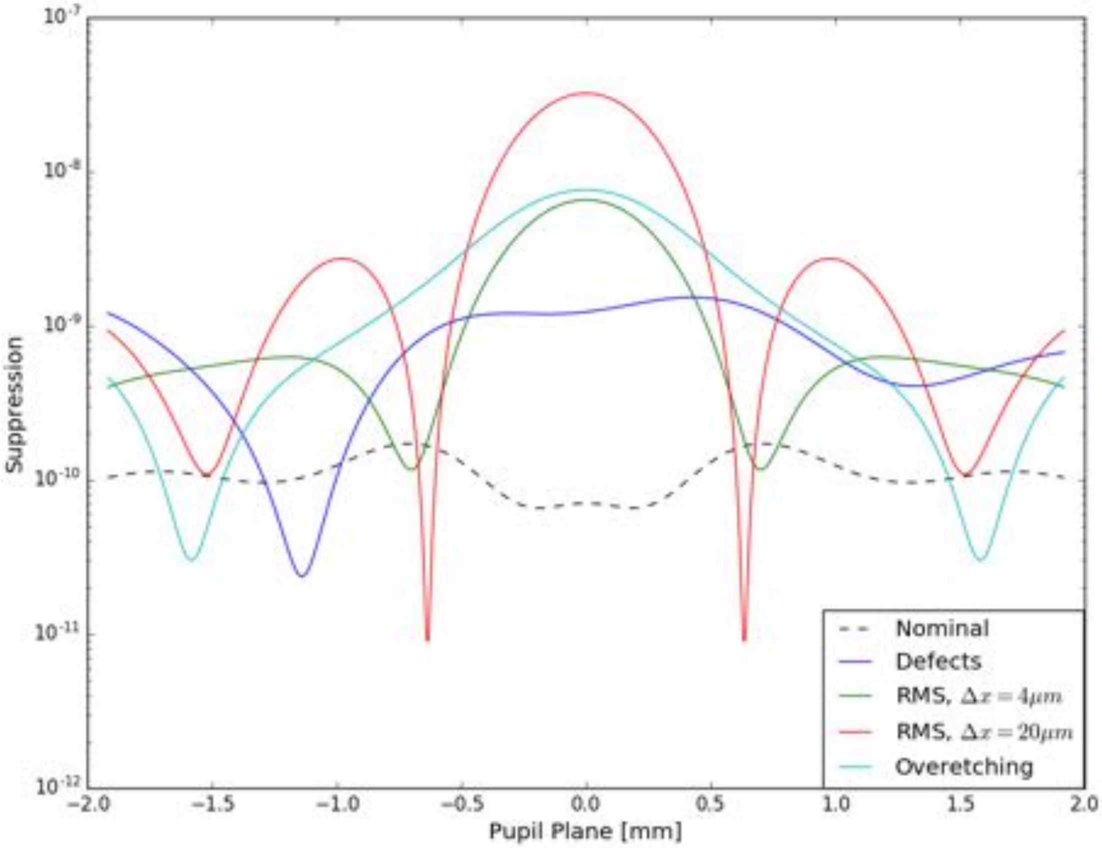

Figure 6.27: Modeled suppression across the pupil in the Princeton testbed for a number of different manufacturing flaws. The "Defects" model includes all the major defects measured on the mask built at JPL. "RMS" models are random errors of 0.1 μm added normally to the edge of the petal with a coherence scale given by Δx. The "Over-etching" model is the nominal shape that is 0.1 μm smaller (in the normal direction) over the entire mask. We no longer achieve 10^{-9} suppression for the RMS or over-etching cases, but are fine for the measured defects.

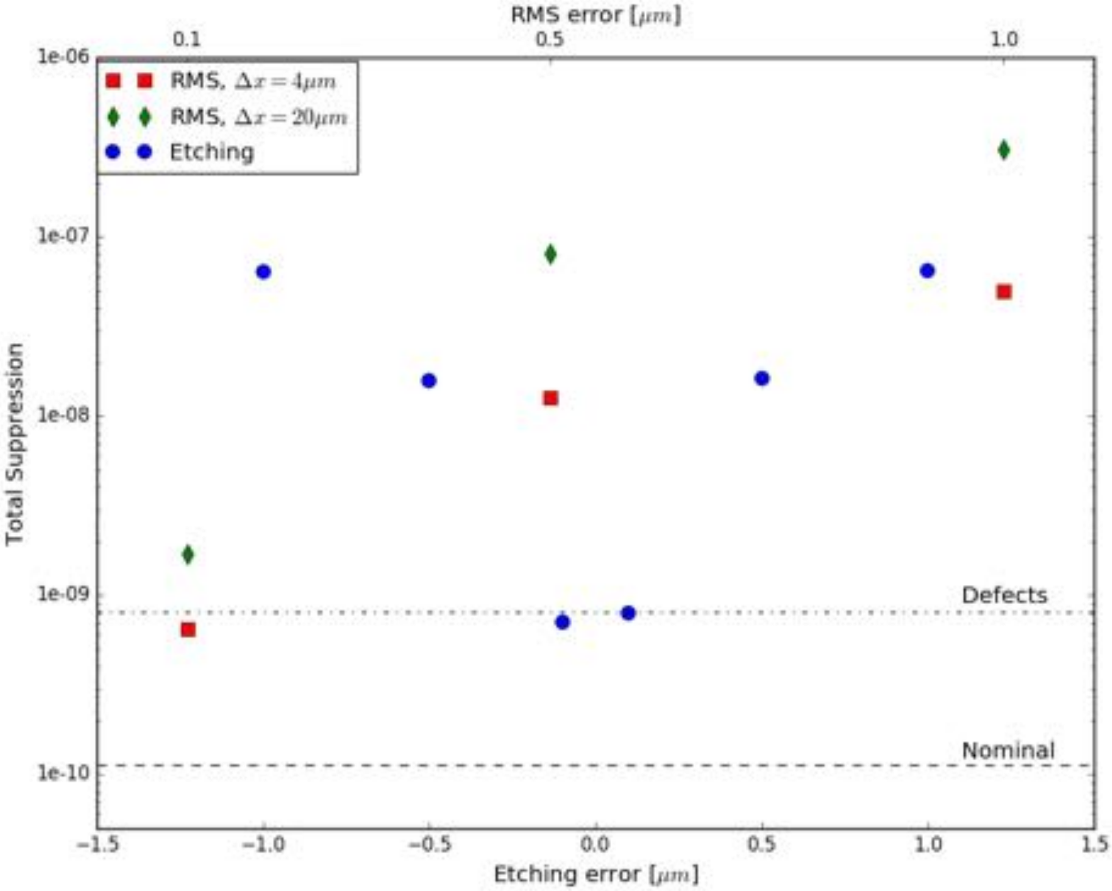

Figure 6.28: The total integrated suppression calculated by summing over the entire aperture, as a function of manufacturing error size. The types of errors are described in Figure 6.27 with positive etching error meaning over-etching.

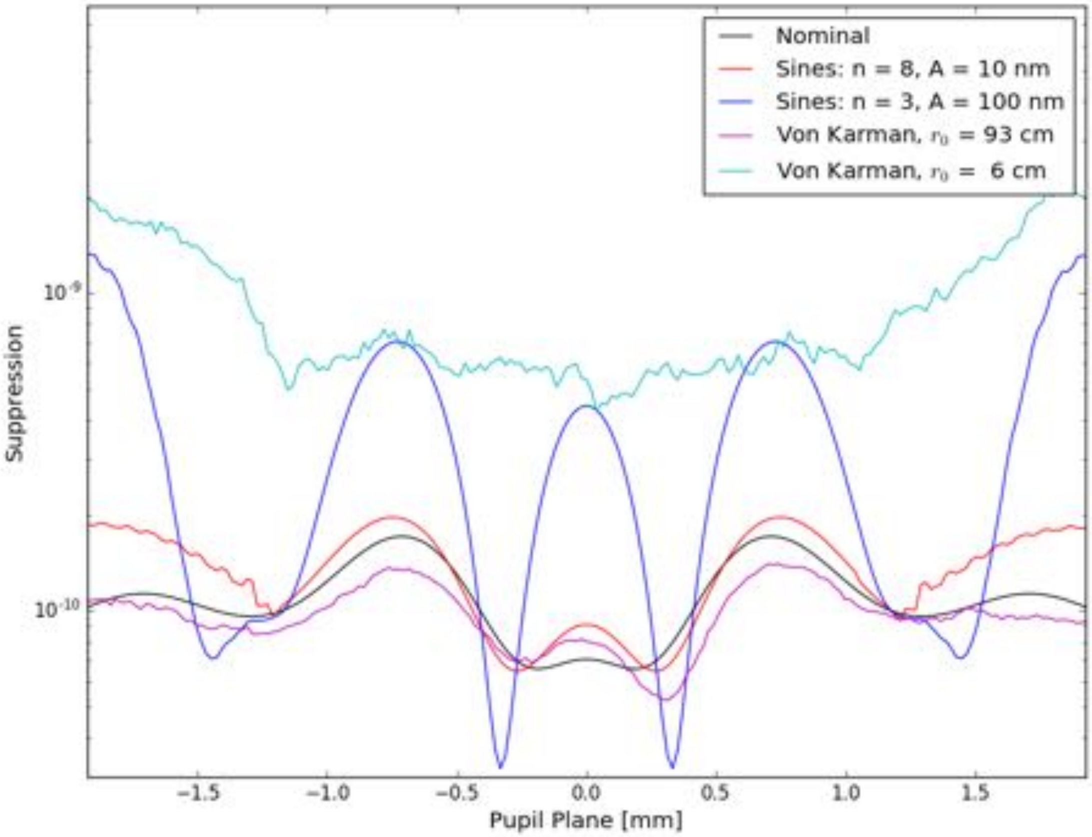

Figure 6.29: The modeled suppression in the Princeton testbed as a function of atmospheric wavefront error incident on the mask. The number of sine modes across the mask is given by n and the amplitude of the error is given by A. The atmospheric turbulence models assume a von Karman power spectrum of turbulence of a certain Fried parameter r_0. All models just barely skirt the 10^{-9} suppression limit.

differential pressure of 4 PSI between the ends of the tube. The expected seeing cell sizes for refractive index structure constants of $C_n^2 = 10^{-15}$ m$^{-2/3}$ (light turbulence) and $C_n^2 = 10^{-13}$ m$^{-2/3}$ (strong turbulence) over the 27 m between light source and starshade are $r_0 \sim 93$ cm and $r_0 \sim 6$ cm, respectively. With a finite outer scale set by the tube diameter, we use the von Kármán turbulence spectrum given in Equation 6.2, which has the same dependence on spatial frequency as the Kolmogorov spectrum, but is modified by the lowest spatial frequency (κ_0). The results of applying atmospheric wavefront errors are shown in Figure 6.29. For a modest periodic wavefront error of 100 nm, or strong turbulence of $C_n^2 = 10^{-13}$ m$^{-2/3}$, the suppression rises above our allowed limit of 10^{-9}. This is strong turbulence, but is not uncommon for propagation through ground layer undergoing diurnal temperature swings. It is likely that the short propagation and relatively benign atmosphere of this testbed will not generate that strength of turbulence, but that remains to be seen.

$$\Phi\left(\kappa\right) = 0.023 \frac{\left|\kappa^2 + \kappa_0^2\right|^{-11/6}}{r_0^{5/3}} \tag{6.2}$$

6.6.4 Misalignment

The shadow across the aperture is shown in Figure 6.30, with the aperture size marked by the vertical lines. There is only about 0.5 mm of allowance for misalignment before the suppression degrades beyond 10^{-9}. Simple tip-tilt aberrations caused by a temperature gradient between the sides of the tube, or flexing in the tube due to thermal expansion, can shift the shadow off the aperture. A 2 arcsecond tilt at the mask can shift the shadow beyond the allowable limit.

6.6.5 Suppression from outer apodization function

These experiments are meant to demonstrate that we understand the physics of the starshade and to instill confidence that a full scale starshade will perform as we expect. In NASA's definition of TRLs, as you reach higher TRLs, you need to test higher fidelity prototypes that match the fit, form, and function of the full-scale technology. This means you must make your prototype as representative of the flight design as possible. I argue that the suppression from the outer apodization

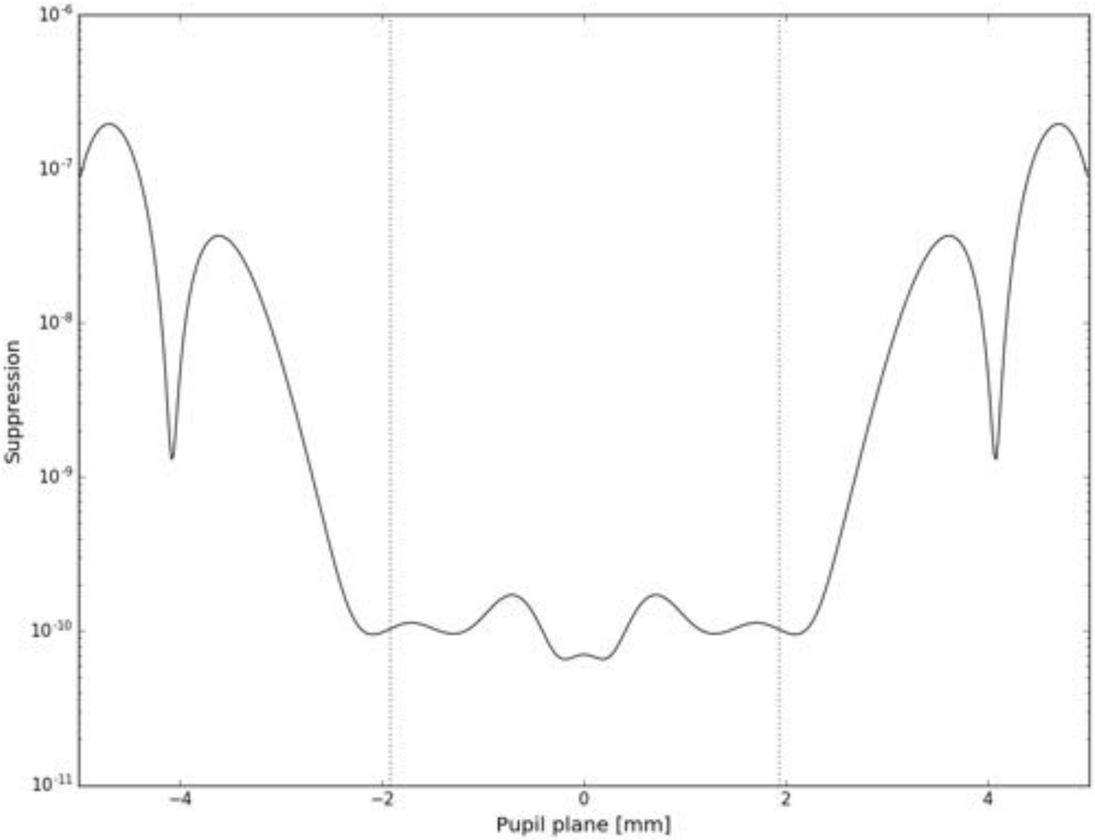

Figure 6.30: Suppression across and beyond the pupil in the Princeton testbed. Marked with vertical lines are the radii of the aperture. There is little wiggle room in the aperture for misalignment of the starshade before the brightness in the starshade begins to rise.

function means this prototype does not match the form of the flight design. With the outer mask, we are squeezing the light through an apodized aperture and Babinet's principle is no necessary to calculate the diffraction, meaning we are not validating our models in a representative fashion. Similar to the argument of requiring demonstration that the scalar diffraction approximation is valid, a demonstration should be required to show Babinet's principle is valid in the way we have implemented it. We know the outer mask is contributing to the suppression, but it is unknown if it is only suppressing diffracted light from the tube, or if it is enhancing the suppression of the light diffracted around the mask. The struts to the outer mask also eliminates any tips of the starshade, which is major source of diffraction for the flight design. If we are not testing tips, then we will not be able to understand the limitations of them in the flight design. I suggest to eliminate as many struts as possible while still being able to hold the mask, and to increase the size of the outer mask to limit the interaction it has with the inner mask. The mask should also be a design in which it is able to work (even if just theoretically) as a standalone occulter.

6.6.6 Potential for testbed to do critical scaling experiments

The current purpose of this testbed is to demonstrate suppression of 10^{-9}, which will be an excellent demonstration of the starshade's capabilities. However, the broader goal of testing starshades is to validate the optical models and show agreement down to a level where we are confident about scaling up to the larger mission. A key requirement of reaching TRL 6 is to understand the critical scaling issues, and to accomplish that, we need to break apart the Fresnel number into its 3 key parameters and demonstrate agreement with our models while scaling each parameter. Section 7.4 makes the case for a long baseline facility using siderostats to perform these scaling experiments, but there is a concern of the effects of the atmosphere in the long baseline. So we ask here if the Princeton testbed has the flexibility to perform the necessary experiments to be able to say that scalar diffraction is sufficient to explain the physics and we completely understand how starshades will scale up to the full mission.

These experiments will need to test multiple combinations of wavelengths, starshade sizes,

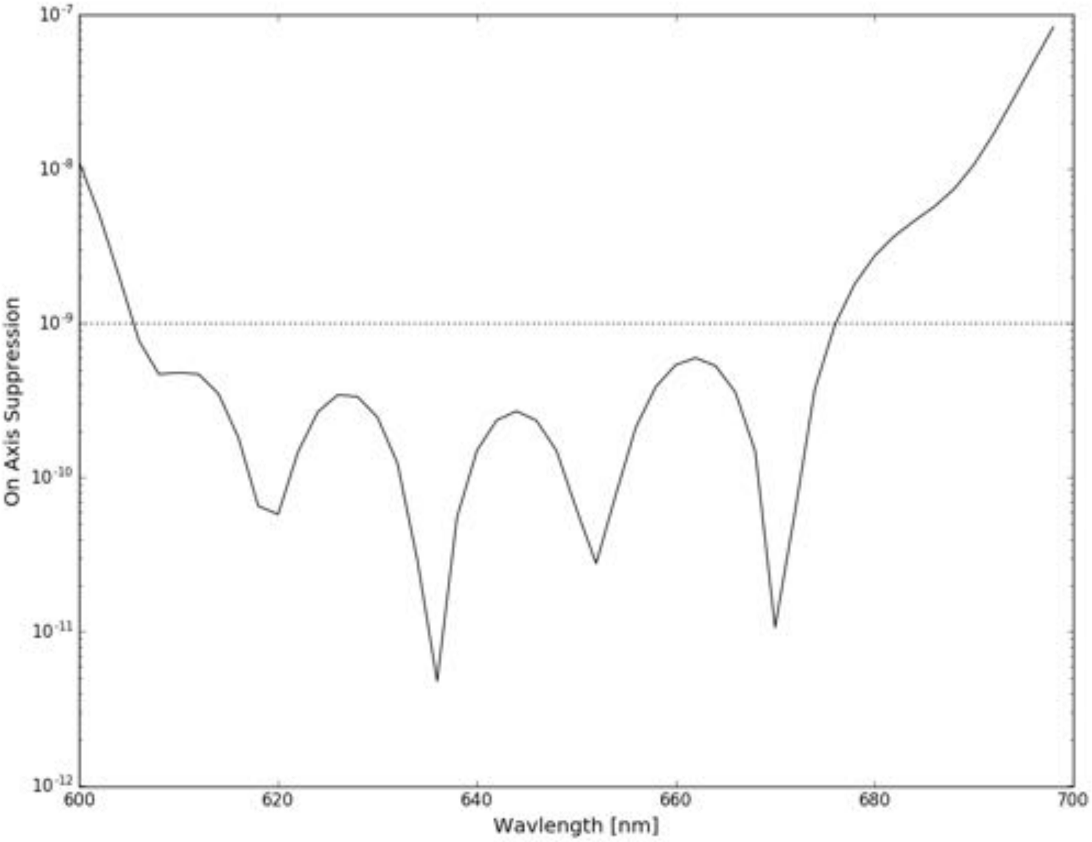

Figure 6.31: The on-axis suppression is charted against wavelength, showing the vary narrow bandpass of the shadow.

and separations at a flight-like Fresnel number and with varying Fresnel number. The goal is to try to find a combination in which scalar diffraction theory is not able to explain the results. With coverage over a large enough domain of parameters, if our scalar diffraction models agree with all combinations, we can sufficiently say our implementation of the models is valid. We want to test in the parameter space where we have high suppression, but we also want to see where the suppression falls apart and make sure we have agreement in those regions as well. We will not be able to do these experiments with the limited range for which the current masks operate; the partial derivative of suppression with respect to any parameter is too steep to test over a wide range. The bandwidth of the current test bed is ~ 70 nm (Figure 6.31). I argue that the first step is to design a broadband mask that will allow us to test over wavelengths $\lambda \in [0.4\ \mu\text{m} - 0.8\ \mu\text{m}]$. The testbed is currently operating at its maximum separation, so we cannot increase the separation. To go any closer would require a smaller starshade, but we are already pushing against feature sizes that are wavelength size, so any smaller and we will start to see non-scalar effects.

I therefore argue that this testbed is *not sufficient* to do the necessary experiments to demonstrate that we understand the critical scaling issues of starshades and that we will *not* have confidence in our models to predict the performance of a full scale mission. A testbed where we can achieve larger separations is necessary to do these experiments. Two options for such a testbed are the XRCF at the NASA Marshall Space Flight Center or the Long Baseline Facility proposed in Section 7.4.

Chapter 7

SIDEROSTAT FACILITY FOR ASTRONOMY WITH STARSHADES

Initial attempts to do astronomy with starshades used flight vehicles to hold the starshade in front of astronomical targets as they rotated across the night sky (Chapter 4). This proved to be difficult given the required tight position control of the vehicle while at altitude. In early 2015, a more practical solution to the alignment problem was found with the McMath-Pierce Solar Telescope (hereafter McMath) at Kitt Peak National Observatory (Figure 7.1). The basic idea is to use the main heliostat of the solar telescope to track stars across the sky and provide a stable beam of parallel light incident on a 30 cm starshade that can be observed by a small telescope at a distance. Initial tests and engineering runs were done in collaboration with the Northrop Grumman team [58, 59][1].

Using a siderostat in the starshade system provides a number of advantages over previous experiments in the lab or on dry lake beds. The most obvious being the opportunity to observe real astronomical targets in an IWA regime with scientifically interesting astronomical targets whose accessibility is unique to starshades. Additionally, with the incident wavefronts being parallel, opposed to diverging, we are able to test at a lower Fresnel number and in a more flight-like configuration. Using the siderostat to stabilize the beam allows us to increase our baseline to kilometers of separation and push on both IWA and Fresnel number. With our long-baseline test at 2.4 km (parameters shown in Table 8.3), we are at a flight-like Fresnel number and resolution, and we have pushed to a moderately low IWA, making this the most flight-like starshade test to

---

[1] University of Colorado's work conducted at McMath was supported by a Strategic University Research Partnership (SURP) between CU and the Jet Propulsion Laboratory (JPL).

date. Testing with broadband light and macroscopic starshades also provide a more representative test for advancing the TRL of starshade technology.

Figure 7.1: McMath-Pierce Solar Telescope at Kitt Peak National Observatory. Photo credit: KPNO

7.1 McMath-Pierce Solar Telescope

The McMath-Pierce Solar Telescope consists of a 2 m flat mirror mounted to a polar-aligned heliostat (we will use the terms heliostat and siderostat interchangeably), followed by a 140 m long optical tunnel containing a 1.6 m converging mirror and various other secondary mirrors (flat and converging). The optical layout for our experiment is shown schematically in Figure 7.2. Incoming starlight hits the main heliostat and is sent down the tunnel, where it immediately hits a starshade supported on a stand. Halfway down the tunnel, a 1 m flat mirror intercepts the light and sends it back up the tunnel to the 0.9 m west auxiliary heliostat flat mirror, located slightly offset from the main heliostat. The west auxiliary directs the light beam out of the facility and towards the direction of our observing telescope located somewhere on Kitt Peak. All mirrors in the system are flat and all are fixed, except for the main heliostat, which is tracking the star across the sky.

The observing telescope, located outside of McMath, is a 13 cm refractor from Explore Scientific that is stopped down to a 2 cm - 6 cm aperture. A 2.5x Barlow lens is used to increase the focal length to ∼2.5 m. The detector used is an Andor iXon 897 Electron Multiplying CCD (EMCCD). EMCCDs are becoming more prevalent in astronomy and future space-based direct imaging missions are baselining their use. EMCCDs differ from traditional CCDs in that they have a series of multiplying stages in the readout register that can provide gains of up to 1000x. This gain effectively eliminates any readout noise and allows for short exposures at a high readout rate without sacrificing signal-to-noise performance. Using this detector allows us to continuously take many short (~ 0.1 s) exposures and keep the exposures in which we have good alignment behind the starshade and throw out those in which light leaking around the starshade is overwhelming our signal.

In order to achieve a smaller IWA while maintaining a starshade big enough for a useful aperture size and maintaining a flight-like Fresnel number, we must increase the separation between the starshade and telescope. The topography of Kitt Peak allows a direct line of sight to McMath from a dirt road on the SW Ridge area of Kitt Peak (Figure 7.5). This provides a separation of 2.4 km, allowing us to reach an IWA of 10 arcseconds and a flight-like Fresnel number of 12. See Table 8.3 for the parameters used in the extended baseline configuration. Another important aspect of the extended baseline configuration is that the resolution of our telescope with respect to the angular size of the starshade is close to that of the full-scale mission. Concerns have been raised with previous tests in which the over-resolved starshade artificially improved the contrast ratio. Our latest tests were the first observations with a starshade at the proper resolution (~ 4 resolution elements across the starshade). These observations are close to a flight-like configuration, providing crucial details on the starshade performance and data product we should expect in flight.

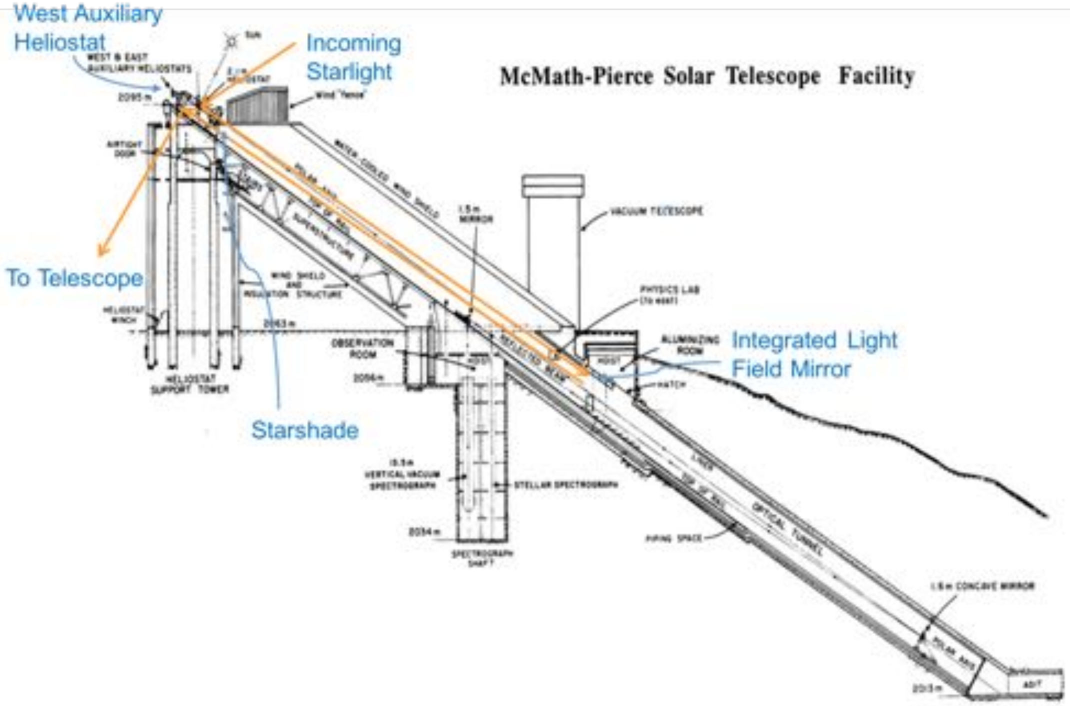

Figure 7.2: Schematic of the optical layout of the McMath facility. Incoming starlight bounces off 3 flat mirrors before being sent out of the facility towards our observing telescope.

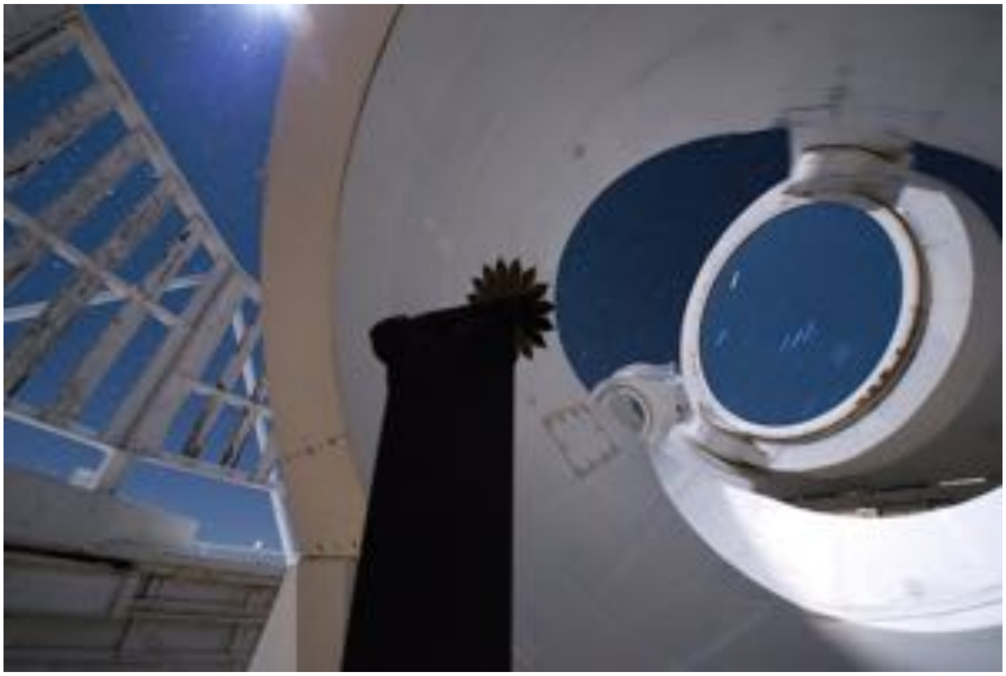

Figure 7.3: 20 cm starshade in front of McMath's 2 m Main Heliostat. Photo Credit: Robert Brown (Northrop Grumman) [90].

Figure 7.4: Looking up towards McMath's 0.9 m West Auxiliary Heliostat. This is the last optic in the chain before the beam is sent to the observing telescope

Figure 7.5: Google Earth$^{\copyright}$ screenshot showing the light path between McMath and SW Ridge.

Figure 7.6: View of McMath through observing telescope on SW Ridge. The dark starshade can be seen in the center of the West Heliostat (upper left of structure).

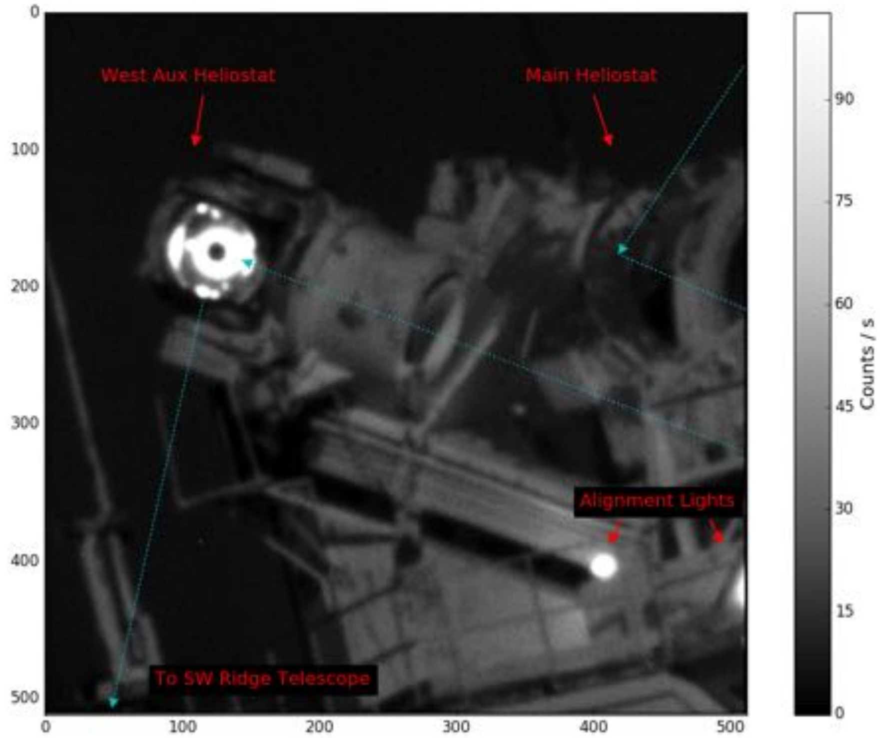

Figure 7.7: View from observing telescope on SW Ridge. The dark starshade can be seen in the center of the West Aux, surrounded by diffracted light. The alignment lights are in the lower right corner. The path of the light beam is shown in cyan.

7.2 Closed-loop Visual Feedback System

The first observing run in this extended baseline configuration (conducted in November 2015) revealed that our main limitation was keeping the star behind the starshade. At this smaller IWA, we were more sensitive to motion of the star due to errors in the main heliostat's tracking system and to atmospheric effects. The additional 2 km of horizontal path length through the atmosphere significantly increased the atmospheric turbulence. Even using the EMCCD to eliminate bad exposures, we did not spend a significant fraction of the time behind the starshade and had to throw out most images. This led us to develop a closed-loop visual feedback system to correct for tracking errors and increase the amount of time spent in the shadow of the starshade [33].

Parameter	**Short Baseline**	**Long Baseline**
Starshade diameter (to inflection point):	16 cm	24 cm
Starshade-Telescope Separation:	570 m	2.4 km
Inner Working Angle:	30”	10”
Fresnel Number:	22	12
Telescope diameter:	2 cm	2 cm
Resolution elements across starshade:	11	4
Wavelength Coverage:	400 nm - 800 nm	400 nm - 800 nm

Table 7.1: Optical parameters of McMath experiment from the short and long baselines.

7.2.1 Feedback system description

The feedback system works essentially as an autoguider, with the sensing done at the SW Ridge and the control at McMath. A second telescope slightly offset from our observing telescope (Figure 7.10) provides an unblocked view of the target star while the view from the observing telescope is blocked. The feedback telescope is a 15 cm Celestron Schmidt-Cassegrain with an Orion Starshoot Autoguider CMOS detector at the focal plane. Once the star is behind the starshade (as seen by the observing telescope), the feedback system is turned on and works to keep the location of the star fixed on the focal plane. We assume both telescopes are sampling the same patch of atmosphere, so any apparent movement of the star is the same in both telescopes. Correction signals generated by the feedback telescope are sent to the McMath control room via XBee radios run by Arduino microprocessors. The McMath control room is underground and radio signals are not able to reach the control room from the SW Ridge, so a relay radio is needed. At the SW Ridge, an XBee connected to a Yagi antenna sends the signal to an XBee/Arduino on top of McMath. This XBee relays the signal down to another XBee/Arduino in the control room. The final Arduino in the McMath control room has a Digital-to-Analog Convertor circuit (Figure 7.8) that converts the digitized control signal to an analog voltage ($\in [-3V, 3V]$), which is mixed with the McMath tracking system. Our correction signal is an addition in rate on top of the nominal sidereal rate.

The process flow for the feedback system is shown in the list below. The image processing software was written in Python and the camera and Arduino software was written in C++.

(1) Take image of star with feedback telescope

(2) Calculate offset from target location in image coordinates

(3) Rotate into heliostat motor coordinates via calibration (see Section 7.2.4)

(4) Pass offset through Proportional-Integral (PI) controller to generate tracking rate control signal

(5) Convert control signal rate to integer $\in [0, 2^{n_{\mathrm{DAC}}} - 1]$

(6) Relay control signal over XBees to McMath control room

(7) Use DAC to convert control signal to analog voltage $\in [-3V, 3V]$

(8) Apply analog voltage to McMath tracking system

The calculated error offset in the image of the guide telescope is given by,

$$e(t) = (x, y)^i_* - (x, y)^i_{\text{target}} \tag{7.1}$$

where $(x, y)^i_*$ are the image coordinates of the star (or target location). The PI control signal $c(t)$

for a given time t, to be applied to the McMath tracking system, is given by,

$$c(t) = g_p e(t) + g_i \int_0^t e(t')\, dt' \tag{7.2}$$

where g_p and g_i are gains for the proportional and integral terms, respectively.

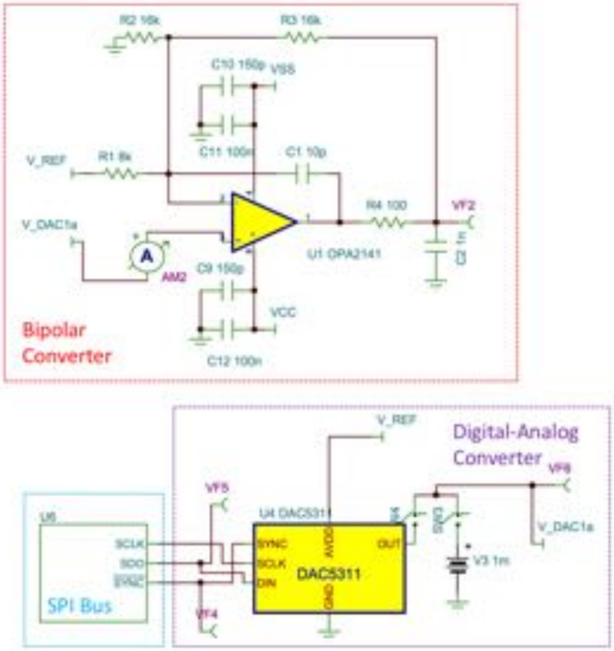

Figure 7.8: Layout of digital-analog-converter circuit in the McMath control room that converts the received feedback signal into an analog voltage to be mixed with McMath's tracking system.

7.2.2 Observing station

On the SW Ridge, an observing station (two tents) was set up to house the telescopes, computers, and personnel during observations (see Figure 7.9). The first tent is a pop-up ice fishing shelter that housed the science and guiding telescopes (Figure 7.10), and the second tent housed the computers, battery packs, and personnel. We had to rely on portable battery packs to provide power for all of the equipment: 2 laptops, 1 EMCCD, 1 CMOS detector, 1 Yagi antenna, and 1 Arduino/XBee microcontroller. The laptops and the EMCCD were power hogs and we used ∼3 kW each night.

Figure 7.9: Image of observing station tucked away on the SW Ridge. The observers and computers are located in the blue tent on the left, the telescopes are located in the red tent on the right.

Figure 7.10: Image of telescope tent. The top telescope is the 12.7 cm science telescope, the bottom telescope is the 15 cm guide telescope.

(a) (b)

Figure 7.11: (a) shows the guide telescope (**bottom**) and science telescope (**top**). (b) shows the science telescope with EMCCD mounted on the back. The EMCCD and the electronics are powered by battery packs.

7.2.3 Graphical User Interface

A GUI (Figure 7.12) was developed to allow for manual control over the feedback system. The GUI provides a live feed of images recorded by the feedback telescope and enables the user to slew the main heliostat from the SW Ridge. With remote control of the main heliostat, once the crew in the McMath control room puts the target star in the FOV of the feedback telescope, we can take over control and run the observations from the SW Ridge. The GUI contains a number of other features to help in the feedback system, such as choosing a target location on the focal plane, toggling the feedback system on, and changing the gains of the PI controller.

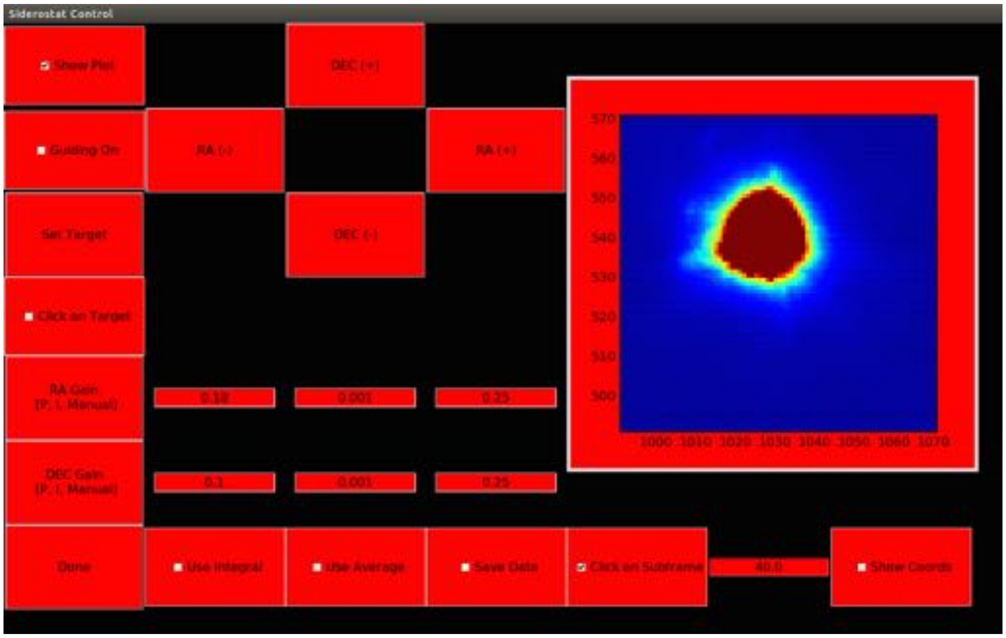

☑ Show Plot
☐ Guiding On
☐ Click on Target
RA Gain (P, I, Manual): 0.18, 0.001, 0.25
DEC Gain (P, I, Manual): 0.1, 0.001, 0.25
☐ Use Integral
☐ Use Average
☐ Save Data
☑ Click on Subframe: 40.0
☐ Show Coords

Figure 7.12: Screenshot of GUI developed to run the feedback system and control McMath from the SW Ridge.

7.2.4 Calibration of coordinate frame transformation

To rotate from the coordinate frame of the image plane to that of the heliostat's axes requires a calibration that changes with target and its position on the celestial sphere. After slewing to a new target, a calibration procedure is performed to determine the rotation angle between the coordinate frames. We assume that this does not change significantly over the period of observations for a given target. The basics of the calibration procedure is to step the heliostat in known increments along its right ascension (α) and declination (δ) axes, recording the position of the target on the image plane at each step. The coordinate transformation from the image frame (X) to the heliostat frame (Y) is given by Equation (7.3), where R is the rotation matrix between the frames (what we are solving for), s is a scale factor, and t is the translation matrix between the frames.

$$Y = sRX + t \tag{7.3}$$

The rotation matrix can be solved for via least squares using Equation 7.4, where X', Y' are the normalized coordinates centered around their means.

$$R = Y'X'^{T}\left[X'X'^{T}\right]^{-1} \tag{7.4}$$

After the calibration procedure is ran, we solve for the rotation matrix by plugging the measured image coordinates at each step (X') and the theoretical movement of the heliostat (Y') into Equation (7.4). To perform the frame transformation, we plug the offset in image coordinates (X) into Equation (7.3) and set $s = 1$ and $t = 0$, assuming these are accounted for in the gain of the PI controller.

7.2.5 Alignment procedures

It is quite an involved process to align three mirrors with a moving target and a telescope 2.4 km away that has a field of view of only 90 arcseconds. The alignment procedure is given here, with more explicit directions below.

(1) Get West Auxiliary close to SW Ridge using sun beam and blue sky

(2) Fine tune West Auxiliary to put starshade in the center of the mirror

(3) Adjust Integrated Light Mirror to remove vignetting

(4) To observe a new target:

(a) Find target on observing table in control room

(b) Move target to 'mark' on the table

(c) Spiral search to get target in FOV from SW Ridge

First, we must get the West Auxiliary (Aux) pointed towards the SW Ridge such that the telescope is aligned in the optical path all through the McMath system and we can see the sky from the Main Heliostat (Main). This is done by shining the Sun on the Aux and projecting the bright beam on the opposite hillside and eyeballing the movements to place it close to the SW Ridge. A team member on the SW Ridge walks around the telescope to find a direction of preferential brightness and uses voice commands over the radio to help steer the Aux into place. The Sun is removed and the telescope observes blue sky through the Aux to serve as a light background. The dark starshade can be seen against the blue sky (Figure 7.6) and voice commands help to steer the Aux such that the starshade is in the center. There is often vignetting that needs to be removed by adjusting the Integrated Light Mirror (ILM), which is again done by looking at the blue sky through the telescope and guiding with voice commands. This only needs to be done once if we do not move the Aux, starshade, or ILM.

To observe a new target, team members in the McMath control room slew the telescope to the proper celestial coordinates and look for an image of the target projected onto the observing table in the control room. The Main is oversized relative to the ILM, so some light is not intercepted by the ILM and continues to the converging M2 mirror at the bottom of the tube. This mirror sends that light halfway back up the tube where it is intercepted by a pickoff mirror and an image forms on the observing table. Since the M2 is not fully illuminated, the target is faint and it is tricky to find the image on the table. If this is not the first time this has been done in the current setup, we will have the location on the table marked that corresponds to the alignment with the SW ridge and we can just return the image to roughly the same spot.

If it is the first time, we need to move the Main until the target is in the FOV of the SW Ridge. This is done mostly by winging it. Doing a spiral search can help cross paths by chance, or a team member near the Main can try to eyeball it to help guide it in, but again, mostly just winging it. Once the star is close, the telescope sees a preferential brightness on one side of the Aux from diffracted light and we can use that to help steer it in. Once we have succeeded in finding the target in the FOV, we mark the location on the table, which helps us get closer next time. As you can see, this process is tricky and finicky. I included the ugly details to explain the difficulties that come with switching targets during the night and the time it can potentially waste. I also include it to gain sympathy from the reader for the frustrating trials and tribulations that were endured.

7.3 Feedback Loop Performance

The main qualitative result of the feedback system is that it makes observing with our unique setup of McMath significantly easier. Before, the crew in McMath control room that was steering the heliostat could not see the star's position relative to the starshade and the crew making the observations did not have control of the heliostat. We had to rely on voice commands over the radio to keep the starshade aligned. We now have both observations and control on the same side, providing closed-loop control.

Figure 7.13 shows the time evolution of the mean count rate for a series of observations with the feedback system turned on (blue dashed line) and turned off (red solid line). With the feedback system turned off, after about 40 seconds, the star drifts out of alignment and the mean count rate goes up as the image is dominated by light leaking around the starshade. Before the addition of the feedback system, this would require a manual adjustment (relayed via voice commands over the radio) to realign the starshade that would eat into potential exposure time. With the feedback system turned on, we are able to maintain alignment indefinitely and take data for the entire time.

Our main limitation to the feedback system is the maximum control rate of the main heliostat set at 1 Hz. In Figure 7.13, the curve for when the feedback system is turned on shows an oscillation in the mean count rate with a period of $\sim$1 Hz. As we add a delta-rate to the heliostat to correct for misalignment, by the time 1 second has passed and we are able to update the correction, we have overshot in alignment, causing us to oscillate around perfect alignment at 1 Hz. The feedback system can correct for the long time scale drift, but cannot correct for atmospheric disturbances above 1 Hz.

The predicted contrast performance as the starshade moves off-axis is shown in Figure 7.14 with a simulation of a 30 cm starshade at different offset amounts. The contrast holds steady for an offset of $< \frac{1}{2}a$ (a being the hypergaussian parameter) as the telescope remains in the "sweet spot" of the shadow, but rises steeply beyond that, giving us little wiggle room to allow for misalignment due to tracking errors or atmospheric image wander. Bear in mind that a lateral offset of the starshade in this case is a movement in the apparent image of the star as the pointing in the heliostat varies. A 3 cm shift in the apparent position of the star is only 2.5 arcseconds of tilt on the heliostat. An atmospheric seeing cell this size (on the lower end of what we would see at KPNO) can also induce this motion. The contrast is still workable 3 cm off-axis, but once it reaches 6 cm, any benefit in suppression from the starshade is lost. Figure 7.15 shows the progression of images as the source is moved behind the starshade and we see the star almost completely disappear.

The closed loop feedback system we built at McMath was the first step demonstration of a novel way to maintain alignment over large separations to enable the testing of and high contrast astronomy with starshades. The lessons we have learned are useful for defining the requirements of a future, larger-scale siderostat facility that can enable exciting astronomy on planetary systems. For a future siderostat facility to be useful, we need to observe at a location with less atmosphere and with a facility that has faster control of the positioning of the starshade.

7.4 Considerations for a Future Siderostat Facility

McMath opened the door to a new method of alignment for suborbital testing of starshades and enabled astronomy with starshades for the first time, using an older facility in a way for which it was not designed. We immediately recognized the potential a dedicated siderostat facility has to enable cutting edge science and technology development. The design considerations of a concept facility is detailed below.

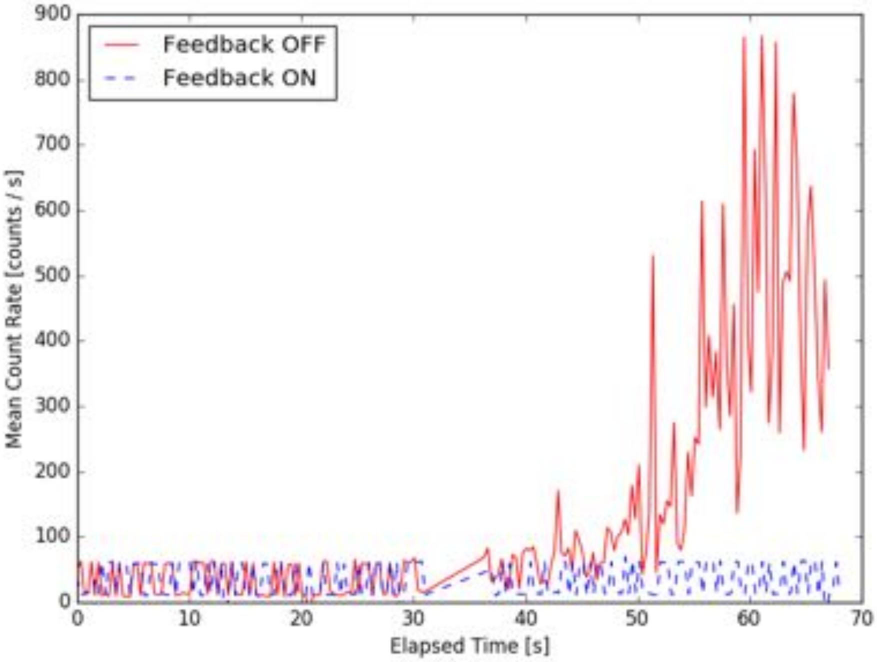

Figure 7.13: The mean count rate as a function of time. The **blue** line shows when the feedback is **on** and the **red** line shows when the feedback is **off**.

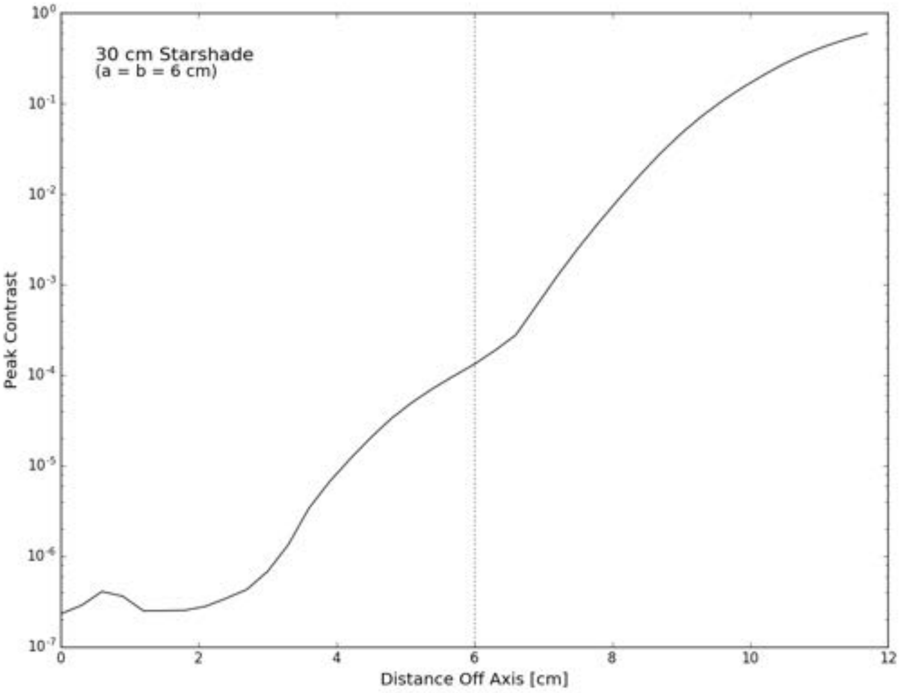

Figure 7.14: Simulation of the peak contrast as a function of misalignment, with the vertical line denoting the a parameter of the starshade. The deep part of the shadow is $\sim \frac{1}{2}a$ in radius.

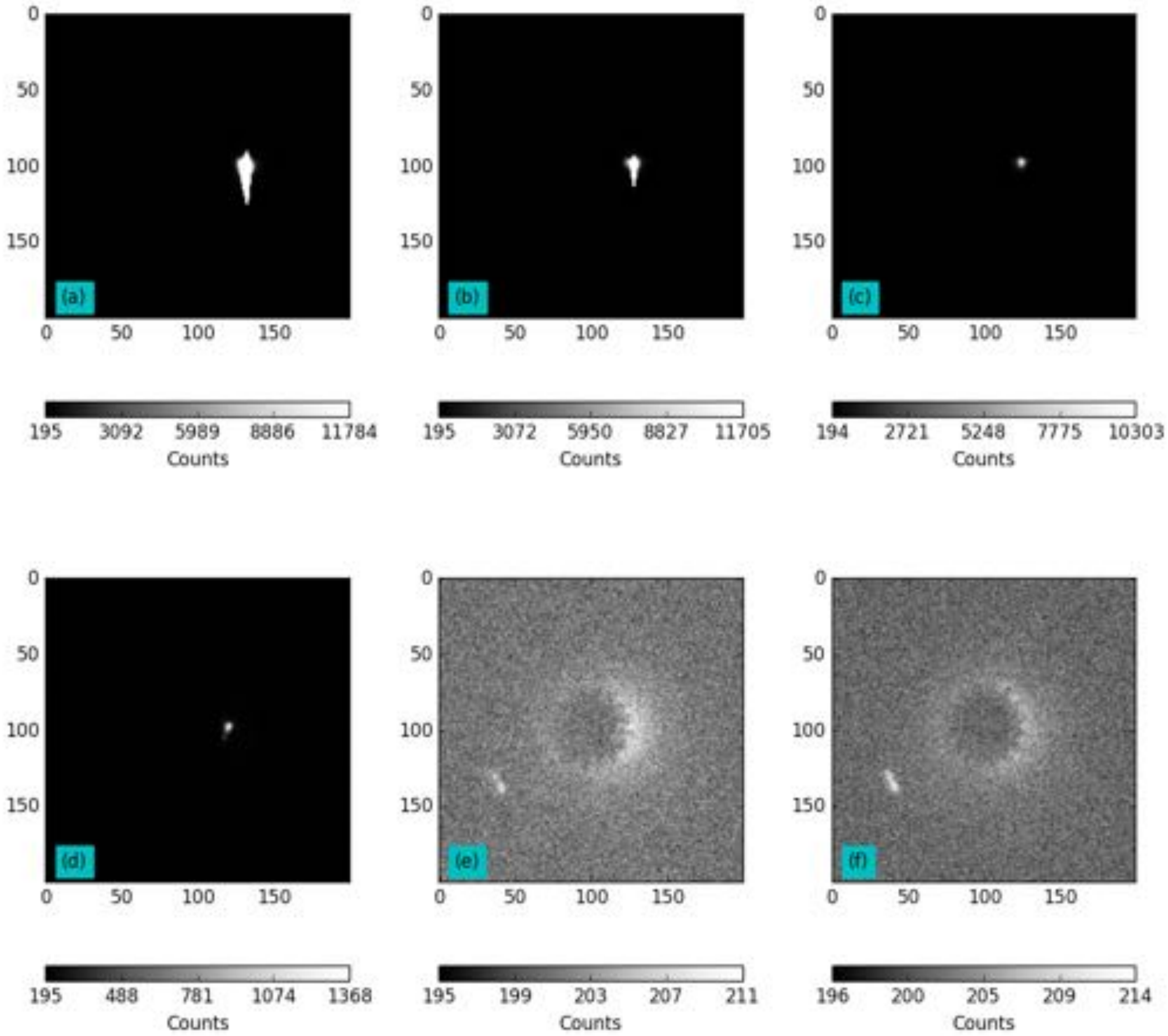

Figure 7.15: The different panels (a)-(f) show images taken at different times as the star is moved behind the starshade. The star is completely saturated in (a) & (b). In (c) & (d), there is a bright spot on the edge of the starshade as the star is behind the starshade, but there is a significant amount of light leaking out. In (e) & (f), the starshade is in near perfect alignment and the star has been nearly completely suppressed.

7.4.1 Long Baseline Facility

The Long Baseline Facility (LBF) is a concept for a dedicated siderostat facility developed for the NASA Exoplanet Exploration Program's Starshade Working Group (SSWG) to help bring starshade technology from TRL 5 to TRL 6. Addressed in Section 6.6.6, there are concerns with current plans to only test starshades at small separations and in order to reach TRL 6, we must demonstrate a high-fidelity model of the appropriate fit, form, and function and demonstrate we understand critical scaling issues. The main argument for LBF is summarized in Figure 7.16; there are six orders of magnitude difference in separation and 3 orders of magnitude difference in starshade size between the planned state of the art tests and flight. The LBF enables us to split those differences by half (in dex) and provides a path toward TRL 6 by allowing us to test at large separations and large sizes without going to space.

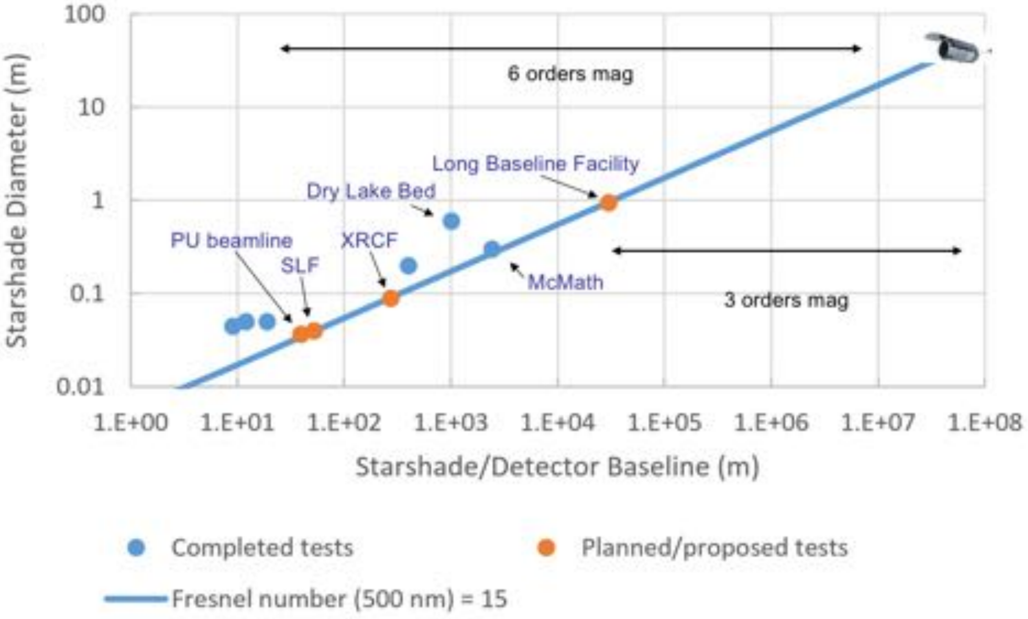

Figure 7.16: Starshade diameter and baseline for all past and future tests. There is 6 orders of magnitude in baseline between the planned state of the art test and flight. The LBF hopes to retire risk by reducing that to only 3 orders of magnitude. Figure credit: Ben Zeiger.

LBF is the same concept as McMath, except at a larger separation and with a purposely built facility that will allow more versatility in testing and better starshade performance. Parameters for a short and long version of the LBF are summarized in Table 7.2. A large ($<$ 4m diameter), high-quality flat mirror on a sidereal mount keeps the beam stabilized on a 10s of centimeters diameter aperture. The mirror needs to be large enough so that the edge of the mirror does not diffract light into our aperture. The edge of the mirror can be apodized with inverse starshades to mitigate some of the diffraction to help reduce the size. The size of the mirror also needs to be considered when deciding which astronomical targets to observe and how a reduced outer working angle will limit those observations and the number of background stars in the field of view to do proper image alignment.

A feedback control system, similar to what was built for McMath, but with tighter control and a faster control rate, will enable us to eliminate tip/tilt misalignment errors. Building LBF at a high and dry site, such as the Atacama Desert, will also help minimize the atmospheric effects that currently limit us at McMath. Higher quality mirrors and darker skies will reduce scatter and lower the background signal, allowing us to reach lower contrast levels. The larger starshade also allows us to use a larger aperture, enabling more interesting astronomy on faint targets.

Parameter	**Short Tests**	**Long Tests**	**Flight**
Separation	10 km	30 km	50,000 km
Starshade Radius	0.28 m	0.49 m	20 m
Telescope Diameter	0.1 m	0.2 m	2.4 m
Fresnel # (at 0.5 μm)	16	16	16
Inner Working Angle	6”	3”	80 mas
Tel. Resolution (at 0.5 μm)	1”	0.5”	40 mas
# Res. Elements over SS	11	13	4

Table 7.2: Parameters for a short and long version of the LBF in comparison to those in flight. The LBF is meant to be adaptable so that the two baselines can be used for different tests. The long tests are at the correct Fresnel number with a modest (20 cm) aperture and is beginning to push into a small IWA regime where there is interesting science.

The LBF enables system level testing of starshades in a more representative configuration with macroscopic starshades at large separations. It provides another point of model validation on the Fresnel number curve and allows us to say with confidence whether or not scalar diffraction theory is sufficient. We can test optical properties of large scale petals of flight design, particularly at the bases where the potential for trouble is the highest.

Achieving high contrast at 3" IWA will enable breakthrough science, photometry and spectroscopy of debris disks and Jupiter-size planets at moderate separations. There is also a potential to address a question critical for future direct imaging missions of what the characteristic brightness of exozodiacal light is in nearby systems.

7.4.2 Limitations of the atmosphere

With a stationary, horizontal telescope, we have the luxury of building a stable platform that can support large instruments. We will want an adaptive optics (AO) system on the collection telescope to overcome wavefront errors accumulated on the horizontal path from the siderostat and enable diffraction limited astronomy. This is critical for a useful testing facility as the main hinderance of long baseline testing on the ground will be the atmosphere. Atmospheric turbulence degrades the resolution of the telescope, broadening the PSF and bringing diffracted light from the inner working angle to the image region of interest. This sets a limit on the best contrast we can achieve and makes it difficult to interpret the results of testing different starshade models and with built-in flaws. The atmosphere also adds error in our contrast measurements with scintillation introducing variance in the “true” value of the unblocked source. Most of these problems are standard in ground-based astronomy and can easily be mollified with a standard AO system. Using only a 20 cm aperture and having a stable, stationary mount that is not introducing further wavefront errors will also help to simplify the AO system.

An AO system on the telescope end will not be able to correct for large misalignments of the starshade that is causing us the most trouble at McMath. For this, we need a closed loop feedback system similar to what was built for McMath, but with faster and tighter control. However, trying to compensate for tip/tilt on atmospheric timescales with a 4 meter mirror is not trivial (or cheap) to implement. Fine tuning of the alignment can be done by moving the starshade, while the siderostat is used for the slower motion of tracking the star across the sky. The starshade is only 1 meter across and made of thin, lightweight material. There also are not any optical level requirements on the starshade position and we are insensitive to a large range of tips, rotations, and lateral movements of the starshade; we just need to keep the shadow centered over the aperture.

One effect of the atmosphere that is more difficult to control is scattering off dust and aerosols in the atmosphere. Light from our object of interest is scattered out of our line of sight and the atmospheric extinction makes it more difficult to detect an already faint object. Unwanted starlight from the target star can be forward scattered into our line of sight and create a diffuse background that raises the noise floor. A possible solution to mitigate these problems is to build the LBF at a high and dry site with low dust, such as the Atacama Desert, Chile or Mauna Kea, Hawaii.

7.4.3 Requirements on mirror quality

In Section 5.4.2, we explained the effects of wavefront errors incident on the starshade, particularly periodic errors imposed by figure error on a siderostat mirror. Equations 5.30 and 5.31 provided an estimate of the frequencies and amplitudes of figure error a starshade with a siderostat is most susceptible to and showed how this mostly dependent on Fresnel number. A more detailed analysis of the spatial frequencies of errors that are common on flat mirrors will need to be done, but we are confident that this will not be a limiting factor.

The limitations we experienced with the mirrors at McMath should not be near the same level of the LBF. To start, at McMath the light bounces off three flat mirrors before it reaches the telescope, with each mirror being over-filled and diffracting. The mirrors are also open to the elements and have a large amount of dust, scratches, and debris on them that add to the scattered light. With clean mirrors with good scratch-dig quality and limiting the number of bounces needed, scattered light from the mirrors should be able to be minimized. Additionally, at the longer baselines any diffuse scatter will become negligible as the solid angle of our telescope becomes increasingly small.

Chapter 8

HIGH CONTRAST ASTRONOMICAL OBSERVATIONS

Working with half-meter starshades at a few kilometers separation provides an opportunity for science in a unique region of parameter space, high contrast but at a moderate IWA. Most high contrast instruments currently in use are on large ground based telescopes such as Sphere on VLT [4] and GPI on Gemini South [47] and have a limited field of view of only a few arcseconds. The state of the art of these instruments is also limited to $\sim 10^{-5}$ - 10^{-6} contrast, is reduced to a throughput of <10%, and works primarily in the NIR. Other telescopes with larger FOVs cannot achieve very low contrast levels even at larger IWAs. These major facilities are also expensive to use and competitive in allocated time. The siderostat observatory detailed in Chapter 7 can fill a unique niche of science. We have the potential to surpass the contrast levels of the best high contrast instruments on world class observatories and at the moderate IWAs not accessible to them. McMath-Pierce is also inexpensive to operate and, it being a solar telescope, is often available for night observations[1]. This chapter details the kind of science that can be done with high contrast at moderate IWA and reports on initial science results from the first few observing runs using a starshade at McMath.

---

[1] Unfortunately, the National Solar Observatory has decided to no longer support McMath-Pierce and will stop operations in Spring 2017. This historic observatory has served the astronomy community well over its years and produced many important scientific results. It is a shame to let such a facility fall to the wayside, especially when the operation costs are minimal to an organization such as the NSO.

8.1 Science at High Contrast and Moderate IWA

The starshade readily provides high contrast, but with a half-meter starshade in the atmosphere, we can only fit a few centimeter aperture in the shadow and our sensitivity is limited by exposure time. The current setup at McMath, with the feedback loop limited to 1 Hz control, also has a low duty cycle for time spent deep in the shadow. As such, our ability to do any science with this system requires a lot of exposure time; time that we have not adequately had as of yet. With the system as is, there is potential to observe bright debris disks or circumstellar dust around AGB stars. With an upgraded, dedicated facility, we can push to smaller IWA and go after hot, exozodiacal dust and possibly large, wide separation planets. There is interesting science to be had revealing the previously inaccessible circumstellar regions around nearby stars.

8.1.1 Debris disks

The first debris disks were detected by the Infrared Astronomical Satellite (IRAS) [3] as an excess of infrared (25 μm - 100 μm) light in the spectral energy distributions (SED) of the stars Vega and Fomalhaut. This IR light, which did not match models of the stars' photosphere, was attributed to starlight being re-radiated by small dust particles around the star. Since then, many more "Vega-like" systems have been discovered at IR and mm wavelengths and census studies are beginning to reveal the connection between debris disks and the formation of planetary systems. A smaller number have been detected in scattered light at visible and NIR wavelengths and help to constrain the properties of the optically thin dust. For a complete catalog of currently known debris disks, see [17], and for reviews on circumstellar dust, see [94] and [93].

Debris disk observations can reveal much about planetary formation processes and the presence of planets. Their mere existence is informative as they are observed around main sequence stars past the lifetime of the primordial disk. By 10 Myr, the primordial dust should have been blown out by radiation pressure, dragged into the star by accreting gas, or locked up in planetesimals, suggesting that debris disks are formed in a regenerative process such as collisions between planetesimals [93]. The size and distribution of dust grains in the disk can provide insight into collisional processes and timescales of planet formation. The total dust mass can estimate the amount of mass available for planet formation. Orbital perturbations from even modest-sized planets can clear gaps in debris disks, shepherd the dust into sharp annuli, or cause warps and asymmetries in the disk. The morphology of the disk can suggest [63] (but not guarantee [46]) the presence of a planet to be followed up with deeper observations.

Imaging debris disks in visible scattered light is a challenging observation, but has high science returns. Most debris disks are detected by the thermal emission of dust causing an infrared excess in a star's SED, but this suffers from a degeneracy in the dust size and orbital distance. A large, cold dust grain can emit as much light as a small, hot dust grain. The total emission also does not reveal anything about the morphology of the disk or the distribution of the dust. Scattered light images can use the morphology of the disk to break the size/temperature degeneracy and point towards the presence of planets. Imaging in the visible allows for higher resolution to detect warps, clumps, and asymmetries that are not resolved in IR and sub-mm images.

With the high contrast achievable with our siderostat system, we have the chance to detect large debris disks in visible scattered light and set upper limits on the presence of circumstellar dust.

8.1.2 Exozodiacal dust

More challenging, but arguably more important, targets are the distributions of hot dust around stars referred to as exozodiacal dust, named so for their parallel to the zodiacal dust seen in the ecliptic plane of our solar system. This dust is located close ($<$ a few AU) to the central star and is considered to be a distinct population from the debris disks at larger orbital distances. The presence, strength, and distribution of exozodiacal dust is particularly important for any future direct imaging mission, be it with a starshade or internal coronagraph. If our solar system is representative of typical planetary system, then habitable planets are embedded in the middle of a cloud of dust generating a bright background out of which the signal of the already faint planet must be pulled [65, 85].

Using measurements of the local zodiacal dust at 1 AU and accounting for the difference between being "inside looking out" versus "outside looking in", the estimate for the expected surface brightness due to a solar system's worth of exozodiacal dust at 1 AU is 22 mag arcsec^{-2} [65]. This surface brightness is commonly referred to as the unit of 1 Zodi. The scattering of starlight by exozodiacal dust at visible wavelengths can serve as a source of photon noise and source of confusion in the attempt to directly image Earth-like exoplanets.

The brightness of a uniform distribution of exozodiacal dust as a function of strength (number of Zodis) for various telescope sizes is shown in Figure 8.1. For a 4 m telescope, an exo-Earth at 10 pc is one-to-one with the exozodi background, for a WFIRST-like 2.4 m telescope, it is 3× fainter. Even with a uniform background, overcoming the photon noise from the background is a challenge. If the dust is clumpy (a reasonable assumption given the warps and clumps observed in debris disks in systems with planets), the contributing background is not as simple as photon noise and clumps of dust could look similar to planets and be a source of confusion. Depending on the amount of dust in the typical star system, exozodiacal dust could make or break a direct imaging mission, where we are at the mercy of the universe and no matter how good our starlight suppression is, the only practical solution to finding Earths is with larger telescopes.

There is little known about the distribution of strengths, morphologies, or commonality of zodiacal dust in other systems. This is concerning given the potential risk it has to rendering a multi-billion dollar direct imaging mission useless. The only plans NASA has laid out for solving this problem is using the Large Binocular Telescope Interferometer (LBTI) to conduct a near-IR survey of nearby systems to measure exozodis down to 10 Zodis [20]. This survey will certainly help, but it is far from solving the problem. There are two reasons this survey could fall short. First, it only has the sensitivity to constrain dust to 10 Zodis, and as Figure 8.1 shows us, if this were a typical value, a direct imaging mission would have a difficult time searching a large enough sample of star systems to stumble upon an Earth. Second, this instrument operates at 3 μm and is potentially probing a different population of dust (longer wavelengths are more sensitive to larger

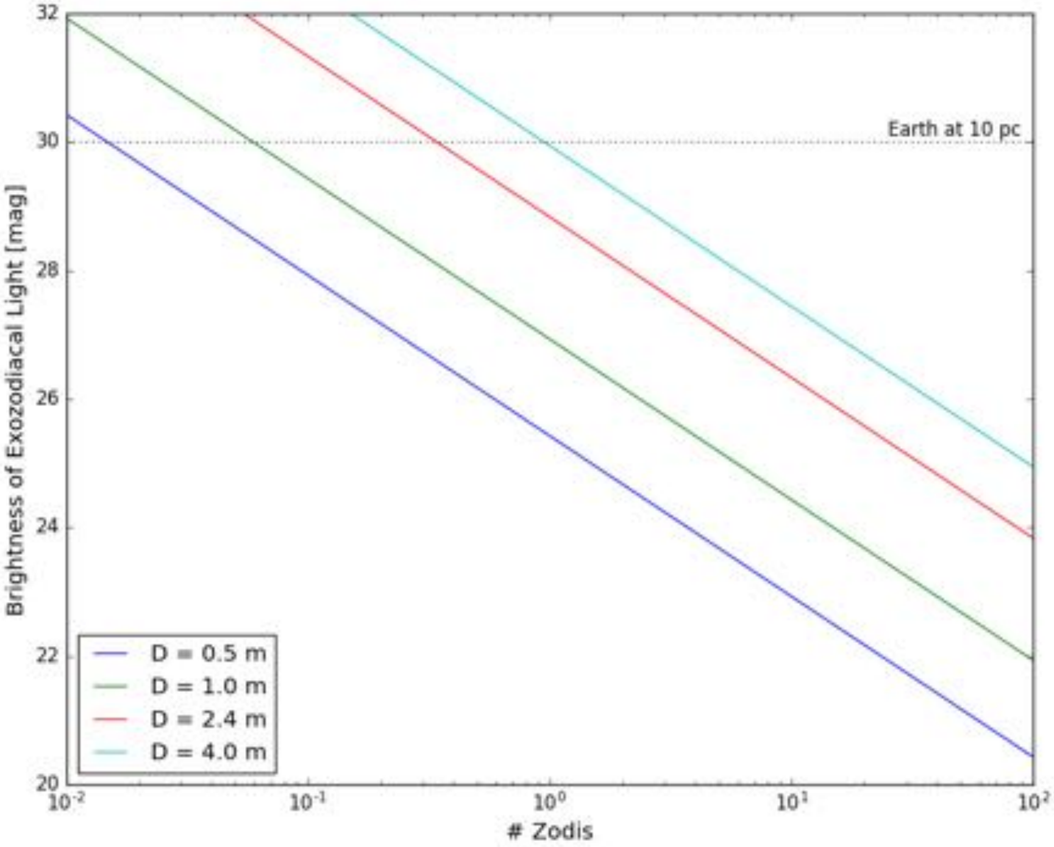

Figure 8.1: Integrated brightness (in magnitudes) of exozodiacal dust as a function of the number of Zodis (1 Zodi = 22 mag arcsec^{-2}) for different telescope diameters. The brightness of the Earth as viewed from 10 pc is denoted by the horizontal dotted line.

dust grains) than the population that could wreak havoc on our direct imaging mission at visible wavelengths.

To adequately address this problem, reduce risk, and have confidence that a direct imaging will achieve its science goals as expected, we need a visible light survey of a handful of nearby stars with a sensitivity down to at least 1 Zodi, to determine the distribution of dust levels at a few AU around solar type stars. A survey of this sort will allow us to confidently extrapolate (in sensitivity and orbital distance) to the habitable zones of the primary targets of a direct imaging mission and give us confidence that we can detect an exo-Earth there. Such a survey is beyond what is capable with a small-scale siderostat setup like what we have at McMath, but it may be possible with a larger ground-based facility such as LBF (Section 7.4).

8.2 Targeting the Fomalhaut Debris Disk

Our ultimate science goal for the McMath experiment was to detect the debris disk around Fomalhaut. We chose this target as it is a relatively bright disk at a large angular separation that we could reach with our modest IWA observations. Fomalhaut is 1$^{\mathrm{st}}$ magnitude and the disk has eluded many ground attempts to image it in scattered light and was not seen in visible light until the Hubble Space Telescope [37]. Detecting it would be a powerful statement about the capability of starshades and broadband photometry would allow us to constrain some models on the size distribution of dust grains. We knew a detection would be a reach goal, but it was within our reach. Here we will give our explanation of why we think it is within reach and what it will take to observe it. The following sections will detail the observations that were made and why we were not successful in a detection.

8.2.1 The target

Fomalhaut, or α Piscis Austrini, is an A4 dwarf [31] with a V band magnitude of 1.16 [23]. It is one of the brightest stars in the sky, so it is no wonder it was able to hide its debris disk for so long. The disk was first detected as an infrared excess with IRAS [3], but was not seen in scattered light until observed with HST [37]. Those observations suggested its sharp ring was being sculpted by a shepherding planet and later analyses claim a detection of a large planet near the orbit of the disk [36]. The disk, an elliptical ring rather, is seen from 133 - 158 AU [37]. With Fomalhaut at 7.7 pc away, this puts the disk at 17 - 20 arcseconds on its major axis, within the IWA of our 2.4 km baseline at McMath. Its surface brightness is ~ 21.3 mag arcsec^{-2} in V band, which is roughly equal to the new moon sky brightness of Kitt Peak [49]. Assuming the starshade achieves perfect suppression, all we need to do is beat against the equal background of the sky brightness. However, the mirrors and the atmosphere limit the starshade from achieving perfect suppression and we have additional noise to contend with.

8.2.2 Signal-to-noise ratio

8.2.2.1 Sources of noise

We perform a simple signal-to-noise estimation to determine the exposure time needed to detect the debris disk. The Signal-to-Noise ratio (SNR) is given in Equation 8.1, with the parameters summarized in Table 8.1.

$$SNR = \frac{\sqrt{N} C_{sig} t}{\sqrt{\left[C_{sig} + C_{sky} + \gamma C_* + C_{mir} + C_{drk}\right] F^2 t + \left(\frac{RON}{G}\right)^2 + (CIC)^2}} \tag{8.1}$$

Most of the parameters in Equation 8.1 are standard to SNR calculations, with a few new additions. γ is the contrast in the focal plane at the location of the signal of interest. In this definition, the contrast is the counts in a given pixel that are from the target star while the starshade is in place, divided by the peak counts from the target star if there were no starshade. Note that the contrast is dependent on the location in the image and also on properties of the telescope (such as resolution). This residual light is leaked around the edge of the starshade and is completely localized to the edge of the starshade, though the telescope's PSF spreads that light out on the focal plane. If the target is separated from the starshade in the image, then the contrast gets better as we fall off the wings of the PSF. C_{mir} is the rate of photons from the target star that

C_{sig}	Count rate [ph/s/px] of signal
C_{sky}	Count rate [ph/s/px] of sky background
C_*	Count rate [ph/s/px] of target star
C_{mir}	Count rate [ph/s/px] of scatter from mirror
C_{drk}	Count rate [e/s/px] of dark current
γ	Contrast at location of interest
F^2	Excess Noise Factor (see Equation 8.2)
G	EM Gain
RON	Read out noise [e^-/px]
CIC	Clock induced charge noise [e^-/px]
t	Exposure time [s]
N	Number of exposures

Table 8.1: Variables, units, and descriptions for parameters used in Equation 8.1 to calculate the signal-to-noise for our observations.

are scattered off the mirror into the aperture, which will depend on the scattering profile of the mirror. RON/G is the readout noise, which is drastically reduced by the EM gain. CIC is also a small value that is dependent on the vertical clocking speed of the CCD chip. F^2, the excess noise factor, is explained below.

8.2.2.2 Excess noise factor

The excess noise factor (ENF) is a noise term that is unique to the Electron Multiplying CCD (EMCCD) and is a result of the probabilistic nature of the generation of the gain. EMCCDs are different from conventional CCDs as they have an additional multiplication register in their readout electronics. As the electrons are being clocked out through this register, each stage of the register has a gate that is held at a higher potential than the others. Electrons that are clocked into this gate are accelerated by the potential difference and there is a small ($\alpha \sim 1\%$), yet finite probability that they will undergo an impact ionization. By the time a packet has reached the N_s^{th} stage, the avalanche of electrons has produced a gain of $G = (1 + \alpha)^{N_s}$. With hundreds of stages, gains of 1000x can be produced. With sufficient gain, the readout noise is essentially eliminated. However, this comes at a cost. Since the amount of electrons produced in each ionization stage is a probabilistic event, there is an uncertainty in the actual gain produced. [64] derives the uncertainty in this process as the ENF (Equation 8.2), which effectively reduces the QE of the system. In the limit of large gains, $F^2 \rightarrow 2$.

$$F^2 = 2\,(G-1)\,G^{-\frac{N_s+1}{N_s}} + \frac{1}{G} \tag{8.2}$$

8.2.2.3 Count rates

The count rates are converted from magnitudes [m] to [ph/s/px] using Equation 8.3, where F_0 is the zeropoint flux [$erg/s/cm^{-2}$/Å], m_z is the zeropoint magnitude, A_{tel} is the collecting area, $\Delta\lambda$ is the bandpass, E is the mean photon energy, QE is the detector quantum efficiency, and $\mathcal{T}$ is the optical throughput.

$$C = F_0 \times 10^{-0.4(m-m_z)} \times A_{tel} \times \Delta\lambda \times E^{-1} \times QE \times \mathcal{T} \tag{8.3}$$

8.2.3 Expected performance at McMath

8.2.3.1 Modeled starshade performance

Using the diffraction model developed in Chapter 5, we can estimate the expected contrast and shadow size for our observations at McMath. We model a 30 cm diameter hypergaussian starshade ($a = b = 6$ cm, $n = 6$) chemically etched out of 10-mil thick stainless steel (these are exactly half-sized models of those used in the dry lake bed tests). We calculate a broadband image from 400 nm - 850 nm weighted by the QE of our detector and the curve of a 8600 K blackbody. We neglect wavefront errors due to the atmosphere or mirrors. Figure 8.2 shows the predicted shadow size at 2.4 km away. We can fit a 6 cm telescope in the deep shadow and achieve 10^{-6} suppression. Figure 8.4 shows the predicted contrast for a 6 cm and 2 cm aperture, with the 2D image for the 6 cm aperture shown in Figure 8.3. At the location of the debris disk at 17 arcseconds, the contrast for the 6 cm aperture is steeply falling and just barely clears 10^{-10} and the contrast for the 2 cm aperture is 10^{-8}, demonstrating the gain in contrast we get from the higher resolution. This does not necessarily mean it is better to use the 6 cm aperture, as the chances of misalignment are higher. Adding a turbulent atmosphere has a similar effect to using a smaller aperture and light from the edge of the starshade is blended into the region of interest and the contrast is reduced (Figure 8.5).

8.2.3.2 SNR estimate

In the limit of the short exposures we are forced to take, readout noise is our dominant error term (neglecting starshade misalignment) and we must have sufficient gain to overcome it. Figure 8.6 shows the SNR as a function of exposure time for different apertures and different EM gains. A 2 cm aperture with high gain can outperform a 4 cm aperture with low gain and can reach a SNR of 5 in 2 hours. A 4 cm aperture with high gain can reach this in a matter of minutes. Figure 8.6 assumes 8" seeing and 0.1 s exposures, with the total exposure time being accumulated with numerous frames. The aperture size is a strong effect on SNR, both due to more collecting area and to a smaller PSF keeping the light leaking around the starshade from blending into our region of interest. After 10^{-6} contrast is reached, there is little benefit in better contrast as other noise terms dominate.

Figure 8.7 shows the effect of gain and individual exposure time on SNR, with the higher gain enabling us to overcome the readout noise of individual images without suffering the consequences of stacking images. In calculations before our observing run, we did not appreciate how short of images we would need to take and thought we were overcoming the readout noise with a gain of 60. However, this was not the case and we could have benefited from the higher gain.

Our SNR estimate has one major caveat in that it does not account for atmospheric extinction from scattering off aerosols in the atmosphere across the horizontal path. Over 2.4 km of ground level air, we are close to doubling the optical depth of atmosphere we are observing through and can see an exponential decay in the source brightness. The error terms from the sky background and diffracted light will be affected in the same manner, so our contrast value will be unchanged, but if we are unable to overcome the readout noise, the attenuation of the signal could significantly lower our SNR.

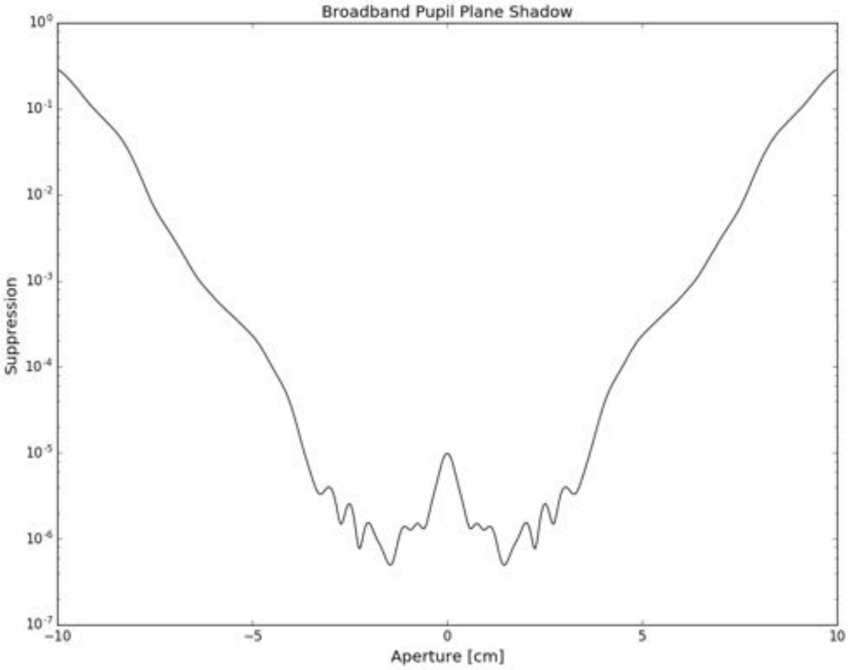

Figure 8.2: Suppression across and beyond the pupil at McMath showing the width of the shadow. Neglecting atmospheric effects, we can fit a 6 cm aperture in the deep part of the shadow.

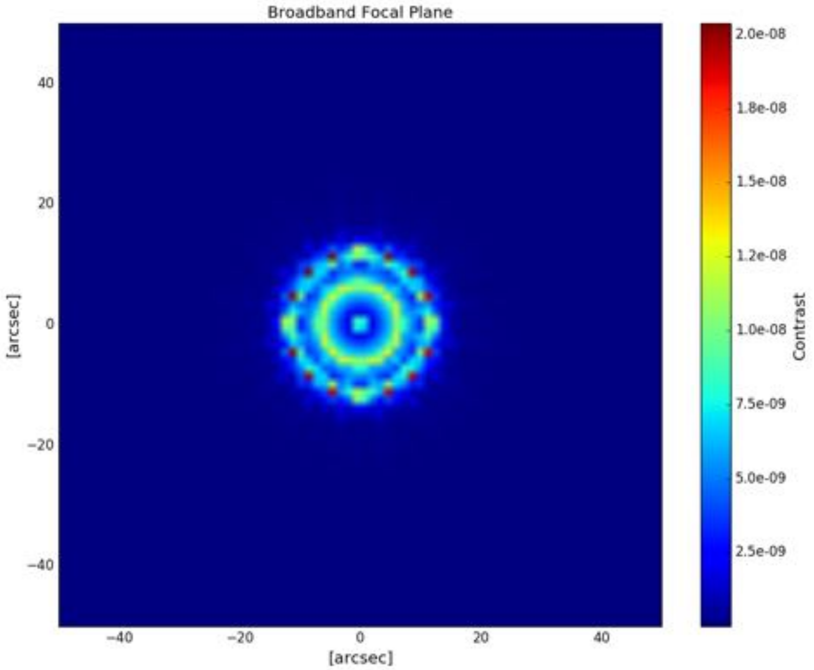

Figure 8.3: Modeled broadband focal plane image with 6 cm aperture. The large aperture is able to resolve the starshade and can separate light coming from different regions on the starshade to reduce the contrast.

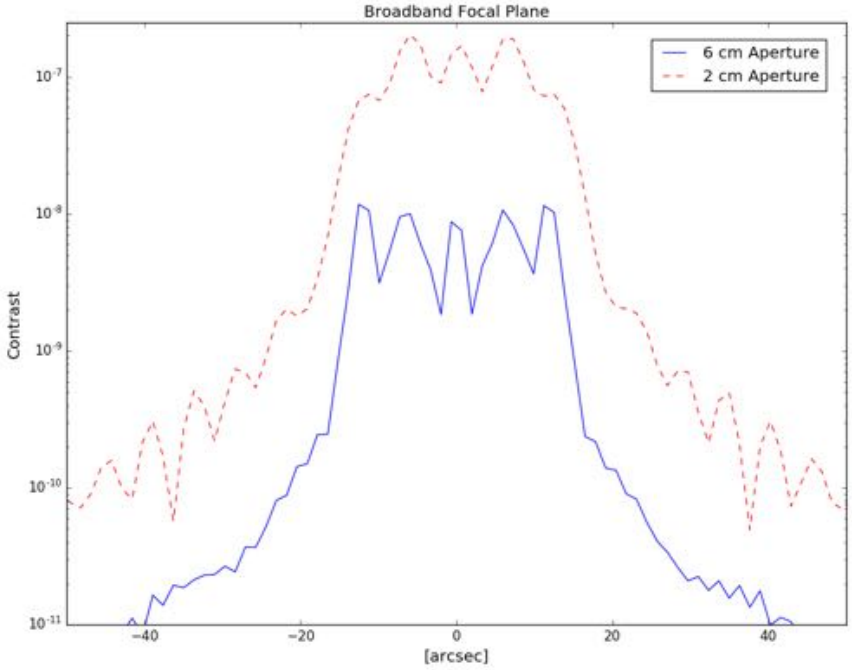

Figure 8.4: Comparison of the predicted contrast for a 2 cm **red** and a 6 cm **blue** aperture. The 6 cm aperture allows an order of magnitude reduction in the contrast as it is able to better resolve the tips and valleys of the starshade and can separate their light.

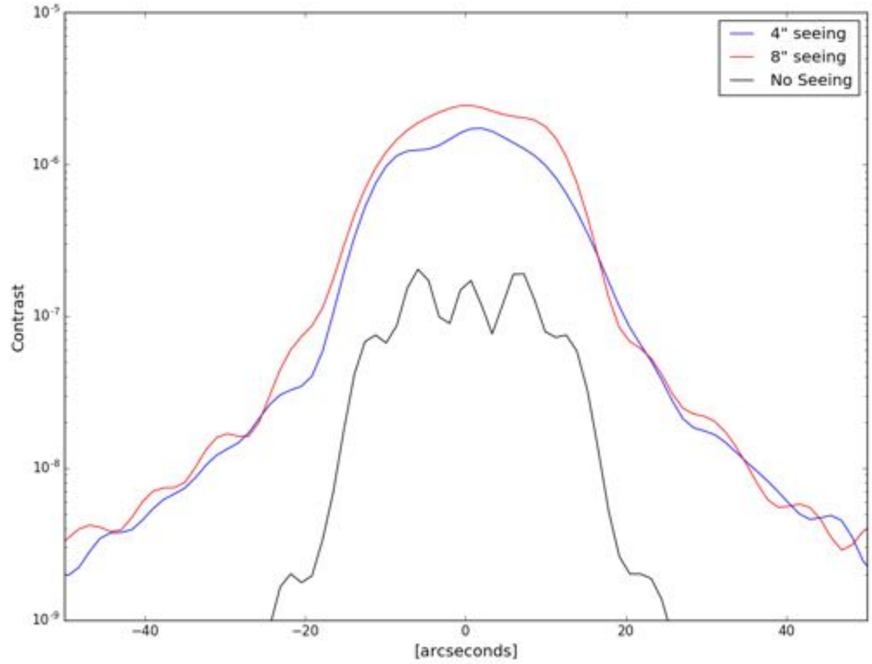

Figure 8.5: Modeled contrast of 2 cm aperture with atmospheric seeing of 4″ (**blue**) and 8″ (**red**), and with no seeing (**black**). There is little difference between 4″ and 8″ seeing.

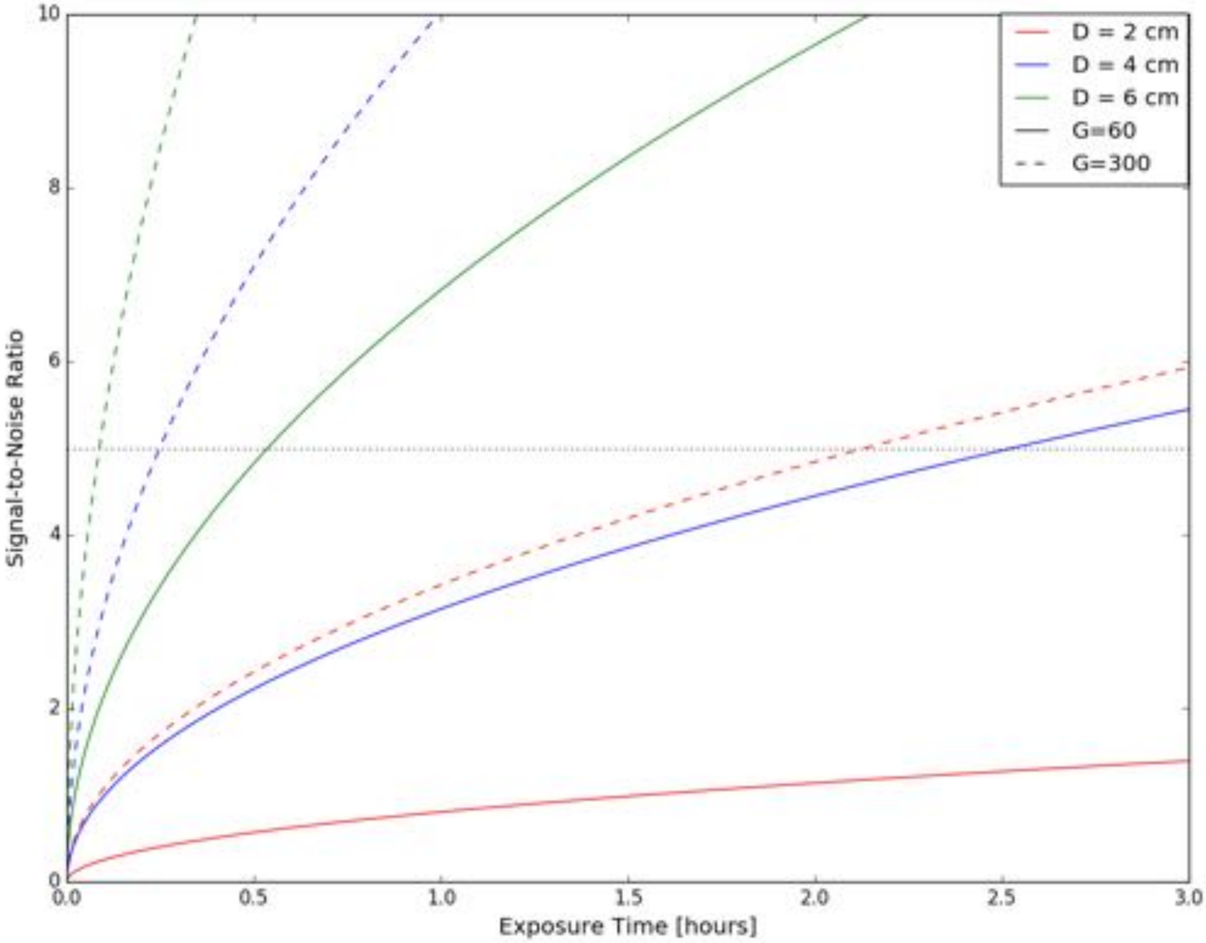

Figure 8.6: We plot the expected SNR vs exposure time for different aperture sizes (**solid**) and gains (**dashed**). The higher gain is able to overcome the readout noise to reach a SNR more quickly. With a 4 cm aperture and high gain, the disk should be detected in 15 minutes. These estimates do not account for atmospheric extinction.

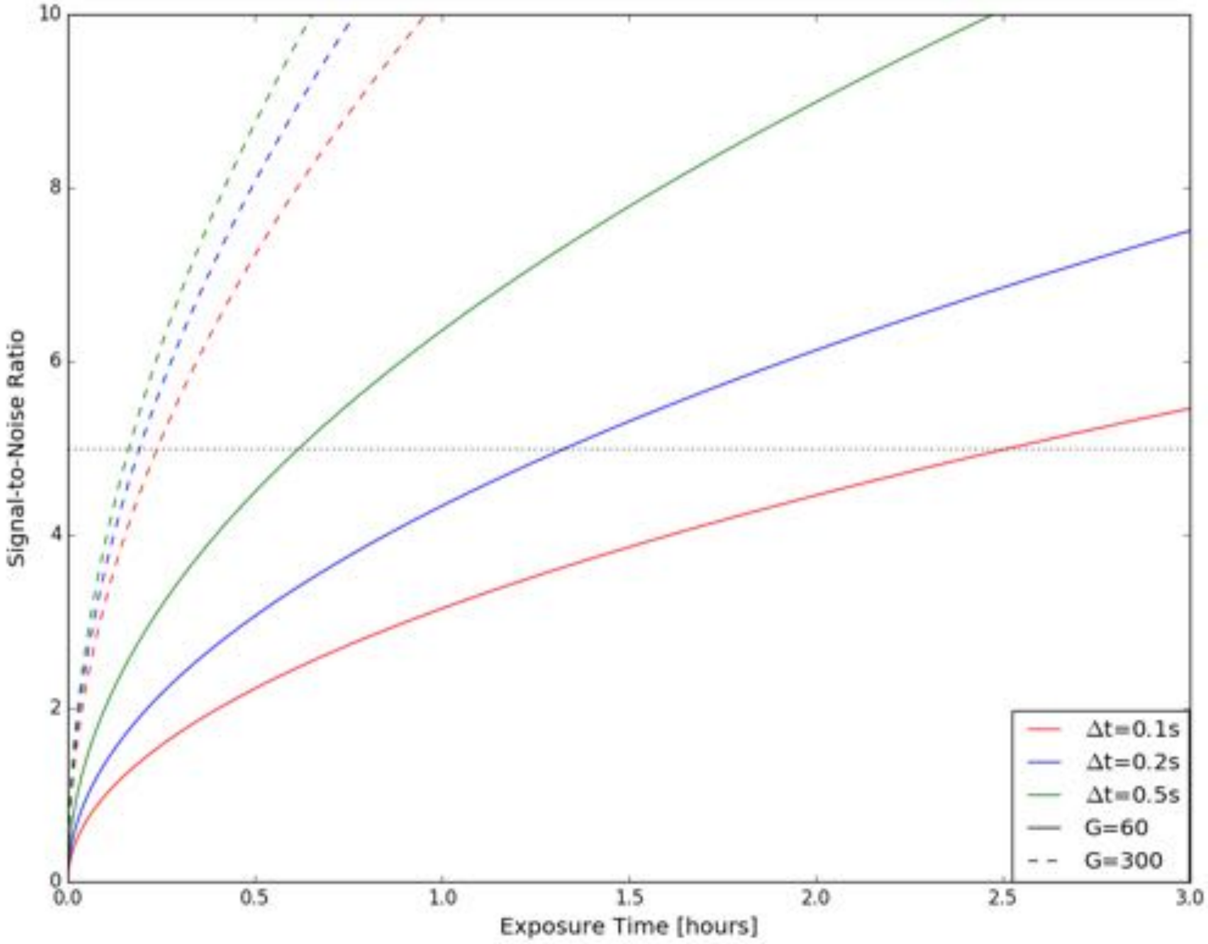

Figure 8.7: We plot the expected SNR vs exposure time for different individual exposure times (**solid**) and gains (**dashed**). The longer the individual exposure time, the fewer images we need to stack together and the less read noise that is contributed. There is little difference when the gain is high enough to overcome the read noise.

Ideally, the larger aperture and longer integration times would be used, but these calculations do not take the motion of the shadow into effect. Tip/tilt errors in the atmosphere move the shadow around on faster timescales than we can correct for in the feedback loop and our aperture moves out of the deep shadow. We therefore have a tradeoff between the number of images that we can keep, which decreases with aperture size, and the collection area, which increases with aperture size. To investigate this tradeoff, we look at the probability of the full aperture being within the shadow and note that the exposure time is proportional to the probability. Note that when we talk about the shadow, we do not mean the geometric shadow, but rather the deep shadow in which we have our maximum suppression.

If we assume the center of an aperture (x_0, y_0) of radius R follows a normal distribution with zero mean and variance $\sigma_x^2 = \sigma_y^2$, then the probability of being in the shadow of radius r follows as,

$$\begin{aligned} P\left(< r\right) &= \frac{1}{\pi} \int_{-(r-R)}^{r-R} \int_{-(r-R)}^{r-R} e^{-\frac{x^2}{2\sigma_x^2}} e^{-\frac{y^2}{2\sigma_y^2}} \, dx \, dy \\ &= \operatorname{erf}^2\left(\frac{r-R}{\sqrt{2}\sigma_x}\right) \end{aligned} \tag{8.4}$$

We see that as $R \to r, P \to 0$. Assuming $t \propto P\left(< r\right)$, we can find the aperture size that maximizes the SNR. Figure 8.8 shows the relative SNR vs aperture size for a number of variances in the shadow motion. We find that σ_x has the strongest dependence on aperture size. For large σ_x, as is the case for bad seeing when the aperture is moving in and out of the shadow, 4 cm tends to be the optimal aperture. As the seeing improves and the shadow is hardly moving, then we have no worry of coming out from behind the shadow and we can fill the shadow with our aperture.

These calculations show that as long as we are able to use larger than 4 cm aperture and use sufficient gain, the debris disk around Fomalhaut is obtainable in a reasonable amount of time. Keep in mind though, that in order to obtain an accumulated hour of usable images, we have to throw away a lot of data when we are too far out of misalignment to use the data. There is also a large overhead in getting initial alignment to a target and taking images of the unblocked source. An hours worth of usable data takes about 3 full nights of observing.

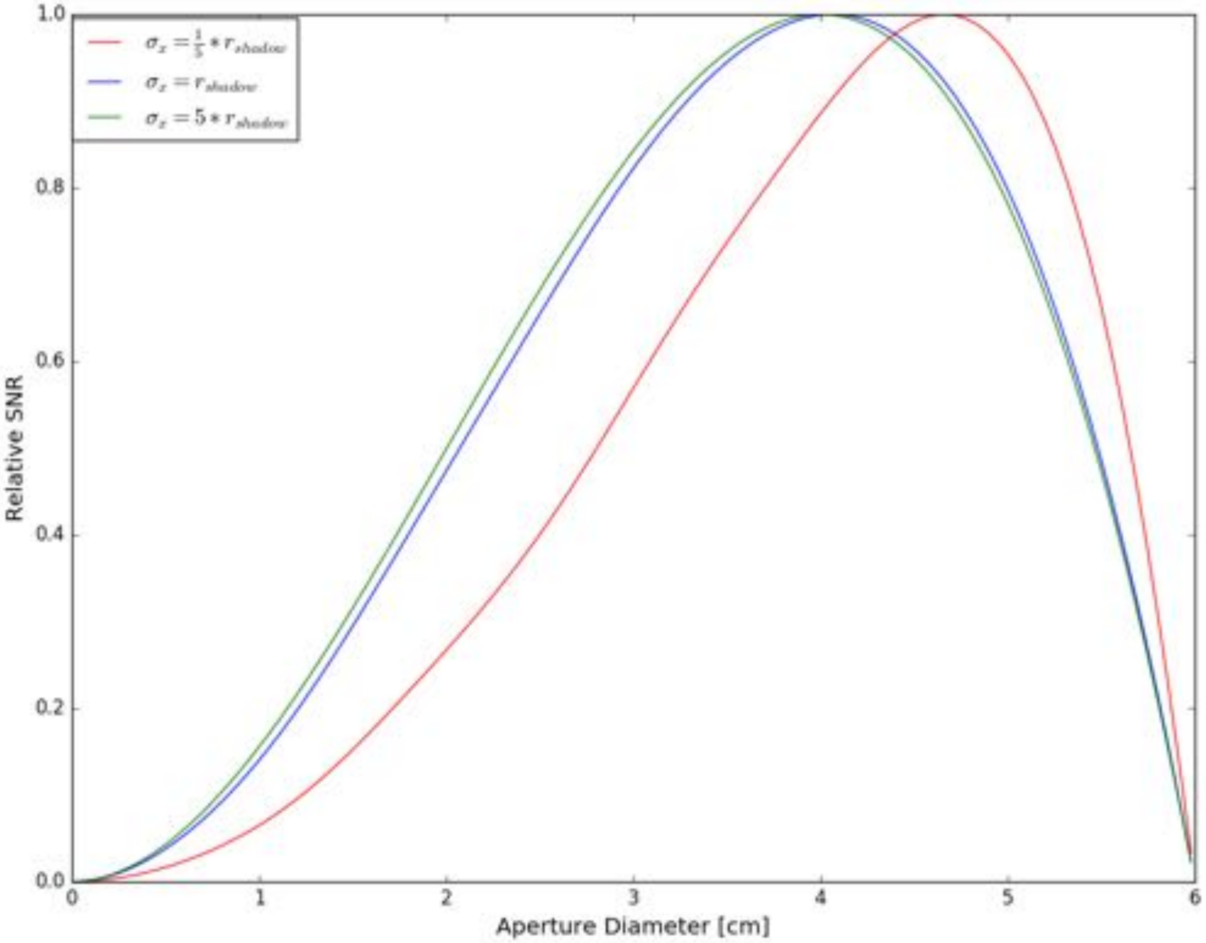

Figure 8.8: The predicted relative SNR as a function of aperture size is plotted for different strengths of random motion of the shadow. Once the image motion is comparable to the aperture size, we are out of alignment often enough that there is no benefit to the larger aperture.

8.2.3.3 Simulated images

As an easy way to visualize the effect that seeing and various aperture sizes have on the image quality, we generated simulated images of Fomalhaut's debris disk. These images simulate sky brightness, contrast leaking around the starshade, detector noise, photon noise, and atmospheric seeing. Figure 8.9 is the worst case with a 2 cm aperture; the large PSF blurs the light from our IWA and the disk is clearly not visible. Figure 8.10 is with a 4 cm aperture and the presence of a disk is obvious. Figure 8.11 is the 6 cm aperture, where we are able to fully resolve the disk. All simulations assume 8" seeing, $G = 60$, 10^{-6} contrast, and a 3.5 hour exposure, but does not include the effect of stacking individual images. In Figure 8.12, we use a 6 cm aperture, but have only 2" of seeing, where we can take full advantage of the resolution of the 6 cm aperture and resolve the ring of the disk.

8.2.4 Science goals

Our main motivation for going after the Fomalhaut debris disk is that it is one of the best suited debris disks for our observations (relatively bright and large IWA) that is within reach. Additionally, it has eluded previous ground-based efforts and detecting it with our setup would be an impressive statement about the power of starshades. I must note that the fact that we did not detect it is not a negative statement about starshades. Besides a few minutes in August, we were only able to observe it on our first run when we did not have a feedback system working. Now that we have experience observing at McMath and an operational system, I believe we have a better chance of getting it on the next serious observing run.

A detection of the disk would not be able to beat the resolution or image quality of HST, or have a chance of observing Fomalhaut b. Our primary goal is simply a detection, so we would first observe with an open filter to collect as many photons as possible. However, once we were confident in a detection, we could make scientific contributions beyond what was provided by HST by doing broadband photometry in filters other than those of HST, which were primarily done at

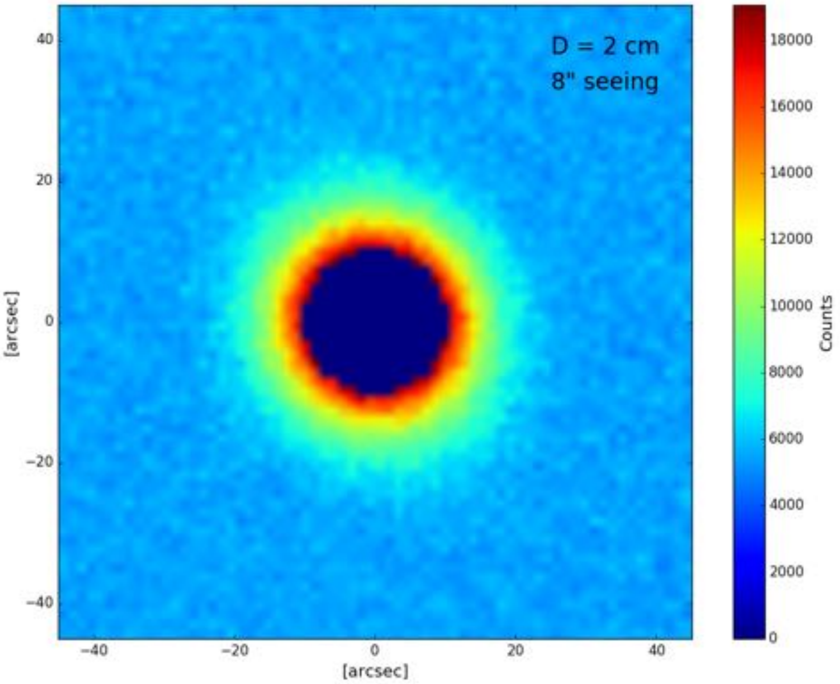

Figure 8.9: Simulated image (3.5 hr total exposure) of Fomalhaut's debris disk with **2 cm** aperture and **8″ seeing**.

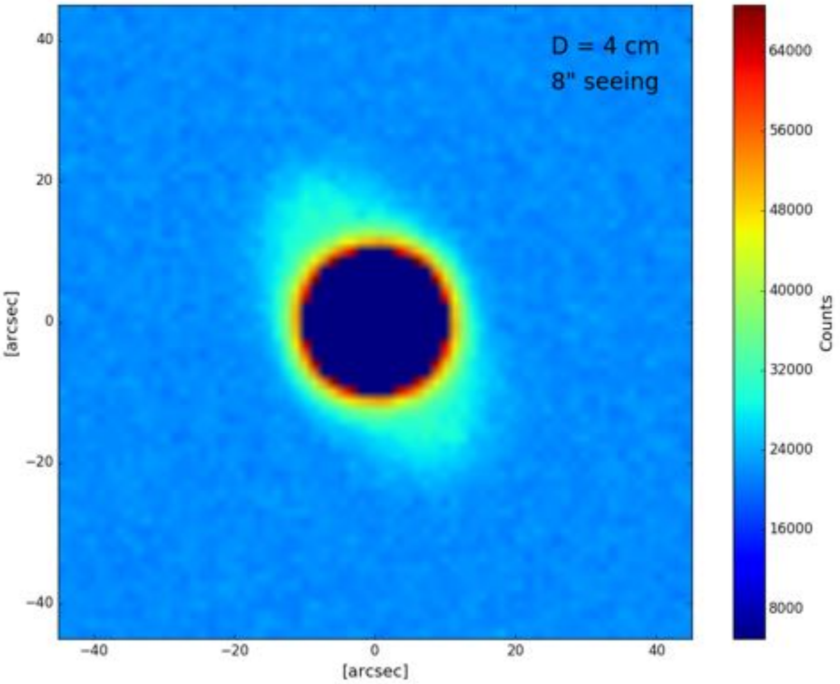

Figure 8.10: Simulated image (3.5 hr total exposure) of Fomalhaut's debris disk with **4 cm** aperture and **8″ seeing**.

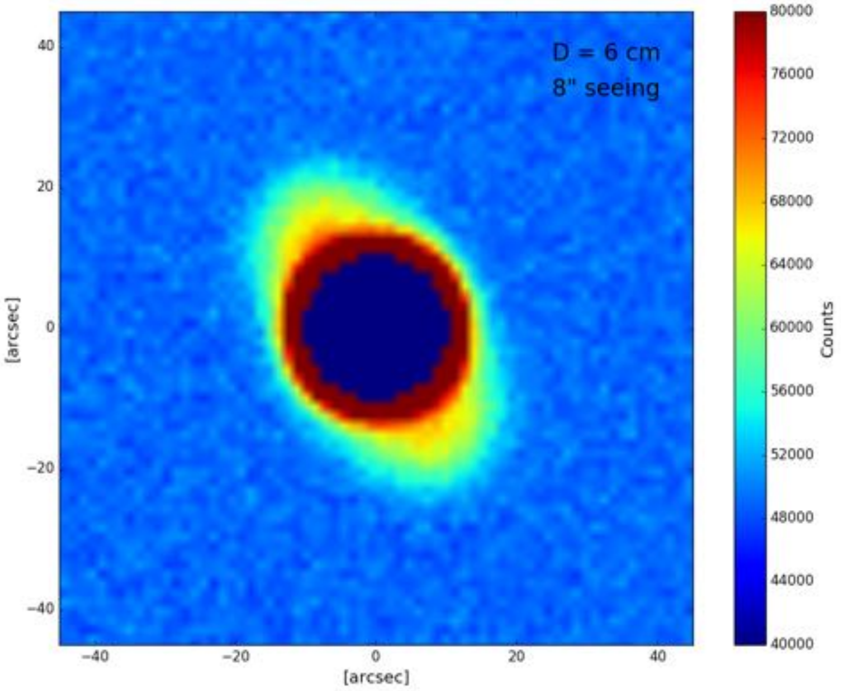

Figure 8.11: Simulated image (3.5 hr total exposure) of Fomalhaut's debris disk with **6 cm** aperture and **8″ seeing**.

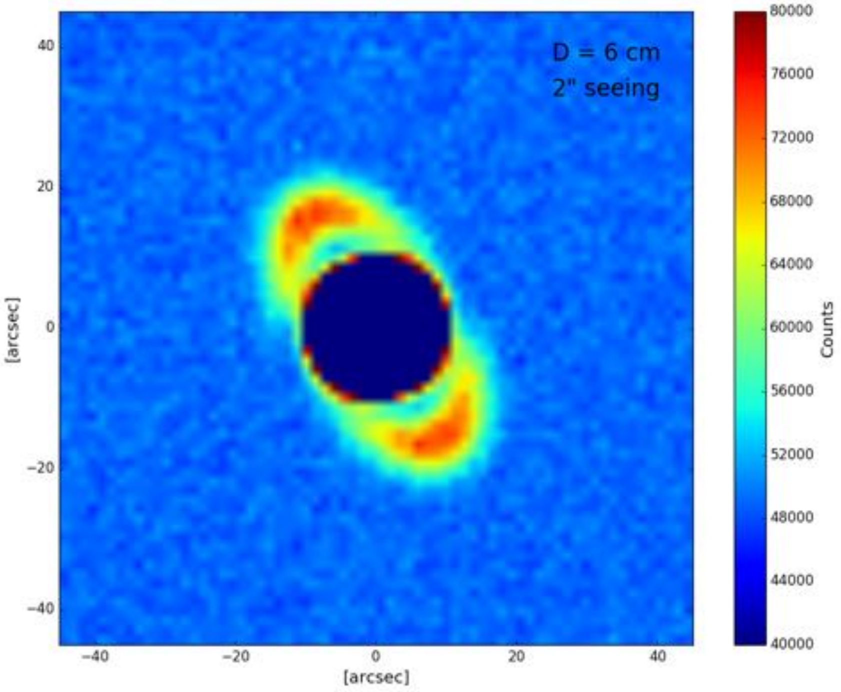

Figure 8.12: Simulated image (3.5 hr total exposure) of Fomalhaut's debris disk with **6 cm** aperture and **2″ seeing**.

0.6 μm and 0.8 μm. Broadband photometry in the blue, where we also have better contrast from the starshade, could provide additional constraints on the size distribution of dust grains in the disk, which could help point towards the formation mechanism of the disk and what Fomalhaut b's role is in the regeneration of the disk.

8.3 Observations

The following sections detail the observations taken at the McMath-Pierce Solar Telescope over the past year using the closed-loop tracking system discussed in Chapter 7. Our ultimate goal was to image the debris disk around Fomalhaut and demonstrate that this facility can be used to do cutting-edge science, but with the understanding that this is a novel observing technique and it would take some work to get to that level. To summarize, we did not detect Fomalhaut's disk, but obtained new visible light photometric measurements of stars in the vicinity of Vega. We were also able to demonstrate this novel way of testing starshades and outline the path towards science with starshades in the near future. Videos of a few observations from McMath can be found at: `http://casa.colorado.edu/~harnessa/movies`

8.3.1 Summary of observations

We conducted two full observing runs at McMath, the first in November 2015, the second in April 2016. We had a short run in early July 2016 to experiment on the mirrors in the system, and were completely weathered out in late July 2016. The dates of these runs, along with the targets we observed, are shown in Table 8.2. The parameters of the starshade architecture used in these observing runs are in Table 8.3. I'll briefly summarize the first three observing runs to lay out what we learned and how that drove the design of the system.

8.3.2 November 2015 observing run

In this week-long campaign we conducted the first tests at the 2.4 km separation on the SW Ridge. The Northrop Grumman team had previously been testing at a closer 400 m location [58],

Run	**Dates**	**Notes**	**Target**	**Total Exposure Time [s]**
1	11/9/15 - 11/13/15	– First test from 2.4 km – No feedback loop	Fomalhaut	8400
			Aldebaran	670
			Vega	290
2	4/5/16 - 4/9/16	– First test of feedback loop	Rasalgethi	3400
			Arcturus	2900
			Sirius	1800
			Altair	1200
			Vega	760
3	7/11/16 - 7/13/16	– Primarily test of mirror scatter	Vega	430
			Antares	360
4	7/31/16 - 8/2/16	– Weathered out	Fomalhaut	140

Table 8.2: Summary of McMath Observations with the total exposure time observed on each target. This total time is not necessarily the total time of usable data.

and we wanted to see if we could practically extend the separation to access a smaller IWA. Our main concern was whether we would be able to align the West Auxiliary across that far distance. Section 7.2.5 provides an explanation on how we are able to use the mirrors to align a star with our telescope. We were able to succeed (more easily than we suspected) and took the first images at the long baseline, with our main target being Fomalhaut. It quickly became apparent that the seeing was worse than we expected and it was difficult keeping the star behind the starshade. At this time, we were maintaining alignment by observing the star on the observing table in the control room and manually tracking. This worked for the shorter baseline, but the alignment was more sensitive at the long baseline and the seeing was significantly worse. We tried our best to keep alignment by watching the camera images as they were coming in and radioing directions for a team member to move the Main from the control room. We obtained a few hours worth of data on Fomalhaut, but most data had to be discarded as we were out of alignment. This run made it clear that we would need an automated tracking system using images taken from the SW Ridge.

Parameter	**Short Baseline**	**Long Baseline**
Starshade diameter (to inflection point):	16 cm	24 cm
Starshade-Telescope Separation:	570 m	2.4 km
Inner Working Angle:	30”	10”
Fresnel Number:	22	12
Telescope diameter:	2 cm	2 cm
Resolution elements across starshade:	11	4
Wavelength Coverage:	400 nm - 800 nm	400 nm - 800 nm

Table 8.3: Optical parameters of McMath experiment in the **short** and **long** baseline configurations.

8.3.3 April 2016 observing run

This observing run was the first implementation of the closed-loop feedback system we developed to help overcome tracking errors and atmospheric disturbances that caused misalignment. The tracking system worked well and significantly improved the amount of time we were behind the starshade, though there were still movements faster than our 1 Hz update rate that we could not control for. As Fomalhaut was not up at this time of the year, we focused our observations on Rasalgethi, which has a 10^{-5} times fainter companion at 20”. After analyzing the data from the November trip, we decided to increase our focal length using a 2x Barlow Lens and added two alignment lights on the McMath structure that made it easier to coadd the images.

8.3.4 July 2016 observing run

We did a short observing run in July 2016 to investigate how starlight diffracted by the starshade and scattered by the siderostat propagates through the rest of the optical train and to infer what the limitations of the McMath configuration is. We observed from a short 500 m baseline and the long baseline and placed various obscurations in the beam path to observe where stray light is coming from. It was not our main priority on this run, but we were able to take 5 minutes of observations of Vega which detected two faint background stars.

8.3.5 Observing procedure

After we follow the alignment and calibration procedures to get the target in our FOV and turn the tracking system on, we can begin our science observations. As we were still learning how the atmosphere behaves at this separation, how well our tracking system works, and what effect misalignment has on our data, we played around with different exposure times, aperture sizes, and gains to understand which works best. We kept track of what parameters were used so that we could take the appropriate dark images. We have a better understanding now of what is ideal, but it has been an iterative process as the setup and observing conditions changed between the first two runs.

Our basic observing procedure is to look at a small number of targets to minimize the overhead in realignment. Once we start observing a target, we sit on it and continuously take images of the star behind the starshade. There is small management required to keep the tracking system updated to account for the tracking telescope and science telescope sampling different patches of atmosphere and we have the control room change the Main's tracking rate periodically to help correct for long term drifts. We watch all images as they are downloaded in real time to assess the atmospheric conditions and change our exposure time accordingly. Every 30 minutes or so, we move the target from behind the starshade and take images of the unblocked star to give us our calibration level for a contrast calculation. We want to take the unblocked images as close in time to our blocked images to sample the same atmospheric conditions, but the time wasted in realigning means we do not want to do it too often.

8.4 Data Analysis + Results

The data product from the observation runs are a large number (~30,000 per night!) of short exposure EMCCD images. The image processing of such a large dataset, particularly low signal images in a varying atmosphere and on an unstable platform, is not trivial. There are a lot of moving parts in this optical system that makes the image registration difficult. The star field we are observing is an image projected by the siderostat mirror, which is moving in a random motion as our tracking system is compensating for misalignments. This is also made difficult by the low resolution of the large pixel size of the camera and small aperture. However, we try our best with the data we have to stack the images and increase the signal-to-noise. Note that many of the problems we encounter with this system could be alleviated and controlled for with a dedicated siderostat facility.

8.4.1 Image alignment

For a given night, the position of the starshade in the image is fixed, although the entire scene can move due to vibrations of the telescope. We correct for movements of the scene by registering the images with two alignment lights mounted to the exterior of McMath (see Figure 8.3). For each image, the image positions of the alignment lights are found with an intensity-weighted centroid and the images are translated to register on the lights. This is done for all images observed on the same night. The starshade is viewed through the West Auxiliary heliostat of McMath, which is not necessarily in the same position night-to-night. Images between nights are aligned using the starshade as the registration position. All images for a given night are stacked together and the starshade position is found by centroiding the inverse of the image (since the starshade is the darkest region). This procedure generates images that are aligned on the starshade, which is best for calculating the performance of the starshade, but does not provide alignment of the star field. The field of view through the siderostat is only 90 arcseconds across and we do not have any background stars to align with. The tracking on the siderostat is more concerned with keeping alignment relative to the starshade, which may not correspond to the star field being in the same location on the detector. Future designs of a siderostat facility with a limited field of view will need to address this issue and come up with a way to do image stacking when the field is moving in an unknown fashion; perhaps injecting an artificial guide star that is in the field of view.

8.4.2 Unblocked target brightness

To convert images while the starshade is in place into units of contrast, or to convert into an estimate of surface brightness, we need to know the brightness of the target star without the starshade in place. The brightness of the unblocked source is variable due to the atmospheric effects of traveling on a large horizontal path. Normally we would fit a gaussian to the PSF of the unblocked source to calculate the peak brightness, but the amplitude of that gaussian changes as the variable seeing broadens the PSF beyond the diffraction limit. To account for this broadening, we sum the total number of counts over a subaperture in the image to calculate the total energy in the PSF. This too is variable as scintillation in the atmosphere induces variability in the intensity. The variability in the brightness of the unblocked source is by far the largest source of error in our contrast calculation.

We can lower the error bars on the contrast value by observing the unblocked source frequently and as close to possible as our blocked observations to try to sample the same atmospheric conditions. We did not do a very good job at keeping with this strategy; we wanted to get as much unblocked data as possible and the overhead time for switching between blocked and unblocked images is significant.

For Arcturus in Run 2, we split the unblocked images into 6 distinct 30 second observations over three nights. Figure 8.13 shows the peak brightness and total energy of the unblocked source as a function of time. There is a clear difference in the target brightness between observing nights. The brightness of Arcturus for different observations and the error on the brightness are shown in Table 8.4. The relative contributions from the dominate error terms are provided in Table 8.5. σ_{observed} is the observed variation in the brightness, σ_{shot} is the photon noise following Poisson statistics, σ_{gaussfit} is the RMS error in fitting a gaussian to find the peak brightness, and $\sigma_{\text{scintillation}}$ is the expected variance from scintillation. The scintillation variance is calculated from the scintillation index, σ_I^2, and is given by,

$$\sigma_I^2 = \frac{\langle I^2 \rangle - \langle I \rangle^2}{\langle I \rangle^2} \tag{8.5}$$

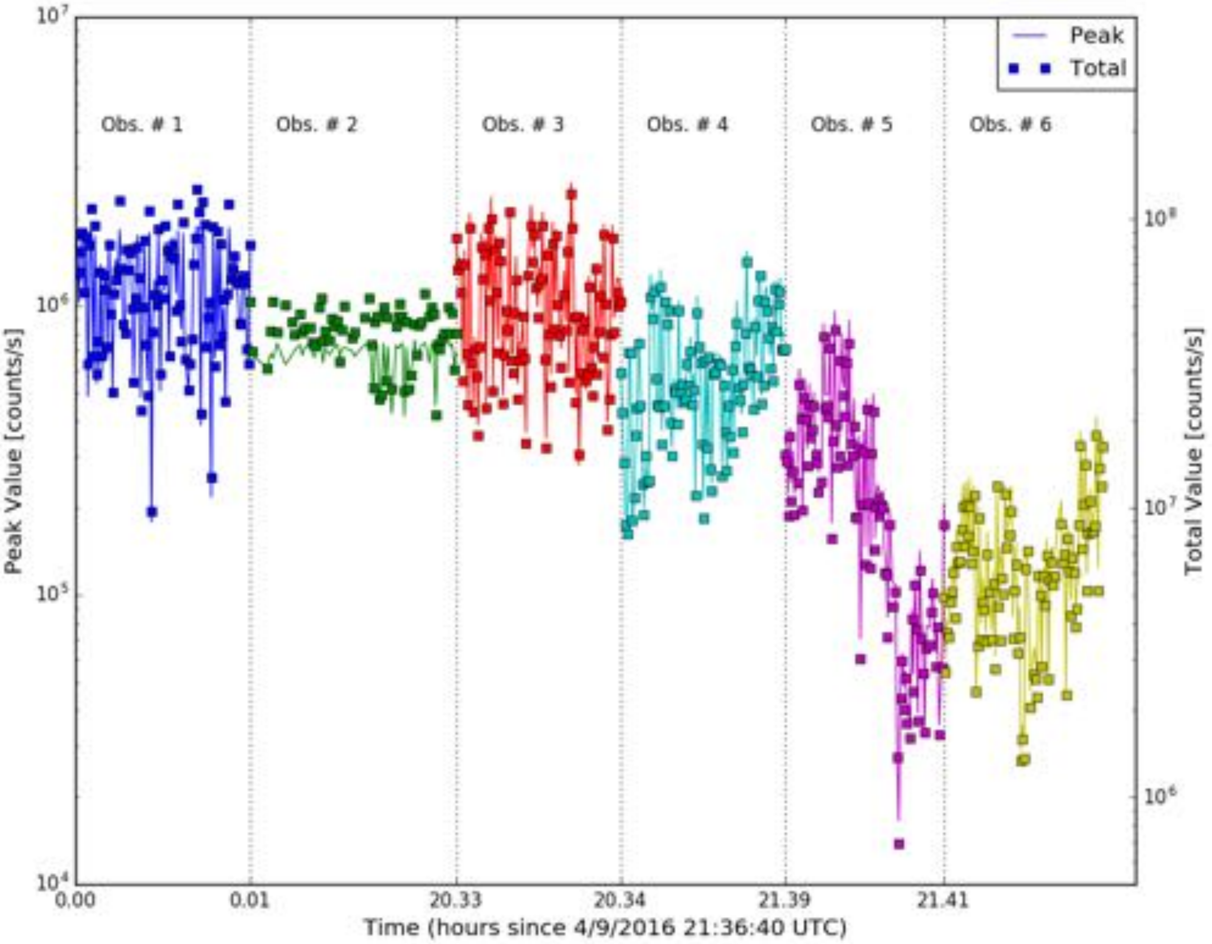

Figure 8.13: The brightness of Arcturus, peak value (**line**) and total amount (**circles**), as a function of time for unblocked images of Arcturus over the course of two nights. These data are taken from the **long** baseline. The vertical lines mark different groups of exposures. The variance in the brightness is due to scintillation in the atmosphere. The lower values in Observations #5 & #6 are most likely due to sampling different atmospheric properties.

where $\langle I \rangle$ is the mean intensity.

Table 8.5 shows that nearly all the error can be attributed to scintillation. The exception being Observation #5 in which a large systematic decrease in the brightness is seen, possibly due to a stable change in the atmospheric properties during that exposure. The exposure time in Observation #2 is longer than the others and looks more stable, but it has an upper cutoff and is believed to be saturated. As scintillation is the dominate effect, we find there is little difference in using the peak brightness vs the total energy in the PSF.

Observation	**1**	**2**	**3**	**4**	**5**	**6**
$\mu_{\text{Peak}} \times 10^5$ ct/s	11.9	7.0	9.4	6.0	2.3	1.3
$\sigma_{\text{Peak}} \times 10^5$ ct/s	4.64	0.83	5.40	3.12	2.18	0.77
% Err_{Peak}	39.0	11.9	57.2	51.9	95.2	58.3
$\mu_{\text{Total}} \times 10^7$ ct/s	5.98	4.18	4.57	2.68	1.03	0.59
$\sigma_{\text{Total}} \times 10^7$ ct/s	2.64	0.82	2.43	1.39	0.93	0.34
% $\text{Err}_{\text{Total}}$	44.1	19.5	53.2	52.0	90.9	57.5

Table 8.4: The mean (μ), standard deviation (σ), and percent error of the peak and total count rates for observations of unblocked Arcturus from the **long** baseline. The observation numbers correspond to those in Figure 8.13. At times, the error in the brightness of the unblocked source is up to 100%.

Figure 8.15 shows the seeing conditions, the estimated FWHM of the seeing PSF and the Fried parameter (r_0), for the unblocked source observations in Figure 8.13. The first thing to notice is how terrible the seeing is; typically around 9 arcseconds. This is due to the large horizontal path through a thick, turbulent ground layer. The vertical profile of the terrain the light path passes over is shown in Figure 8.14. The light's proximity to the ground and the rapid changes in the ground elevation results in large changes in the air temperature that generate turbulent cells of varying index of refraction. Assuming the turbulence is dominated by the horizontal path, we estimate the refractive index structure constant to be $C_n^2 \sim 2 \times 10^{-13}$. Scintillation becomes important when the coherence size approaches the Fresnel radius of the turbulence and diffraction from the seeing disk causes interference at the aperture, i.e., when $r_0 \sim \sqrt{\lambda z}$ [66]. With the strong turbulence seen in these observations, the distance from the turbulence at which scintillation dominates is only 400

Observation	**1**	**2**	**3**	**4**	**5**	**6**
σ_{observed} [%]	39.1	11.7	57.4	51.6	92.3	63.7
σ_{shot} [%]	0.1	0.1	0.1	0.1	0.2	0.3
$\sigma_{\text{gaussifit}}$ [%]	2.2	4.5	2.2	2.4	3.6	4.6
$\sigma_{\text{scintillation}}$ [%]	38.9	12.3	49.8	48.8	76.0	59.0

Table 8.5: Relative contribution of different sources of error to the total error in the **unblocked** source brightness. The variance in the brightness due to scintillation in the atmosphere is by far the dominant error term. These data are for Arcturus from the **long** baseline.

m, meaning the strong turbulence in the horizontal layer is dominating the scintillation effects.

8.4.3 Contrast

We examine the performance of the starshade working in the siderostat system by calculating the contrast ratio as a function of inner working angle. Recalling from Section 2.2.2, the previous definition of contrast is the ratio of the count rate of photons in a resolution element to the peak brightness of the unblocked source. This definition is strongly dependent on parameters of the telescope. Since our main motivation for measuring the contrast is to quantify how faint of a target we can detect, we instead use a signal-to-noise argument to set an upper limit on the contrast.

We follow the procedure of [29] to calculate the contrast level from the background noise. We draw photometric subapertures in the image as if we were trying to pull a point source out of the noise and calculate the standard deviation of pixel counts within that subaperture. This is considered the 1-σ noise level in our PSF (note that this does not include a term for the variance in the source since we are setting the limit of a non-detection and we assume this to be zero). Detecting a point source at n-σ confidence requires the signal to be $n \times \sigma$ higher than the background noise. This means we can describe our n-σ contrast value as the faintest value for which we have an n-σ detection. We convert the error to a contrast value by dividing by the peak brightness of the unblocked source (F_*) and our contrast becomes,

$$C_n = \frac{n\sigma}{F_*} \tag{8.6}$$

The dominant source of error in the contrast calculation is the true brightness of the unblocked

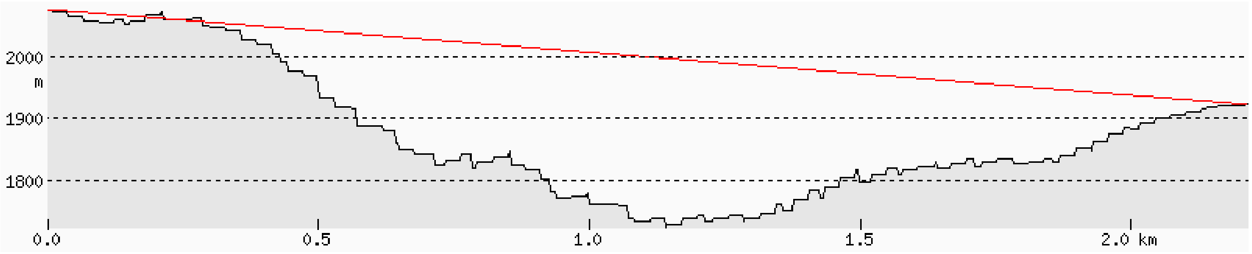

Figure 8.14: Vertical profile of the terrain along the line of sight from McMath (starting on the **left**) to the SW Ridge (on the **right**). The steep drops in terrain and the vicinity to the ground as the light passes over a ridge after it leaves McMath causes strong turbulence in the atmosphere. (http://www.heywhatsthat.com/profiler.html)

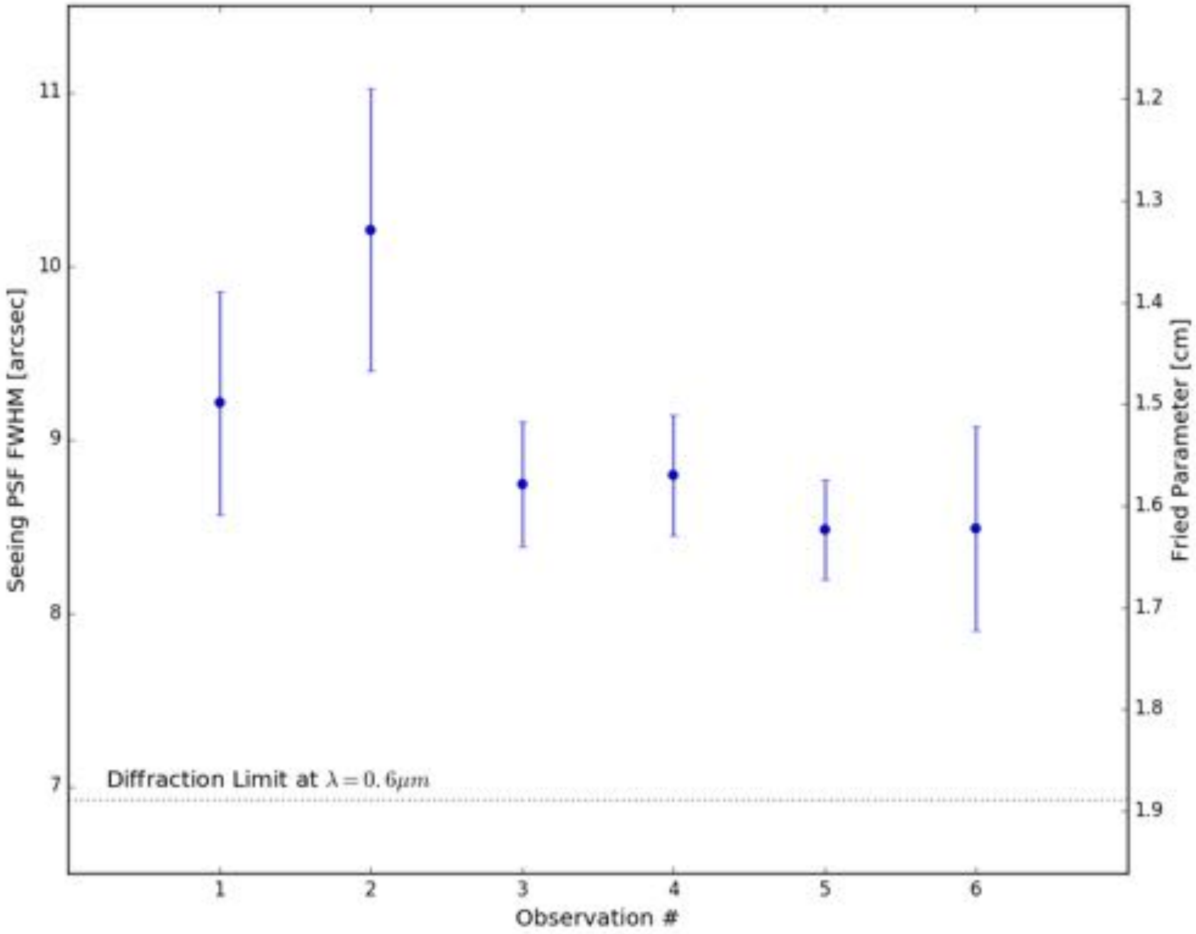

Figure 8.15: The estimate of atmospheric seeing, obtained from the width of the PSF in the image, for the different observations of Figure 8.13. The large seeing suggests very strong atmospheric turbulence.

source. To set bounds on the contrast, we calculate the contrast in Equation 8.6 using $F_* = \mu_{F_*} + \sigma_{F_*}$ and $F_* = \mu_{F_*} - \sigma_{F_*}$ as the lower and upper bounds of the contrast, respectively. Here, μ, σ are the mean and error in the unblocked source brightness.

The best contrast we achieve at the short baseline is with Vega and is $5.6^{+8.4}_{-2.1} \times 10^{-7}$. The best contrast we achieve at the long baseline is with Arcturus and is $2.0^{+1.57}_{-0.49} \times 10^{-5}$.

8.4.4 Suppression

The contrast ratio is a convolution of many factors external to the starshade and is a metric to determine the performance of the system, but can not determine the performance of the starshade alone. Suppression is the ratio of the total light entering the aperture while the starshade is in place relative to the total light entering without the starshade. In a space-based starshade mission, the suppression will reflect directly and depend solely on the light suppression capability of the starshade, making it a better metric for describing the starshade performance. However, in ground based experiments, external light contributions such as scattering off dust, mirrors, and the atmosphere will limit the ability to determine how much light is due to unsuppressed starlight and how much is due to the external factors. The relative faintness of these sources compared to the unblocked star is much too low to take into account in the unblocked images.

The ideal way to calculate suppression is by directly measuring the amount of light incident on the aperture; this can be done with a pupil imaging camera or a simple photodetector. However, for most experiments the only data taken are focal plane images, which have convolved the telescope's response with the light distribution. We attempt to calculate the suppression from our focal plane images by counting all the light that is coming from the edge of the starshade and compare that to the total amount of light from the unblocked source. All the light that comes from the target star that is unsuppressed by the starshade will be confined to an annulus around the edge of the starshade with the width of the PSF. Light from any other location in the image comes from an external factor and is not reflective of the performance of the starshade.

To calculate suppression, we sum the total number of counts in a box drawn around the starshade that encompasses the starshade diameter plus one PSF width on each side of the starshade. In this way we minimize the contribution from any light that is not coming from directly around the starshade. If there is an obvious bright spot on the starshade due to either the starshade stand or a preferred misalignment direction, we mask it out and replace it with the median value around the rest of the starshade. We sum the total counts in a same-sized box around the unblocked source. Dividing the two gives the suppression value.

The best suppression we achieve at the short baseline is with Antares and is $4.0^{+73}_{-1.9} \times 10^{-4}$. The best suppression we achieve at the long baseline is with Arcturus and is $4.2_{-2.1} \times 10^{-4}$.

8.4.5 Observations from 570 m short baseline

During our Run 3 observations, when our main focus was experiments on the mirrors in McMath and how light is propagating through the system, we took observations from the shorter baseline where we had 570 m separation between starshade and telescope. Observations are easier from this shorter baseline for a number of reasons. We are looking through less atmosphere and have better image quality from the lower seeing, the inner working angle to the starshade is larger and we are less susceptible to misalignment, and we have a wider field of view around the main target and have the opportunity to see background stars.

In this setup, we were able to achieve our best contrast of 5.5×10^{-7} at $30''$ and provided photometric constraints on background stars near Vega. Due to the lesser atmospheric extinction (and because our main goal of the test was not observations and we did not expect to use this data), our images of the unblocked sources, Vega and Antares, are saturated and we do not have a good flux calibration of blocked images. However, we can leverage observations of these targets from the long baseline to provide a calibration, with the caveat that there is significantly more extinction at the long baseline and our contrast and brightness measurements are most likely upper limits.

Our dominant source of error is variation in the system throughput due to scintillation of the atmosphere. To capture this uncertainty in the unblocked source, we report estimated, upper limit, and lower limit measurements that are calculated using the unblocked value (of mean μ_* and standard deviation σ_*) as either μ_*, $\mu_* - \sigma_*$, or $\mu_* + \sigma_*$, respectively. Note that this still does not capture the systematic error due to atmospheric extinction.

8.4.5.1 Photometric constraints on background stars near Vega

A stacked image of Vega with a total exposure time of 405 seconds is shown in Figure 8.16. These images are shifted to align on the star to the lower right of the starshade. During some of the images, the main siderostat was in motion, so the image of the stars move on the detector, but flaws on the mirror and starshade remain fixed. By correlating the motion of the sources in the image with each other and with the predicted motion of the main source (estimated by brightness of light leaked around the starshade), we can separate flaws on the starshade and mirrors from astronomical sources. We easily see two companions around Vega, one at the 12 o'clock position and one at the 5 o'clock position. We attribute these to be background stars that are listed in catalogs, but do not have photometric measurements in the visible band. There is a diffuse scatter around Vega, which is difficult to attribute to being astronomical in nature or being scatter from the mirror.

We compare Figure 8.16 to a 2MASS image showing the known sources around Vega (Figure 8.17) and contribute the two brightest point sources in the image to background stars, 2MASS J18370125+3848126 [19] (hereafter, J1837) and PPM 81557 [67]. We measure the brightness of the background stars to serve as our photometric calibration. The measured properties of the background stars are presented in Table 8.6. We calculate the total signal from the source with a photometric aperture equal to 1.5 times the PSF width (inner circle of black circle in Figure 8.16) and the average background level is calculated using the annulus between the inner and outer (5× PSF width) circles of Figure 8.16. We calculate the signal-to-noise of a detection using Equation 8.7, where S is the total number of counts in the photometric aperture minus the average background (μ_B), n_S is the number of pixels in the photometric aperture, n_B is the number of pixels in the background aperture, RON is the readout noise of the detector, and G is the detector gain. We

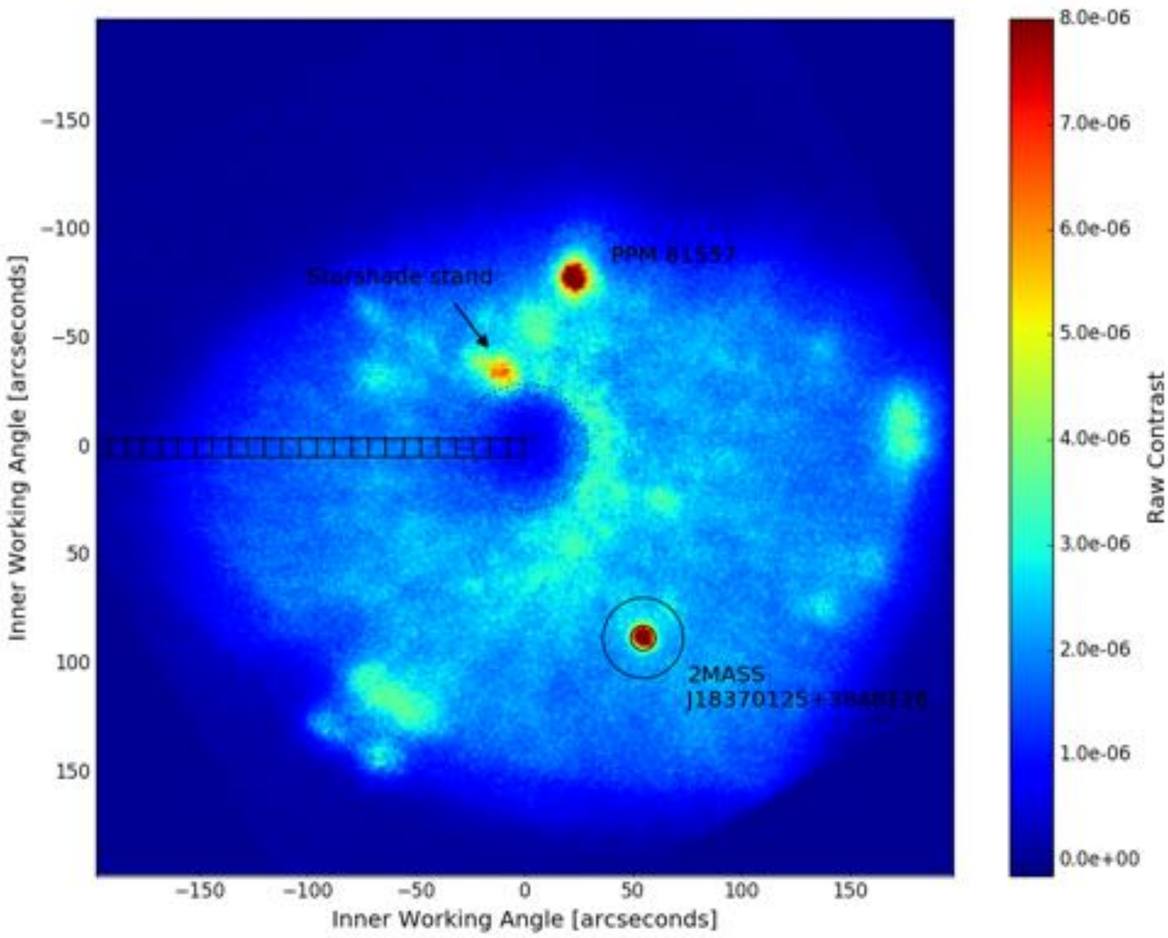

Figure 8.16: Stacked image (units of raw contrast) of **Vega** with a total exposure time of 405 seconds from the **short** baseline. The background stars 2MASS J18370125+3848126 and PPM 81557 are labeled. The **dotted circle** in the center corresponds to the IWA. The **boxes** mark the subapertures that the 3σ contrast values are calculated in. The **inner** and **outer** circles around J1837 correspond to the photometric and background apertures used to calculate the total signal and total noise, respectively, of the stars.

can safely neglect dark noise as the exposures are short and the detector is cooled to -60 °C.

$$SNR = \frac{S}{\sqrt{S + n_s \mu_b \left(1 + \frac{n_s}{n_b}\right) + \left(\frac{RON}{G}\right)^2}} \tag{8.7}$$

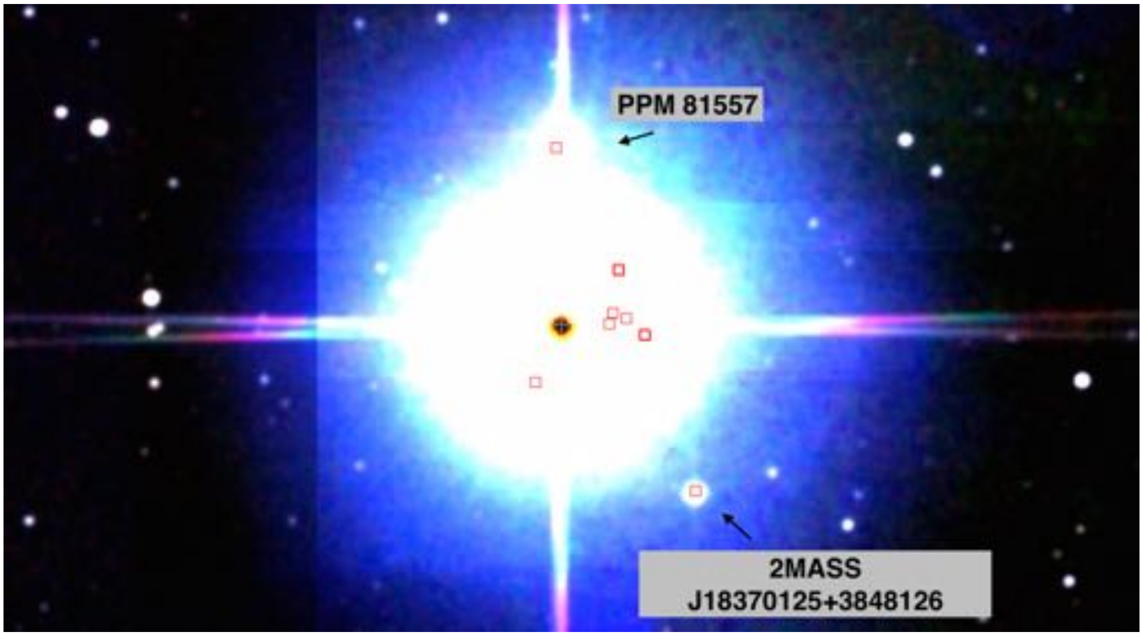

Figure 8.17: 2MASS image of Vega. The background stars 2MASS J18370125+3848126 and PPM 81557 are labeled. Even at 1.2 μm, Vega completely swamps the image. PPM 81557 is commonly listed as an artifact in the 2MASS catalog. Image obtained from [92].

Since our observations of Vega without the starshade in place are saturated, we must rely on the observations of unblocked Vega from the longer baseline, but since these observations are at a higher airmass and on a different night that is sampling different atmospheric conditions, they are not directly transferable to the short baseline observations. The procedure for calibrating the flux of the two stars is as follows.

(1) Measure unblocked Vega flux from long baseline

  - Clip observations that are above and below 3σ from the mean

(2) Integrate Vega spectrum [5] with detector QE to get expected flux from Vega

  - We ignore any other wavelength dependence of the throughput

(3) The throughput of our system at the long baseline is the measured flux divided by the expected flux

(4) Measure signal and noise from J1837 using the procedure described in the first paragraph

(5) Multiply measured flux by throughput to get theoretical flux of J1837

  - This assumes that the atmospheric throughput is the same between the two baselines, which is not true. The throughput for the long baseline will be higher than that of the short baseline, so we will overestimate the brightness of J8137

(6) Assume a flat spectrum and calculate AB magnitude of J1837

  - $m_{AB} = -2.5 \log_{10}\left(\frac{f_\nu}{3631\mathrm{Jy}}\right)$

The measured count rate from unblocked Vega at the long baseline is $(2.5 \pm 1.5) \times 10^6$ ph/s. We estimate the expected count rate by integrating the detector response function over a spectrum of Vega [5]; we neglect any other wavelength dependence on the throughput that could vary between Vega and J1837. The expected count rate is 1.0×10^7 ph/s, meaning we see a total system throughput (three reflections off mirrors in McMath, atmosphere between McMath and telescope, and telescope optics) of $(24 \pm 15)\%$, which we believe to be dominated by the atmosphere. Atmospheric extinction on this horizontal baseline should decrease exponentially with decreasing distance, so we expect the atmospheric throughput at the short baseline to be significantly higher and our estimations and error bars should be taken as the worst case scenario.

We use the total system throughput as measured from the unblocked Vega observations to scale our measured count rate of the stars to a theoretical total irradiance in our bandpass (defined where the detector QE $> 50\%$ and assuming a flat spectrum). The estimated spectral irradiance and AB magnitudes of J1837 and PPM 81557 are presented in Table 8.6. The quoted error bars are the 1σ errors arising from the detection of the source itself and the upper and lower limits are the estimated values if we take the lower or upper limits for the unblocked source value. These limits correspond to scintillation error in the unblocked source, but do not account for a systematic error that is expected due to the unblocked measurements being obtained at a higher airmass.

Combining our observations of J1837 with those from 2MASS [19], we fit a blackbody to the photometric measurements (Figure 8.18). We find the lower limit fits the data best with a reduced chi-squared of 2 and the fit gets better as our photometric data point gets fainter, which is consistent with our expectation of our data points being an upper limit. We find the best fit temperature is 4400 K, suggesting that this star (which we believe to be a K dwarf) is more red than Vega and is why it was detected at longer wavelengths only. Figure 8.19 illustrates this point by comparing blackbody curves of the same temperature and brightness as Vega and J1837, and the ratio between the two. In the visible band, J1837 is 10^{-5} times as faint as Vega and rises to 10^{-4} times fainter in the IR, where it was measured by 2MASS [19]. PPM 81557 (listed in an astrometric catalogue [67]) is brighter than J1837, but is 15 arcseconds closer to Vega. Even in the 2MASS NIR images, it is blended with the PSF of Vega and is flagged as a persistent artifact [61]. We did not find any reported photometric measurements of PPM 81557.

8.4.5.2 10^{-7} contrast measurements of Vega

We use the unblocked measurements of Vega to convert the images into contrast measurements. Again, since we are underestimating the true brightness of Vega, the contrast achieved is most likely better than reported. We follow the procedure outlined in Section 8.4.3 to calculate the 3σ contrast level in a series of boxes (seen in Figure 8.16) extending radially from one side of the starshade. These results are shown in Figure 8.20, where our measured contrast at the inner working angle of $30''$ is $5.6^{+8.4}_{-2.1} \times 10^{-7}$. Depending on which limit is used for the unblocked source value, we can set an upper limit on point sources at $30''$ at $m_V = 15.7$, $m_V = 14.7$, $m_V = 16.2$, for the measured, upper, and lower limits, respectively.

Detecting extended sources is more difficult, particularly with the high level of mirror scatter. In the future, we need to quantify the mirror scatter by observing targets that do not have circumstellar material and provide a clean template for a pseudo-PSF subtraction. We say “pseudo-PSF”

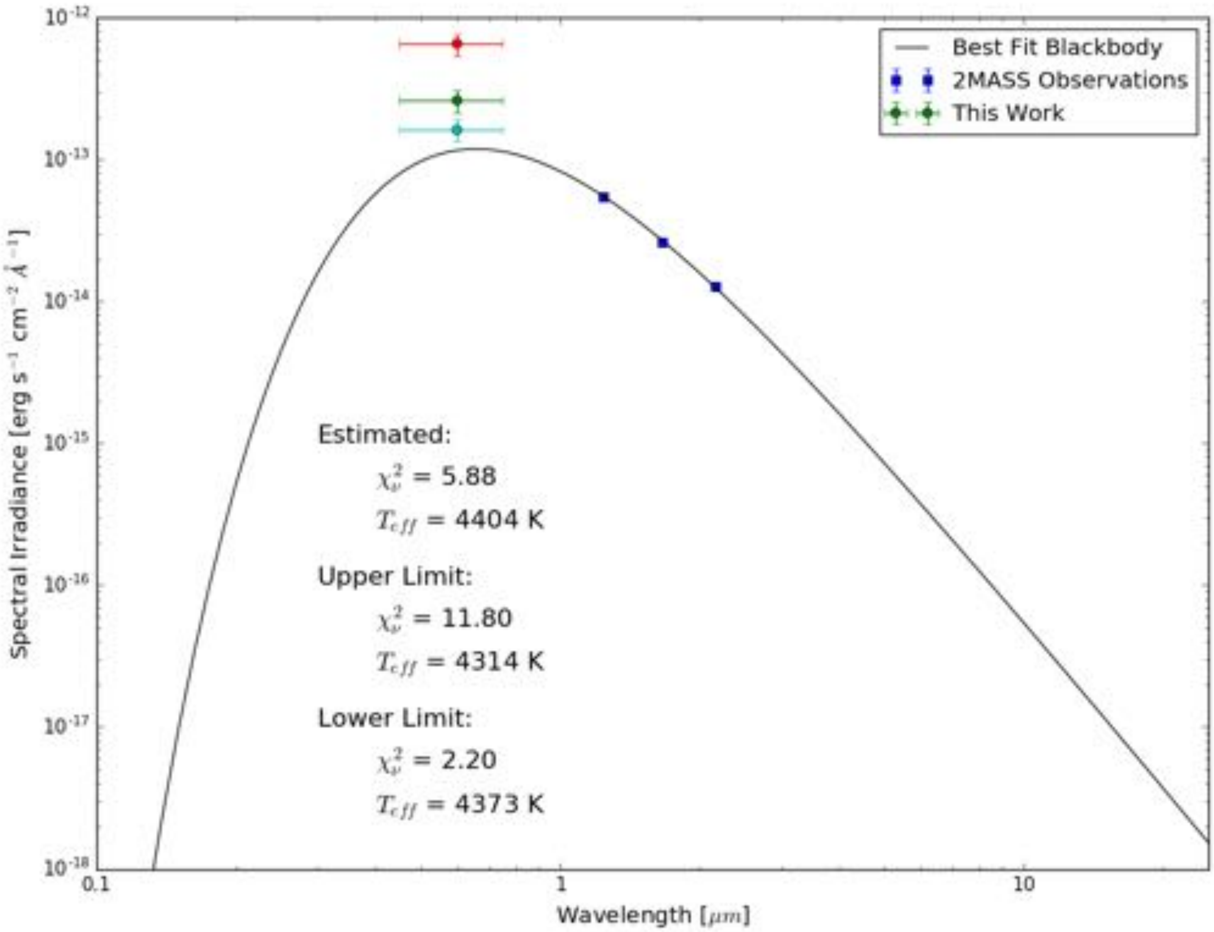

Figure 8.18: Best fit blackbody to 2MASS J18370125+3848126 using photometry from 2MASS (**circles**) and measurements from this work (**diamonds**). The different fits correspond to the values calculated using the estimate, upper limit, and lower limit values for the unblocked source. We find it is best fit with the lower limit, which is consistent with our estimate that we are underestimating the value of the unblocked source.

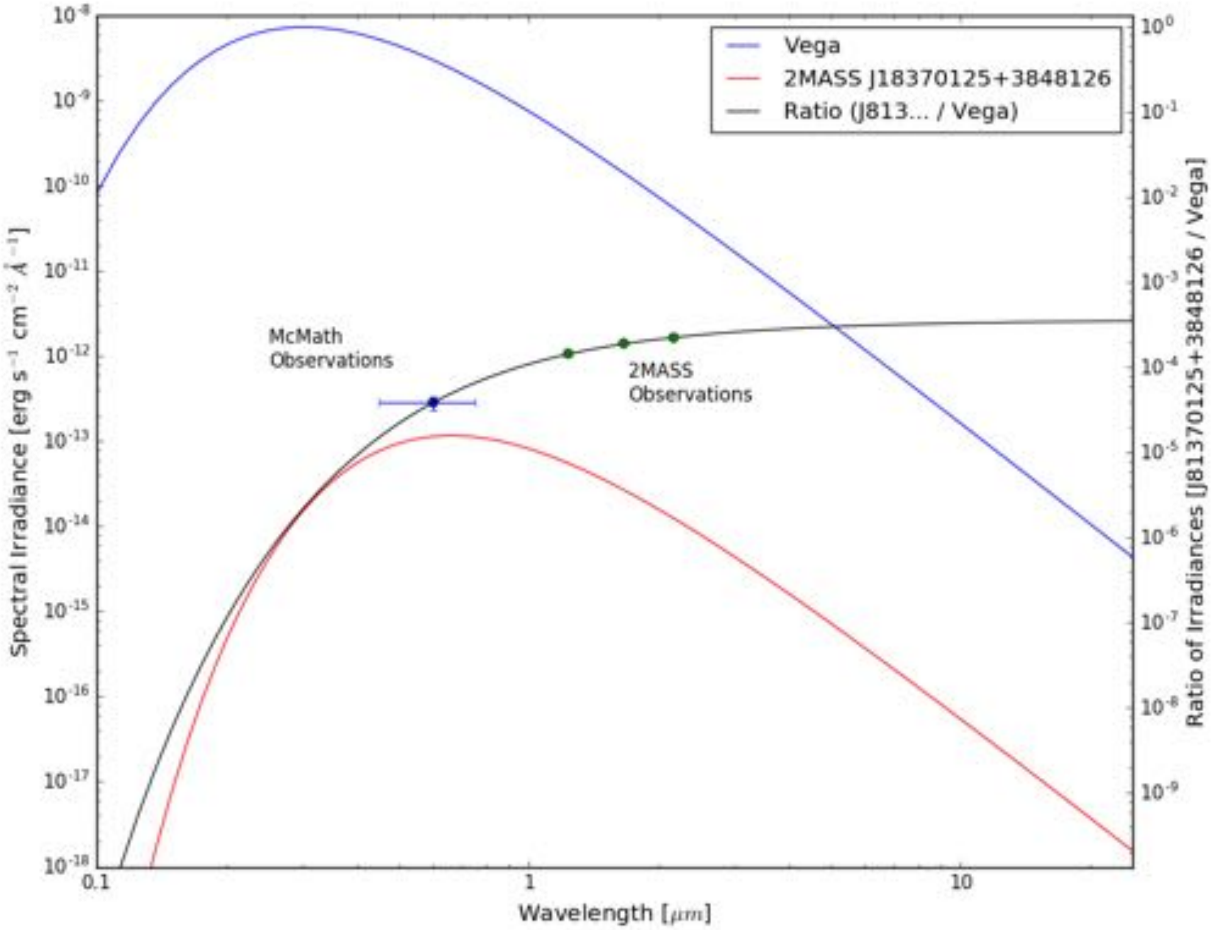

Figure 8.19: Model blackbody spectra for Vega (**blue**) and 2MASS J18370125+3848126 (**red**), and the ratio of them (**black**) are shown. The brightness between the two are more similar in the NIR and explains why J1837 has not been measured in the visible.

because our PSF is not stable with time nor repeatable. As we look at different locations on the sky, or try to move back to the same spot after moving off, we sample different sections of the oversized main heliostat mirror and are sampling different scratches, dust, etc. that change the scattered and diffracted light profile. This can clearly be seen when comparing the images of Vega (Figure 8.16) and Antares (Figure 8.21) from the short baseline. The artifacts in the two images are different, as is the level of diffuse scatter, and it is difficult to determine what is an artifact of the system and what is real. In future designs, limiting the number of mirrors in the system and having more stable control and repeatability of the siderostat position will help to mitigate these problems and reference PSF subtractions may be possible.

8.4.5.3 Possible sources around Antares

For Antares at the short baseline, we follow the same procedure as the analysis of Vega, again using measurements of unblocked Antares from the long baseline as Antares was saturated at the short baseline. The combined 200 second image of Antares behind the starshade is shown in Figure 8.21 and the raw and 3σ contrast plots are shown in Figure 8.22 and Figure 8.23, respectively. Our measured contrast of Antares at the IWA is 1.8×10^{-6}. There are obvious artifacts in the image around the starshade and where the vertical starshade stand crosses a horizontal handrail that is in the beamline.

There are a number of point sources extended from Antares, but it is not possible to discern if these are background stars or artifacts on one of the mirrors. Unlike the Vega observations, we do not have images where the heliostat is being slewed and cannot correlate the motions of the point sources, and we did not observe long enough for field rotation. We have not found stars in these locations recorded in any star catalogs. The estimated brightness of these sources (if they are stars) are in Table 8.7. The horizontal alignment of Source A and Source B and their symmetry around the position of the starshade stand make them suspect as being artifacts of the system.

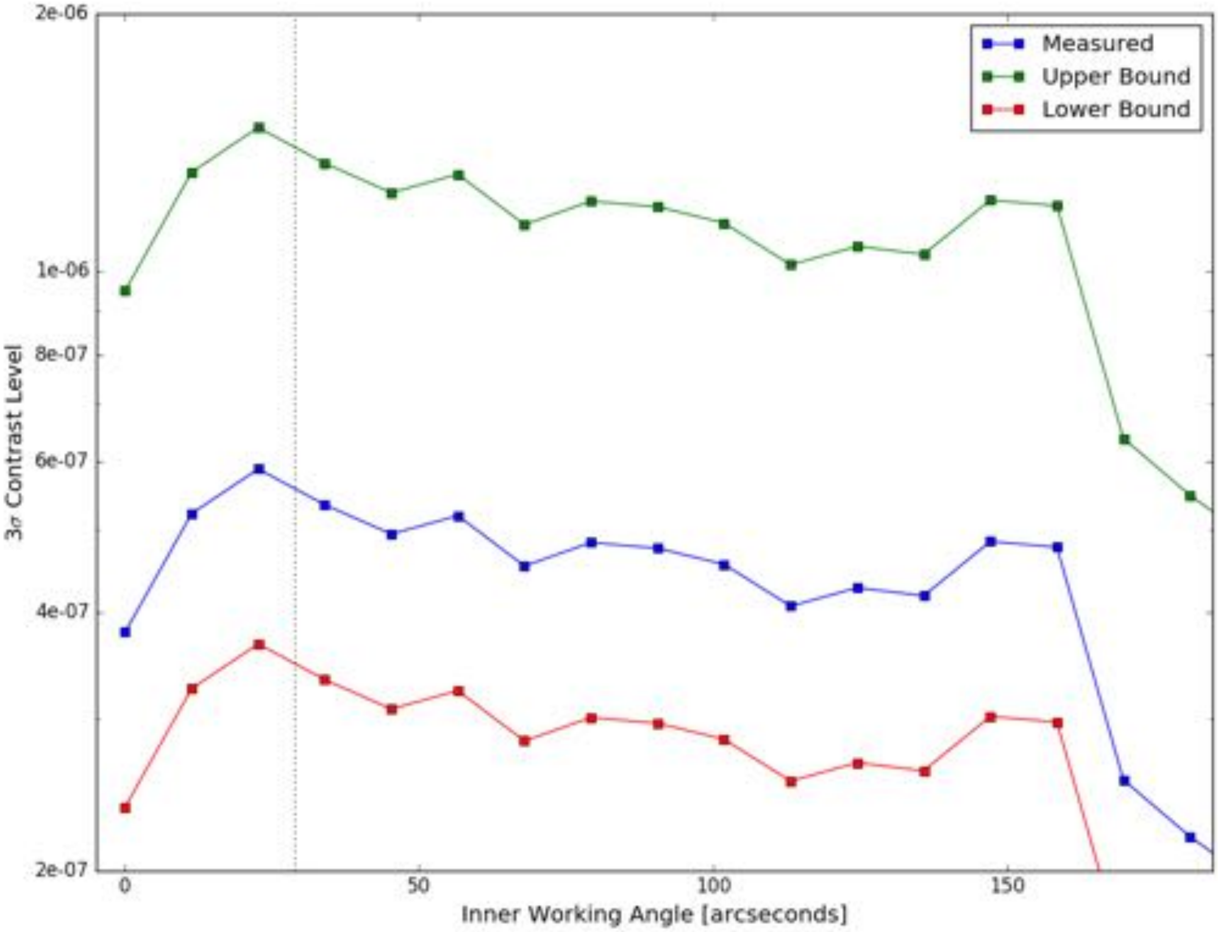

Figure 8.20: 3σ contrast values calculated in the boxes of Figure 8.16 for observations of **Vega** at the **short** baseline. The different lines correspond to if the calculations were made with the measured, upper, and lower bound values of the unblocked source.

Source	A	B
Count rate [ph/s]	289.1	989.5
SNR	94.8	46.5
Measured $\theta_{\text{sep}}['']$	92 ± 15	85 ± 15
Estimated Brightness		
$[m_{AB}]$	10.05 ± 0.18	8.71 ± 0.07
[erg s^{-1} cm^{-2} $Å^{-1}$]	$(2.61 \pm 0.46) \times 10^{-13}$	$(8.98 \pm 0.60) \times 10^{-13}$
Brightness Upper Limit		
$[m_{AB}]$	9.06 ± 0.18	7.72 ± 0.07
[erg s^{-1} cm^{-2} $Å^{-1}$]	$(6.53 \pm 1.14) \times 10^{-13}$	$(22.5 \pm 1.5) \times 10^{-13}$
Brightness Lower Limit		
$[m_{AB}]$	10.57 ± 0.18	9.22 ± 0.07
[erg s^{-1} cm^{-2} $Å^{-1}$]	$(1.63 \pm 0.29) \times 10^{-13}$	$(5.61 \pm 0.38) \times 10^{-13}$
Catalog ID	J18370125+3848126	PPM 81557
Catalog $\theta_{\text{sep}}['']$	91.69	76.49
Catalog Brightness	$m_J = 9.402$	$m_B \sim 10.8$

Table 8.6: Measured properties of J18370125+3848126 & PPM 81557 (seen around **Vega**) and comparison to their catalog values. The error bars are 1σ errors from the detection of the source and the upper and lower limits correspond to which limit of the unblocked source brightness is taken.

Source	A	B	C
Count rate [ph/s]	227.5	432.3	103.9
SNR	24.4	45.9	11.2
Measured $\theta_{\text{sep}}['']$	100 ± 15	105 ± 15	93 ± 15
Estimated Brightness			
$[m_{AB}]$	10.43 ± 0.50	9.70 ± 0.29	11.27 ± 0.88
[erg s^{-1} cm^{-2} $Å^{-1}$]	$(1.85 \pm 1.08) \times 10^{-13}$	$(3.60 \pm 1.10) \times 10^{-13}$	$(0.85 \pm 1.07) \times 10^{-13}$
Brightness Upper Limit			
$[m_{AB}]$	7.22 ± 0.50	6.50 ± 0.29	8.06 ± 0.88
[erg s^{-1} cm^{-2} $Å^{-1}$]	$(35.4 \pm 20.7) \times 10^{-13}$	$(69.0 \pm 20.9) \times 10^{-13}$	$(16.3 \pm 20.5) \times 10^{-13}$
Brightness Lower Limit			
$[m_{AB}]$	11.15 ± 0.50	10.43 ± 0.29	12.0 ± 0.88
[erg s^{-1} cm^{-2} $Å^{-1}$]	$(0.95 \pm 0.55) \times 10^{-13}$	$(1.85 \pm 0.56) \times 10^{-13}$	$(0.44 \pm 0.55) \times 10^{-13}$

Table 8.7: Measured properties of the three potential stars seen in Figure 8.21 around **Antares**. The error bars are 1σ errors from the detection of the source and the upper and lower limits correspond to which limit of the unblocked source brightness is taken.

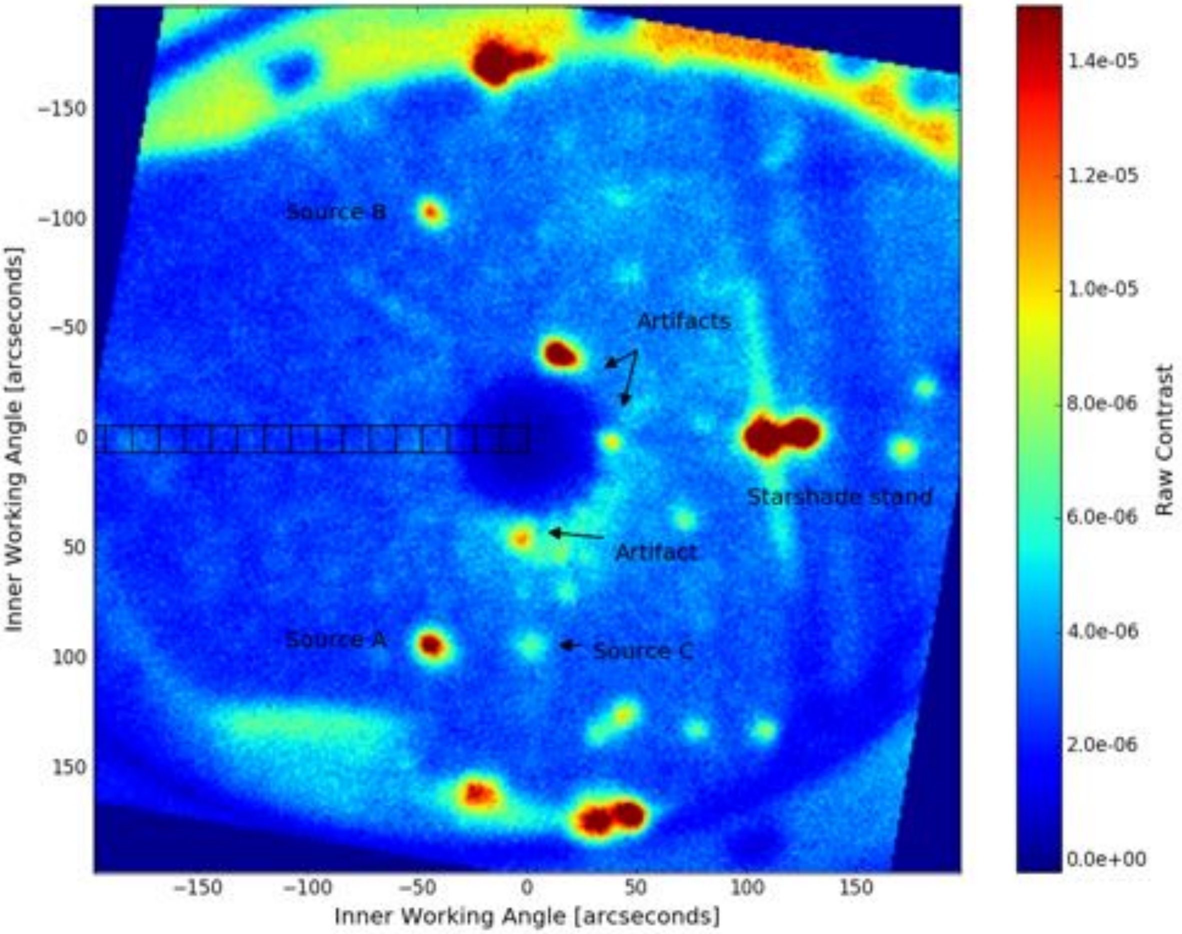

Figure 8.21: Stacked image (units of raw contrast) of **Antares** with a total exposure time of 200 seconds from the **short** baseline. The **dotted circle** in the center corresponds to the IWA. The **boxes** mark the subapertures that the 3σ contrast values are calculated in. We have labeled obvious artifacts due to the starshade or starshade stand. There are three possible sources that we can not determine if they are background stars or scratches on the mirror. There are a significant number of fainter point sources in the image as well.

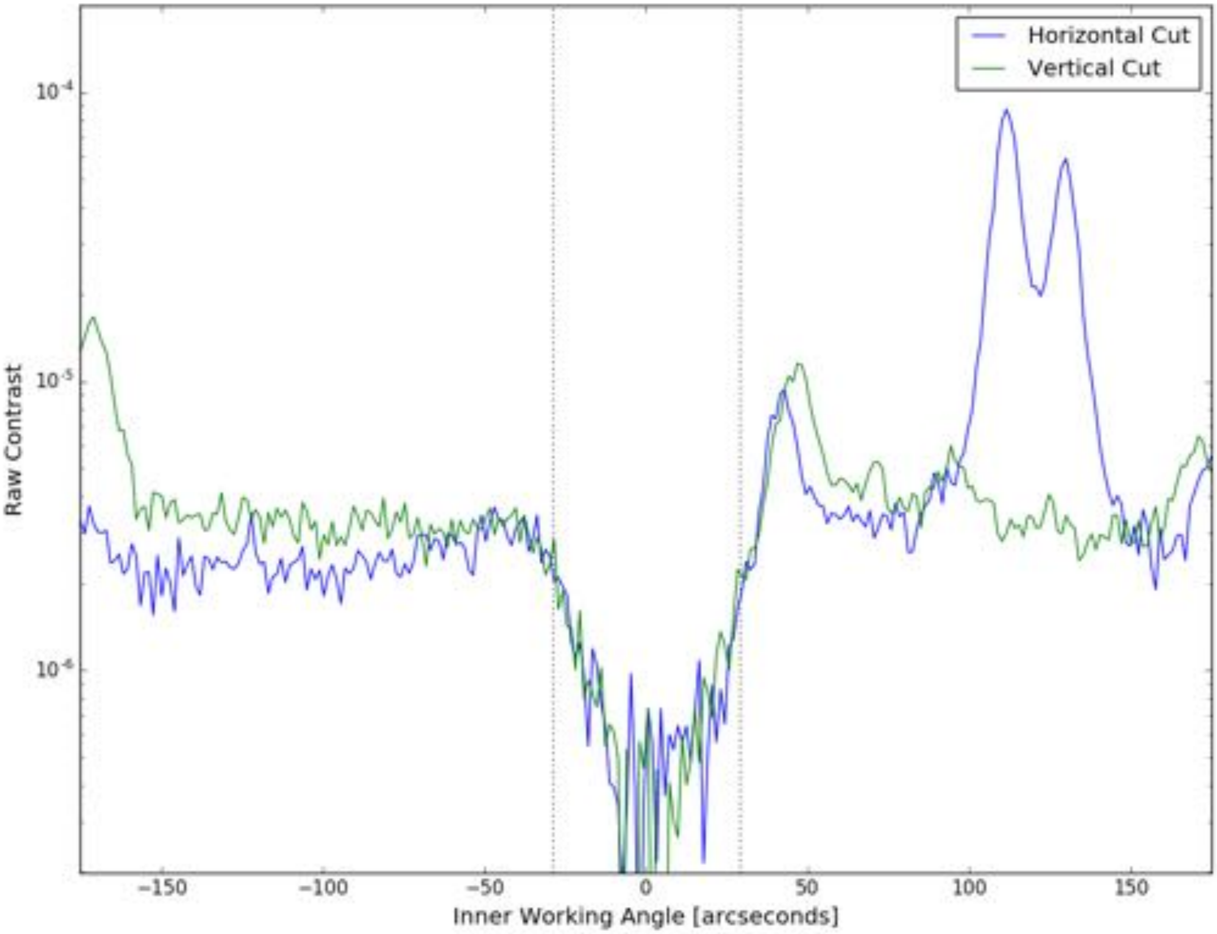

Figure 8.22: Raw contrast cut across image for **Antares** observations at the **short** baseline.

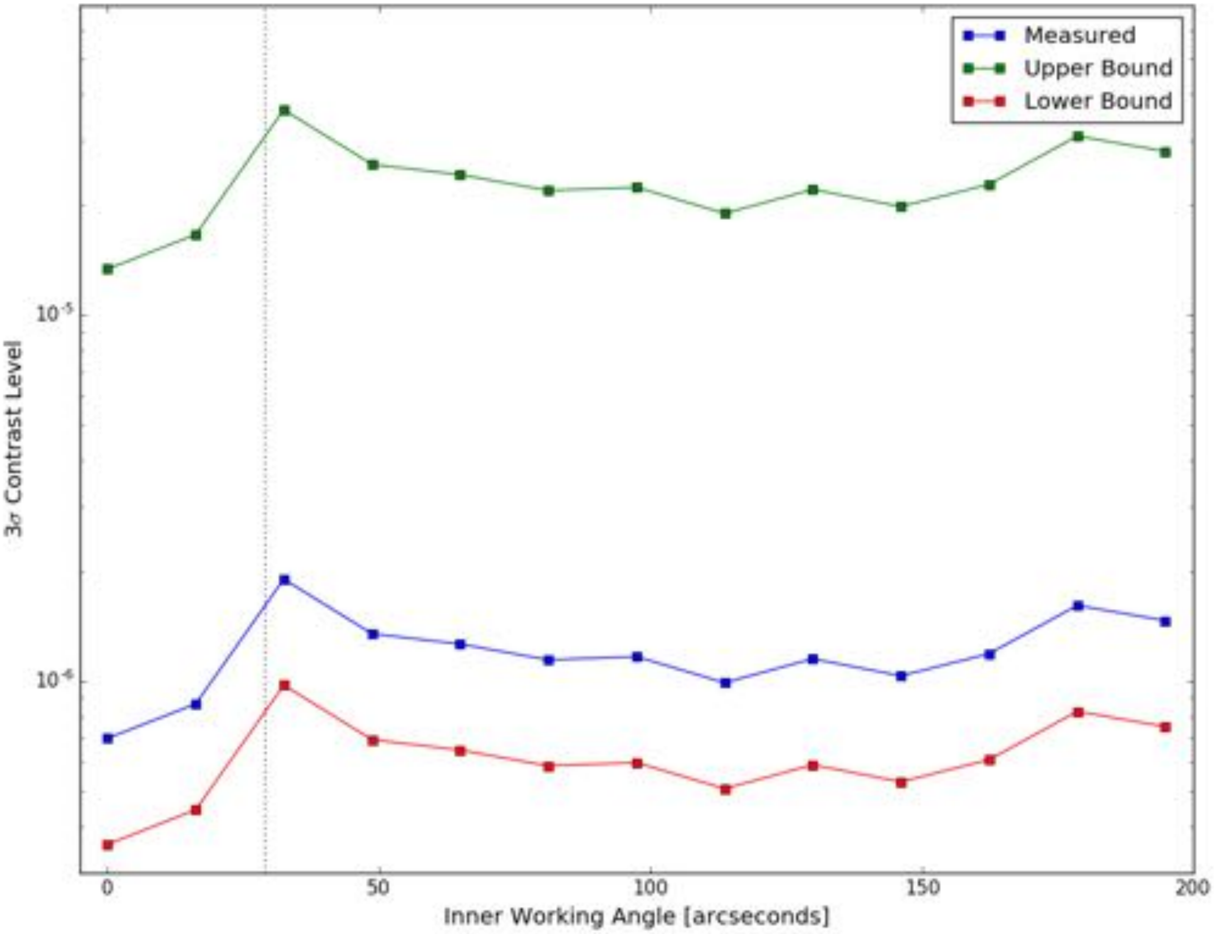

Figure 8.23: 3σ contrast values calculated in the boxes of Figure 8.21 for observations of **Antares** at the **short** baseline. The different lines correspond to if the calculations were made with the measured, upper, and lower bound values of the unblocked source.

8.4.6 Observations from 2.4 km long baseline

Observing from the long baseline brings a host of problems to the observations (discussed in Chapter 7) and to the data analysis. The problems encountered in Section 8.4.5 are compounded with a smaller IWA, smaller field of view, and greater atmospheric turbulence. Despite these challenges, we were still able to achieve high contrast with the most flight-like representation of a starshade to date. The best contrast we achieved from the long baseline at 15 arcseconds IWA was $2.0^{+1.57}_{-0.49} \times 10^{-5}$, which was achieved with Arcturus and is presented in Figure 8.25.

With the large number of short exposures taken, we can select the images in which we achieve the best contrast and throw out the rest. We convert each image into a raw contrast value, sum the total contrast in our region of interest, and sort the images by that sum. We impose a cut to reject images that have a total contrast above a specified value and median combine to create a master image. There is a tradeoff in the number of images to include in stacking the data, where including more images results in a longer integrated exposure time and will reduce the noise ($\propto \sqrt{t}$ if read noise is negligible). However, as the images are sorted by quality of alignment, including more images will start to use images of worse alignment where the noise from diffracted light dominates. Although there may be a more intelligent approach to selecting the number of images that enable the best contrast measurement, for now, we use trial and error to choose the number of images to keep.

The arc of light at the edge of the West Auxiliary mirror that is seen in the long baseline images (Figures 8.24, 8.28, 8.30) is light that is diffracted by the starshade 140 m upstream of the mirror that is again diffracted as the West Aux clips it. In Figure 8.26, we moved the starshade so that it is only 5 m upstream of the West Aux and therefore has less distance to diffract to a larger angle that would be clipped by the final mirror. In this configuration, the arc is still present, but to a lesser extent.

8.4.6.1 Long baseline results from Arcturus, Fomalhaut, Altair, and Vega

Figures 8.24 - 8.31 contain the results from long baseline observations of Arcturus, Fomalhaut, Altair, and Vega.

8.5 Discussion

I consider our observations at McMath a major success, as they were (along with [58]) the first astronomical observations with starshades. We demonstrated a practical method to doing astronomy with starshades, achieved high contrast (5.6×10^{-7}) at a moderate IWA ($30''$) on astronomical targets, and provided photometric measurements of stars near Vega in a new wavelength regime. While we did not observe the Fomalhaut debris disk, we now have the right tools and experience to do so.

At the long baseline, we did not achieve the contrast we were hoping for due to constant misalignment from errors in McMath's tracking system and disturbances in the atmosphere. The systematic errors in our measurements are large due to the loose constraint on the brightness of the unblocked source. Despite these setbacks, we have identified the source of many problems and now know how to best proceed forward.

The contrast we were able to achieve at the short baseline is impressive, given the conditions and quality of optics we were working with, and speaks volumes about the durability, efficiency, and potential that starshades possess. To try to put this in perspective, the state of the art for the GPI coronagraph on the 8.1 m Gemini South telescope is 5σ contrast of 6×10^{-7} at $1''$ IWA on a 1st magnitude star with 1 hour exposure time[2]. While they certainly have us beat on IWA and collecting power, they have the PSF of an 8 m telescope to work with. We achieved a 5σ contrast of $< 8 \times 10^{-7}$ in broadband visible light (at 4 λ/D), with a 5 minute exposure and a 2 cm aperture. They achieved high contrast at a 30 times smaller IWA, but their PSF is also 400 times smaller. This is by no means a criticism of the amazing work of GPI, but rather, this comparison is highlighting the potential power of starshades.

---

[2] http://www.gemini.edu/sciops/instruments/gpi/contrast

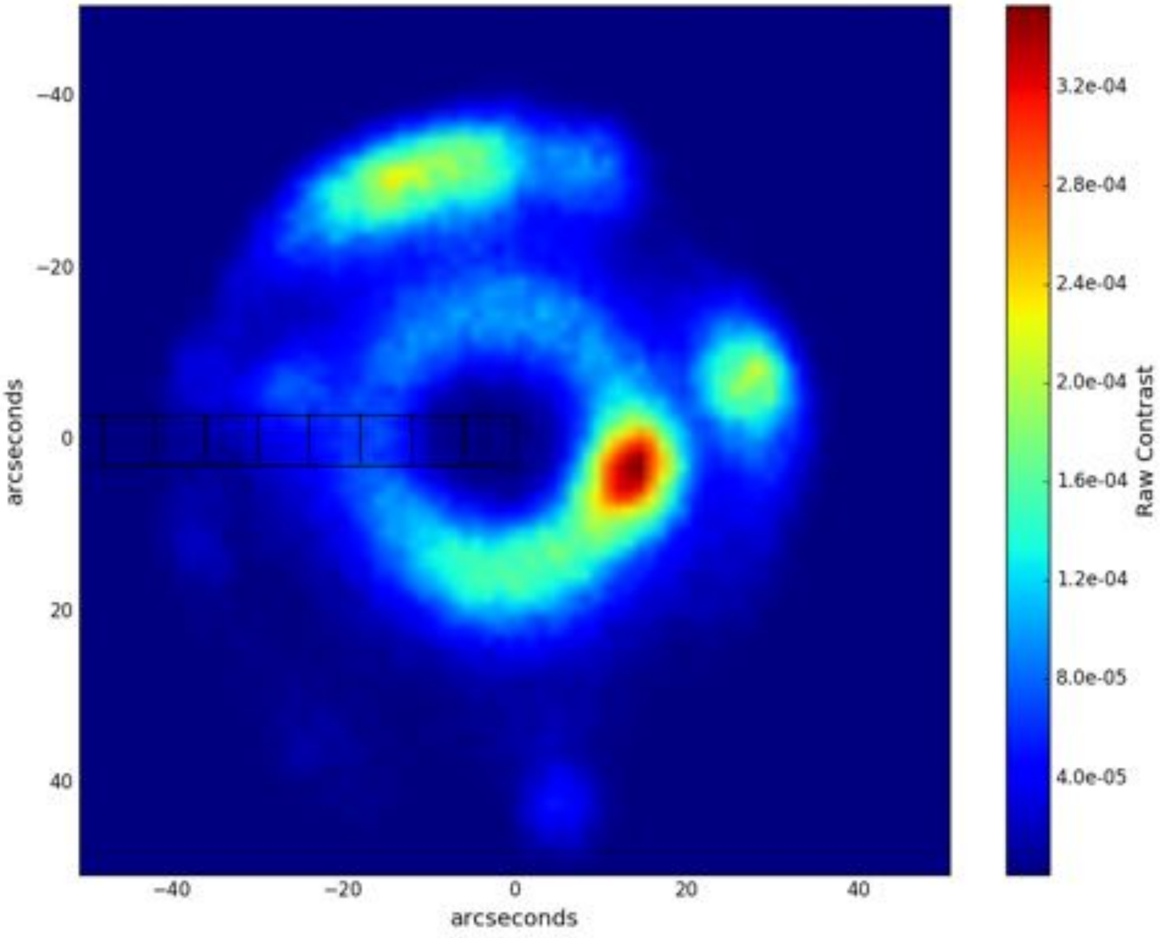

Figure 8.24: Stacked image (units of raw contrast) of **Arcturus** with a total exposure time of 177 seconds from the **long** baseline. The **boxes** mark the subapertures that the 3σ contrast values are calculated in. We can clearly see the ring of light from the tips of the starshade, along with a brighter component where there was preferential misalignment. Diffraction off the edge of the West Aux can be seen on the outer edge.

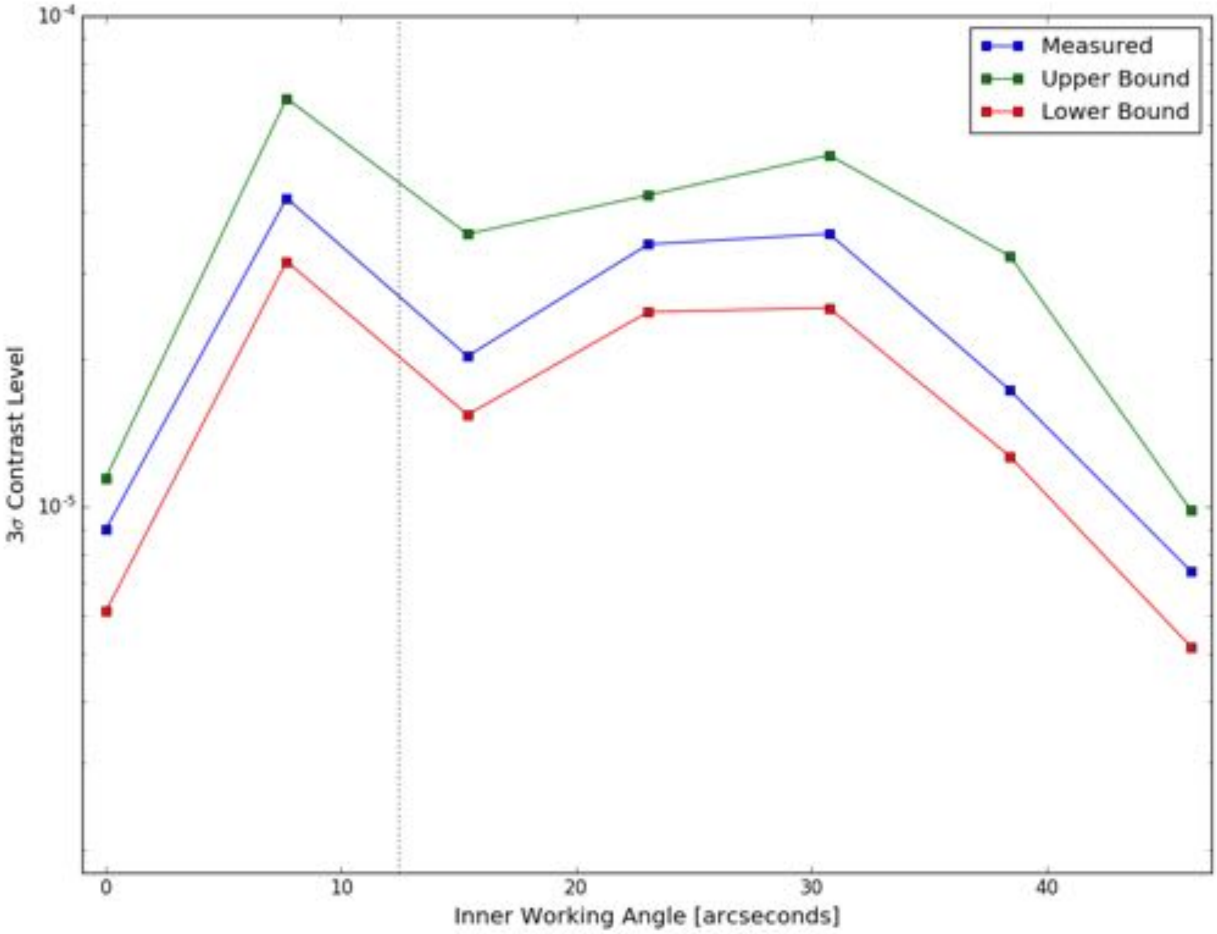

Figure 8.25: 3σ contrast values calculated in the boxes of Figure 8.24 for observations of **Arcturus** at the **long** baseline. The different lines correspond to if the calculations were made with the measured, upper, and lower bound values of the unblocked source.

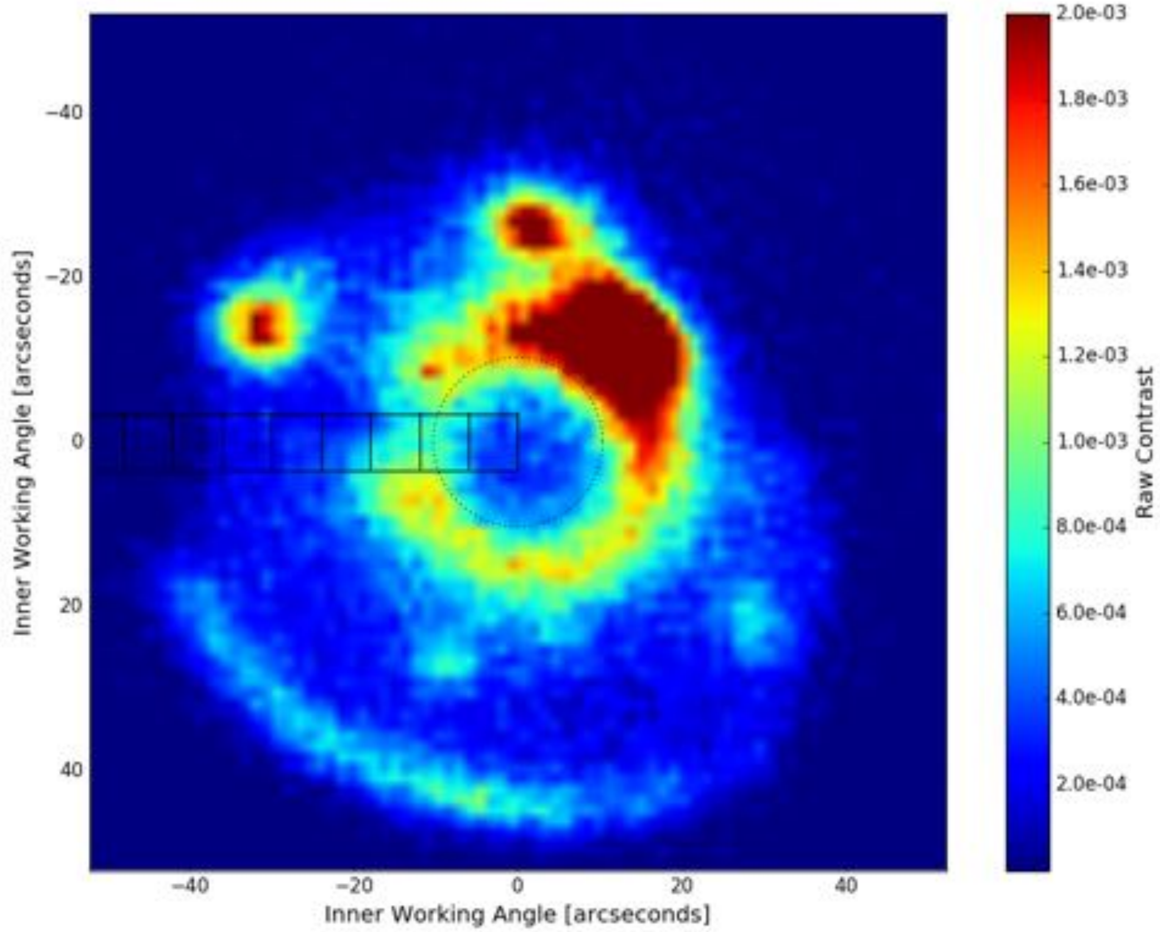

Figure 8.26: Stacked image (units of raw contrast) of **Fomalhaut** with a total exposure time of 120 seconds from the **long** baseline.

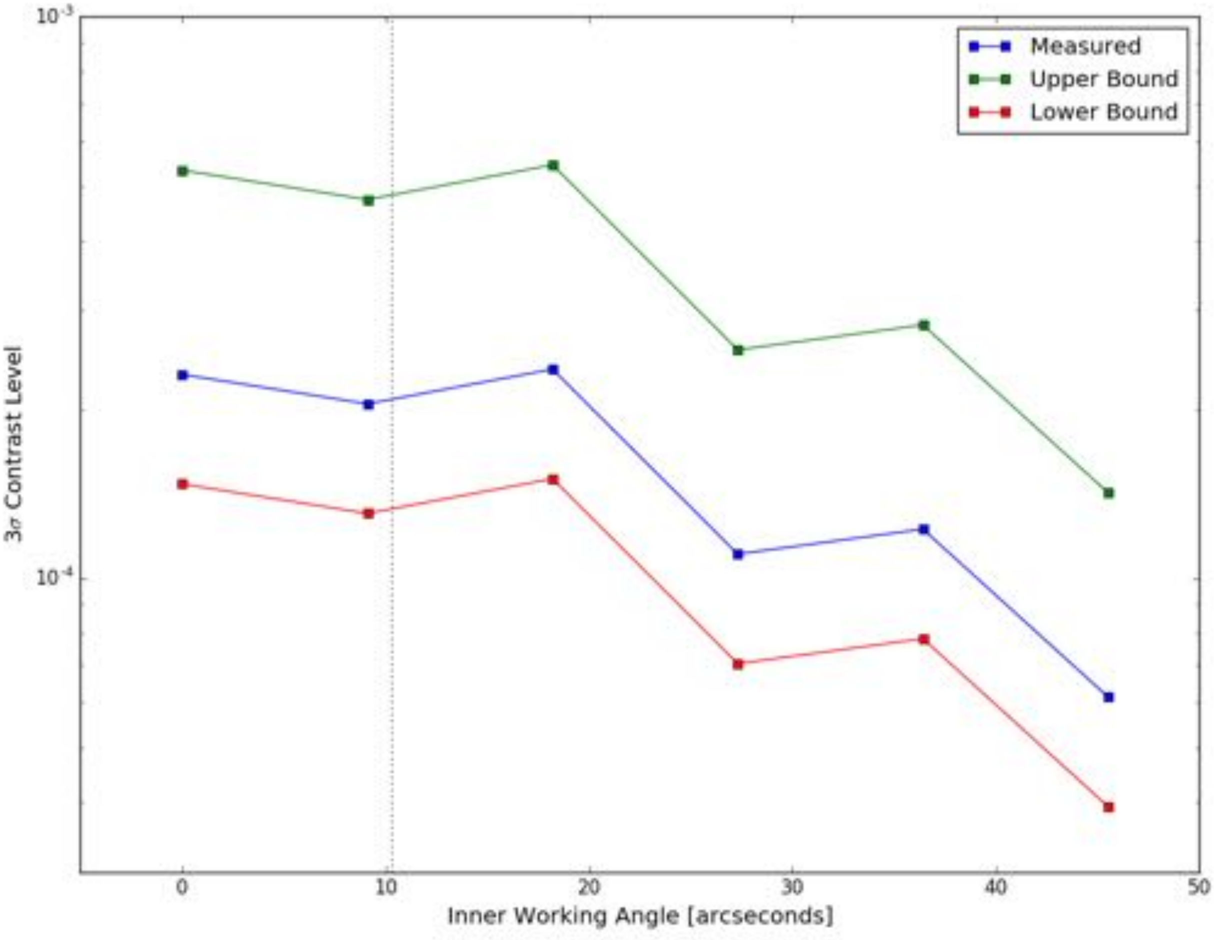

Figure 8.27: 3σ contrast values calculated in the boxes of Figure 8.26 for observations of **Fomalhaut** at the **long** baseline.

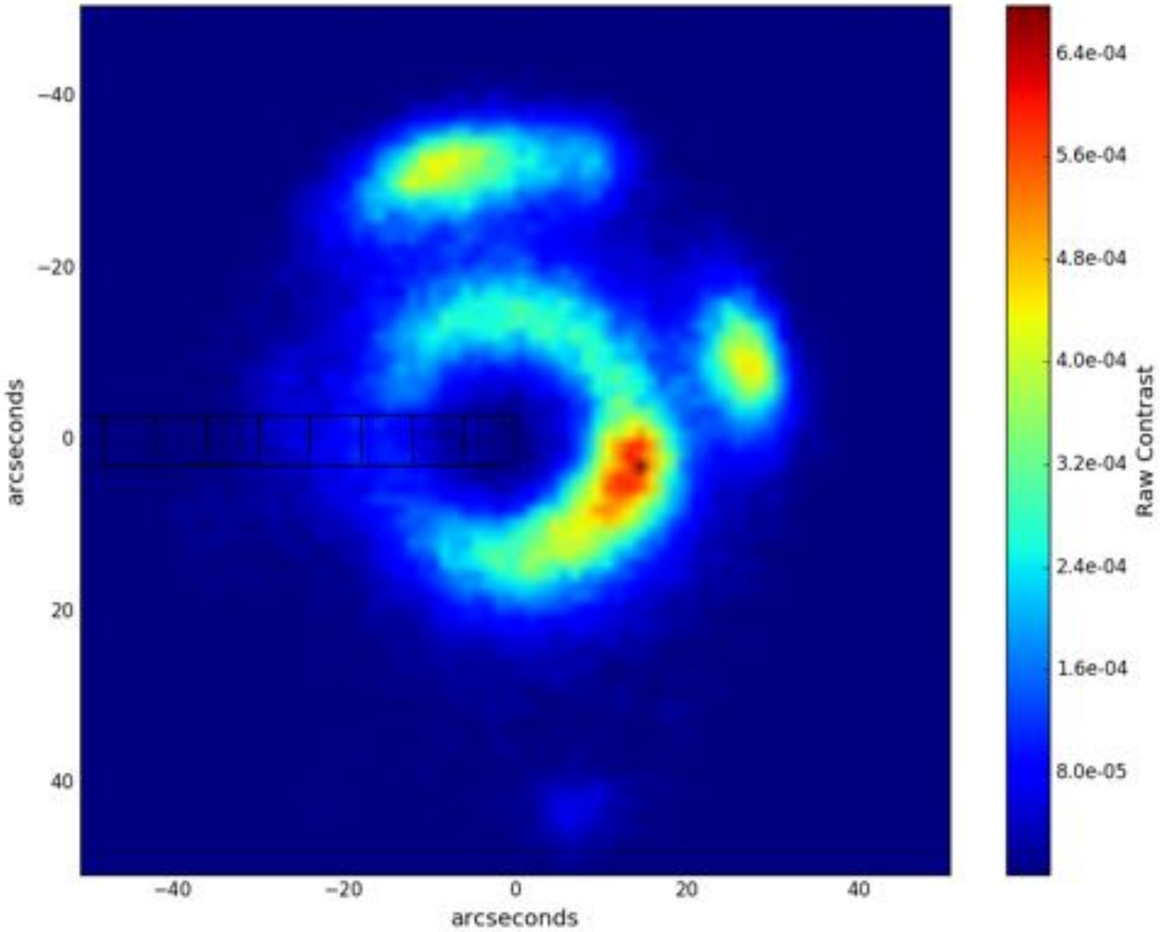

Figure 8.28: Stacked image (units of raw contrast) of **Vega** with a total exposure time of 40 seconds from the **long** baseline.

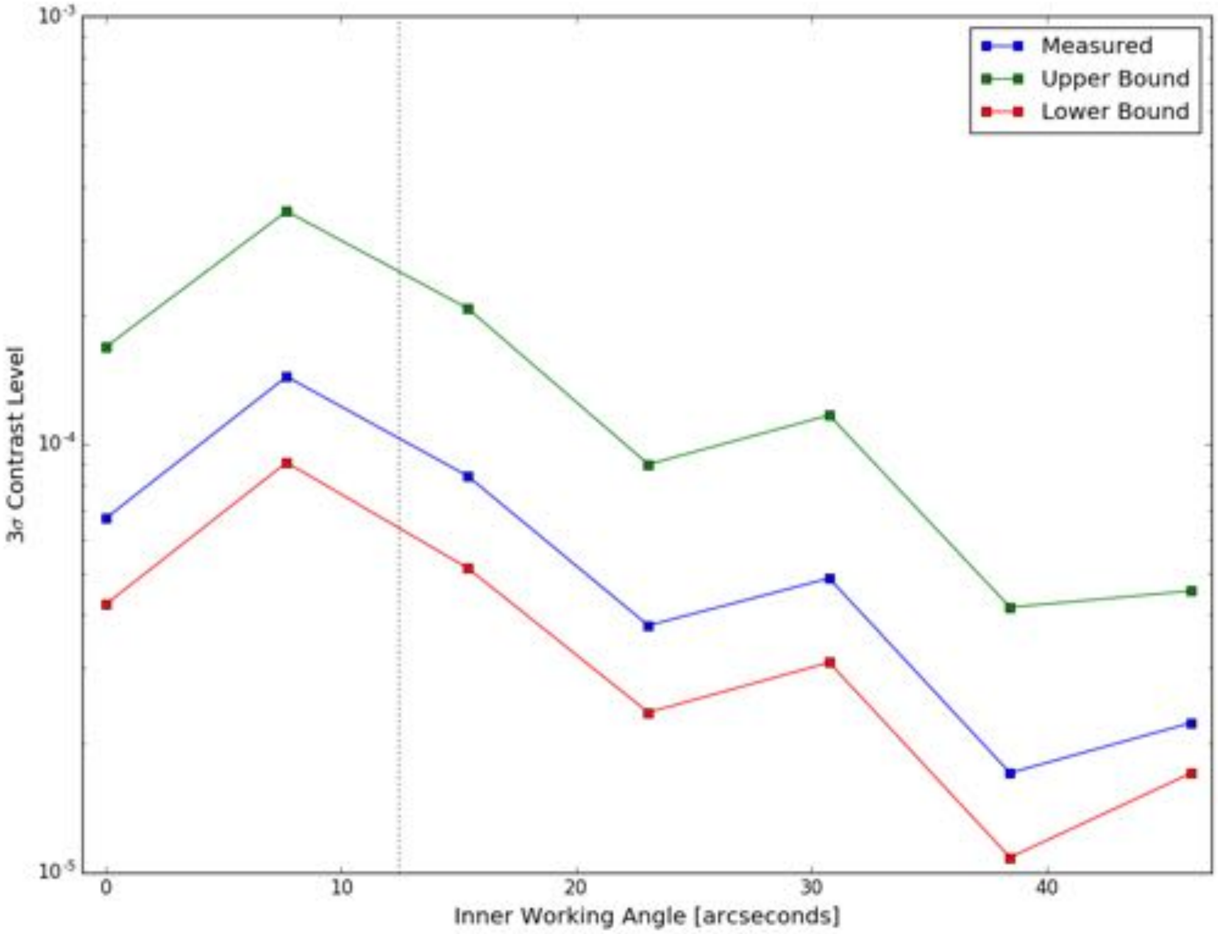

Figure 8.29: 3σ contrast values calculated in the boxes of Figure 8.28 for observations of **Vega** at the **long** baseline.

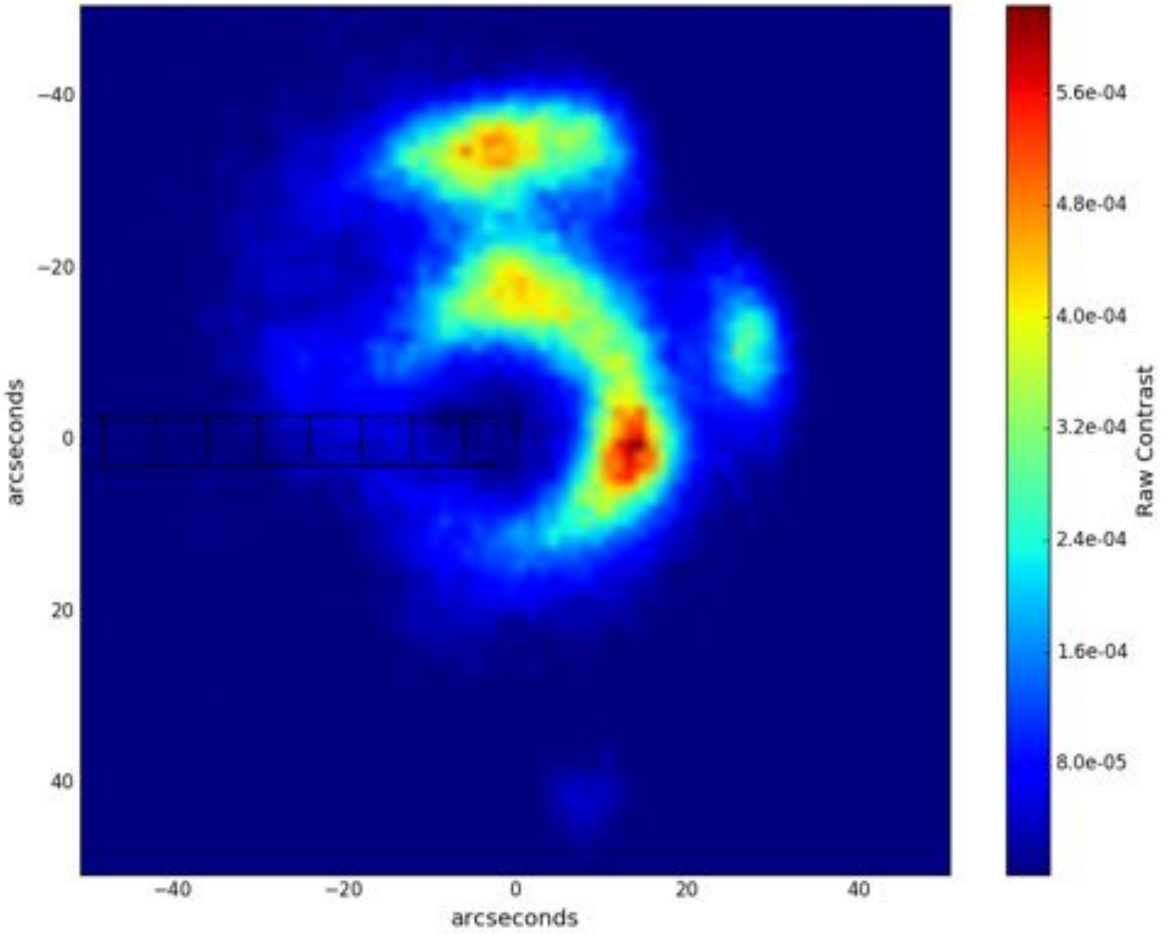

Figure 8.30: Stacked image (units of raw contrast) of **Altair** with a total exposure time of 75 seconds from the **long** baseline.

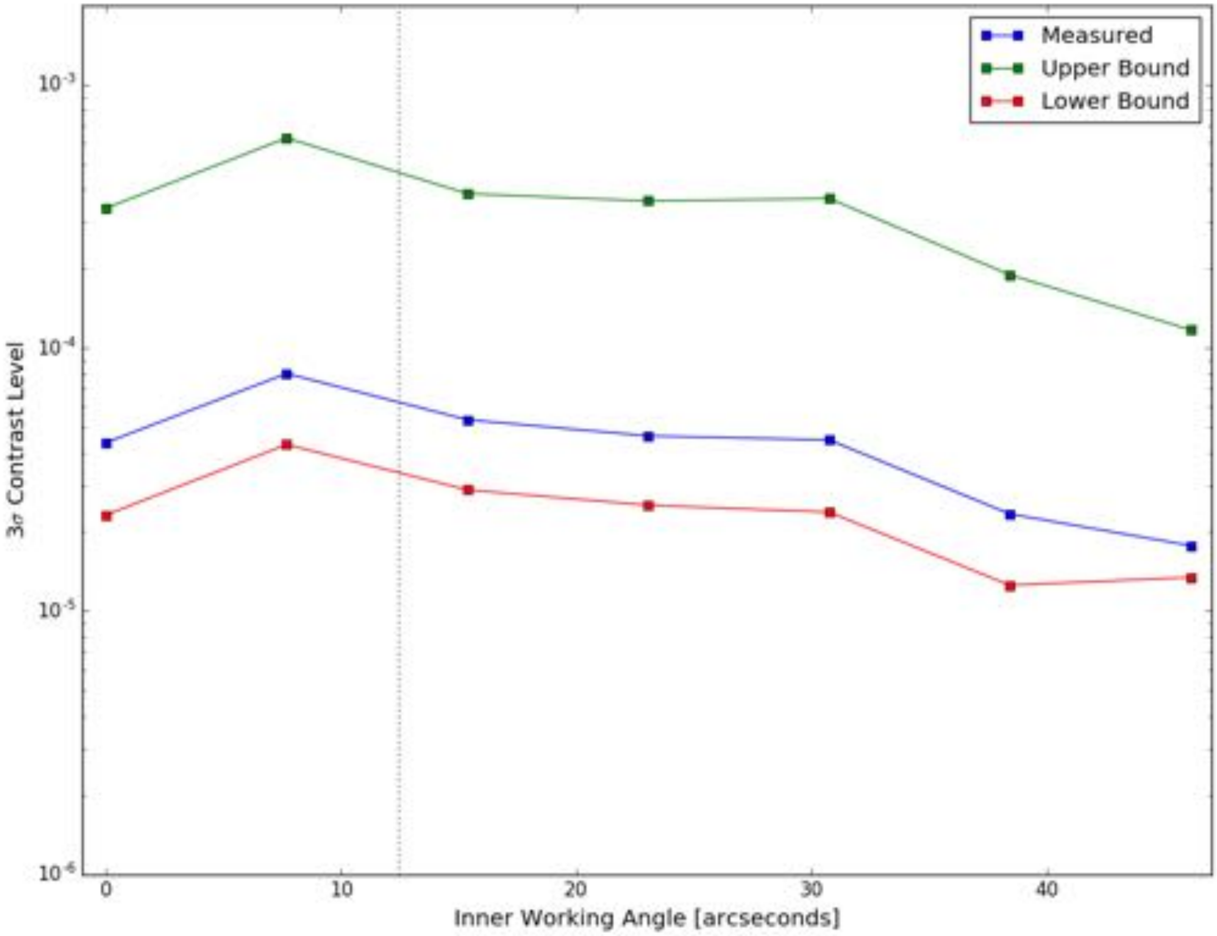

Figure 8.31: 3σ contrast values calculated in the boxes of Figure 8.30 for observations of **Altair** at the **long** baseline.

8.5.1 Lessons learned for future observations

We briefly summarize the lessons learned from these observations and how this work can inform future observations using siderostats and starshades.

- Misalignment of the starshade is by far our limiting factor
    - Move to a site with less atmosphere (Atacama or Mauna Kea)
    - Need faster control on the position of the starshade
        - This could be done with faster, more precise tip/tilt control of the siderostat
        - Or, use the siderostat for rough alignment and put the starshade on a translation stage for quick and precise alignment
        - Both would still utilize the feedback system developed in this work
- Variance in the unblocked source brightness leads to large errors in contrast measurements
    - More frequent observations of the unblocked source need to be made and closer in time to the blocked observations to try and sample the same atmospheric conditions
    - A larger number of unblocked images need to be made to knock down the brightness sample variance
    - Using neutral density filters will allow for exposure times comparable to those of the blocked observations to sample the same scintillation statistics
    - An always visible calibration source that has a constant and known brightness could be used to have a relative measurement of the scintillation of every image. It could periodically be calibrated by doing unblocked observations.
- Atmospheric turbulence is ruining image quality, causing variance in brightness, and lowering the throughput of the system
    - Move to a site with less atmosphere

  - Put adaptive optics on observing telescope

- Scatter and diffraction from the mirrors are beginning to limit contrast
  - Use cleaner, higher quality mirrors
  - Use fewer mirrors in the system (ideally only one)
  - Apodize the outer edge of the mirrors

- The movement of the siderostat to compensate for tracking errors is constantly moving the star field and makes it difficult for image alignment
  - Use a laser guide star to have an off-axis field star at all times for image alignment

Chapter 9

CONCLUSIONS

9.1 Summary of Results

We briefly summarize the main results of this dissertation.

- We studied two formation flying sensors to allow for precision alignment of starshades
  - The **Offset Sensor** for formation flying with suborbital vehicles
  - The **Arago Sensor** for precision formation flying over 10s of megameters in space
- We investigated using Vertical Takeoff Vertical Landing rockets as a starshade platform to do astronomy with starshades in the stratosphere
- We developed an optical model that efficiently calculates diffraction by a starshade
  - We have shown consistent agreement with another model down to $< 5\%$, at contrast levels of 10^{-9}
  - This model will be used to conduct sensitivity and tolerance analyses to inform starshade design
- We report tests of starshades with different classes of flaws built into the shape to be used for validation of our optical model
  - We have shown rough agreement between the data and our model for a number of the flawed shapes

  - However, we have not reached agreement on all shapes
  - Reaching agreement between data and model is ongoing work
- We have shown that a siderostat (heliostat) can be used to maintain alignment between a starshade and astronomical source
  - This has allowed us to conduct the first astronomical observations with starshades
- We achieved on-sky contrast of $< 5 \times 10^{-7}$ at a $30''$ IWA
- We obtained photometric measurements of 10^{th} magnitude stars in the proximity of Vega in the visible band
  - These are new measurements on these stars in a previously unavailable wavelength regime
- We developed a closed-loop feedback system to improve the stability of the starlight beam from the heliostat over large separations (2.4 km)
  - At this baseline, we achieved 2×10^{-5} contrast at $15''$ IWA
  - These observations were done at a flight-like Fresnel number and are in the most flight-like starshade configuration to date
- We have outlined design considerations for a long baseline siderostat facility to enable testing starshades on the ground at large separations
  - There is potential for this facility to do interesting science at high contrast and smaller inner working angles
- We have shown that starshades work
  - We have demonstrated their robustness by achieving high contrast in extreme environments

  - We have inspired faith in starshades amongst the community
  - We have paved the way forward for future development and testing of starshades

9.2 Planned Continuation of Work

The immediate plan for continuing optical testing is to conduct the high contrast experiments at the Princeton testbed outlined in Section 6.6. The goal of these tests is to achieve 10^{-9} suppression on a 1 inch starshade at a near flight-like Fresnel number. The results of these experiments will be used to validate optical models in the regime of high suppression. This test has been identified as the critical step in reaching TRL 5 for the optical performance of starshades. The testbed is just now finishing completion and should start taking data soon.

The Princeton tests will not be the end of optical testing and we need to reach TRL 6 before key decisions on a starshade mission can be made. To reach TRL 6, we need to test a high-fidelity prototype that has a fit, form, and function similar to the flight design. We also need to demonstrate we understand the critical scaling relations that provide the confidence we can move from testing small-scale starshades to building the full-scale flight hardware. To understand scaling issues, we need to test over a wide range of the Fresnel number parameter space. This will require a testbed larger than that at Princeton and has not yet been identified yet. I will use my experience in testing starshades and the results from the Princeton testbed to help design a testbed that is large enough to satisfy our needs. This testbed may be able to utilize the XRCF at NASA Marshall Space Flight Center or it may require building the LBF we outlined in Chapter 7.

I would like to continue pursuing astronomy with starshades and believe there is high potential for exciting results, especially if a facility such as the LBF is built. However, with the imminent closure of McMath, it is unclear on how to proceed further. There is more to learn about mirror quality, starshade alignment, atmospheric effects, etc. from testing at McMath and it is cheap to do so; we just need a source of financial support to keep McMath alive. Even without McMath operational, there is much to do to flesh out the design of the LBF. I plan to continue this investigation and try to make the case that the atmosphere will not severely limit our interpretation of results that could prevent a successful test. I would also like to determine with confidence if we have a shot at solving the exozodi problem using the LBF. If this is possible, I believe there to be significant interest in the construction of such a facility.

9.3 The Future of Starshades

It is an exciting time in the world of starshades as they continue to gather momentum and as there is talk to fly a starshade with the WFIRST mission in the late 2020's [73]. WFIRST is a 2.4 m space telescope working in the visible and near-IR that was donated to NASA by the National Reconnaissance Office and has a primary science goal of doing a wide-field survey of galaxies for cosmology [82]. In 2015, an internal coronagraph was added to the mission as a tech demo to do direct imaging and low resolution spectroscopy of Jupiter- and Neptune- sized planets [82]. WFIRST was originally designed to fly in a geosynchronous orbit, but has since been moved to L2, a decision that was perhaps made to accommodate a starshade.

As of now, the WFIRST team has been directed to keep open the option of making the observatory "starshade-ready", which means it could be adapted at a later date to be compatible with a starshade mission. This would include adding communication between starshade and telescope, allowing the telescope to use one of its guide cameras to do formation sensing with the starshade, and possibly adding a laser beacon on the telescope so the starshade can find it in space. The idea is to launch a starshade a few years after WFIRST, have it rendezvous with the telescope at L2, and dedicate 1 year to a starshade direct imaging mission.

A 30 - 40 m starshade with WFIRST could be a powerful instrument and as the telescope is already going to be built, it is the best option we have at getting starshades on the board. This has the potential to discover and characterize many Jupiter-sized planets and at least one exo-Earth [73]. The starshade with WFIRST would also serve as a technology demonstration for a starshade with the next generation of space telescopes in the 2030's. Concept studies are already underway for what the next flagship mission will be after JWST and WFIRST. Two of the four options have baselined a starshade to help meet their science goals. The first, called HabEx, is a 4 - 6 m visible/IR telescope with the primary mission of discovering and characterizing habitable planets [52]. The other is called LUVOIR, and is a large (upwards to 12 m) general purpose UVOIR observatory to serve as the replacement of Hubble as the workhorse for general astronomy [26]. A large starshade with LUVOIR is the best chance of discovering life in the universe in the near future.

In the past decade, the starshade solution to searching for life in the universe was invented, proven to be efficient in starlight suppression, and used in its first high contrast astronomical observations. The next decade will take this work and scale up to a space-based starshade mission where the first Earth-like exoplanet can be spectrally characterized and begin the search for another habitable world. The following decade will focus on building a bigger telescope and bigger starshade to begin the search for life in the universe and forever change the understanding of humankind's place in the cosmos.

Bibliography

[1] Yann Alibert. A maximum radius for habitable planets. Origins of Life and Evolution of Biospheres, 45(3):319–325, 2015.

[2] J. W. Arenberg, A. S. Lo, T. M. Glassman, and W. Cash. Optical performance of the New Worlds Occulter. Comptes Rendus Physique, 8:438–447, April 2007.

[3] H. H. Aumann, C. A. Beichman, F. C. Gillett, T. de Jong, J. R. Houck, F. J. Low, G. Neugebauer, R. G. Walker, and P. R. Wesselius. Discovery of a shell around Alpha Lyrae. ApJL, 278:L23–L27, March 1984.

[4] Jean-Luc Beuzit, Markus Feldt, Kjetil Dohlen, David Mouillet, Pascal Puget, Francois Wildi, Lyu Abe, Jacopo Antichi, Andrea Baruffolo, Pierre Baudoz, Anthony Boccaletti, Marcel Carbillet, Julien Charton, Riccardo Claudi, Mark Downing, Christophe Fabron, Philippe Feautrier, Enrico Fedrigo, Thierry Fusco, Jean-Luc Gach, Raffaele Gratton, Thomas Henning, Norbert Hubin, Franco Joos, Markus Kasper, Maud Langlois, Rainer Lenzen, Claire Moutou, Alexey Pavlov, Cyril Petit, Johan Pragt, Patrick Rabou, Florence Rigal, Ronald Roelfsema, Grard Rousset, Michel Saisse, Hans-Martin Schmid, Eric Stadler, Christian Thalmann, Massimo Turatto, Stphane Udry, Farrokh Vakili, and Rens Waters. Sphere: a 'planet finder' instrument for the vlt. In Proc. SPIE, volume 7014, pages 701418–701418–12, 2008.

[5] R. C. Bohlin. Spectrophotometric Standards From the Far-UV to the Near-IR on the White Dwarf Flux Scale. AJ, 111:1743, April 1996.

[6] M. Born and E. Wolf. Principles of Optics. Cambridge University Press, oct 1999.

[7] W. J. Borucki, D. Koch, G. Basri, N. Batalha, T. Brown, D. Caldwell, J. Caldwell, J. Christensen-Dalsgaard, W. D. Cochran, E. DeVore, E. W. Dunham, A. K. Dupree, T. N. Gautier, J. C. Geary, R. Gilliland, A. Gould, S. B. Howell, J. M. Jenkins, Y. Kondo, D. W. Latham, G. W. Marcy, S. Meibom, H. Kjeldsen, J. J. Lissauer, D. G. Monet, D. Morrison, D. Sasselov, J. Tarter, A. Boss, D. Brownlee, T. Owen, D. Buzasi, D. Charbonneau, L. Doyle, J. Fortney, E. B. Ford, M. J. Holman, S. Seager, J. H. Steffen, W. F. Welsh, J. Rowe, H. Anderson, L. Buchhave, D. Ciardi, L. Walkowicz, W. Sherry, E. Horch, H. Isaacson, M. E. Everett, D. Fischer, G. Torres, J. A. Johnson, M. Endl, P. MacQueen, S. T. Bryson, J. Dotson, M. Haas, J. Kolodziejczak, J. Van Cleve, H. Chandrasekaran, J. D. Twicken, E. V. Quintana, B. D. Clarke, C. Allen, J. Li, H. Wu, P. Tenenbaum, E. Verner, F. Bruhweiler, J. Barnes, and A. Prsa. Kepler Planet-Detection Mission: Introduction and First Results. Science, 327:977, February 2010.

[8] Roshawn Elizabeth Bowers. Estimation algorithm for autonomous aerial refueling using a vision based relative navigation system. Master's thesis, Texas A&M University, 2005.

[9] Eric Cady. Boundary diffraction wave integrals for diffraction modeling of external occulters. Opt. Express, 20(14):15196–15208, Jul 2012.

[10] W. Cash. Detection of Earth-like planets around nearby stars using a petal-shaped occulter. Nature, 442:51–53, July 2006.

[11] W. Cash. Analytic Modeling of Starshades. ApJ, 738:76, September 2011.

[12] W. Cash, S. Kendrick, C. Noecker, J. Bally, J. Demarines, J. Green, P. Oakley, A. Shipley, S. Benson, S. Oleson, D. Content, D. Folta, S. Garrison, K. Gendreau, K. Hartman, J. Howard, T. Hyde, D. Lakins, J. Leitner, D. Leviton, R. Luquette, B. Oegerley, K. Richon, A. Roberge, S. Tompkins, J. Tveekrem, B. Woodgate, M. Turnbull, D. Dailey, K. Decker, R. Dehmohseni, B. Gaugh, T. Glassman, M. Haney, R. Hejal, C. Lillie, A. Lo, D. O'Conner, G. Oleas, R. Polidan, R. Samuele, S. Shields, J. Shirvanian, D. Soohoo, G. Tinetti, B. Dorland, R. Dudik, R. Gaume, and B. Mason. The New Worlds Observer: the astrophysics strategic mission concept study. In Society of Photo-Optical Instrumentation Engineers (SPIE) Conference Series, volume 7436 of Society of Photo-Optical Instrumentation Engineers (SPIE) Conference Series, page 6, August 2009.

[13] Mikhail Charnotskii. Arago spot and turbulent distortions. In Proc. SPIE, volume 8161, pages 816103–816103–14, 2011.

[14] Sergei S Chesnokov, Valerii P Kandidov, Victor I Shmalhausen, and Vladimir V Shuvalov. Numerical/optical simulation of laser beam propagation through atmospheric turbulence. Technical report, DTIC Document, 1995.

[15] Christopher F. Chyba and Kevin P. Hand. Astrobiology: The study of the living universe. Annual Review of Astronomy and Astrophysics, 43(1):31–74, 2005.

[16] C. L. Cole and J. L. Crassidis. Fast Star-Pattern Recognition Using Planar Triangles. Journal of Guidance Control Dynamics, 29:64–71, January 2006.

[17] T. H. Cotten and I. Song. A Comprehensive Census of Nearby Infrared Excess Stars. ApJS, 225:15, July 2016.

[18] "National Research Council". "The Limits of Organic Life in Planetary Systems". "The National Academies Press", "Washington, DC", 2007.

[19] R. M. Cutri, M. F. Skrutskie, S. van Dyk, C. A. Beichman, J. M. Carpenter, T. Chester, L. Cambresy, T. Evans, J. Fowler, J. Gizis, E. Howard, J. Huchra, T. Jarrett, E. L. Kopan, J. D. Kirkpatrick, R. M. Light, K. A. Marsh, H. McCallon, S. Schneider, R. Stiening, M. Sykes, M. Weinberg, W. A. Wheaton, S. Wheelock, and N. Zacarias. VizieR Online Data Catalog: 2MASS All-Sky Catalog of Point Sources (Cutri+ 2003). VizieR Online Data Catalog, 2246, June 2003.

[20] D. Defrère, P. M. Hinz, A. J. Skemer, G. M. Kennedy, V. P. Bailey, W. F. Hoffmann, B. Mennesson, R. Millan-Gabet, W. C. Danchi, O. Absil, P. Arbo, C. Beichman, G. Brusa, G. Bryden, E. C. Downey, O. Durney, S. Esposito, A. Gaspar, P. Grenz, C. Haniff, J. M. Hill, J. Lebreton,

J. M. Leisenring, J. R. Males, L. Marion, T. J. McMahon, M. Montoya, K. M. Morzinski, E. Pinna, A. Puglisi, G. Rieke, A. Roberge, E. Serabyn, R. Sosa, K. Stapeldfeldt, K. Su, V. Vaitheeswaran, A. Vaz, A. J. Weinberger, and M. C. Wyatt. First-light LBT Nulling Interferometric Observations: Warm Exozodiacal Dust Resolved within a Few AU of η Crv. ApJ, 799:42, January 2015.

[21] D. J. Des Marais, M. O. Harwit, K. W. Jucks, J. F. Kasting, D. N. C. Lin, J. I. Lunine, J. Schneider, S. Seager, W. A. Traub, and N. J. Woolf. Remote Sensing of Planetary Properties and Biosignatures on Extrasolar Terrestrial Planets. Astrobiology, 2:153–181, June 2002.

[22] Alfredo Dubra and Jos A. Ferrari. Diffracted field by an arbitrary aperture. American Journal of Physics, 67(1):87–92, 1999.

[23] J. R. Ducati. VizieR Online Data Catalog: Catalogue of Stellar Photometry in Johnson's 11-color system. VizieR Online Data Catalog, 2237, 2002.

[24] "Epicurus". "Letter to Herodotus". "Translated by: Cyril Bailey in [Epicurus: The Extant Remains], Oxford University Press (1926)", 300 BCE.

[25] D. A. Fischer, G. Anglada-Escude, P. Arriagada, R. V. Baluev, J. L. Bean, F. Bouchy, L. A. Buchhave, T. Carroll, A. Chakraborty, J. R. Crepp, R. I. Dawson, S. A. Diddams, X. Dumusque, J. D. Eastman, M. Endl, P. Figueira, E. B. Ford, D. Foreman-Mackey, P. Fournier, G. Fűrész, B. S. Gaudi, P. C. Gregory, F. Grundahl, A. P. Hatzes, G. Hébrard, E. Herrero, D. W. Hogg, A. W. Howard, J. A. Johnson, P. Jorden, C. A. Jurgenson, D. W. Latham, G. Laughlin, T. J. Loredo, C. Lovis, S. Mahadevan, T. M. McCracken, F. Pepe, M. Perez, D. F. Phillips, P. P. Plavchan, L. Prato, A. Quirrenbach, A. Reiners, P. Robertson, N. C. Santos, D. Sawyer, D. Segransan, A. Sozzetti, T. Steinmetz, A. Szentgyorgyi, S. Udry, J. A. Valenti, S. X. Wang, R. A. Wittenmyer, and J. T. Wright. State of the Field: Extreme Precision Radial Velocities. PASP, 128(6):066001, June 2016.

[26] Kevin France. The luvoir science and technology definition team (stdt): overview and status. In Proc. SPIE, volume 9904, pages 99040M–99040M–16, 2016.

[27] A. Fresnel. Oeuvres. Ann Chim et Phys, 1:129, 1816.

[28] D. L. Fried. Optical Resolution Through a Randomly Inhomogeneous Medium for Very Long and Very Short Exposures. Journal of the Optical Society of America (1917-1983), 56:1372, October 1966.

[29] T. Glassman, S. Casement, S. Warwick, and M. Novicki. Measurements of high-contrast starshade performance. In Society of Photo-Optical Instrumentation Engineers (SPIE) Conference Series, volume 9143 of Society of Photo-Optical Instrumentation Engineers (SPIE) Conference Series, page 2, aug 2014.

[30] T. Glassman, M. Novicki, M. Richards, D. Smith, S. Warwick, K. Patterson, and A. Harness. 2012 TDEM: Demonstration of Starshade Starlight-Suppression Performance in the Field. Final Report. Jet Propulsion Laboratory Publications, JPL Document 1469885, sep 2012.

[31] R. O. Gray, C. J. Corbally, R. F. Garrison, M. T. McFadden, E. J. Bubar, C. E. McGahee, A. A. O'Donoghue, and E. R. Knox. Contributions to the Nearby Stars (NStars) Project: Spectroscopy of Stars Earlier than M0 within 40 pc-The Southern Sample. AJ, 132:161–170, July 2006.

[32] A. Harness, W. Cash, A. Shipley, T. Glassman, and S. Warwick. New Worlds Airship. In *Techniques and Instrumentation for Detection of Exoplanets VI*, volume 8864 of *Proc. SPIE*, page 886407, September 2013.

[33] A. Harness, S. Warwick, A. Shipley, and W. Cash. Ground-based testing and demonstrations of starshades. In *Society of Photo-Optical Instrumentation Engineers (SPIE) Conference Series*, volume 9904 of *Proc. SPIE*, page 99043I, July 2016.

[34] C. Huygens. *Traité de la Lumière*. Leyden, 1690.

[35] John L Junkins, Declan C Hughes, Karim P Wazni, and Vatee Pariyapong. Vision-based navigation for rendezvous, docking and proximity operations. In *22nd Annual AAS Guidance and Control Conference, Breckenridge, CO*, pages 99–021. Citeseer, 1999.

[36] P. Kalas, J. R. Graham, E. Chiang, M. P. Fitzgerald, M. Clampin, E. S. Kite, K. Stapelfeldt, C. Marois, and J. Krist. Optical Images of an Exosolar Planet 25 Light-Years from Earth. *Science*, 322:1345, November 2008.

[37] P. Kalas, J. R. Graham, and M. Clampin. A planetary system as the origin of structure in Fomalhaut's dust belt. *Nature*, 435:1067–1070, June 2005.

[38] J. F. Kasting, D. P. Whitmire, and R. T. Reynolds. Habitable Zones around Main Sequence Stars. *Icarus*, 101:108–128, January 1993.

[39] Y. Kim, D. Sirbu, M. Galvin, N. J. Kasdin, and R. J. Vanderbei. Experimental study of starshade at flight Fresnel numbers in the laboratory. In *Society of Photo-Optical Instrumentation Engineers (SPIE) Conference Series*, volume 9904 of *Proc. SPIE*, page 99043G, July 2016.

[40] A. Kolmogorov. The Local Structure of Turbulence in Incompressible Viscous Fluid for Very Large Reynolds' Numbers. *Akademiia Nauk SSSR Doklady*, 30:301–305, 1941.

[41] Ravi Kumar Kopparapu, Ramses Ramirez, James F. Kasting, Vincent Eymet, Tyler D. Robinson, Suvrath Mahadevan, Ryan C. Terrien, Shawn Domagal-Goldman, Victoria Meadows, and Rohit Deshpande. Habitable zones around main-sequence stars: New estimates. *The Astrophysical Journal*, 765(2):131, 2013.

[42] F Künhe, J Gomes, and W Fetter. Mobile robot trajectory tracking using model predictive control. In *II IEEE latin-american robotics symposium*, 2005.

[43] P. Lawson. Exoplanet Exploration Program Technology Plan Appendix: 2013. *Jet Propulsion Laboratory Publications*, JPL Document D-8156, 2013.

[44] D. B. Leviton, W. C. Cash, B. Gleason, M. J. Kaiser, S. A. Levine, A. S. Lo, E. Schindhelm, and A. F. Shipley. White-light demonstration of one hundred parts per billion irradiance suppression in air by new starshade occulters. In *UV/Optical/IR Space Telescopes: Innovative Technologies and Concepts III*, volume 6687 of *Proc. SPIE*, page 66871B, September 2007.

[45] B. Lyot. The study of the solar corona and prominences without eclipses (George Darwin Lecture, 1939). *MNRAS*, 99:580, June 1939.

[46] W. Lyra and M. Kuchner. Formation of sharp eccentric rings in debris disks with gas but without planets. *Nature*, 499:184–187, July 2013.

[47] Bruce Macintosh, James R. Graham, Patrick Ingraham, Quinn Konopacky, Christian Marois, Marshall Perrin, Lisa Poyneer, Brian Bauman, Travis Barman, Adam S. Burrows, Andrew Cardwell, Jeffrey Chilcote, Robert J. De Rosa, Daren Dillon, Rene Doyon, Jennifer Dunn, Darren Erikson, Michael P. Fitzgerald, Donald Gavel, Stephen Goodsell, Markus Hartung, Pascale Hibon, Paul Kalas, James Larkin, Jerome Maire, Franck Marchis, Mark S. Marley, James McBride, Max Millar-Blanchaer, Katie Morzinski, Andrew Norton, B. R. Oppenheimer, David Palmer, Jennifer Patience, Laurent Pueyo, Fredrik Rantakyro, Naru Sadakuni, Leslie Saddlemyer, Dmitry Savransky, Andrew Serio, Remi Soummer, Anand Sivaramakrishnan, Inseok Song, Sandrine Thomas, J. Kent Wallace, Sloane Wiktorowicz, and Schuyler Wolff. First light of the gemini planet imager. Proceedings of the National Academy of Sciences, 111(35):12661–12666, 2014.

[48] C. Marchal. Concept of a space telescope able to see the planets and even the satellites around the nearest stars. Acta Astronautica, 12:195–201, 1985.

[49] P. Massey and C. B. Foltz. The Spectrum of the Night Sky over Mount Hopkins and Kitt Peak: Changes after a Decade. PASP, 112:566–573, April 2000.

[50] Michel Mayor and Didier Queloz. A jupiter-mass companion to a solar-type star. Nature, 378(6555):355–359, 11 1995.

[51] Grant McColley, Ph.D. The seventeenth-century doctrine of a plurality of worlds. Annals of Science, 1(4):385–430, 1936.

[52] B. Mennesson, S. Gaudi, S. Seager, K. Cahoy, S. Domagal-Goldman, L. Feinberg, O. Guyon, J. Kasdin, C. Marois, D. Mawet, M. Tamura, D. Mouillet, T. Prusti, A. Quirrenbach, T. Robinson, L. Rogers, P. Scowen, R. Somerville, K. Stapelfeldt, D. Stern, M. Still, M. Turnbull, J. Booth, A. Kiessling, G. Kuan, and K. Warfield. The Habitable Exoplanet (HabEx) Imaging Mission: preliminary science drivers and technical requirements. In Society of Photo-Optical Instrumentation Engineers (SPIE) Conference Series, volume 9904 of Proc. SPIE, page 99040L, July 2016.

[53] K. Miyamoto and E. Wolf. Generalization of the Maggi-Rubinowicz Theory of the Boundary Diffraction Wave - Part I. J. Opt. Soc. Am., 52:615, jun 1962.

[54] K. Miyamoto and E. Wolf. Generalization of the Maggi-Rubinowicz Theory of the Boundary Diffraction Wave - Part II. J. Opt. Soc. Am., 52:626, jun 1962.

[55] M. C. Noecker. Alignment of a terrestrial planet finder starshade at 20-100 megameters. In Society of Photo-Optical Instrumentation Engineers (SPIE) Conference Series, volume 6693 of Society of Photo-Optical Instrumentation Engineers (SPIE) Conference Series, page 6, September 2007.

[56] M. C. Noecker. Alignment control for an external-occulter terrestrial planet finder mission. In Journal of Guidance, Control, and Dynamics, volume 137, pages 10–39, feb 2010.

[57] M. Novicki. Starshade field testing and optical model validation. ExoPAG 15, 2016.

[58] M. Novicki, S. Warwick, D. Smith, M. Richards, and A. Harness. Suppression of Astronomical Sources Using Starshades and the McMath-Pierce Solar Telescope. In American Astronomical Society Meeting Abstracts, volume 227 of American Astronomical Society Meeting Abstracts, page 137.27, January 2016.

[59] M. Novicki, S. Warwick, D. Smith, M. Richards, and A. Harness. Suppression of astronomical sources using the McMath-Pierce Solar Telescope and starshades with flight-like optics. In Space Telescopes and Instrumentation 2016: Optical, Infrared, and Millimeter Wave, volume 9904 of Proc. SPIE, page 72, June 2016.

[60] B. R. Oppenheimer and S. Hinkley. High-Contrast Observations in Optical and Infrared Astronomy. ARA&A, 47:253–289, September 2009.

[61] N. M. Phillips, J. S. Greaves, W. R. F. Dent, B. C. Matthews, W. S. Holland, M. C. Wyatt, and B. Sibthorpe. Target selection for the SUNS and DEBRIS surveys for debris discs in the solar neighbourhood. MNRAS, 403:1089–1101, April 2010.

[62] W. H. Press, S. A. Teukolsky, W. T. Vetterling, and B. P. Flannery. Numerical recipes in C. The art of scientific computing. Cambridge: University Press, —c1992, 2nd ed., 1992.

[63] A. C. Quillen. Predictions for a planet just inside Fomalhaut's eccentric ring. MNRAS, 372:L14–L18, October 2006.

[64] M. S. Robbins and B. J. Hadwen. The noise performance of electron multiplying charge-coupled devices. IEEE Transactions on Electron Devices, 50:1227–1232, May 2003.

[65] A. Roberge, C. H. Chen, R. Millan-Gabet, A. J. Weinberger, P. M. Hinz, K. R. Stapelfeldt, O. Absil, M. J. Kuchner, and G. Bryden. The Exozodiacal Dust Problem for Direct Observations of Exo-Earths. PASP, 124:799–808, August 2012.

[66] F. Roddier. The effects of atmospheric turbulence in optical astronomy. Progress in optics. Volume 19. Amsterdam, North-Holland Publishing Co., 1981, p. 281-376., 19:281–376, 1981.

[67] S. Roeser and U. Bastian. A new star catalogue of SAO type. A&AS, 74:449–451, September 1988.

[68] C. Sagan, W. R. Thompson, R. Carlson, D. Gurnett, and C. Hord. A search for life on Earth from the Galileo spacecraft. Nature, 365:715–721, October 1993.

[69] E. Schindhelm, A. Shipley, P. Oakley, D. Leviton, W. Cash, and G. Card. Laboratory studies of petal-shaped occulters. In Techniques and Instrumentation for Detection of Exoplanets III, volume 6693 of Proc. SPIE, page 669305, September 2007.

[70] S. Seager, W. Bains, and J. J. Petkowski. Toward a List of Molecules as Potential Biosignature Gases for the Search for Life on Exoplanets and Applications to Terrestrial Biochemistry. Astrobiology, 16:465–485, June 2016.

[71] S. Seager and D. Deming. Exoplanet Atmospheres. ARA&A, 48:631–672, September 2010.

[72] S. Seager, M. Schrenk, and W. Bains. An Astrophysical View of Earth-Based Metabolic Biosignature Gases. Astrobiology, 12:61–82, January 2012.

[73] S. Seager, M. Turnbull, W. Sparks, M. Thomson, S. B. Shaklan, A. Roberge, M. Kuchner, N. J. Kasdin, S. Domagal-Goldman, W. Cash, K. Warfield, D. Lisman, D. Scharf, D. Webb, R. Trabert, S. Martin, E. Cady, and C. Heneghan. The Exo-S probe class starshade mission. In

Techniques and Instrumentation for Detection of Exoplanets VII, volume 9605 of Proc. SPIE, page 96050W, September 2015.

[74] M. D. SHUSTER and S. D. OH. Three-axis attitude determination from vector observations. Journal of Guidance, Control, and Dynamics, 4(1):70–77, 2016/09/18 1981.

[75] N. Siegler. Exoplanet Exploration Program Technology Plan Appendix: 2016. Jet Propulsion Laboratory Publications, JPL Document No. 1513240, 2016.

[76] D. Sirbu, N. J. Kasdin, and R. J. Vanderbei. Diffractive analysis of limits of an occulter experiment. In Space Telescopes and Instrumentation 2014: Optical, Infrared, and Millimeter Wave, volume 9143 of Proc. SPIE, page 91432P, August 2014.

[77] G. K. Skinner, B. R. Dennis, J. F. Krizmanic, and E. P. Kontar. Science enabled by high precision inertial formation flying. ArXiv e-prints, November 2013.

[78] D. Smith, S. Warwick, T. M. Glassman, M. C. Novicki, M. C. Richards, A. Harness, and K. D. Patterson. Measurements of high-contrast starshade performance in the field. In Society of Photo-Optical Instrumentation Engineers (SPIE) Conference Series, volume 9904 of Proc. SPIE, page 99043K, July 2016.

[79] Gary E. Sommargren and H. Joseph Weaver. Diffraction of light by an opaque sphere. 1: Description and properties of the diffraction pattern. Appl. Opt., 29(31):4646–4657, Nov 1990.

[80] M. Sorgenfrei, D. Kemp, A. Harness, and M. Nehrenz. Validation of a low-cost avionics package for small spacecraft via rocket-based field tests. In AIAA Science and Technology Forum and Exposition, 2017. Grapevine, Texas.

[81] M. Sorgenfrei, M. Nehrenz, R. Edwards, and S. Joshi. Formulation of a small spacecraft avionics testbed. In Proc. of AAS Guidance, Navigation, and Control Conference, 2014. Breckenridge, CO.

[82] D. Spergel, N. Gehrels, C. Baltay, D. Bennett, J. Breckinridge, M. Donahue, A. Dressler, B. S. Gaudi, T. Greene, O. Guyon, C. Hirata, J. Kalirai, N. J. Kasdin, B. Macintosh, W. Moos, S. Perlmutter, M. Postman, B. Rauscher, J. Rhodes, Y. Wang, D. Weinberg, D. Benford, M. Hudson, W.-S. Jeong, Y. Mellier, W. Traub, T. Yamada, P. Capak, J. Colbert, D. Masters, M. Penny, D. Savransky, D. Stern, N. Zimmerman, R. Barry, L. Bartusek, K. Carpenter, E. Cheng, D. Content, F. Dekens, R. Demers, K. Grady, C. Jackson, G. Kuan, J. Kruk, M. Melton, B. Nemati, B. Parvin, I. Poberezhskiy, C. Peddie, J. Ruffa, J. K. Wallace, A. Whipple, E. Wollack, and F. Zhao. Wide-Field InfrarRed Survey Telescope-Astrophysics Focused Telescope Assets WFIRST-AFTA 2015 Report. ArXiv e-prints, March 2015.

[83] LYMAN SPITZER. The beginnings and future of space astronomy. American Scientist, 50(3):473–484, 1962.

[84] C. C. Stark, E. J. Cady, M. Clampin, S. Domagal-Goldman, D. Lisman, A. M. Mandell, M. W. McElwain, A. Roberge, T. D. Robinson, D. Savransky, S. B. Shaklan, and K. R. Stapelfeldt. A direct comparison of exoEarth yields for starshades and coronagraphs. In Society of Photo-Optical Instrumentation Engineers (SPIE) Conference Series, volume 9904 of Proc. SPIE, page 99041U, July 2016.

[85] C. C. Stark and M. J. Kuchner. The Detectability of Exo-Earths and Super-Earths Via Resonant Signatures in Exozodiacal Clouds. ApJ, 686:637–648, October 2008.

[86] C. C. Stark, A. Roberge, A. Mandell, and T. D. Robinson. Maximizing the ExoEarth Candidate Yield from a Future Direct Imaging Mission. ApJ, 795:122, November 2014.

[87] C. C. Stark, S. Shaklan, D. Lisman, E. Cady, D. Savransky, A. Roberge, and A. M. Mandell. Maximized ExoEarth Candidate Yields for Starshades. ArXiv e-prints, May 2016.

[88] M. C. Turnbull, T. Glassman, A. Roberge, W. Cash, C. Noecker, A. Lo, B. Mason, P. Oakley, and J. Bally. The Search for Habitable Worlds. 1. The Viability of a Starshade Mission. PASP, 124:418–447, May 2012.

[89] R. J. Vanderbei, E. Cady, and N. J. Kasdin. Optimal Occulter Design for Finding Extrasolar Planets. ApJ, 665:794–798, August 2007.

[90] S. Warwick. Starshade field tests. ExoPAG 13, 2015.

[91] G. N. Watson. A treatise on the theory of Bessel functions. Cambridge, [Eng.]: The University press, 1922., 1922.

[92] M. Wenger, F. Ochsenbein, D. Egret, P. Dubois, F. Bonnarel, S. Borde, F. Genova, G. Jasniewicz, S. Laloë, S. Lesteven, and R. Monier. The SIMBAD astronomical database. The CDS reference database for astronomical objects. A&AS, 143:9–22, April 2000.

[93] M. C. Wyatt. Evolution of Debris Disks. ARA&A, 46:339–383, September 2008.

[94] B. Zuckerman. Dusty Circumstellar Disks. ARA&A, 39:549–580, 2001.